GRAPHENE MODIFIED INDIUM TIN OXIDE ELECTRODES FOR ORGANIC SOLAR CELLS

CHANG CI'EN SHARON

(B. Sc.(Hons.), NATIONAL UNIVERSITY OF SINGAPORE)

A THESIS SUBMITTED

FOR THE DEGREE OF DOCTOR OF PHILOSOPHY

NUS GRADUATE SCHOOL FOR INTEGRATIVE SCIENCES AND ENGINEERING

NATIONAL UNIVERSITY OF SINGAPORE

&

DEPARTMENT OF MATERIALS

IMPERIAL COLLEGE LONDON

2014

Declaration

I hereby declare that this thesis is my original work and it has been written by me in its entirety. I have duly acknowledged all the sources of information which have been used in the thesis.

This thesis has also not been submitted for any degree in any university previously.

Chang Ci'En Sharon

28 July 2014

Dedicated to my loving family and my partner

Acknowledgement

Praise God from whom all blessings flow

These four years of PhD could not have been made possible without the help of many people who rendered assistance at work, gave a listening year, or blessed me with their friendship and prayers. To begin, I would like to express my gratitude towards my supervisors, Prof Andrew Wee and Sandrine Heutz, for their invaluable support, advice and guidance that goes beyond the sciences; for knowing when to push me to achieve more, and when to encourage a break to refresh and take stock. Chen Wei and David McPhail, as part of my thesis advisory committee, also provided timely feedback and useful discussions.

I would like to thank my colleagues past and present in the Surface Science Lab NUS, in Heutz's group in the ICL, and in the LCN office. Their friendship and aid, shared joys and grieves, encouragement and small talks, helped me through the bleak parts of my PhD (and the bleak London winter). I would like to specially thank Hendrik Glowatzki, Cao Liang, Wei Da Cheng, Wang Rui, Luke Fleet and James Gilchrist who invested so much time and energy in imparting experimental techniques and safety considerations; patiently discussed and analysed experimental data; and even advising on the finer details such as the presentation of data. Their integrity and rigor towards proper scientific methodology and data handling have left a lasting impression on me. I am grateful to the assistance of Kendra Kam and Dr. Chua Lay Lay for the provision of some of the samples for synchrotron measurements, to James for his partnership with all the solar cell device work, and to Sarah Fearn for her expertise with all the TOF-SIMS measurements.

These people beyond the scope of work have also played an integral part in this process: Fish, Nadia, Clarence, Jiahui, Cedric, Boredin, Valerie, Peggy, Ivy, Aunt Sau Har and the many others

behind the scenes whom I cherish in my heart. I am deeply indebted to my loving family throughout all these years who encouraged and prayed for me; who selflessly sacrificed their time, energy, sleep and resources to walk this journey with me. Thank you for being my pillar of support throughout all the years of my life, for being my best friends, and for making this dream of graduate studies a reality. Finally, to my dearest Taffy, who embarked on life's journey together with me over the last five and a half years, thank you for loving, blessing, and waiting for me.

List of Publications

Gilchrist, J. B., Basey-Fisher, T. H., Chang, S. C' E.*, Scheltens, F., McComb, D. W. & Heutz, S. Uncovering the Buried Interface in Molecular Photovoltaics. *Adv. Funct. Mater.* **24**, 6473-6483 (2014).

Chang, S. C' E.*, Fearn, S., McPhail, D., Wee, A. T. S. & Heutz, S. TOF-SIMS Investigation of F4-TCNQ Diffusion Through CuPc Molecules. *In preparation (2014).*

Chang, S. C' E.*, Liang, C., Gilchrist, J. B., Wei, C., Heutz, S. & Wee, A. T. S. Molecular Modification of Graphene to Control the Structural and Electronic Properties of CuPc in Organic Solar Cells. *In preparation (2014).*

Chang, S. C' E.*, Liang, C., Wei, C., Heutz, S. & Wee, A. T. S. Thin Film Properties of F_4-TCNQ as an Interface Dopant on ITO and Graphene Modified ITO. *In preparation (2014).*

Table of Contents

Summary

In this thesis, we explore the use of graphene incorporated onto indium tin oxide (G/ITO) as a structural template to modify the orientation of copper phthalocyanine (CuPc) molecules for organic photovoltaic (OPV) device applications. We also investigate the effectiveness of 2,3,5,6-tetrafluoro-7,7,8,8-tetracyanoquinodimethane (F_4-TCNQ) as a work function modifier for G/ITO without compromising the templating properties of graphene. Photoemission spectroscopy (PES) is employed to assess the electronic properties at the anode-CuPc interface, while X-ray diffraction (XRD) and near-edge X-ray absorption fine structure (NEXAFS) are used to determine the molecular orientation of CuPc. OPV devices are fabricated to attempt to correlate the observations at the microscopic level with the macroscopic device performance.

First, we investigate the electronic properties of CuPc deposited on G/ITO and ITO using PES. While the interaction between CuPc molecules and ITO and G/ITO is similar, the hole injection barrier (HIB) is ~0.9 eV for CuPc/G/ITO as compared to 0.5 eV for CuPc/ITO. Therefore, further modification of G/ITO to reduce the HIB is required. The XRD spectrum of CuPc molecules deposited onto graphene grown on copper foil (G/Cu) verifies that graphene is an effective structural template, causing CuPc molecules to 'lie' on the substrate. NEXAFS data shows that the orientation of CuPc molecules changes from 'standing' on ITO to 'tilted' on G/ITO.

Next, the effectiveness of F_4-TCNQ deposited on ITO and G/ITO as a work function modifier is assessed. A thin layer of F_4-TCNQ is able to increase the substrate work function to ~5 eV, which is close to the ionization potential of CuPc molecules. This suggests that barrierless extraction of holes from CuPc into F_4-TCNQ modified ITO or G/ITO may be possible. F_4-TCNQ molecules are found to be predominantly tilted on G/ITO, suggesting that the templating property of graphene may be propagated through F_4-TCNQ molecules. CuPc molecules deposited onto F_4-TCNQ/G/ITO attain a 'lying' configuration, confirming that the templating property of graphene

is preserved despite the inclusion of a layer of F_4-TCNQ. The HIB is dramatically reduced to ~0.2 eV for CuPc/F_4-TCNQ/G/ITO, and ~0.1 eV for CuPc/F_4-TCNQ/ITO. Optical absorption of templated CuPc molecules over the visible range is enhanced by over 40% as compared to the non-templated molecules. Therefore, the structure of F_4-TCNQ/G/ITO appears to be a potential anode design to improve OPV device performance. Our test cells however do not show an improvement in OPV parameters due to the poor quality of transferred graphene, and the high series resistance in our unoptimized OPV device.

Finally, the diffusion of F_4-TCNQ through a CuPc film is studied using time-of-flight secondary ion mass spectrometry (TOF-SIMS). The F^- depth profiles establish that a higher quantity of F_4-TCNQ molecules diffuse into CuPc on the G/ITO sample. This is attributed to the weaker interfacial adhesion between F_4-TCNQ and graphene, and the crystallinity of the templated CuPc film. The quantity of diffused F_4-TCNQ in the G/ITO sample is only about 0.2 mol%. At this dopant concentration, the conductivity of the film should increase; thus doping of the whole organic film may be favourable for OPV devices.

List of Tables

List of Figures

List of Abbreviations

AFM	Atomic Force Microscopy
Al	Aluminium
BCP	Bathocuproine
BE	Binding Energy
Bi	Bismuth
C_{60}	Fullerene
Cs	Caesium
CuPc	Copper Phthalocyanine
D/A	Donor-Acceptor Interface
DOS	Density of States
E_F	Fermi Level
F_4-TCNQ	2,3,5,6-Tetrafluoro-7,7,8,8-tetracyanoquinodimethane
FF	Fill Factor
G/ITO	Graphene modified Indium Tin Oxide deposited on Glass
G/Cu	Graphene grown on Copper foil
G/Si	Graphene modified Silicon
HOMO	Highest Occupied Molecular Orbital
HIB	Hole Injection Barrier

IP	Ionization Potential
ITO	Indium Tin Oxide deposited on Glass
J_{sc}	Short Circuit Current
KE	Kinetic Energy
LUMO	Lowest Occupied Molecular Orbital
NEXAFS	Near-Edge X-ray Absorption Fine Structure
OMBD	Organic Molecular Beam Deposition
OPV	Organic Photovoltaic
OSC	Organic Semiconductors
PES	Photoemission Spectroscopy
PTCDA	Perylene-3,4,9,10-tetracarboxylic dianhydride
QCM	Quartz Crystal Microbalance
RMS	Root Mean Square
R_S	Series Resistance
R_{sh}	Shunt Resistance
SEM	Scanning Electron Microscopy
Si	Silicon
TC_{hkl}	Texture Coefficient of the (h k l) plane
TEM	Transmission Electron Microscopy
TOF-SIMS	Time-of-Flight Secondary Ion Mass Spectrometry

UPS	Ultraviolet Photoelectron Spectroscopy
UV-Vis	Ultraviolet-Visible
V_{oc}	Open Circuit Voltage
XPS	X-ray Photoelectron Spectroscopy
XRD	X-Ray Diffraction
α	Angle between the molecular and substrate planes
θ	Angle between the incident beam and substrate plane
Φ	Work function
θ_{CuPc}(Å)	CuPc film thickness in Å
$\theta_{F4\text{-}TCNQ}$(Å)	F_4-TCNQ film thickness Å

Chapter 1 : Introduction

This chapter serves to provide an overview of the key areas relevant to this thesis. To begin with, an introduction to organic solar cells and its basic working principles will be briefly presented. Following which, structural templating as a method to control the molecular orientation of the donor molecules, and the importance of energy level alignment in an organic solar cell will be discussed to provide a background for the work in this dissertation. Lastly, the structure of copper phthalocyanine (CuPc) molecules, which will be used extensively in this investigation, will be described.

1.1 Organic Photovoltaics Devices

The harvesting of energy directly from sunlight using photovoltaic devices (PV) is an essential component in renewable energy production. PV using organic semiconducting (OSC) materials, or organic photovoltaic (OPV) devices, have attracted much attention since Tang demonstrated a ~1% power conversion efficiency (PCE) in 1986 using a single donor/acceptor (D/A) heterojunction.[1] Coupled with the potential for low cost production, low weight, increased device lifetimes, and tuneable electronic and structural properties, OPV devices are increasingly popular as an energy source.[2–7] Although rapid improvements have been made in OPV devices over the past three decades with the PCE up to ~8% for single heterojunction solar cells,[6–8] and ~10% for tandem solar cells,[9] these values fall well short of the 24% achieved for crystalline silicon-based PV.[10] Therefore, considerable research has to be undertaken to improve the performance of OPV devices to make them commercially viable. To design strategies for device improvement, it is necessary to understand the basic working principles and intrinsic limitations of OPV devices. For this dissertation, we will focus on phthalocyanine-based small molecule OPV devices as they have well-defined molecular structures, easily achieved chemical purity and better batch-to-batch reproducibility.[6] In particular, they serve as well defined systems and are compatible with

vacuum based deposition systems for the investigation of fundamental interface energetics and structural properties.

1.1.1 Basic Properties of OPV Devices

A basic OPV device consists of a transparent front anode through which light enters the device, an active layer of p-type donors and n-type acceptor OSC materials, a back cathode, and optional intermediate layers such as electron or hole blocking layers (Figure 1-1). The materials used for each layer in this dissertation are labelled in Figure 1-1. The ability of OSC materials to absorb visible light and transport charges is due to the hybridization of the carbon atoms, leading to the formation of π-conjugated electron systems.[11,12] The main (idealized) processes for converting light into energy can be described in the following steps: 1) *Absorption* of photons by the active layer, leading to the formation of excitons. 2) *Diffusion* of the excitons towards the D/A interface, 3) *separation* of the excitons into Coulombically bound electron-hole pairs, and subsequently into free charges due to an energetic offset. 4) Subsequently, *charge transport* to the electrodes with the aid of a built-in electric field that originates from the different work functions of the chosen electrodes and 5) *collection* of the charges at the electrodes.[13–15]

There are several challenges involved with OSC materials[16] that limit the current efficiency of OPV devices as compared to inorganic PV. OSC materials have low dielectric constants ε (ε ~4.5),[2,17,18] resulting in exciton binding energies (E_b) of up to 1 eV.[19] Therefore excitons are unable to dissociate immediately into free charges upon formation. The excitons have to diffuse to the D/A interface, without recombining, where a sharp potential drop at the interface results in charge separation.[1] This process is limited by the exciton diffusion length of around ~10 nm,[20] which is smaller than the thickness of the film required for efficient light absorption.[2,17,21] OSC materials are associated with low carrier mobilities typically between 10^{-5} – 10^{-1} cm^2/Vs due to the limited π-orbital overlap and numerous defects in the (poly)crystalline film.

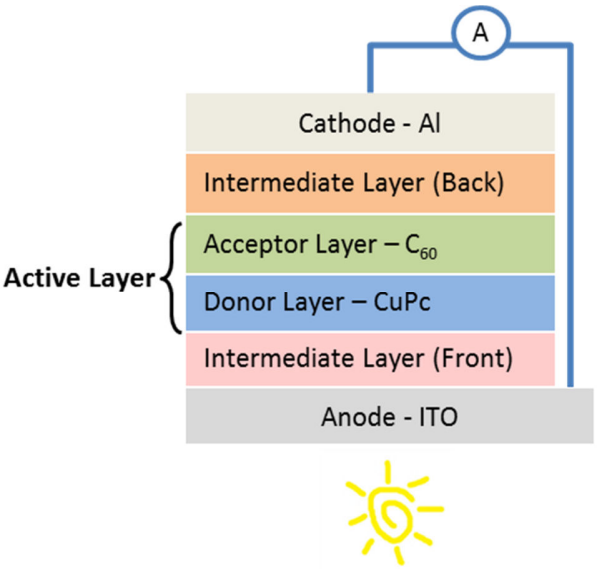

Figure 1-1 A schematic drawing showing the typical layers in an OPV device. The materials used in this dissertation are annotated in the diagram; for the intermediate layers, the front layer is graphene and F_4-TCNQ, and the back layer is BCP. A planar heterojunction is shown for simplicity. Light enters the cell from the anode side.

Over the years, strategies have been developed to enhance the absorption strength and the exciton diffusion length, the efficiency of charge separation at the D/A interface and charge carrier mobility. These strategies include the chemical synthesis of new materials, improving the design architecture of OPV devices, controlling the structure and crystalline order, and optimizing the interface electronic properties.[2,6,7,9,15,18,21–25] For example, using small molecules with the donor and acceptor groups incorporated in a single unit has shown to be an efficient method to increase device performance through efficient exciton transport and separation.[6,9] In terms of design architecture, bulk heterojunction PV which consists of an interpenetrating network of donor and acceptor materials in the active layer, reduces the distance between an exciton and a D/A interface without compromising the optical absorption of the film.[22,23] Tandem solar cells are able to capture a wider spectrum of light by utilizing two complementary stacked solar cells.[26] Interface layers may also be introduced at the electrodes (Figure 1-1). These layers may serve several purposes, including limiting charge recombination at the electrodes, adjusting the energetic barrier height and preventing physical and chemical damage between the electrodes and the active layers.[15] They can also improve OPV devices performance by controlling the molecular

orientation of the organic film through structural templating.[27–29] More details regarding structural templating in planar heterojunction OPV devices (Figure 1-1), which will form the backbone of this thesis, are presented in the next section.

1.1.2 Structural Templating in OPV Devices

Structural templating in OPV devices refers to the control of molecular orientation and crystallinity of the active layer film by altering the surface property of the substrate, such as through the introduction of an interfacial (template) layer. OSC films are made up of individual molecules held together by weak Van der Waals interactions; therefore, their physical properties are dependent on the coupling between adjacent molecules. Furthermore, the anisotropy inherent to planar OSC molecules implies that charge and exciton transport depends on the orientation of the molecules. For example, the peak charge mobility in planar copper phthalocyanine (CuPc) thin films is found along the one-dimensional stacking axis (Figure 1-2) due to enhanced intermolecular orbital overlap. High hole mobility of around ~1 cm^2/Vs has been observed along the stacking direction,[30,31] while that between stacks is estimated to be 10^{-3} cm^2/Vs.[32] The works by Rand *et al.*[28] and Irkhin *et al.*[33] reveal that exciton diffusion is also enhanced along the stacking axis of planar molecules. Furthermore, the relative orientations of the donor and acceptor molecules in OPV devices affect the coupling at the D/A interface which has direct impact on the charge separation efficiency.[28,34] Optical absorption by planar organic molecules is likewise anisotropic since it depends on the overlap between the transition dipole moment and the electric field vector. For planar phthalocyanines, stronger optical absorption in the visible range is observed when the molecules are perpendicular to the incident beam as the transition dipole lies in the plane of the molecule.[28,29,35] Therefore, the thickness of the active layer required to absorb the incoming photons can be reduced, consequently reducing the distance between the excitons generated and a D/A interface. In view of the simultaneous enhancement of these properties by

controlling the molecular orientation of the active layer, structural templating is a promising route to improving OPV device performance.

For planar heterojunction OPV devices, it is desirable for the planar donor molecule within thin films to stack with their molecular planes parallel to the substrate, i.e. 'lie flat' on the substrate [Figure 1-2 (b)]. In this orientation, exciton and charge transport is favoured in the vertical direction (perpendicular to the electrodes), charge separation at the D/A interface is enhanced, and the light absorption strength is increased. However, phthalocyanines as the donor layer tend to pack with their molecular planes perpendicular to the electrode [typically indium tin oxide (ITO)] substrate, or 'standing' orientation as shown in Figure 1-2 (a), due to stronger intermolecular than interfacial interactions.[36] Examples of structural template that have been used to modify the orientations of phthalocyanines such that the molecules lie parallel to the substrate include perylene-3,4,9,10-tetracarboxylic dianhydride (PTCDA),[24,37–39] pentacene,[40] copper(I) iodide (CuI),[28,29] and graphene.[32,41–43] Regardless of the template layer, the underlying principle that bestows the templating ability originates from the stronger template layer-molecule interaction.

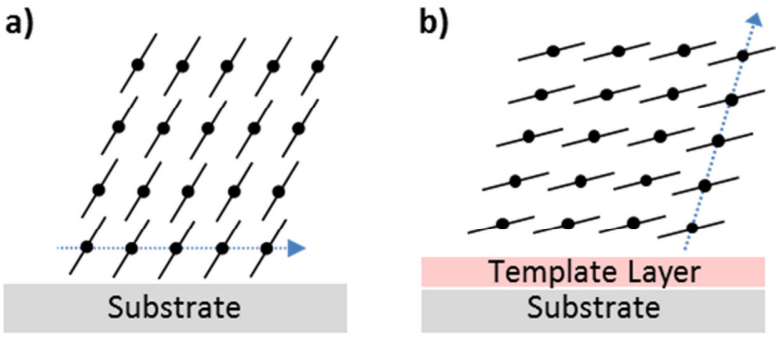

Figure 1-2 Schematic drawings showing the effect of structural templating on planar molecules. Individual molecules are shown and the direction of the stacking axis is indicated by the dashed arrow. (a) 'Standing' orientation of the molecules before templating, and (b) the 'lying' orientation with the inclusion of a template layer.

While templating the donor layer in OPV devices has several advantages as detailed in the preceding paragraphs, it should be noted that this may not translate directly into improved device performance. This is because 1) the interfacial energetics may be disrupted with the insertion of the template layer, 2) the optical absorptivity by the template layer may be too high, or the layer is opaque, 3) the crystallinity or morphology of the donor layer is modified, and 4) unfavourable chemical interaction between the template and active layers (or substrate and template layer) may occur. Using a PTCDA structural template for a CuPc-fullerene OPV device, Sullivan *et al.* observe an increase in short circuit current (J_{sc}) for the templated (lying) CuPc molecules as compared to a reference unmodified OPV device.[24] This has been attributed to the improved charge mobility perpendicular to the substrate. However, an insulating PTCDA layer with a deep HOMO level hinders effective charge extraction at the anode by introducing a ~1.5 eV barrier, consequently reducing the open-circuit voltage (V_{oc}). Separately, Lassiter *et al.* note that the RMS roughness of CuPc increased by a factor of more than two by introducing a PTCDA layer, and the surface becomes more uneven.[37] The absorption spectrum of PTCDA overlaps with the absorption of phthalocyanine molecules, thereby reducing the amount of reaching the active layer in organic solar cells by ~20% for 10 nm thick PTCDA templating layer.[38] Pentacene structural template has a more favourable energy level as compared to PTCDA, but causes the morphology of H_2Pc to change dramatically from elongated crystallites of ~200 nm in length, to ~30 nm spherical crystallites with numerous grain boundaries.[40] Thus there was no improvement in the overall PCE of the device. In the past two years, CuI has been discovered as a potential structural template layer. To date, reports have shown that it can simultaneously raise the work function of ITO, enhance light absorption, and smooth the rough surface of ITO.[28,29] A drawback however is that slow growth rates of ~0.05 Å/s is required for the deposition of CuI, or undesirably large crystals may form which can cause shorting in OPV devices.[44] These examples indicate that in order for structural templating to realise its full potential, the layers have to be carefully chosen, or further modifications (e.g. annealing, surface functionalization etc.) may be required.

More recently, graphene has been used as a structural template.[32,41–43,45] Graphene is a two-dimensional single layer of carbon atoms arranged in a honeycomb structure. It is chemically inert and thermally stable,[46] absorbs only ~2.3% of visible light per layer and has uniformly high transmittance in both visible and IR regions.[47] Furthermore, graphene sheets show low interfacial contact resistance with organic materials[46] and similar work function range as ITO.[42,45] These properties suggest that graphene is well-suited as a template layer in OPV devices without introducing high resistance charge injection barrier and reducing the amount of light transmitted to the active layer. Using graphene as a template layer will be the focus of this thesis.

An important consideration concerning the change in orientation of the donor molecules is the modification of the energy level of the molecules. The dependence of the ionization potential (IP) energy on the orientation of molecules has been reported.[48,49] For CuPc molecules, a difference of up to 0.4 eV between the lying and standing orientations have been observed due the oriented C-H dipoles at the exposed surface for the standing orientation.[50,51] This directly affects the energetic offsets at the D/A interface,[52] and can contribute to a build-up of holes at the electrode. The importance of the energy level alignment in OPV devices will be briefly covered in the next section.

1.1.3 Energy Level Alignment in OPV Devices

An OPV device is made up of several interfaces between materials that have different electronic energy levels. The respective energy levels are crucial in determining the efficiency of charge separation and collection. Here we briefly mention some of the essential energetic considerations.

The difference in work functions between the front anode and the back cathode creates an internal field in an OPV devices which aids in the separation of the photoinduced charges at the D/A interface.[25,53] The work function of the front (back) electrode is usually larger (smaller) than the back (front) electrode so that holes (electrons) are collected at the front (back) electrode. A

reverse order in the magnitude of the work functions would cause charges to flow in the opposite direction, such as in an inverse OPV device. The built-in electric field from the electrodes alone is insufficient to overcome E_b; therefore an additional potential drop at the D/A interface is required for exciton separation as shown in Figure 1-3. If E_b is smaller than the lowest unoccupied molecular orbital (LUMO) offset between the donor and acceptor ($LUMO_A$ - $LUMO_D$), exciton separation at the D/A interface is favoured (Figure 1-3).[53] The difference in $HOMO_D$ - $LUMO_A$ is also correlated to the maximum V_{oc} attainable.[3,54]

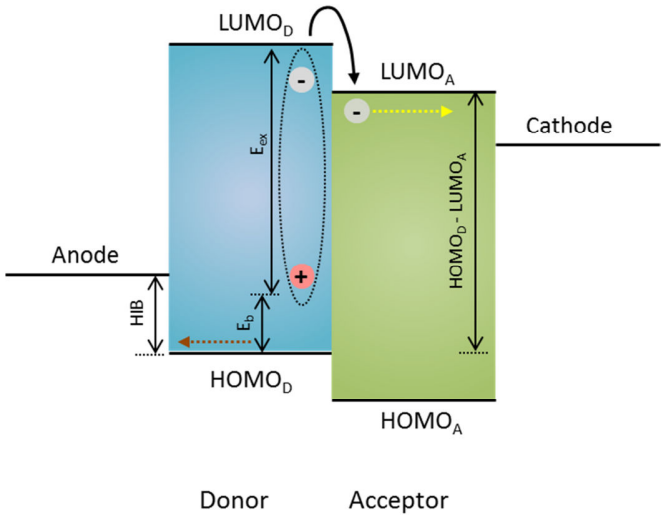

Figure 1-3 Schematic drawing showing the energy levels in an OPV. E_{ex} and E_b refer to the Coulombically bound exciton energy and exciton binding energy respectively. The HOMO and LUMO positions of the donor (subscript D) and acceptor (subscript A) materials, and the HIB are also shown. The dashed arrows in the donor and acceptor bands indicate the directions of the hole and electron diffusion respectively.

After the charges have separated and diffused to the electrodes, the energy offset between the organic layer and the electrode can limit the charge collection efficiency and recombination of charges. Ideally an ohmic contact between the work function of the anode (cathode) and the HOMO (LUMO) of the donor (acceptor) molecule is desirable for barrierless charge extraction. The anode (ITO) portion of an OPV device will be investigated in this thesis. We propose that complementary strategies may apply to the cathode to reduce the barrier for charge extraction. For phthalocyanines and commonly used polymers in OPV devices, the HOMO level is usually >5 eV[55] while the work function of ITO ranges from 3.7 eV – 5.1 eV.[56–60] To reduce the energy

gap between the HOMO of the donor and the work function of the anode, or hole injection barrier (HIB), high ITO work function is desirable. The significant variability in the anode work function necessitates that, to be commercially viable, consistent and reliable methods of adjusting the substrate work function to ~5 eV are required to ensure reproducibly high performance between different batches of OPV devices. This can be accomplished by exposing the ITO surface to plasma or acid treatments,[56,57,61] or by coating the ITO with high work function materials [62] including, but not limited to, the polymer poly(ethylenedioxythiophene) doped with poly(styrenesulfonate) (PEDOT:PSS),[63] metal oxides[64,65] such as MoO_x and V_2O_5, and small molecules to manipulate the surface dipole[66] like 2,3,5,6-Tetrafluoro-7,7,8,8-tetracyanoquinodimethane (F_4-TCNQ).[67] While these interfacial materials may be successful at increasing the effective sample work function, they may also suffer from some drawbacks. For example PEDOT:PSS is highly acidic and has been reported to corrode ITO and organic layers[68] and it has non-uniform conductivity throughout the film.[69] The work function of the metal oxide MoO_x is reported to be unstable in air and moisture, decreasing by over 1.2 eV due to exposure to air,[70] while F_4-TCNQ is found to be able to diffuse through organic small molecule active layers.[71] Thus, careful selection of these materials is crucial to minimize the detrimental effect on the OPV device system.

As a concluding statement, it should be noted that the energy levels discussed in this short section assume an idealised case of flat band energy levels. However, this is often not the case due to electronic coupling and band bending at the D/A interface,[34,42] the formation of surface or interface dipoles[72,73] etc. for the organic-organic heterojunction interfaces.[50] Comprehensive insights into the processes at the various interfaces can be found in the literature.[74,75]

1.2 Structural Properties of CuPc

CuPc (chemical formula $C_{32}H_{16}CuN_8$) is a planar, highly symmetrical small molecule with lateral dimensions of around 1.4 nm[76] as shown in Figure 1-4 (a). They are π-conjugated systems with electrons delocalised around the aromatic structure. CuPc molecules belong to a class of metal-organic molecules which possess semiconducting properties.[77] Chemical flexibility of this class of molecules allows tailoring of the physical, electronic and optical properties by altering the central metal ion or periphery atoms.[78] CuPc and other phthalocyanine molecules absorb strongly in the range of 620 – 720 nm with high extinction coefficient in the range of 10^5 $Lmol^{-1}cm^{-1}$.[79]

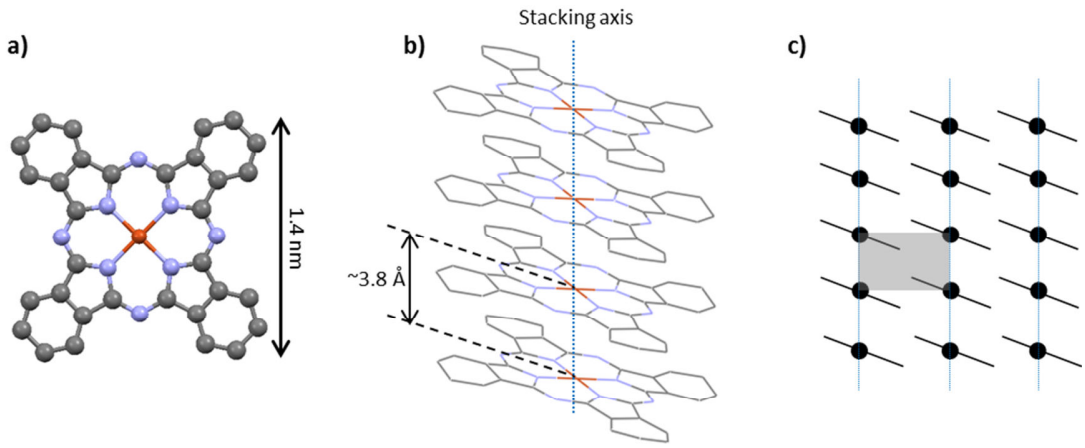

Figure 1-4 (a) Chemical structure of a CuPc molecule. The structure consists of carbon atoms (grey), nitrogen atoms (blue) and a central Cu (red). (b) Geometric illustration of a CuPc column, and (c) a brick-stack arrangement of the one-dimensional CuPc column as proposed by Hoshino.[86] The grey shaded area in (c) represents a 2-dimensional unit cell.

Therefore these molecules were used as dyes and pigments due to their intense blue colour prior to the discovery of their semiconducting properties.[78] Since then, research into phthalocyanines has progressed to find applications in optoelectronic devices and field effect transistors to name a few examples.[1,27,80–84] These molecules have great potential in organic semiconductors since they are low cost, easy to purify and deposit, and are thermally and chemically stable.[85]

CuPc molecules pack cofacially to form a one-dimensional columnar structure as shown in Figure 1-4 (b), held together by intermolecular Van der Waals and π-π interactions. The π-π orbital

overlap between adjacent molecules enables electron delocalization along the stacking axis of the column. There is more than one crystalline form of CuPc (polymorphism), but only the α-polymorph, which is the most common form for room temperature deposition,[86] will be discussed since this is the condition used in this thesis. The most acceptable form of the α-polymorph is that determined by Hoshino *et al.* [38,86,87] which defines a brick-stack arrangement of the CuPc one-dimensional columns such as that shown in Figure 1-4 (c). The stacking axis is parallel to the substrate when CuPc is deposited on non-chemically interacting substrates such as ITO, SiO_2 and glass,[36] concomitantly suggesting that the π-π interaction dominates over the interfacial interactions. However on substrates such as HOPG[49] and PTCDA,[24] the crystal structure is maintained but the whole brick-stack structure is rotated by nearly 90^o so that the stacking axis is perpendicular to the substrate, similar to the schematic illustrations in Figure 1-2 (b).

1.3 Thesis Overview

While small molecule OPV devices have been researched intensively over the past decade, their performance is still unable to match that of their inorganic counterparts. Hence, it is of interest to understand the physical limitations of these devices and to develop strategies to overcome them. In particular there is an intimate structure-function relationship of planar donor molecules since the physical properties of the film depend strongly on the degree of orbital overlap between adjacent molecules. As discussed in Section 1.1.2, light absorption, the exciton diffusion length and charge mobility may be simultaneously enhanced by controlling the orientation of the molecules in the donor layer. This can be achieved through the use of a structural template layer. However, the introduction of a template layer and the change in molecular orientation will alter the energy levels of the OPV devices. It is therefore beneficial to study the structural and electronic properties of the donor layer at the anode interface in tandem. This will enable us to control and tailor the interfacial energetics according to the requirements of the modified donor layer.

In this thesis, we focus on understanding the processes at the anode side of a planar heterojunction OPV device, in particular the energy level alignment at interfaces and structural properties of the thin film. The materials and experimental investigations are selected to impact an actual OPV device configuration. We select the widely used CuPc as the planar donor layer due to its well defined structure-function relationship. The isomorphous nature across planar phthalocyanines means the results from this thesis can be readily extended to other planar phthalocyanines. ITO will be used as the anode as it is readily and commercially available, and also widely used in solar cell devices. Our focus will be on the CuPc/ITO region in a well-studied OPV device architecture of aluminium/Bathocuproine (BCP)/Fullerene C_{60}/CuPc/ITO.

The aim of this thesis is to use a combination of structural templating using graphene, and *simultaneous* modification of the work function using F_4-TCNQ, to control both the orientation and electronic properties of CuPc in an OPV device. We perform step-wise modification of the CuPc/ITO structure by first focussing on the control of the orientation of CuPc using graphene transferred onto ITO (G/ITO) in Chapter 3. The associated electronic properties of the samples are investigated concurrently, especially since we predict unfavourable energy level alignment at the CuPc-G/ITO interface based on literature data for graphene and CuPc. In Chapter 4, we address the energy level misfit between CuPc and G/ITO by proposing to use F_4-TCNQ to increase the substrate work function. It is essential that the work function modifier does not disrupt the templating property of graphene. Therefore, the work function modification ability of F_4-TCNQ and its thin film properties are examined in this chapter to determine its suitability. Chapter 5 investigates the effect of combining the strategies proposed in Chapters 3 and 4 to simultaneously control the orientation of CuPc and substrate work function, and to assess the effectiveness of interface doping of graphene with F_4-TCNQ on CuPc. The electronic, structural and optical properties of the resulting structure CuPc/F_4-TCNQ/G/ITO are investigated. We finally attempt to fabricate OPV devices based on this structure to understand the limitations of

our proposed system. The experimental investigation concludes in Chapter 6 with an investigation and discussion concerning the diffusion of F_4-TCNQ through CuPc film. A summary of the flow and cohesion of the chapters is shown in Figure 1-5.

The key techniques that are employed to study the organic molecule-anode systems are photoemission spectroscopy (PES), near edge X-ray absorption fine structure measurements (NEXAFS), and X-ray diffraction (XRD) measurements. NEXAFS and XRD enable us to study the structural properties of the donor film on ultra-thin and bulk films respectively on ITO and G/ITO, and to elucidate the efficacy of transferred graphene as structural template. The effects of physical modification of the anode and structural modifications of CuPc on the electronic properties are mapped out via PES measurements. OPV devices are fabricated to correlate the phenomena observed at the microscopic level with macroscale device performance. Finally time-of-flight secondary ion mass spectrometry (TOF-SIMS) is used to gain an understanding of F_4-TCNQ diffusion as a function of distance from the anode interface, and to determine if diffusion has a detrimental effect on our proposed system. The working principles of these experimental techniques will be explained in Chapter 2, followed by a description of the transfer of graphene onto ITO substrates which will be a key substrate used for all subsequent experiments carried out.

The thesis concludes with a summary of the key findings and proposes areas which can be explored in more detail or techniques that can be improved.

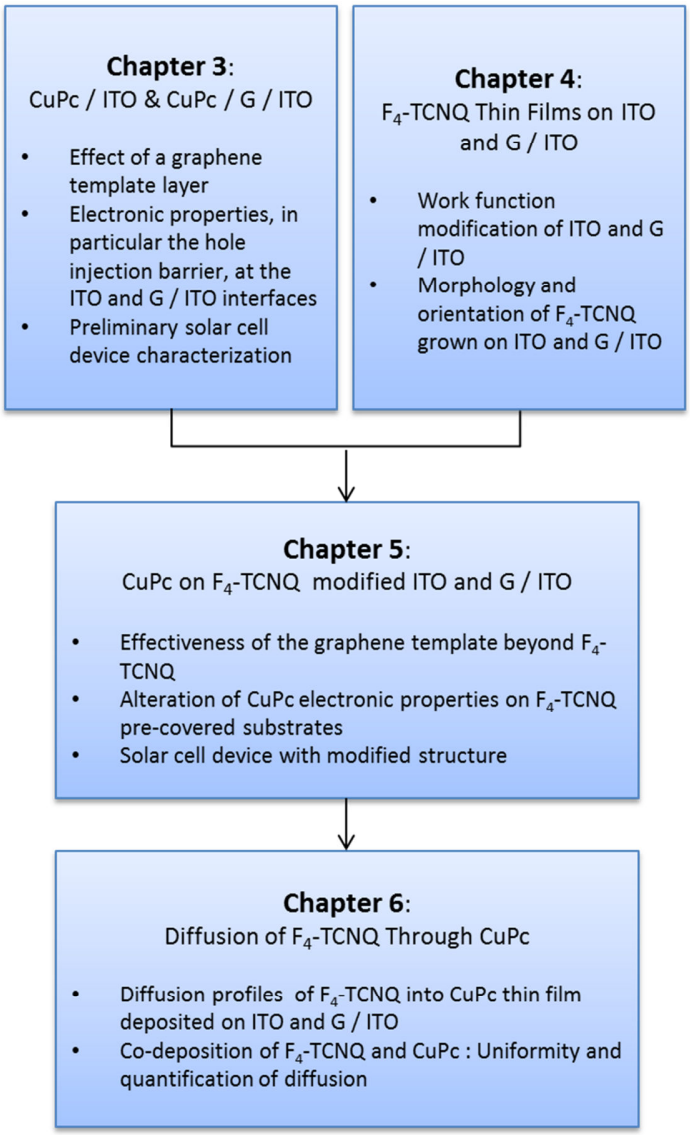

Figure 1-5 Flow chart showing the key systems and experimental investigations in each chapter, and cohesion between the chapters

1.4 References

1. Tang, C. W. Two-layer organic photovoltaic cell. *Appl. Phys. Lett.* **48,** 183 (1986).

2. Forrest, S. R. The path to ubiquitous and low-cost organic electronic appliances on plastic. *Nature* **428,** 911–8 (2004).

3. Brabec, C. J., Sariciftci, N. S. & Hummelen, J. C. Plastic Solar Cells. *Adv. Funct. Mater.* **11,** 15–26 (2001).

4. Song, Q. L. *et al.* Small-molecule organic solar cells with improved stability. *Chem. Phys. Lett.* **416,** 42–46 (2005).

5. Jørgensen, M., Norrman, K. & Krebs, F. C. Stability/degradation of polymer solar cells. *Sol. Energy Mater. Sol. Cells* **92,** 686–714 (2008).

6. Chen, Y.-H. *et al.* Vacuum-deposited small-molecule organic solar cells with high power conversion efficiencies by judicious molecular design and device optimization. *J. Am. Chem. Soc.* **134,** 13616–23 (2012).

7. Sun, Y. *et al.* Solution-processed small-molecule solar cells with 6.7% efficiency. *Nat. Mater.* **11,** 44–8 (2012).

8. He, Z. *et al.* Simultaneous enhancement of open-circuit voltage, short-circuit current density, and fill factor in polymer solar cells. *Adv. Mater.* **23,** 4636–43 (2011).

9. Liu, Y. *et al.* Solution-processed small-molecule solar cells: breaking the 10% power conversion efficiency. *Sci. Rep.* **3,** 3356 (2013).

10. Green, M. A., Emery, K., Hishikawa, Y. & Warta, W. Solar cell efficiency tables (version 37). *Prog. Photovoltaics Res. Appl.* **19,** 84–92 (2011).

11. Sirringhaus, H. *et al.* Two-dimensional charge transport in self-organized, high-mobility conjugated polymers. *Nature* **401,** 685–688 (1999).

12. Cornil, J., Beljonne, D., Calbert, J.-P. & Brédas, J.-L. Interchain Interactions in Organic π-Conjugated Materials: Impact on Electronic Structure, Optical Response, and Charge Transport. *Adv. Mater.* **13,** 1053–1067 (2001).

13. Blom, P. W. M., Mihailetchi, V. D., Koster, L. J. A. & Markov, D. E. Device Physics of Polymer:Fullerene Bulk Heterojunction Solar Cells. *Adv. Mater.* **19,** 1551–1566 (2007).

14. Heremans, P., Cheyns, D. & Rand, B. P. Strategies for increasing the efficiency of heterojunction organic solar cells: material selection and device architecture. *Acc. Chem. Res.* **42,** 1740–7 (2009).

15. Steim, R., Kogler, F. R. & Brabec, C. J. Interface materials for organic solar cells. *J. Mater. Chem.* **20,** 2499 (2010).

16. Hains, A. W., Liang, Z., Woodhouse, M. a & Gregg, B. a. Molecular semiconductors in organic photovoltaic cells. *Chem. Rev.* **110,** 6689–735 (2010).

17. Walzer, K., Maennig, B., Pfeiffer, M. & Leo, K. Highly efficient organic devices based on electrically doped transport layers. *Chem. Rev.* **107,** 1233–71 (2007).

18. Peumans, P., Yakimov, A. & Forrest, S. R. Small molecular weight organic thin-film photodetectors and solar cells. *J. Appl. Phys.* **93,** 3693 (2003).

19. Gregg, B. A. & Hanna, M. C. Comparing organic to inorganic photovoltaic cells: Theory, experiment, and simulation. *J. Appl. Phys.* **93,** 3605 (2003).

20. Kurrle, D. & Pflaum, J. Exciton diffusion length in the organic semiconductor diindenoperylene. *Appl. Phys. Lett.* **92,** 133306 (2008).

21. Forrest, S. R. Ultrathin Organic Films Grown by Organic Molecular Beam Deposition and Related Techniques. *Chem. Rev.* **97,** 1793–1896 (1997).

22. Yu, G., Gao, J., Hummelen, J. C., Wudl, F. & Heeger, A. J. Polymer Photovoltaic Cells: Enhanced Efficiencies via a Network of Internal Donor-Acceptor Heterojunctions. *Science (80-.).* **270,** 1789–1791 (1995).

23. Yu, G. & Heeger, A. J. Charge separation and photovoltaic conversion in polymer composites with internal donor/acceptor heterojunctions. *J. Appl. Phys.* **78,** 4510 (1995).

24. Sullivan, P., Jones, T. S., Ferguson, a. J. & Heutz, S. Structural templating as a route to improved photovoltaic performance in copper phthalocyanine/fullerene (C60) heterojunctions. *Appl. Phys. Lett.* **91,** 233114 (2007).

25. Hoppe, H. & Sariciftci, N. S. Organic solar cells: An overview. *J. Mater. Res.* **19,** 1924–1945 (2011).

26. Ameri, T., Dennler, G., Lungenschmied, C. & Brabec, C. J. Organic tandem solar cells: A review. *Energy Environ. Sci.* **2,** 347 (2009).

27. Heutz, S., Sullivan, P., Sanderson, B. M., Schultes, S. M. & Jones, T. S. Influence of molecular architecture and intermixing on the photovoltaic, morphological and spectroscopic properties of CuPc–C60 heterojunctions. *Sol. Energy Mater. Sol. Cells* **83,** 229–245 (2004).

28. Rand, B. P. *et al.* The Impact of Molecular Orientation on the Photovoltaic Properties of a Phthalocyanine/Fullerene Heterojunction. *Adv. Funct. Mater.* **22,** 2987–2995 (2012).

29. Cheng, C. H. *et al.* Organic solar cells with remarkable enhanced efficiency by using a CuI buffer to control the molecular orientation and modify the anode. *Appl. Phys. Lett.* **97,** 083305 (2010).

30. Zeis, R., Siegrist, T. & Kloc, C. Single-crystal field-effect transistors based on copper phthalocyanine. *Appl. Phys. Lett.* **86,** 022103 (2005).

31. Tang, Q., Tong, Y., Hu, W., Wan, Q. & Bjornholm, T. Assembly of Nanoscale Organic Single-Crystal Cross-Wire Circuits. *Adv. Mater.* **21,** 4234–4237 (2009).

32. Mativetsky, J. M., Wang, H., Lee, S. S., Whittaker-Brooks, L. & Loo, Y.-L. Face-on stacking and enhanced out-of-plane hole mobility in graphene-templated copper phthalocyanine. *Chem. Commun.* **50,** 5319–5321 (2014).

33. Irkhin, P. & Biaggio, I. Direct Imaging of Anisotropic Exciton Diffusion and Triplet Diffusion Length in Rubrene Single Crystals. *Phys. Rev. Lett.* **107,** 017402 (2011).

34. Verlaak, S. *et al.* Electronic Structure and Geminate Pair Energetics at Organic-Organic Interfaces: The Case of Pentacene/C60 Heterojunctions. *Adv. Funct. Mater.* **19,** 3809–3814 (2009).

35. Videlot, C., Kassmi, A. El & Fichou, D. Photovoltaic properties of octithiophene-based Schottky and p/n junction cells: Influence of molecular orientation. *Sol. energy Mater. Sol. cells* **63,** 69–82 (2000).

36. Peisert, H. *et al.* Order on disorder: Copper phthalocyanine thin films on technical substrates. *J. Appl. Phys.* **90,** 466 (2001).

37. Lassiter, B. E., Lunt, R. R., Renshaw, C. K. & Forrest, S. R. Structural templating of multiple polycrystalline layers in organic photovoltaic cells. *Opt. Express* **18,** A444–50 (2010).

38. Warner, M. *et al.* Spin-based diagnostic of nanostructure in copper phthalocyanine-C60 solar cell blends. *ACS Nano* **6,** 10808–15 (2012).

39. Chauhan, K. V., Sullivan, P., Yang, J. L. & Jones, T. S. Efficient Organic Photovoltaic Cells through Structural Modification of Chloroaluminum Phthalocyanine/Fullerene Heterojunctions. *J. Phys. Chem. C* **114,** 3304–3308 (2010).

40. Naito, R., Toyoshima, S., Ohashi, T., Sakurai, T. & Akimoto, K. Molecular Orientation Control of Phthalocyanine Thin Film by Inserting Pentacene Buffer Layer. *Jpn. J. Appl. Phys.* **47,** 1416–1418 (2008).

41. Singha Roy, S., Bindl, D. J. & Arnold, M. S. Templating Highly Crystalline Organic Semiconductors Using Atomic Membranes of Graphene at the Anode/Organic Interface. *J. Phys. Chem. Lett.* **3,** 873–878 (2012).

42. Zhong, S. *et al.* CVD graphene as interfacial layer to engineer the organic donor-acceptor heterojunction interface properties. *ACS Appl. Mater. Interfaces* **4,** 3134–40 (2012).

43. Xiao, K. *et al.* Surface-induced orientation control of CuPc molecules for the epitaxial growth of highly ordered organic crystals on graphene. *J. Am. Chem. Soc.* **135,** 3680–7 (2013).

44. Cattin, L. *et al.* Improved performance of organic solar cells by growth optimization of MoO3/CuI double-anode buffer. *Phys. Status Solidi* **210,** 802–808 (2013).

45. Ying Mao, H. *et al.* Chemical vapor deposition graphene as structural template to control interfacial molecular orientation of chloroaluminium phthalocyanine. *Appl. Phys. Lett.* **99,** 093301 (2011).

46. Blake, P. *et al.* Graphene-based liquid crystal device. *Nano Lett.* **8,** 1704–8 (2008).

47. Nair, R. R. *et al.* Fine structure constant defines visual transparency of graphene. *Science* **320,** 1308 (2008).

48. Duhm, S. *et al.* Orientation-dependent ionization energies and interface dipoles in ordered molecular assemblies. *Nat. Mater.* **7,** 326–32 (2008).

49. Chen, W. *et al.* Molecular Orientation-Dependent Ionization Potential of Organic Thin Films. *Chem. Mater.* **20,** 7017–7021 (2008).

50. Chen, W., Qi, D.-C., Huang, H., Gao, X. & Wee, A. T. S. Organic-Organic Heterojunction Interfaces: Effect of Molecular Orientation. *Adv. Funct. Mater.* **21,** 410–424 (2011).

51. Toader, T., Gavrila, G., Braun, W., Ivanco, J. & Zahn, D. R. T. Valence band fine structure of copper phthalocyanine thin films: Effect of molecular orientation. *Phys. Status Solidi* **246,** 1510–1518 (2009).

52. Wang, C., Turinske, A. J. & Gao, Y. Orientation-dependent ionization potential of CuPc and energy level alignment at C60/CuPc interface. *Appl. Phys. B* **113,** 361–365 (2013).

53. Clarke, T. M. & Durrant, J. R. Charge photogeneration in organic solar cells. *Chem. Rev.* **110,** 6736–67 (2010).

54. Scharber, M. C. *et al.* Design Rules for Donors in Bulk-Heterojunction Solar Cells—Towards 10 % Energy-Conversion Efficiency. *Adv. Mater.* **18,** 789–794 (2006).

55. Ratcliff, E., Zacher, B. & Armstrong, N. Selective interlayers and contacts in organic photovoltaic cells. *J. Phys. Chem. Lett.* **2,** 1337–1350 (2011).

56. Kim, J. S. *et al.* Indium–tin oxide treatments for single- and double-layer polymeric light-emitting diodes: The relation between the anode physical, chemical, and morphological properties and the device performance. *J. Appl. Phys.* **84,** 6859 (1998).

57. Sugiyama, K., Ishii, H., Ouchi, Y. & Seki, K. Dependence of indium–tin–oxide work function on surface cleaning method as studied by ultraviolet and x-ray photoemission spectroscopies. *J. Appl. Phys.* **87,** 295 (2000).

58. Wu, C. C., Wu, C. I., Sturm, J. C. & Kahn, A. Surface modification of indium tin oxide by plasma treatment: An effective method to improve the efficiency, brightness, and reliability of organic light emitting devices. *Appl. Phys. Lett.* **70,** 1348 (1997).

59. Schlaf, R., Murata, H. & Kafafi, Z. Work function measurements on indium tin oxide films. *J. Electron Spectros. Relat. Phenomena* **120,** 149–154 (2001).

60. Park, Y., Choong, V., Gao, Y., Hsieh, B. R. & Tang, C. W. Work function of indium tin oxide transparent conductor measured by photoelectron spectroscopy. *Appl. Phys. Lett.* **68,** 2699 (1996).

61. Armstrong, N. R. *et al.* Interface modification of ITO thin films: organic photovoltaic cells. *Thin Solid Films* **445,** 342–352 (2003).

62. Ma, H., Yip, H.-L., Huang, F. & Jen, A. K.-Y. Interface Engineering for Organic Electronics. *Adv. Funct. Mater.* **20,** 1371–1388 (2010).

63. Zhang, F. L., Gadisa, a., Inganäs, O., Svensson, M. & Andersson, M. R. Influence of buffer layers on the performance of polymer solar cells. *Appl. Phys. Lett.* **84,** 3906 (2004).

64. Shrotriya, V., Li, G., Yao, Y., Chu, C.-W. & Yang, Y. Transition metal oxides as the buffer layer for polymer photovoltaic cells. *Appl. Phys. Lett.* **88,** 073508 (2006).

65. Irwin, M. D., Buchholz, D. B., Hains, A. W., Chang, R. P. H. & Marks, T. J. p-Type semiconducting nickel oxide as an efficiency-enhancing anode interfacial layer in polymer bulk-heterojunction solar cells. *Proc. Natl. Acad. Sci.* **105,** 2783–2787 (2008).

66. Ishii, H., Sugiyama, K., Ito, E. & Seki, K. Energy Level Alignment and Interfacial Electronic Structures at Organic/Metal and Organic/Organic Interfaces. *Adv. Mater.* **11,** 605–625 (1999).

67. Fehse, K. *et al.* Energy level alignment of electrically doped hole transport layers with transparent and conductive indium tin oxide and polymer anodes. *J. Appl. Phys.* **102,** 073719 (2007).

68. De Jong, M. P., van IJzendoorn, L. J. & de Voigt, M. J. A. Stability of the interface between indium-tin-oxide and poly (3, 4-ethylenedioxythiophene)/poly (styrenesulfonate) in polymer light-emitting diodes. *Appl. Phys. Lett.* **77,** 2255–2257 (2000).

69. Pingree, L. S. C., MacLeod, B. A. & Ginger, D. S. The Changing Face of PEDOT:PSS Films: Substrate, Bias, and Processing Effects on Vertical Charge Transport. *J. Phys. Chem. C* **112,** 7922–7927 (2008).

70. Irfan, I., James Turinske, A., Bao, Z. & Gao, Y. Work function recovery of air exposed molybdenum oxide thin films. *Appl. Phys. Lett.* **101,** 093305 (2012).

71. Gao, W. & Kahn, A. Controlled p-doping of zinc phthalocyanine by coevaporation with tetrafluorotetracyanoquinodimethane: A direct and inverse photoemission study. *Appl. Phys. Lett.* **79,** 4040 (2001).

72. Kera, S. *et al.* Impact of an interface dipole layer on molecular level alignment at an organic-conductor interface studied by ultraviolet photoemission spectroscopy. *Phys. Rev. B* **70,** 085304 (2004).

73. Akaike, K., Kanai, K., Ouchi, Y. & Seki, K. Impact of Ground-State Charge Transfer and Polarization Energy Change on Energy Band Offsets at Donor/Acceptor Interface in Organic Photovoltaics. *Adv. Funct. Mater.* **20,** 715–721 (2010).

74. Koch, N. Organic electronic devices and their functional interfaces. *Chemphyschem* **8,** 1438–55 (2007).

75. Braun, S., Salaneck, W. R. & Fahlman, M. Energy-Level Alignment at Organic/Metal and Organic/Organic Interfaces. *Adv. Mater.* **21,** 1450–1472 (2009).

76. Dufour, G. *et al.* Metal phthalocyanines (MPc, M=Ni, Cu) on Cu(001) and Si(001) surfaces studied by XPS, XAS and STM. *J. Electron Spectros. Relat. Phenomena* **76,** 219–224 (1995).

77. Eley, D. D. Phthalocyanines as Semiconductors. *Nature* **162,** 819 (1948).

78. McKeown, N. B. *Phthalocyanine Materials: Synthesis, Structure, and Function*. (Cambridge University Press, 1998).

79. Kumar, A., Jose, G., Thomas, V., Unnikrishnan, N. V & Nampoori, V. P. N. NIR to UV absorption spectra and the optical constants of phthalocyanines in glassy medium. *Spectrochim. Acta. A. Mol. Biomol. Spectrosc.* **59,** 1–11 (2003).

80. Xue, J., Uchida, S., Rand, B. P. & Forrest, S. R. 4.2% efficient organic photovoltaic cells with low series resistances. *Appl. Phys. Lett.* **84,** 3013 (2004).

81. Peumans, P. & Forrest, S. R. Very-high-efficiency double-heterostructure copper phthalocyanine/C60 photovoltaic cells. *Appl. Phys. Lett.* **79,** 126 (2001).

82. Bao, Z., Lovinger, A. J. & Dodabalapur, A. Organic field-effect transistors with high mobility based on copper phthalocyanine. *Appl. Phys. Lett.* **69,** 3066 (1996).

83. Claessens, C. G., Hahn, U. & Torres, T. Phthalocyanines: from outstanding electronic properties to emerging applications. *Chem. Rec.* **8,** 75–97 (2008).

84. Walter, M. G., Rudine, A. B. & Wamser, C. C. Porphyrins and phthalocyanines in solar photovoltaic cells. *J. Porphyr. Phthalocyanines* **14,** 759–792 (2010).

85. Leznoff, C. C. & Lever, A. B. P. *Phthalocyanines, Properties and Applications, Volume 4*. 536 (Wiley, 1996).

86. Hoshino, A., Takenaka, Y. & Miyaji, H. Redetermination of the crystal structure of alpha-copper phthalocyanine grown on KCl. *Acta Crystallogr. B.* **59,** 393–403 (2003).

87. Mauthoor, S. Structural Analysis of Molecular Nanostructures and Thin Films. (2011).

Chapter 2 : Experimental Methodology

The different experimental techniques used in this dissertation will be presented in this chapter. The chapter begins with thin film growth in an organic molecular beam deposition (OMBD) chamber, followed by several thin film characterization techniques, and finally the chapter concludes with the preparation of samples.

2.1 The OMBD Growth System

The deposition technique of organic molecular beam deposition (OMBD) is used for the growth of all the thin films used in this dissertation. In OMBD, organic film growth is attained by subliming a solid source to produce a molecular beam which impinges on and may interact with a substrate placed within its path. This process takes place under (ultra) high vacuum (pressure < 10^{-7} mbar). Using an OMBD system to grow organic thin films affords a good degree of control over the deposition parameters, and also reduces airborne contaminants during film deposition due to the low pressure of the system. The vacuum system is also required to reduce collision between the molecular beam and residual gas molecules in the chamber. The mean free path of a gas molecule (λ_{gas}) is related to the pressure P of the system by:

$$\lambda_{gas} = \frac{k_B T}{\sqrt{2}\pi d_{mol}^2 P} \qquad (2\text{-}1)$$

where k_B is the Boltzmann constant, T is the temperature of the gas molecule (Kelvin) and πd_{mol}^2 is the cross section area of molecular collision. Therefore low pressure systems are required to increase λ_{gas} to obtain a straight and uniform path between the source and the substrate.

A typical setup of an OMBD system consists of a polished stainless steel chamber, a series of vacuum pumps (roughing pumps, turbo or cryogenic pumps for high vacuum, ion pumps for ultra-high vacuum), Knudsen cells consisting of tantalum coils wrapped around ceramic crucibles, and a sample holder. Some of the components are shown in Figure 2-1. Other accessories may include resistive or radiative heaters to alter the sample temperature, and sputter guns for *in-situ* sample cleaning. A quartz crystal microbalance (QCM) is commonly included to monitor the growth rate and thickness of the film by measuring the changes in frequency of its quartz crystal resonator. Powdered source materials are placed in the ceramic crucibles which are heated by applying a current through tantalum coils around the crucibles. A thermocouple is attached to the bottom of the crucible to measure the source temperature. The flux of the

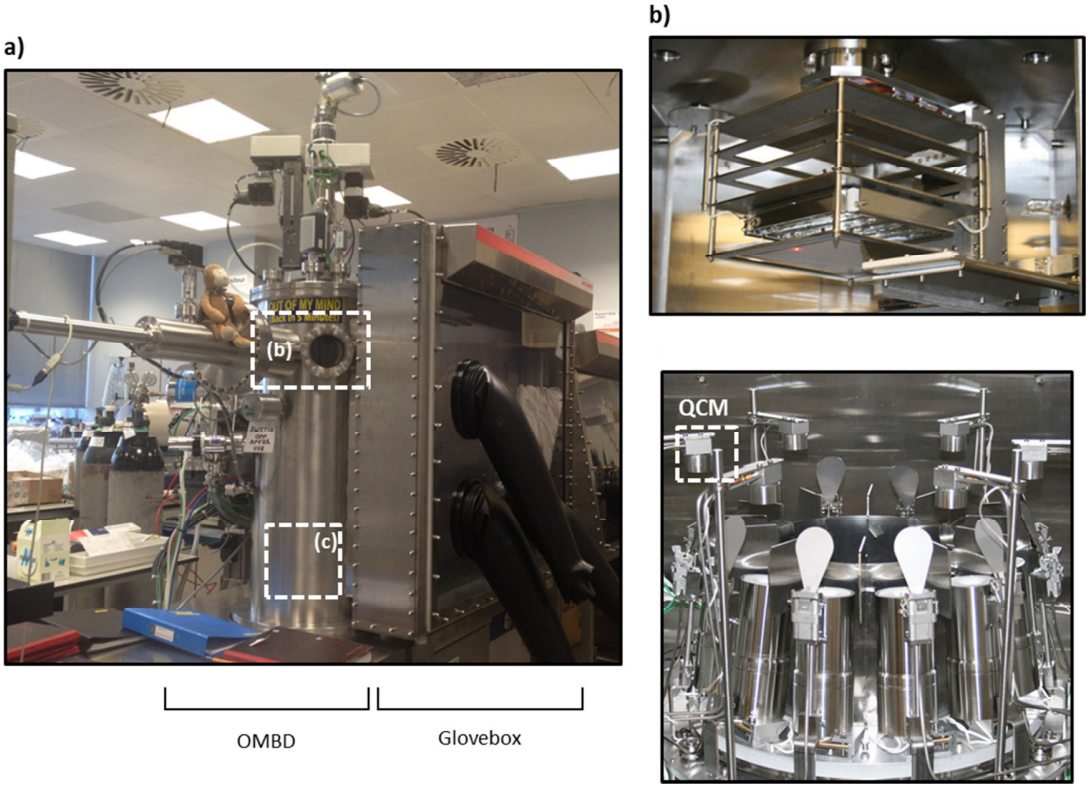

Figure 2-1 (a) Experimental setup of an OMBD system with a glove box. The positions of the sample holder and organic sources within the OMBD chamber are shown by the dashed boxes marked (b) and (c) respectively. Images of (b) the sample holder and (c) several sources for organic materials. A QCM is highlighted in (c). Figures (b) and (c) are obtained from the Kurt J. Lesker website.[29]

molecular beam (growth rate) can be controlled by adjusting the temperature of the source. The well-controlled OMBD environment enables this technique to be used for both ultra-thin film preparation for surface science experiments, as well as the deposition of thicker films for macroscopic characterization and even device fabrication.

The OMBD system used for the preparation of our thin films consists of a 10 cm x 10 cm sample plate which is loaded into a sample holder shown in Figure 2-1 (b), six sources for the deposition of organic materials [similar to the image in Figure 2-1 (c)] and two metal sources. The parameters used for the deposition of thin films for this dissertation will be presented in Section 2.3.3.

2.2 Characterization Techniques

In this section, a brief introduction to the working principles of the characterization techniques used in this thesis will be presented, followed by the experimental details and configurations employed. The main techniques used are photoemission spectroscopy (PES) including near-edge X-ray absorption fine structure (NEXAFS), time-of-flight secondary mass ion spectrometry (TOF-SIMS) and X-ray diffraction (XRD), while secondary characterization techniques include atomic force microscopy (AFM), secondary electron microscopy (SEM), ultraviolet-visible light (UV-Vis) absorption spectroscopy and current-voltage (J-V) characterization.

2.2.1 Working Principle of PES Measurements

PES is a powerful technique to determine the electronic properties of samples. Depending on the energy of the incident radiation, energy levels of atomic core electrons or valence levels can be studied. For instance, in X-ray photoelectron spectroscopy (XPS), high energy X-ray photons excite electrons in the core level of atoms, while lower energy ultraviolet photons excite electrons from shallow valence states near the Fermi level to probe the valence band of solid films in ultraviolet photoelectron spectroscopy (UPS). The sources of radiation may range from

monochromatized synchrotron radiation which is capable of delivering tuneable photons in the range of 50 eV to 1200 eV, noble gas discharges such as helium for UPS (21.2 eV or 40.8 eV) , or Mg (1253.6 eV) or Al K_α (1486.6 eV) radiation for XPS. All these processes are carried out under ultra-high vacuum (< 10^{-9} mbar) to minimize inelastic scattering of the photoelectrons by gas molecules while traveling to the analyser.

During PES measurement, the sample is irradiated with a photon beam of a specific energy (hv) which excites electrons within the sample. If the energy of the incoming photon beam is sufficient to overcome both the binding energy (BE) and the work function of the sample (ϕ_s), the electrons can escape from the sample to the vacuum in a process similar to the photoelectric effect.[1] The kinetic energy of the ejected electrons is (KE') and is dependent on the incident photon energy and the BE of the electron according to the equation below

$$KE' = hv - BE - \phi_s \qquad (2\text{-}2)$$

The process is shown schematically on the left hand side in Figure 2-2 (a). However, the kinetic energy (KE) measured by the analyser may not be equal to KE' due to the difference in work functions between the sample and the analyser (ϕ_a) as shown in Figure 2-2 (a). When the sample and the analyser are in good electrical contact, Equation (2-2) can be rewritten as

$$BE = hv - KE - \phi_a \qquad (2\text{-}3)$$

This equation eliminates the need for prior knowledge of ϕ_s, and allows direct comparison of the BE for the various samples.

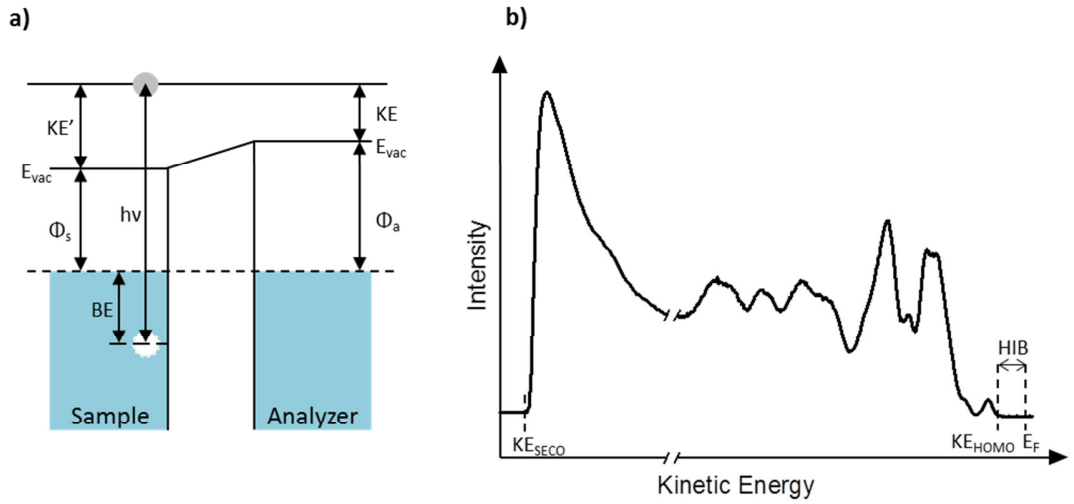

Figure 2-2 (a) Energy level alignment between the sample and analyser when they are in good electrical contact. (b) A typical UPS spectrum of organic molecular thin films.

For organic thin films, UPS is often used to measure ϕ_s and the ionization potential (IP) of the sample. A typical UPS spectrum showing the kinetic energy distribution of photoelectrons for organic films is shown in Figure 2-2 (b). The secondary electron cutoff (SECO) provides information about the position of the vacuum level as it corresponds to electrons with minimum energy required to overcome the ϕ_s. For samples with $\phi_s < \phi_a$, the low KE photoelectrons cannot be detected by the analyser, thus giving erroneous values of ϕ_s or IP. Therefore, a small bias of between -3 V to -10 V is applied to the sample when measuring the SECO in order to facilitate the detection of low energy electrons and to eliminate influence of the analyser. ϕ_s can be determined using the following equation:

$$\phi_s = h\nu - (E_F - KE_{SECO}) \qquad (2\text{-}4)$$

The high kinetic energy features in the UPS spectrum correspond to spectroscopic features in the valence band such as the HOMO, HOMO+1 etc. The position of the HOMO onset (KE_{HOMO}) is determined by extrapolating the leading slope of the HOMO feature to the background intensity. The IP of the system is thus determined by

$$IP = \phi_s + (E_F - KE_{HOMO}) = \phi_s + HIB \qquad (2\text{-}5)$$

where HIB is the hole injection barrier as denoted in Figure 2-2 (b).

Due to the higher excitation energies of X-rays, core level electrons of atoms can be excited in XPS. Using Equation (2-3), the BE of the detected electrons can be determined. Since the BE of core level electrons are unique and element specific, the associated element from which the electrons are detected from can be identified. Furthermore, changes in chemical environment, such as charge transfer or bond formation, can be detected through shifts in BE or the introduction of new peaks. Finally, the intensity of the detected photoelectrons is proportional to the concentration and the atomic sensitivity of the element within the area probed, thereby providing semi-quantitative analysis of the elemental species present.

An advantage of using PES to study surfaces and interfaces is that it can provide surface sensitivity. For our synchrotron based PES system with a maximum photon energy of up to 1200 eV, the KE of the ejected electrons must be <1200 eV according to Equation (2-2). In this range of energy, the escape depth of an electron in solid, or its inelastic mean free path, is related to its KE as shown in the universal curve[2] in Figure 2-3. When the KE of electrons are in the range of 30 to 100 eV, the escape depth is very short (of the order of a few monolayers or angstroms), indicating that PES probes only the photoelectron from the top few layers of the sample.

Using the attenuation of the substrate signal, the nominal thickness of the molecular film deposited on the substrate can be deduced. Assuming a simple case of layer-by-layer growth mode,

$$I_d = I_o \exp(-\frac{d}{\lambda_{IMFP} \cos\gamma}) \qquad (2\text{-}6)$$

where I_d is the intensity of the photoelectron after deposition of a film of thickness d, I_o is the photoelectron intensity of the bare substrate, γ is the angle between the analyser and substrate normal. λ_{IMFP} (in nm) is the inelastic mean free path of electrons in the molecular film and is

related to the KE of the detected electron and density of the film (ρ) (in g/cm^3) according to the equation for organic molecules:[2]

$$\lambda_{IMFP} = \frac{49\,KE^{-2}+0.11\,KE^{0.5}}{\rho} \quad (2\text{-}7)$$

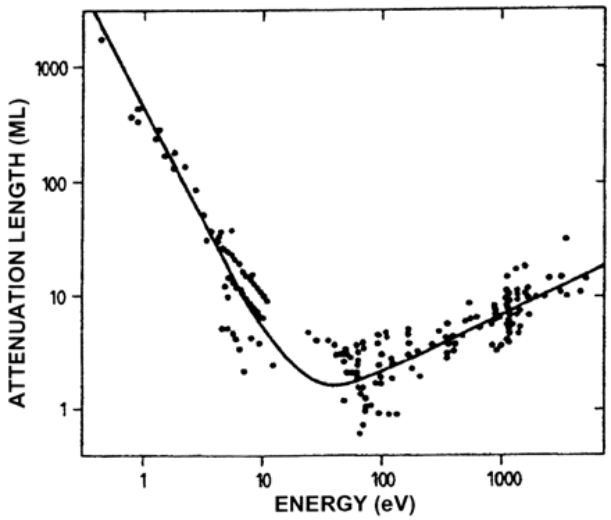

Figure 2-3 'Universal curve' showing the typical electron escape depth (attenuation length) in monolayers as a function of the electron kinetic energy. Reproduced from Reference [2].

2.2.2 NEXAFS Measurements

The underlying principle behind NEXAFS is similar to the photoemission process. However, while PES measurements probe electrons ejected from occupied states to the vacuum (free electron state) where they are directly detected, NEXAFS measurements involve the transitions of photoexcited electrons from a core level to an unoccupied state[3–5]. The energy of the primary photoelectron itself is not detected in NEXAFS. In addition, during NEXAFS measurements, the photon energy is scanned over the range of transitions from the core level to the unoccupied molecular orbitals near the transition edge (between 10 – 50 eV), while PES utilizes fixed photon beam energy within a measurement. NEXAFS monitors resonant electronic transitions from the inner shell of specific atomic species (eg. C 1s, O 1s or N 1s) to unoccupied molecular orbitals or states (eg. to π* and σ* orbitals) governed by dipole selection rule. It is generally accepted that

the resonant intensity is enhanced when the electric field vector $\vec{E}$ of synchrotron light polarization is parallel to the direction of the molecular orbital, and the intensity of the resonance is suppressed when $\vec{E}$ is perpendicular to the orbital direction. For planar π-conjugated molecules such as PTCDA, the σ* and π* orbitals are orthogonal to each other, being respectively polarised parallel or normal to the molecular plane. Therefore, the molecular orientation within a layer can easily be derived from the relationship between the resonant intensities and incident angle of light.[3] Synchrotron radiation, with its highly polarized beam, and the ability to vary the energy of

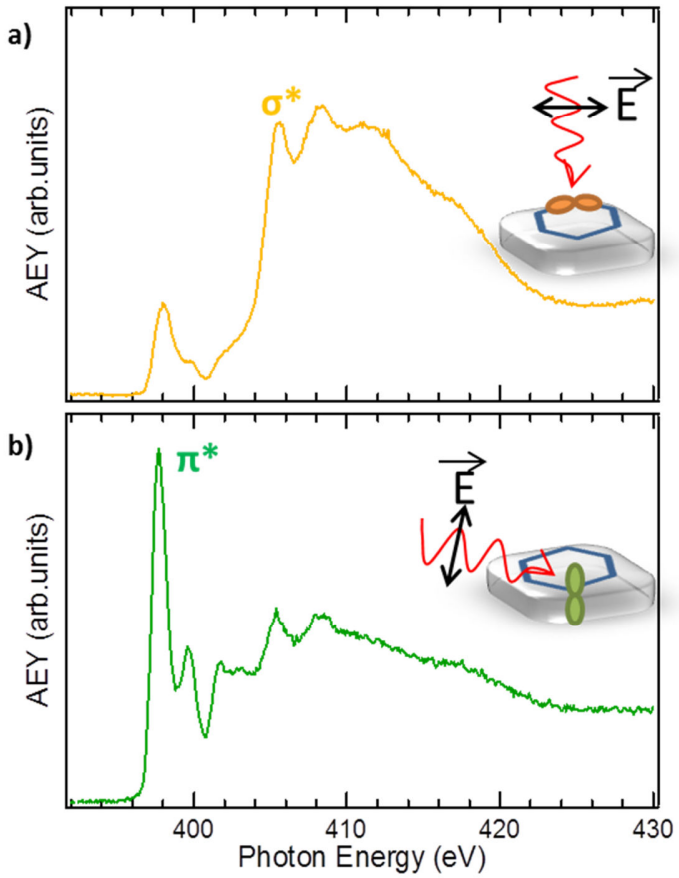

Figure 2-4 Polarization dependent NEXAFS spectra showing the ability of this technique to differentiate different orientations of the chemical bonds. For a molecule lying flat on a substrate, the σ* transitions are maximized at normal incidence to the substrate (θ = 90°) (a), while π* transitions are maximised at grazing incidence (θ = 20°) (b).

the incident photon energy is used as the excitation source in NEXAFS measurements.

Figure 2-4 (a) and (b) show an example of NEXAFS N K-edge performed on planar aromatic molecules containing nitrogen (e.g. CuPc) which are almost lying flat on the substrate. As shown in the schematic drawings in Figure 2-4 (a) and (b), when the molecules are lying flat on the substrate, the σ* orbitals are in-plane or parallel to the substrate surface, while the π* orbitals are out-of-plane. When the varying incident photon energy is sufficient to cause photo-excitation from the C 1s core level to the unoccupied σ* or π* anti-bonding orbitals, a core hole is formed in the C 1s state. The core hole is then filled by an electron from a higher energy state either radiatively through the emission of fluorescent photons, or non-radiatively through the subsequent ejection of an Auger electron. The detection of the electron flux from a particular Auger process as a function of the incident photon energy is termed Auger electron yield mode (AEY). This mode has excellent surface sensitivity as only elastically scattered Auger electrons from the surface of the sample are recorded. There are other modes such as fluorescence yield mode which does not require conductive sample but have low yield; total electron yield (TEY) mode that has high signal-to-noise ratio but is not as surface sensitive etc. For probing the changes in orientation at the top few monolayers, AEY is the preferred mode.

Figure 2-4 (b) and (c) exemplify the angle dependence resonant transitions on the incident beam at normal incidence ($\theta = 90^o$) and grazing incidence ($\theta = 20^o$) respectively. The tilt angle between the molecular plane and the substrate plane (α) is related to the intensity, I, of the resonant transition at θ incident angle by the equation

$$I(\theta) \propto 1 + \frac{1}{2}(3\cos^2\theta - 1)(3\cos^2\alpha - 1) \qquad (2\text{-}8)$$

Therefore, by conducting NEXAFS measurements at two or more angles, the orientations of anti-bonding orbitals and thus the molecular orientation of the absorbed molecules with respect to the substrate can be determined.[3]

2.2.2.1 Experimental

All PES and NEXAFS experiments were carried out at the Surface, Interface and Nanostructure Science (SINS) beamline of the Singapore Synchrotron Light Source (SSLS).[7] Two UPS experiments in Chapter 5 were carried out using He I (21.2 eV) excitation source in a separate custom built UPS chamber. The SINS beamline has a fixed endstation which consists of a preparation chamber for molecular deposition, connected to an analysis chamber where PES and NEXAFS measurements are performed via a gatevalve. Synchrotron radiation in the range of 50 eV to 1200 eV is available for surface science measurement at the SINS beamline. The photon energy for each experiment is calibrated using Au $4f_{7/2}$ core level binding energy (84.4 eV) of a sputtered gold foil which is electrically connected to the sample holder. The BE of all the PES spectra are therefore referenced to the Fermi level of the gold foil. The total incident photon flux of the monochromated beam is measured by a Keithley at the gold coated re-focussing mirror placed in the path of the incoming beam, and is used to normalise the intensities of all the collected spectra. A VG Scienta hemispherical electron analyser detects the KE of the photoelectrons. The energy resolution for PES is 0.05 eV while that for NEXAFS is 0.3 eV. The base pressure in the analysis chamber is 1×10^{-10} mbar. Figure 2-5 describes a typical PES setup and also shows the relevant components in the analysis chamber used in PES and NEXAFS measurements.

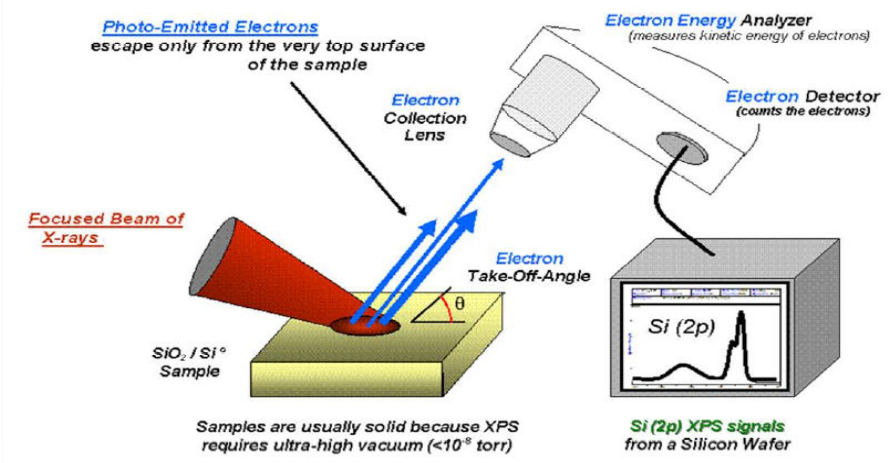

Figure 2-5 Schematic drawing showing a typical PES experimental setup, specifically for XPS in this example. For UPS, the incident beam is changed to ultraviolet light. Reproduced from Reference [28]

All the thin films that were prepared for PES and NEXAFS measurements were grown and measured *in-situ*. Detailed growth parameters are presented in Section 2.3.3. The chemically cleaned substrates were degassed for about one hour in the vacuum chamber using resistive heating prior to measurement and film growth. The photon energy used for UPS valence band and SECO measurements at the SINS beamline is 60 eV, while the C 1s core level spectra were obtained using 350 eV incident photon energy. A -7 V sample bias is applied during SECO measurements. For UPS measurements using He I source, the excitation energy is 21.2 eV and a -5 V bias is applied for SECO measurements. During NEXAFS N K-edge measurements, the photon energy is scanned over 40 eV from 390 eV to 430 eV. Angle-dependent NEXAFS measurements were carried out at $\theta = 90^{o}$ (normal incidence) where the incident beam is perpendicular to the substrate surface, and $\theta = 20^{o}$ (grazing incidence). All the spectra were analysed using IGORPro software.

2.2.3 Time-of-Flight Secondary Ion Mass Spectrometry Working Principles

Secondary ion mass spectroscopy (SIMS) is a technique used to analyse the chemical composition of samples by bombarding the sample with a high energy focused primary ion beam, and collecting the emitted secondary ions. Information regarding the chemical composition of the

target can be obtained from the resulting mass spectrum. Since the surface layers are sputtered away during primary ion bombardment, the variation of chemical composition with depth can also be determined. The sputtering process by the primary ion beam leads to the emission of a variety of particles ranging from electrons, neutral species of atoms and molecules, to ionized atomic and molecular fragments. Only the ionized fragments are detected and measured by the mass spectrometers.

SIMS measurements which use a time-of-flight (TOF) mass analyser, or TOF-SIMS, form mass spectra of secondary ions from the target during a single incident ion pulsed beam. Upon sample bombardment with the primary ion beam, the resulting ionized particles emitted from the surface are accelerated through an applied electric field into a TOF-SIMS mass analyser. The equation that relates the time-of-flight, t, to the mass to charge ratio (m/e) of each secondary ion fragment is given by

$$t = \left(\frac{L}{\sqrt{2U}}\right)\sqrt{\frac{m}{e}} \qquad (2\text{-}9)$$

where L is the length of the TOF analyser column and U is the applied voltage within the analyser. Since the term in the parenthesis depends only on the experimental setup, mass spectrometers separate ions according to their $\frac{m}{e}$ ratio, or flight time to the detector. The pulsed primary ion beam on the target generates the full mass spectrum of the surface; however the yield per pulsed beam is low. Therefore, secondary ions from several pulses are accumulated to generate a mass spectrum. The main advantages of using TOF-SIMS mass analyser compared to the traditional hemispherical magnetic sector and quadrupole analysers is the high mass resolution and parallel detection of all ions.[8]

Secondary ion mass spectrometry can be carried out in two modes: Static SIMS in which the primary ion beam interacts with and ionizes only the top few layers of the samples, and dynamic

SIMS which sputters material away, forming a crater in the sample. For surface mass spectrometry, static SIMS is carried out. Low primary ion beam doses are used ($<10^{13}$ ions/cm^2) to ensure that less than 1% of the analysis area is irradiated by the ion beam and no significant surface erosion occurs. During dynamic SIMS, a sputter ion beam erodes the sample, forming a sputter crater. The intensity of the ionized species of interest can be plotted as a function of crater depth to obtain a depth profile. The sputter beam is operated at low energies to enhance depth resolution and minimise ion beam induced mixing of the sample.[9]

2.2.3.1 Experimental

All the TOF-SIMS investigations were carried out in an Ion-ToF TOF-SIMS V. The base pressure of the system was 10^{-10} mbar. A schematic drawing of the setup showing the main layout of the instrument is shown in Figure 2-6 (a). An electron flood gun which is used for charge compensation is not shown in the schematic. Separate ion guns for sputtering and analysis enable the system to be operated in dual-beam mode. To erode the surface for depth profiling, caesium (Cs) and oxygen sources are available, and are used to enhance electronegative and

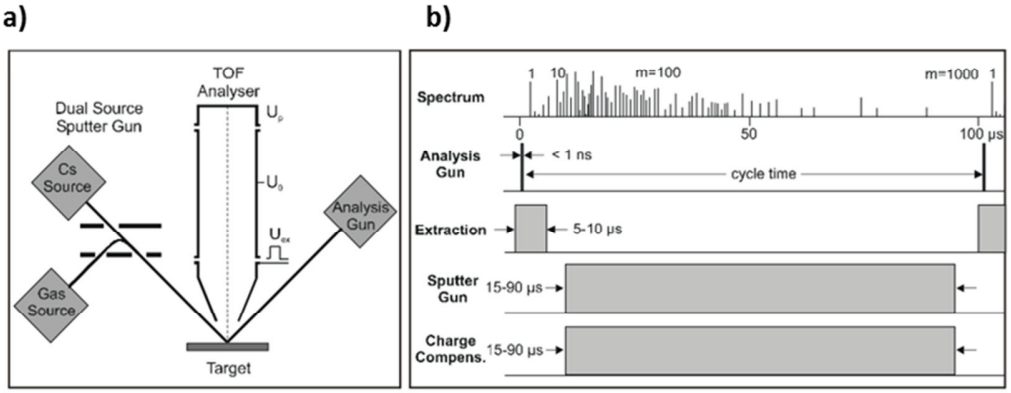

Figure 2-6 Schematics showing (a) the main instrumental layout, and (b) the timescales of the analysis and sputter guns, and the detection of the secondary ions in dual-beam interlace mode. Reproduced from Reference [27].

electropositive ions respectively. The energy of the sputter beam can vary from 0.25 – 10 keV and the beam spot size of the order of several µm. Bismuth ions (Bi_3^+) are used as the analysis

beam due to the high secondary ion yield for organic materials.[10] The spot size is several hundred nanometers, and the current applied may range from 0.1 pA to 25 nA.

The TOF analyser column is located vertically above the target sample and has a total drift length of 2 m. Secondary ions emitted from the sample are accelerated towards the analyser by applying an extracting voltage between the sample and the analyser. The accelerating voltage applied within the analyser is 2 kV. The mass resolution $m/\Delta m$ is approximately 6000 which is sufficient for our analysis.

When TOF-SIMS measurements are carried out in dual beam interlaced mode, the analysis and sputter beams are pulsed separately with different durations and at different times. An example of the timescales of the analysis and sputter beams is shown schematically in Figure 2-6 (b). This is performed to ensure that only secondary ions generated by the analysis beam are detected to preserve surface sensitivity of the detected ions. The primary analysis beam pulse is extremely short with duration of less than 1 ns to ensure that all the secondary ions are sputtered within a very short time interval. This ensures that the spectral resolution, which depends on the spread of time Δt over which the secondary ions are generated and detected, is not degraded. During the pulse of the analysis beam and up to 10 μs after, a voltage is applied between the analyser and the sample to extract the secondary ions. As the secondary ions move towards the analyser column, the extraction voltage is turned off. An opposite bias may be applied, or beam blanking may be used, to prevent secondary ions from the subsequent sample erosion from entering the analyser.

The sputter gun is subsequently turned on to erode the surface, creating a crater in the process. During this cycle, the electron flood gun may simultaneously be turned on to compensate for sample charging which may deflect the low energy primary ion beams. The erosion area is larger than the analysis area to ensure that secondary ions are ejected from the same uniform depth, and the sloping edge of the crater does not interfere with the analysis.

In our TOF-SIMS experiments, negative ions were detected and analysed. The samples were bombarded with a 1 keV Cs^+ primary ion beam with a pulsed current of 75 nA, interlaced with a Bi_3^+ analysis beam at ~1 pA. For each analysis, the sputter beam scanned an area of 400 μm x 400 μm while the analysis beam was centred in the crater with a size of 100 μm x 100 μm. The sputter time within the organic layer was converted to crater depth by considering the point at which the intensity of one of the stable fragments (CH^-) decreased to half its value compared to that within the thickness of the film.

2.2.4 X-ray Diffraction

X-ray diffraction (XRD) is a technique that is used to study crystallographic structures of materials. This technique is non-destructive and no special sample preparation is required before measurement. Monochromatic, collimated X-rays are directed onto a sample at an angle θ as shown in Figure 2-7. The X-rays are diffracted and scattered by the periodic arrangement of atoms and molecules in a crystal structure. Depending on the phase of the scattered X-rays, they may interfere destructively (out-of-phase) or constructively (in-phase). Constructive interference occurs when the optical path difference between parallel beams of rays is an integer multiple of the X-ray wavelength λ. For a crystal with interplanar spacing of d such as that shown schematically in Figure 2-7, constructive interference occurs when the equation

$$2\,d\sin\theta = n\,\lambda \qquad (2\text{-}10)$$

is satisfied. This is also known as Bragg's law.

The width of the diffraction peak in an XRD spectrum can be used to determine the average grain size, t, perpendicular to the substrate according to Scherrer's equation.[11] The equation takes the form of

$$t = \frac{k\lambda}{B\cos\theta} \qquad (2\text{-}11)$$

where λ is the wavelength of the of the X-ray, B is the full width at half maximum (FWHM) of the diffraction peak (in radians), θ is the Bragg angle and k is a constant depending on the shape of the grains. The value of k is close to unity but can vary by 20%.[12] In this thesis, k is assumed to be 1 and an error of 20% is included.

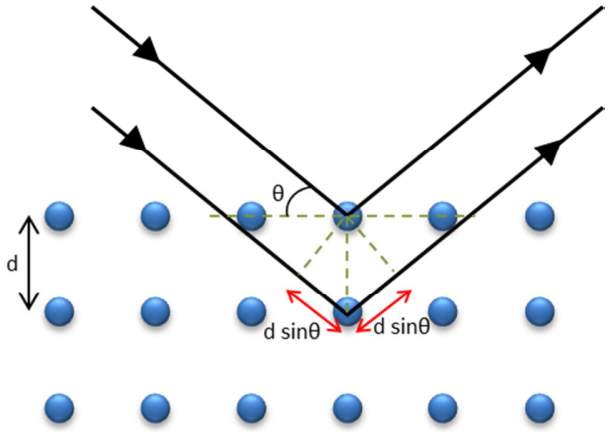

Figure 2-7 A schematic drawing showing X-ray diffraction from a crystal lattice. The X-ray beam is depicted as the black solid lines and forms an angle θ with the sample. The blue circles are scattering centres and the interplanar lattice spacing is d.

A unit cell is the simplest repeating unit of atoms, molecules or motifs that is used to construct a crystal when it is arranged spatially in three dimensions. It is defined by three vectors a, b and c in real space, and a*, b* and c* respectively in reciprocal space. The planes in a unit cell can be described by a set of integers h, k and l which is referred to as Miller indices. Crystallographic planes are represented as (h k l), while [h k l] refers to a direction perpendicular to the (h k l) plane. These notations will be used to describe the planes in our thin film crystals.

2.2.4.1 Experimental

All XRD measurements were carried out in ambient conditions using a Panalytical X'Pert PRO MPD X-Ray diffractometer with a Cu Kα X-ray source (λ = 1.54 Å). XRD scans were operated in symmetrical θ-2θ mode with a step size of 0.33° and in the range of 2θ = 5° to 30°. The substrate signal was subtracted prior to the presentation of the data.

2.2.5 Atomic Force Microscopy

Atomic force microscopy (AFM) provides three-dimensional topography information by using a very sharp tip attached to a cantilever to scan the surface of the sample being analysed. AFM measurements may be performed on a variety of substrates without the need for additional special treatments (such as metal coating of the sample) that may irreversibly alter the sample. This technique may be performed in ambient or under ultra-high vacuum. The basic AFM setup is shown schematically in Figure 2-8. A laser beam is directed onto the back of a cantilever which is in turn attached to a piezoelectric scanner. The position of the deflected beam is detected by photodiodes. Weak interactions between the sample and tip change the position of the deflected

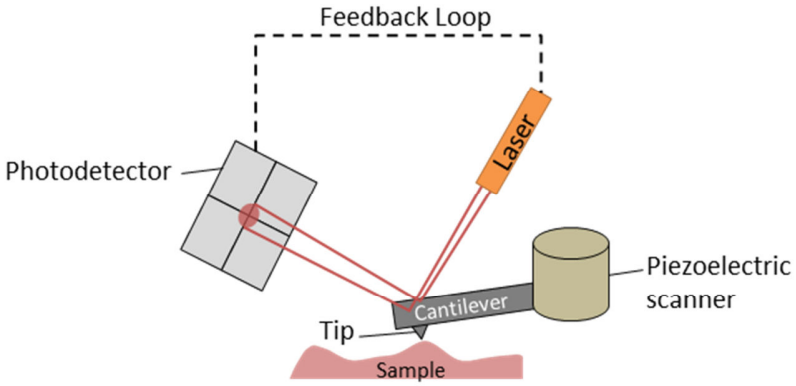

Figure 2-8 Schematic drawing of a basic AFM setup.

beam on the photodiodes. A feedback mechanism adjusts the position of the cantilever to maintain the tip-to-sample distance, or the amplitude of oscillations of the tip, depending on the mode it is operated in.

AFM can operate in contact or tapping mode. In the former, the tip is 'dragged' across the scan area of the sample and the deflection of the cantilever, or the feedback signal require to maintain a constant tip-sample distance, is recorded to map out the contours of the surface. This technique might damage fragile samples due to the close contact between the tip and sample. Tapping mode is more commonly used for soft organic and biological samples as it contacts the sample

intermittently and thus causes less sample damage. In this mode of operation, the cantilever oscillates close to its resonance frequency. When the tip approaches the sample during oscillations, forces such as Van der Waals interaction and electrostatic forces alters the amplitude of the oscillation. A feedback signal adjusts the height of the tip above the sample to maintain a constant oscillation amplitude. The feedback signal maps out the topography of the surface.

2.2.5.1 Experimental

AFM images were obtained in ambient conditions from a Veeco Dimension 3100 AFM. All the measurements were performed in tapping mode using Silicon tips with 8 nm radius and Al back coating on the cantilever from MikroMasch (NSC15/ Al BS). The resonant frequency of the cantilever was ~325 Hz.

2.2.6 Scanning Electron Microscopy

Scanning electron microscopy (SEM) is a technique to image the surface morphology (and indirectly composition) of samples. Electrons are generated at the top of an electron gun and accelerated towards the sample with high energy between 1 – 30 keV. The beam is focused onto the sample by using a series of electromagnetic lenses. Scanning coils raster the electron beam in two dimensions across the sample surface. The interaction of the high energy primary electron beam with the sample induces the emission of secondary electron from the surface. Backscattered electrons and X-rays may also be produced during the process. Depending on the signals detected, information regarding surface morphology, chemical composition, and electrical conductivity of the sample can be determined.

For sample imaging, secondary electrons are most commonly detected to form an image as they are most sensitive to topography. Secondary electrons originate from the near surface region, thus providing surface sensitive information, and are also very abundant which gives rise to high signal level.[13] A small positive bias is applied around the detector to enhance the detection of low

kinetic energy secondary electrons. The sample has to be conductive, or sample charging, which may distort the morphology of surface features, may occur.

2.2.6.1 Experimental

A LEO GEMINI 1525 FEG-SEM, which uses a field emission gun to generate electrons, is used in this dissertation for the investigation of surface morphology. The system operates at high vacuum of 10^{-5} mbar. The images are formed by collecting the secondary electrons using an in-lens detector. An operating voltage of 5 kV was used for all investigations. Chromium coating of approximately 15 Å were deposited on all the substrate before measurement to minimize sample charging.

2.2.7 Ultraviolet-Visible Spectroscopy

In ultraviolet (UV) (280 – 400 nm) and visible (Vis) light (400 – 700 nm) spectroscopy (collectively abbreviated UV-Vis), the incident radiation may be absorbed by molecules, resulting in electronic transitions from a ground state to an unoccupied state. Organic materials such as phthalocyanines absorb radiation in the UV-Vis range.[14]

A typical UV-Vis spectrometer has a dual-beam system consisting of a UV light source (deuterium lamp) and a visible tungsten or tungsten / halogen lamp. The beam of light passes then through a monochromator and is split into two parallel beams. One beam passes through the sample to be measured, while the other through a reference sample. The intensity of the transmitted beam through the reference (I_o) and the sample (I) are detected by separate photo-detectors. The absorbance of radiation by the sample is defined by the equation[15]

$$A = \log_{10} \frac{I_o}{I} \qquad (2\text{-}12)$$

The intensity of the absorbance spectra is related to the concentration of substance present in the sample through the Beer-Lambert law. This law relates the absorbance of light at a given

wavelength to the concentration, c, of the absorbing species, the optical path length b, and the molar extinction coefficient ε. The equation for solutes in a non-interacting solvent is expressed as

$$A = \varepsilon bc \tag{2-13}$$

For thin films deposited on transparent materials, Equation (2-13) is slightly modified such that the absorbance of the molecular thin film is related to the thickness of the film (L) and the absorption coefficient of the material (χ) via the equation

$$A = \chi L \tag{2-14}$$

2.2.7.1 Experimental

The absorption spectrum of thin films and solutions used in this thesis were obtained from UV-Vis spectroscopy performed using a Perkin Elmer Lambda 25 UV/VIS spectrometer. The absorbance spectra were recorded from 300 nm to 1000 nm. CuPc thin films and graphene transferred onto ITO were measured as-deposited, while F_4-TCNQ molecules and films were dissolved in dichloromethane and measured in a quartz cuvette which has an optical path length of 1 cm.

2.2.8 Current-Voltage Characterization

The current-voltage (J-V) relationship of OPV devices measures the output current of solar cells as a function of the external applied voltage. From this, the power and efficiency of the solar cell can be extracted. The two main parameters that are of interest are the open circuit voltage (V_{oc}) and the short circuit current density (J_{sc}) (short circuit current is denoted as I_{sc}). A schematic drawing showing a J-V response curve for solar cells is presented in Figure 2-9. V_{oc} is measured at the point when the drift current, I_R, which is due to the overall electric field in the solar cell (external applied field and internal electric field), is balanced by the diffusion current, I_F, which is

due to the chemical potential difference. J_{sc} is the current density measured in the absence of an external field as shown in Figure 2-9.

The fill factor, FF, which is a measure of how 'square' the shaded region in Figure 2-9 is, is given by the equation

$$FF = \frac{P_m}{V_{oc}\, x\, J_{sc}} \qquad (2\text{-}15)$$

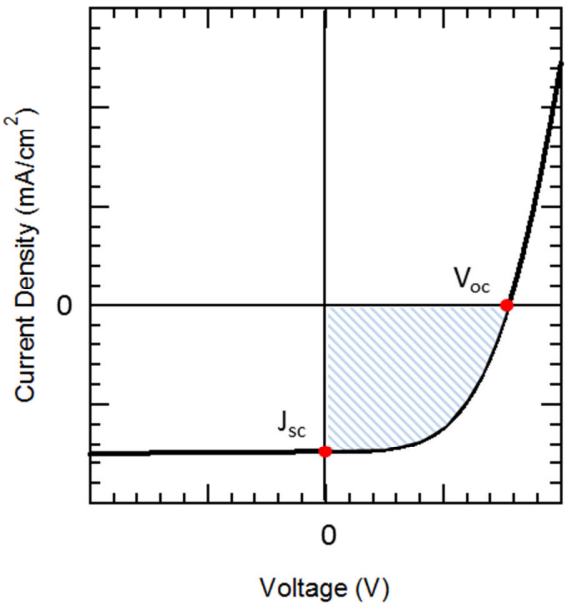

Figure 2-9 A typical J-V response curve for a solar cell device under illumination. J_{sc} is measured the external voltage is 0 V; V_{oc} corresponds to the point where the drift current in a solar cell is balanced by the diffusion current.

where P_m is the is the maximum power density in the OPV device. The power conversion efficiency η is the ratio between P_m and P_{in}, the input power density.

$$\eta = \frac{P_m}{P_{in}} = \frac{V_{oc}\, J_{sc}\, FF}{P_{in}} \qquad (2\text{-}16)$$

2.2.8.1 Experimental

Device efficiencies and J-V characterization in this thesis were measured using a Keithley Source meter. The solar cells were illuminated using a 300 W xenon arc lamp solar simulator. The illumination intensity was 100 mW/cm^2 at 1 sun AM 1.5 as calibrated with a silicon photodiode. The voltage was typically varied from -1 V to 1 V and the solar cell device area was 0.12 cm^2. All

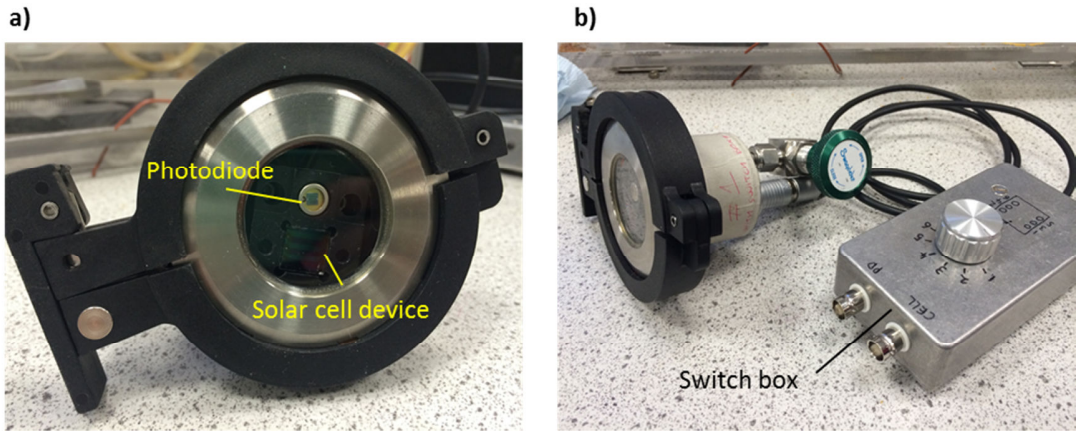

Figure 2-10 (a) Top view of the solar cell device chamber used in the experiment. (b) The solar cell device chamber is interfaced with a switch box that allows for independent measurement up to six solar cell devices fabricated on a single substrate.

the measurements were performed immediately after device fabrication. The solar cells were measured in a nitrogen environment in a custom made solar cell measurement chamber [Figure 2-10 (a)]. All the samples were loaded into the measurement chamber in a glove box to minimize exposure to oxygen and moisture. The solar cell chamber is interfaced to a switch box [Figure 2-10 (b)] which allows for independent measurement of up to six solar cell devices fabricated on a single substrate. All the devices were measured under illumination and in the dark.

2.3 Sample Preparation

2.3.1 Sample Cleaning

Commercially available silicon oxide <1 0 0> (SiO_2) [Virginia semiconductor] and indium tin oxide 100 nm thick deposited on glass (referred to as 'ITO' henceforth) (Psiotec) substrates were

cleaned by sequential sonication twice each in fresh acetone and isopropyl alcohol (IPA) for a duration of 20 minutes for each step, and dried with compressed air. The substrates that were used for graphene transfer were additionally exposed to UV-ozone plasma for 5 minutes immediate after they were dried in order to make the surface hydrophilic for ease of transferring graphene from deionized water to the surface, and in 'spreading' graphene out uniformly on the surface[16] (details are found in the next section). Graphene is transferred onto the clean substrate within 10 minutes of UV-ozone exposure. Predominantly monolayer graphene on copper foil (G/Cu) (Graphene Supermarket) were cut to the desired size and used as-received.

2.3.2 Transfer of Graphene to ITO

Graphene was transferred to SiO_2 and ITO via a wet transfer technique using polymethylmethacrylate (PMMA) as a support for graphene. This technique is described in detail in References [[17] & [18]]. As-grown graphene on Cu foil was cut into squares of at least 10 mm x 10 mm and spin coated with PMMA (Microchem, 950k, 4% by volume dissolved in anisole) at 3000 rpm and cured on a hot plate at 180 ^{o}C for 2 minutes to remove the solvent and to allow PMMA to harden. Graphene grown on the side of Cu foil not protected by PMMA was removed using O_2 plasma at 60 W for 2 minutes as it tends to interfere with the transfer process.[16,19] The edges of the PMMA/G/Cu samples were trimmed down by about 1 mm each before floating the stack in in 0.05 M ammonia persulfate (Sigma Aldrich, ACS reagent, ≥98% purity) to etch the Cu foil. The remaining PMMA/graphene was floated in three cycles of deionized water for 20 minutes each to remove residual ammonia persulfate before transferring it to the UV-ozone treated SiO_2 or ITO substrates. The ozone treatment is required as the intrinsically hydrophobic surfaces of SiO_2 and ITO before UV-ozone treatment cause the thin film of water under the PMMA/graphene stack to coalesce and drag graphene along with it in the process, resulting in crumpling of graphene. The sample was dried slowly at room temperature for 30 minutes before baking on a hotplate at 120 ^{o}C for 30 minutes to remove any excess liquid. After cooling to room temperature, a few drops of

anisole (FCC, ≥98% purity, Sigma Aldrich) were placed on the PMMA surface for 5 minutes to solubilize PMMA before exposing the sample to acetone vapour for 1 hour and subsequently immersing it in a clean beaker of acetone overnight to remove PMMA. The sample was then removed from acetone and submerged in IPA for 2 minutes before being carefully blown dry with purified nitrogen gas. The resulting graphene samples transferred onto ITO were ~ 8 mm x 8 mm in size, which covers the width of the exposed ITO on the ITO/glass substrate.

2.3.2.1 Characterization of Graphene Films

As-grown and transferred graphene films were characterized using Raman spectroscopy and SEM. For graphene transferred onto ITO (G/ITO) which will be one of the main samples used in the subsequent experiments in Chapters 3 to 6, AFM imaging was further carried out to identify the topography of the substrates. The characterization of G/Si can be found in Appendix A.

Raman spectroscopy is a non-contact and non-destructive technique routinely used to probe the quality of the as-grown or transferred graphene.[20] There are two peaks associate with pristine graphene, the 2D peak at ~2680 cm^{-1} and G peak at 1580 cm^{-1}; an additional D peak at ~ 1350 cm^{-1} associated with defects in graphene such as dislocation, cracks and vacancies.[20–22] Raman measurements were performed at room temperature and pressure using a Renishaw spectrometer system using a 514 nm laser as the excitation source. The laser power was kept below 0.5 mW to prevent laser-induced damage of the sample. A 50x objective lens was used to image the sample and also focus the probe in the Raman experiment. Raman data was collected with the WIRE2.0 software and processed using IGORPro software. Figure 2-11 shows the typical Raman spectra for as-received G/Cu (top) and transferred G/ITO (bottom). Both G/Cu and G/ITO spectra show the typical 2D and G peaks of graphene located at around 2680 cm^{-1} and 1585 cm^{-1} respectively. The FWHM of the symmetrical 2D peaks in both spectra is around 40 cm^{-1}, and the ratios of the peak intensities of G:2D is between 0.4 – 0.5, suggesting that the samples consist of

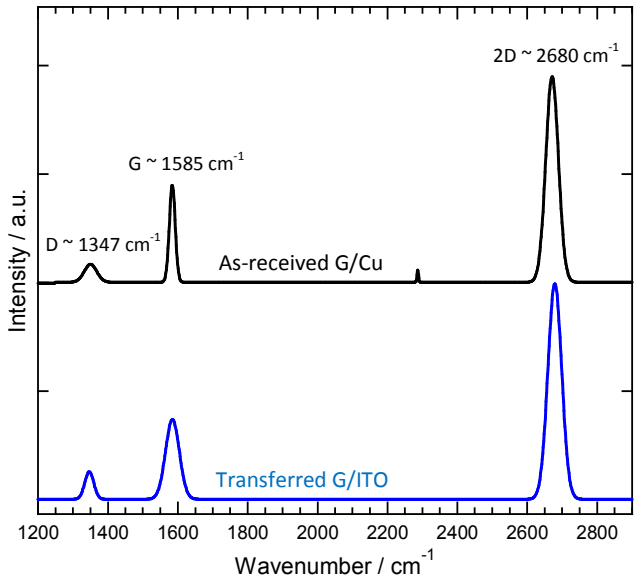

Figure 2-11 Average Raman spectrum of as-received G/Cu foil (top) and transferred G/ITO (bottom) after subtracting their baseline, using 514 nm laser excitation. The characteristic 2D and G peaks of graphene, and the defect induced D peak are shown. The peak at ~2330 cm^{-1} in the top spectrum comes from the Raman mode of N_2 gas.[26]

predominantly mono- to bi- layer graphene[23,24]. The D peak at ~1347 cm^{-1} in both spectra indicates that the as-received and transferred graphene sheet contain defects. Using the intensity ratio of the D:G peak,[25] the density of defect is estimated to be 4.5 x 10^{10} cm^{-2} for G/Cu and 7.7 x 10^{10} cm^{-2} for G/ITO. The increase in defect density by over 50% for the latter sample as compared to the former suggests that the transfer process introduces additional defects in the graphene sheet.

SEM is used to visualize the quality of G/Cu and G/ITO in order to determine the coverage of defects (wrinkles, residues, tears, holes etc.) which may hamper the templating of the subsequent organic molecules.[30] Figure 2-12 (a) shows the SEM image of G/Cu, and reveals that the graphene sheet is not continuous over the whole Cu foil surface. The absence of graphene is seen from the brighter areas in the image, in which the underlying Cu substrate is revealed. The absence of graphene represents not more than 5% of the whole image. Figure 2-12 (b) and (c) show the SEM images of G/ITO at two areas close to the centre of the graphene sheet, revealing residues and wrinkles in the former image, and tears and/or holes in the graphene sheet in the

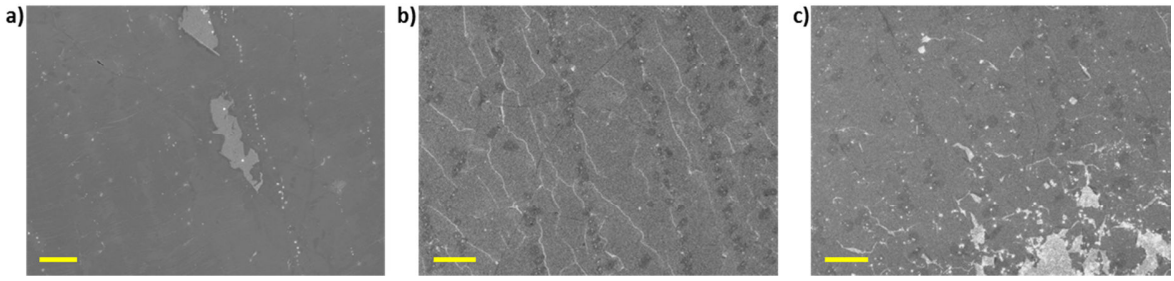

Figure 2-12 SEM images of (a) G/Cu (x5000 magnification), and (b) and (c) G/ITO at two different areas (x3000 magnification). (a) Bright contrast areas and spots correspond to holes in the as-grown graphene and residues respectively; (b) bright streaks and spots correspond to wrinkles and residues respectively; (c) brighter areas are due to tears in the graphene sheet, thus revealing the underlying substrate. Scale bars are 5 µm for all the images.

latter. The tears in graphene cover ~15% in Figure 2-12 (c). These images clearly show that the graphene transfer process introduces defects such as wrinkles, residues, and a higher percentage of tears. The fraction of defects may vary between samples and with the location of the graphene sheet imaged. The effects of these imperfections and unreliable coverage of graphene on the templating of organic molecules and device performance will be investigated in detail in Chapters 3 and 5. The topographies of ITO and G/ITO are shown in the AFM images in Figure 2-13 (a) and (b) for ITO and (c) for G/ITO respectively. Figure 2-13 (b) which is a 3-dimesional view of ITO surface shown in Figure 2-13 (a) reveals that the surface is extremely rough with height variations up to 30 nm. This poses a problem for the wet transfer of graphene as described in the Section 2.3.2 since water is trapped between the PMMA supported graphene and the substrate after graphene is lifted out of the deionized water. When water evaporates rapidly upon heating, it might cause the impermeable PMMA/graphene stack to tear; therefore it is important to allow the sample to dry slowly at room temperature. Figure 2-13 (c) shows the AFM image of G/ITO substrate with the middle area devoid of graphene, which may have been torn during the transfer process or might be due to incomplete growth of graphene on Cu foil [Figure 2-12 (a) and (c)]. Graphene masks the distinct grains of the underlying substrate but does not form a smooth and uniform layer on ITO. Instead it appears crumpled and its topography is mediated by the variation in grain heights of ITO. Therefore, while the local RMS roughness of the substrate decreases

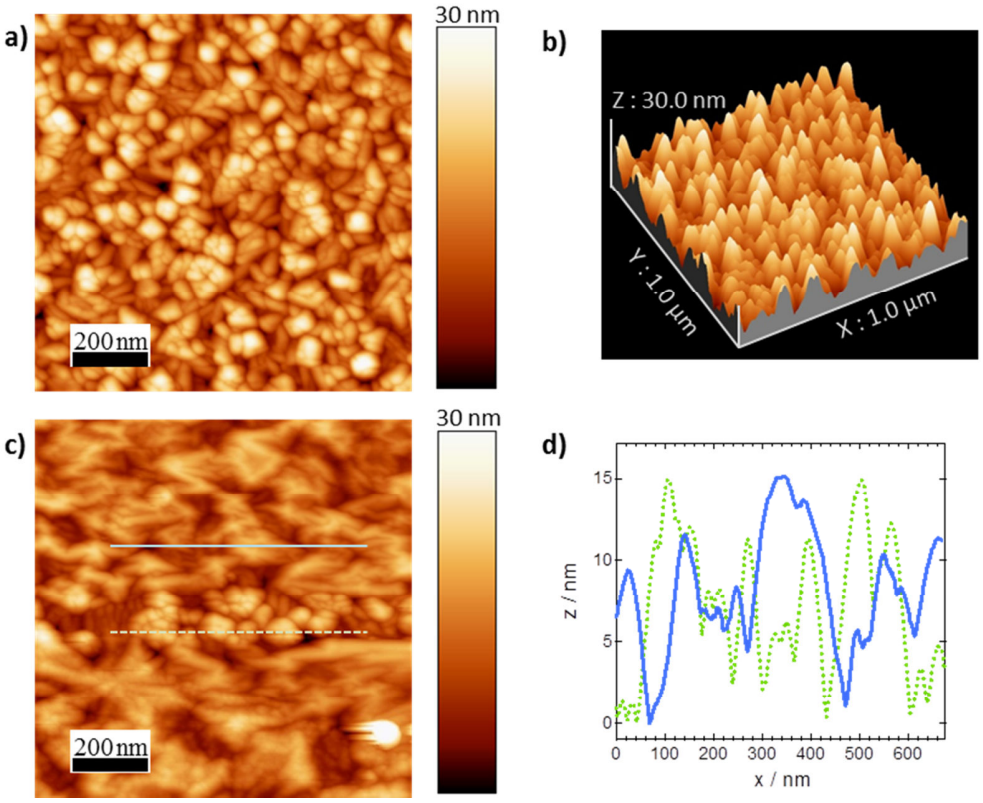

Figure 2-13 1 µm x 1 µm AFM images of (a) bare ITO in plane view and (b) 3-dimensional view, and (c) G/ITO with the central area devoid of graphene to show the contrast in surface features. (d) Line profiles of the solid and dashed line in (c) indicate that while the variation in z-height is similar on G/ITO and ITO, the surface features become indistinct. RMS surface roughness is (a) 5.0 nm, and (c) 4.0 nm excluding the bright feature and the uncovered region.

from 5.0 nm for ITO to 4.0 nm for G/ITO (the latter is less undulating), both surfaces have similar height variations as seen from the corresponding line scans in Figure 2-13 (c) and (d).

2.3.3 Thin Film Deposition

Clean substrates of ITO and G/ITO were loaded into the OMBD chamber immediately after preparation. Organic molecules were deposited on the various substrates via thermal evaporation from separate Knudsen cells in an OMBD system with base pressure of better than 10^{-7} mbar. All the depositions were performed at room temperature. The organic molecules used in this dissertation are CuPc (Sigma-Aldrich, twice purified using gradient sublimation), 2,3,5,6-Tetrafluoro-7,7,8,8-tetracyanoquinodimethane (F_4-TCNQ) (Nichem, 99% purity), Fullerene C_{60}

(Alfa Aesar, 99% purity), Bathocuproine (BCP) (Sigma-Aldrich, 96% purity) and Perylene-3,4,9,10-tetracarboxylic dianhydride (PTCDA) (Sigma-Aldrich, 97% purity), while metal aluminium pellets (Sigma-Aldrich, >99.99% purity) were used for solar cell devices. The organic sources were degassed for an hour prior to deposition. The growth rates and deposition temperatures for the various organic molecules used in this dissertation are tabulated in Table 2-1 (unless otherwise stated within the text). Several samples were prepared within a single growth to ensure repeatability of results and to allow for direct comparison between substrates under identical growth conditions.

For in-situ PES and NEXAFS measurements of film growth on ITO, the growth rates and nominal film thicknesses were calculated by following the attenuation of the In $3d_{5/2}$ signal using Equations (2-6) and (2-7). For all other films, the deposition rates were monitored by QCM that are placed in the path of the beam but not obstructing the sample holder. A tooling factor is used to correct for the geometric offset between the locations of the QCM and sample holder. All the materials except for F_4-TCNQ have been calibrated prior to thin film deposition in this dissertation; the thickness calibration of F_4-TCNQ will be addressed in Chapter 4. The error in determining the thickness of the film is approximately 5%. The samples were stored in a glove box before characterization, with the exception of organic solar cells and thin films for PES and NEXAFS measurements which were measured immediately after deposition.

Material	Growth Rate / $Å s^{-1}$	Deposition Temperature /°C	Notes
F_4 - TCNQ	0.02	90	For ultra-thin film PES and NEXAFS measurement
CuPc	0.04	295	
F_4 - TCNQ	0.02	90	For films ≥ 30nm and solar cell devices
CuPc	1	350	
PTCDA	1	300	
BCP	1	165	
C60	1	490	
Al	0.2 / 0.5	--	

Table 2-1 Growth rates and deposition temperatures of the various materials used in this thesis. The growth rate of Al was 0.2 Å/s for the first 20 nm deposited directly on the organic materials to minimize sample damage by the hot Al molecules, but increased to 0.5 Å/s for the next 80 nm.

2.4 References

1. Einstein, A. Concerning an heuristic point of view toward the emission and transformation of light. *Am. J. Phys.* **33,** 132 (1965).

2. Seah, M. P. & Dench, W. A. Quantitative electron spectroscopy of surfaces: A standard data base for electron inelastic mean free paths in solids. *Surf. Interface Anal.* **1,** 2–11 (1979).

3. Stöhr, J. *NEXAFS Spectroscopy*. (Springer, 1992).

4. Hähner, G. Near edge X-ray absorption fine structure spectroscopy as a tool to probe electronic and structural properties of thin organic films and liquids. *Chem. Soc. Rev.* **35,** 1244–55 (2006).

5. De Oteyza, D. G. *et al.* Inversed linear dichroism in F K-edge NEXAFS spectra of fluorinated planar aromatic molecules. *Phys. Rev. B* **86,** 075469 (2012).

6. Chen, W. *et al.* Molecular orientation of 3, 4, 9, 10-perylene-tetracarboxylic-dianhydride thin films at organic heterojunction interfaces. *Appl. Phys. Lett.* **91,** 114102 (2007).

7. Yu, X. *et al.* New soft X-ray facility SINS for surface and nanoscale science at SSLS. *J. Electron Spectros. Relat. Phenomena* **144-147,** 1031–1034 (2005).

8. Desouza, R., Zehnpfenning, J., Martin, M. & Maier, J. Determining oxygen isotope profiles in oxides with Time-of-Flight SIMS. *Solid State Ionics* **176,** 1465–1471 (2005).

9. Brison, J., Muramoto, S. & Castner, D. G. ToF-SIMS Depth Profiling of Organic Films: A Comparison between Single-Beam and Dual-Beam Analysis. *J. Phys. Chem. C Nanomater Interface* **114,** 5565–5573 (2010).

10. Touboul, D., Kollmer, F., Niehuis, E., Brunelle, A. & Laprévote, O. Improvement of biological time-of-flight-secondary ion mass spectrometry imaging with a bismuth cluster ion source. *J. Am. Soc. Mass Spectrom.* **16,** 1608–18 (2005).

11. Scherrer, P. No Title. *Göttinger Nachrichten Gesell.* **2,** 98 (1918).

12. Wilson, A. J. C. *Mathematical Theory of X-ray Powder Diffractometry*. (Pan MacMillan, 1963).

13. Zhu, Y., Inada, H., Nakamura, K. & Wall, J. Imaging single atoms using secondary electrons with an aberration-corrected electron microscope. *Nat. Mater.* **8,** 808–12 (2009).

14. Kumar, A., Jose, G., Thomas, V., Unnikrishnan, N. V & Nampoori, V. P. N. NIR to UV absorption spectra and the optical constants of phthalocyanines in glassy medium. *Spectrochim. Acta. A. Mol. Biomol. Spectrosc.* **59,** 1–11 (2003).

15. Clark, B. J., Frost, T., Russell, M. A. & Ultraviolet Spectrometry Group (Great Britain). *UV spectroscopy : techniques, instrumentation, data handling*. (Chapman & Hall, London ; New York, 1993).

16. Liang, X. *et al.* Toward clean and crackless transfer of graphene. *ACS Nano* **5,** 9144–53 (2011).

17. Li, X. *et al.* Transfer of large-area graphene films for high-performance transparent conductive electrodes. *Nano Lett.* **9,** 4359–63 (2009).

18. Li, X. *et al.* Large-area synthesis of high-quality and uniform graphene films on copper foils. *Science* **324,** 1312–4 (2009).

19. Van der Zande, A. M. *et al.* Large-scale arrays of single-layer graphene resonators. *Nano Lett.* **10,** 4869–73 (2010).

20. Ferrari, a. C. *et al.* Raman Spectrum of Graphene and Graphene Layers. *Phys. Rev. Lett.* **97,** 187401 (2006).

21. Ferrari, A. Raman spectroscopy of graphene and graphite: disorder, electron–phonon coupling, doping and nonadiabatic effects. *Solid State Commun.* **143,** 47–57 (2007).

22. Malard, L. M., Pimenta, M. a., Dresselhaus, G. & Dresselhaus, M. S. Raman spectroscopy in graphene. *Phys. Rep.* **473,** 51–87 (2009).

23. Graf, D. *et al.* Spatially resolved Raman spectroscopy of single- and few-layer graphene. *Nano Lett.* **7,** 238–42 (2007).

24. Gupta, A., Chen, G., Joshi, P., Tadigadapa, S. & Eklund, P. C. Raman Scattering from High-Frequency Phonons in Supported n-Graphene Layer Films. *Nano Lett.* **6,** 2667–73 (2006).

25. Cançado, L., Jorio, A. & Ferreira, E. Quantifying defects in graphene via Raman spectroscopy at different excitation energies. *Nano Lett.* **11,** 3190–6 (2011).

26. Pimenta, M. A. *et al.* Studying disorder in graphite-based systems by Raman spectroscopy. *Phys. Chem. Chem. Phys.* **9,** 1276–91 (2007).

27. Grehl, T. Improvement in ToF-SIMS instrumentation for analytical application and fundamental research. (2003).

28. Qi, D. C. Organic Molecules on Diamond (001) : A Synchrotron Study. (2009).

29. Kurt J. Lesker Website. Assessed 18 May 2014. at <https://www.lesker.com/newweb/vacuum_systems/deposition_systems_pvd_mini_spectros.cfm>

Chapter 3 : Controlling the Molecular Orientation of CuPc Using Graphene Interlayer on ITO

3.1 Introduction

The importance of the molecular orientation in the active layer of OPV devices has been discussed in Chapter 1. For planar heterojunction OPV devices, vertical π-π stacking of the aromatic molecules is highly desirable. One of the methods to control the molecular orientation is to use a structural template layer.

In this experiment, we use CVD graphene transferred onto ITO as the interface template layer due to its excellent optical transparency[1] and its similarity in work function[2,3] with ITO.[4,5] The advantages of choosing graphene over the well-studied PTCDA structural template layer has been detailed in Section 1.1.2. Briefly, the similarity in work functions between graphene and ITO suggests that there may not be additional barriers for hole extraction at the interface due to the inclusion of graphene on ITO, while the high optical transparency of graphene minimizes light attenuation through the templating layer in an OPV device. In contrast, the PTCDA layer traps charge at the interface due to the 1.5 eV HIB, thus lowering the open circuit voltage in organic solar cells, and the optical absorption of PTCDA (~20%) overlaps with CuPc.[6] Finally, conductive graphene itself can be used as a flexible electrode in OPV (on a non-conducting flexible support) without the ITO layer.[7–10] While this is beyond the scope of this thesis, the investigations concerning the structural and electronic properties of organic films deposited on G/ITO in this thesis have the potential to be extrapolated for commercial applications in flexible electronics using only graphene as the anode.

A hole injection barrier (HIB) between CuPc and ITO of up to 1 eV has been reported.[11] For organic semiconductor devices utilizing ITO as a transparent electrode, the magnitude of the HIB

can affect charge accumulation or injection.[12–15] This implies that both ITO and the graphene interlayer require work function modification in order to attain near ohmic contact with the HOMO of CuPc for efficient charge extraction. While a few groups have used graphene as an interlayer to template CuPc,[16–18] their focus was mainly on the control of orientation of CuPc. Furthermore, the reports reveal some ambiguity concerning the effectiveness of graphene as a structural template at room temperature deposition since there appear to be two competing molecular orientations.[2,16–18] Detailed investigations of the electronic properties of CuPc deposited on graphene transferred onto ITO have not been previously reported.

In this chapter, we use PES to perform a comprehensive study of the electronic properties of CuPc films of varying thicknesses deposited on two different substrates, ITO and graphene covered bare ITO (G/ITO). This will allow us to determine the barrier to charge extraction at the interface and to propose strategies to overcome this issue. NEXAFS and XRD are used to confirm the molecular orientation of CuPc on both substrates to determine the efficacy of CVD graphene transferred onto rough ITO as a structural template. These substrates will form the anode portion in an organic photovoltaic device which will be fabricated in the last section. The PES investigation begins with sub-monolayer coverage to understand the processes at the interface, and progresses gradually to the bulk properties of CuPc which will mimic the OPV systems more closely.

3.2 Energetic Properties of CuPc on ITO and G/ITO

Figure 3-1 presents the data obtained by synchrotron based PES measurements for CuPc molecules sequentially deposited onto ITO. Figure 3-1 (a) shows the evolution of the low kinetic energy region of the PES spectra as a function of CuPc thickness on ITO. The sample work function is determined from the kinetic energy cutoff position. All the PES measurements have an error of ±0.05 eV. The work function of clean bare ITO was determined to be 4.56 eV which is

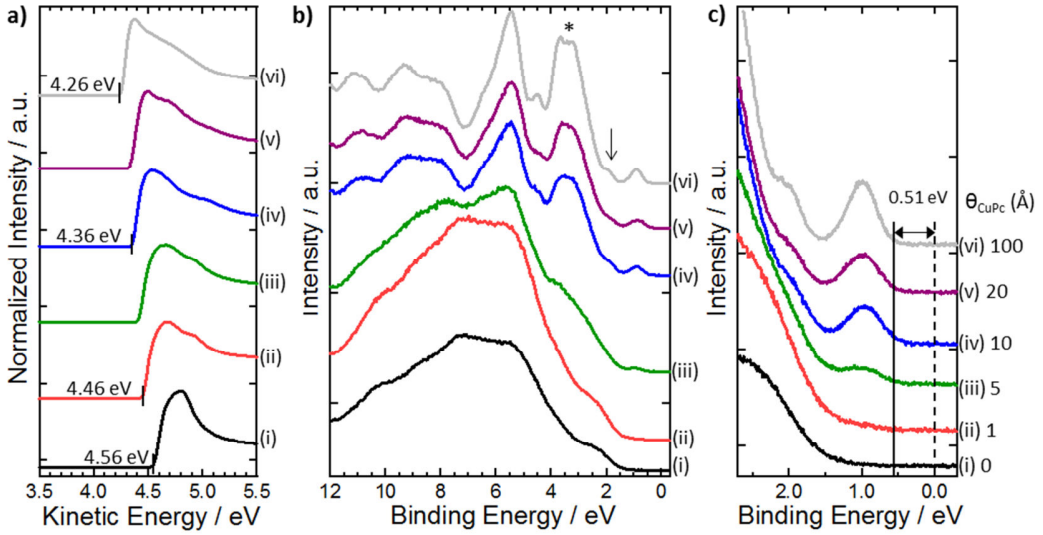

Figure 3-1 Synchrotron based PES spectra evolution of CuPc on ITO. (a) Low kinetic energy region, (b) valence band spectra at low binding energy and (c) near the Fermi level region. The thickness of the CuPc film in (a) – (c) is denoted as θ_{CuPc} and increases from (i) 1 Å to (vi) 100 Å. The peak position in (b) indicated by ' * ' is formed by the overlap between the HOMO-4 and HOMO-5 orbitals of CuPc;[27] their respective intensities depend on orientation of the molecules. The arrow in (b) marks another spectra feature (HOMO-1) of CuPc that depends on molecular orientation.

within the range of reported values from 4.20 eV to 4.85 eV depending on the preparation conditions.[4,5] Deposition of 1 Å CuPc on ITO results in a downward shift in vacuum level by 0.10 eV, corresponding to a decrease in work function by the same amount, as shown in Figure 3-1 (a). Beyond this initial change at low coverage, the work function continues to decrease gradually by another 0.10 eV at 10 Å CuPc, and finally saturates at 4.26 eV for bulk CuPc. While the total change in work function of 0.3 eV is small, it is non-negligible and larger than the error associated with the measurement (±0.05 eV). We propose that the change of work function for CuPc deposited on ITO up to 10 Å arises from the polarization and charge redistribution of the organic molecule upon deposition.[19] This may also be attributed to morphological and orientation disordering at the interface of the rough ITO substrate.[20,21] The latter can also be invoked to address the subsequent but more gradual change in work function beyond 10 Å CuPc. Band bending induced by charge transfer between ITO and CuPc is unlikely as the substrate work function (4.56 eV) is smaller than the ionization energy of CuPc - 4.80 eV for standing CuPc,[22,23] 5.15 eV for lying CuPc.[22] The corresponding electron affinities are 2.60 eV and 2.95 eV

respectively with respect to the vacuum level.[24] Based on previous results, the CuPc molecules are predominantly standing on weakly interacting substrates such as ITO.[6,25,26] This will be discussed in detail in the next section. Assuming vacuum level alignment, the Fermi level (E_F) of ITO lies within the HOMO-LUMO gap of CuPc, thus excluding the possibility of spontaneous interfacial charge transfer.

Figure 3-1 (b) shows the CuPc coverage dependent valence band features on ITO. The broad and featureless spectrum of clean ITO is presented as (i) at the bottom of the plots. The intensity of the ITO valence band signal is gradually attenuated with increasing CuPc deposition, and the spectra are almost entirely dominated by CuPc valence band features [27,28] beyond 10 Å [(iv) in Figure 3-1 (b)]. All the spectra features of CuPc do not exhibit any shift in binding energy with increasing CuPc thickness up to 20 Å; however they shift by ~0.09 eV to higher binding energy when the thickness is increased from 20 Å to 100 Å. This observation is consistent with the lack of significant shift in the vacuum level excluding the minor fluctuations due to morphological disordering which have been previously explained. More information regarding the highest occupied molecular orbital (HOMO) derived state of CuPc can be found in the close-up of the valence band region close to the Fermi level in Figure 3-1 (c). All the values of binding energy are referenced to E_F. The peak position of the CuPc HOMO state located at about 0.97 eV first becomes visible at 5 Å CuPc and increases in intensity with thicker CuPc films.

The position of the HOMO onset can be determined by extrapolating the leading edge of the HOMO peak at the lower binding energy portion to the background intensity. This position is useful in specifying the hole injection barrier (HIB) in organic solar cells which is defined as the difference between the HOMO onset and Fermi level.[29–33] For the 5 - 100 Å thick CuPc film, the HIB is determined to be around 0.51 eV. Indeed this large barrier precludes strong charge transfer at the CuPc-ITO interface. It should be pointed out that values of HIB ranging from 0.5 eV to 1.0 eV have been reported, depending on the work function of ITO.[11,14,15,33,34] Therefore, the HIB can

be tuned by modifying the initial work function of the ITO substrate through surface modifications.[12–15,34] Finally, the ionization potential (IP) of CuPc is calculated using Equation (2-5) and is determined to be 4.77 eV. This value is close to the 4.80 eV obtained for standing CuPc,[22,27,35] suggesting that the CuPc molecules in our sample are oriented likewise.

C 1s photoemission core level spectroscopy for different CuPc film thickness shown in Figure 3-2 is performed to confirm that there is no observable chemical interaction between the ITO and CuPc. A linear background subtraction is introduced before fitting each spectrum. The spectrum for clean ITO [plot (i) in Figure 3-2] reveals surface carbon contaminants despite oxygen plasma treatment before loading the sample into the measurement chamber and degassing the sample in ultra high vacuum. The constituent spectrum of the surface carbon contaminant on the ITO substrate is presented as black dotted lines in Figure 3-2. The substrate signal is gradually attenuated with increasing CuPc deposition and disappears fully above 10 Å. This agrees well with the CuPc valence band spectra in which the substrate signal is almost completely attenuated beyond 10 Å CuPc [Figure 3-1 (b)]. The C 1s peak of pristine CuPc is displayed as orange solid lines and consists of three distinct features around 284.2 eV, 285.6 eV, and 287.6 eV. These peaks are attributed to the aromatic C-C bond of the benzene ring, the C-N bonded pyrrole carbon and a π-π^* shake-up of the C-N peak respectively.[36–39] There is also a shake-up peak corresponding to the C-C bond which is mostly obscured by the C-N bonded feature and is not well resolved in our spectra.[37–39] The ratio of the aromatic to pyrrole carbon is approximately 3:1 which agrees well with the stoichiometric ratio of the 24 C-C and 8 C-N bonded carbons in CuPc.[37] The intensities of the C-C and C-N peaks increase with thicker CuPc films, whereas the binding energy of each feature remains unchanged. Since no new states are observed in the C 1s core level spectra, this suggests that CuPc interacts very weakly with the ITO substrate. The weak chemical interaction is further supported by the absence of gap states close to the Fermi level in the valence band spectra shown in Figure 3-1 (b) and (c).

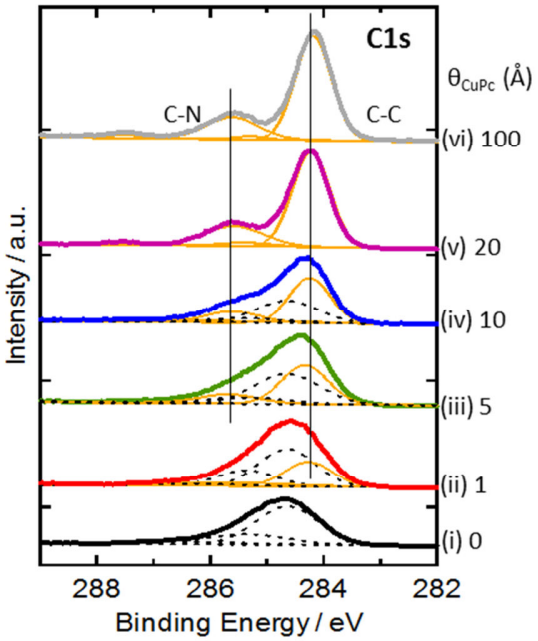

Figure 3-2 C 1s core level spectra for different film thicknesses of CuPc deposited on ITO. Dashed black lines represent the signal originating from the substrate, whereas the solid orange lines are attributed to CuPc.

The electronic structures, chemical interaction and energy level alignment of CuPc thin film on graphene modified substrate (G/ITO) are similarly investigated using synchrotron based PES. The interfacial energetics of CuPc on this inert modified G/ITO surface are not expected to differ significantly from the results obtained in Figure 3-1 as the work function of graphene is within the range of ITO work function.[40–42] However, graphene has been reported to be able to change the orientation of planar molecules from standing on weakly interacting substrates such as SiO_2 and ITO, to a tilted or lying configuration when deposited on graphene modified substrates at room temperature deposition.[2,3,16,17] Therefore, the electronic structure and interfacial properties which are orientation-dependent will be changed accordingly.[22,27,43] Detailed discussions regarding the molecular orientations of CuPc on ITO and G/ITO will be presented in Section 3.3.

Figure 3-3 shows results of PES measurements for CuPc dependent thickness series on G/ITO. The evolution of the low kinetic energy region of the PES spectra as a function of CuPc thickness on G/ITO is presented in Figure 3-3 (a). The work function of the G/ITO substrate is found to be

4.24 eV. While this value is slightly lower than the work function of free-standing single layer graphene (4.5 eV),[40–42] similar observations for graphene transferred on ITO[2,3] and SiO_2[44] have been previously reported. It has been suggested that the underlying substrate can affect the electronic properties of graphene; for instance, graphene transferred to SiO_2 is doped due to the formation of a dipole at the graphene/SiO_2 interface, resulting in a lowering of the substrate work function to 4.12 eV.[44,45] A dipole induced by charge transfer between graphene and ITO may also be present at the G/ITO interface, causing a similar decrease in the work function.

Upon depositing 1 Å CuPc on G/ITO, the substrate work function is reduced by 0.08 eV [Figure 3-3 (a)] at the interface. The work function remains almost constant up to 20 Å CuPc on G/ITO, but decreases by about 0.09 eV when the thickness of CuPc is increased to 100 Å, resulting in a final work function of 4.05 eV. The mild change in work function may be attributed to the morphological disordering of CuPc,[20,21] or to the weak interaction between graphene and CuPc.[46] Strong charge transfer between CuPc and G/ITO is unlikely to take place as the work function of G/ITO is located in the middle of CuPc bandgap.

CuPc thickness dependent valence band features are shown in Figure 3-3 (b) and a close-up of the spectral features near Fermi level in Figure 3-3 (c). Spectrum (i) in Figure 3-3 (b) of G/ITO before CuPc deposition reveals the characteristic 2p π peak of graphene at around 3.25 eV.[40,44,47] The spectrum also shows a non-zero sloping signal at low binding energy which extends to the Fermi level due to the absence of a bandgap and a distinct HOMO level in pristine monolayer graphene.[48] This is consistent with the linear dispersion relation of graphene where filled states can be found all the way to the Fermi level. Following the deposition of 1 Å CuPc, the HOMO derived feature of CuPc with peak position located at around 1.30 eV below E_F becomes visible. The intensity of this feature increases with thicker CuPc films, and the peak positions remain constant within the margins of error. The position of the HOMO onset can be resolved from the valence band region close to the Fermi level as shown in Figure 3-3 (c) using the method

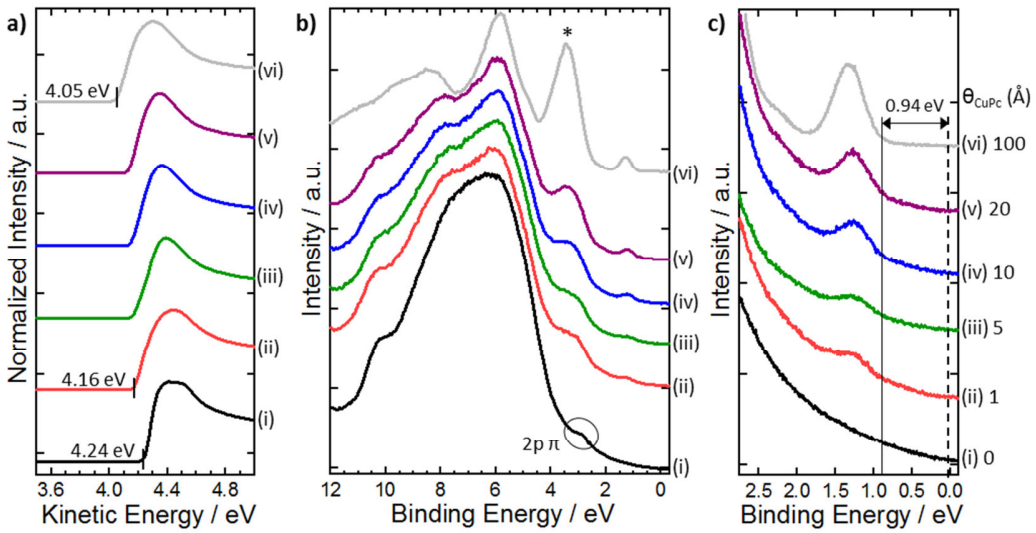

Figure 3-3 Synchrotron based PES spectra evolution of CuPc deposited on G/ITO. (a) Secondary electron cutoff region at low kinetic energy, (b) valence band spectra at low binding energy and (c) near the Fermi level region. ' * ' in (b) corresponds to the same symbol in Figure 3-1(b).

described in the preceding paragraphs. We find that the positions of HOMO onset does not vary with CuPc thickness up to 20 Å. Beyond this thickness, there is a shift of the HOMO onset and HOMO peak position to higher binding energy by 0.06 eV, which is of similar magnitude to the shift in vacuum level. The large HIB of 0.94 eV makes this setup unsuitable for use as the anode in an organic solar cell as it creates a large barrier to hole extraction at the donor-electrode interface. The IP calculated from the HIB and work function of CuPc on G/ITO is found to be 4.99 eV, which is 0.22 eV higher than CuPc deposited on ITO. The difference in IP may be assigned to a change in molecular orientation of CuPc from standing to tilted or lying when deposited on ITO as compared to G/ITO respectively, concomitantly changing the direction of surface dipole which originates from the C-H bonds at the periphery of the CuPc molecules. The difference in IP obtained in this experiment is smaller than the 0.4 eV change observed by Chen *et al.* for CuPc molecules in a standing *versus* lying orientation on a self-assembled monolayer terminated Au substrate and HOPG respectively.[22] This suggests that CuPc molecules on our G/ITO substrate acquire a spread of orientations, or are tilted at an intermediate angle to the

substrate, as opposed to the uniform flat lying layers reported by Chen *et al.*. Detailed investigation on the molecular orientation of CuPc will follow in Section 3.3.

C 1s core level spectroscopy was performed to study the interaction between CuPc and G/ITO. The resultant spectra are shown in Figure 3-4. A linear background was subtracted from the spectra prior to decomposing the spectra into their respective contributions from the substrate (black dashed lines) and the CuPc molecules (solid orange lines). The C 1s spectrum for G/ITO substrate can be fitted by 3 peaks at 284.4 eV, 285.1 eV and a shoulder at 286.2 eV. The most intense peak at 284.4 eV is unambiguously attributed to the C-C bond in graphene; while the 285.1 eV peak corresponding to C-O bonded carbon and the 286.2 eV shoulder to C=O bond may arise from residual PMMA.[40,49] For the fitted peaks of CuPc molecules, the peak positions and their ratios are the same as the core level spectra for the CuPc/ITO sample (Figure 3-2). Since the binding energies of the CuPc fitted peaks are invariant with increasing /film thickness, and there

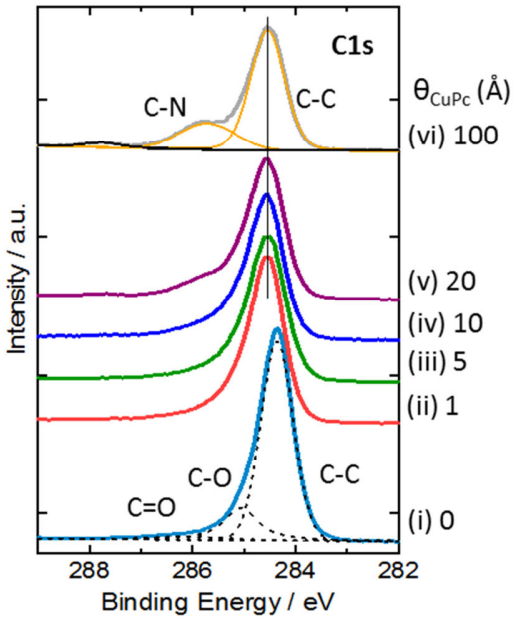

Figure 3-4 C 1s core level spectra CuPc deposited on G/ITO. Dashed black lines represent the signal originating from the substrate, whereas the solid orange lines are attributed to CuPc.

are no new peaks observed in the C 1s spectra in Figure 3-4, we conclude that CuPc molecules does not undergo chemical interactions with G/ITO.

The energy level diagrams of CuPc/ITO and CuPc/G/ITO are illustrated in Figure 3-5 (a) and (b) respectively. The position of the HOMO onset (HIB), sample work function and IP are derived from PES measurement, while the position of the LUMO was defined using the transport gap of CuPc molecules (2.2 eV).[24] The energy level diagrams of both samples show near vacuum level alignment and flat energy band conditions. The Fermi level of ITO and G/ITO lies within the bandgap of CuPc, and there is a large energy offset between the substrate work function and the HOMO or LUMO positions. Therefore charge transfer between the substrates and CuPc is energetically unfavourable. Both the IP and the HIB are larger for CuPc deposited on G/ITO as compared to ITO. In particular, the HIB is nearly twice as large for the former sample; hence the graphene interface layer by itself is energetically unfavourable to be used at the anode portion in an OPV device.

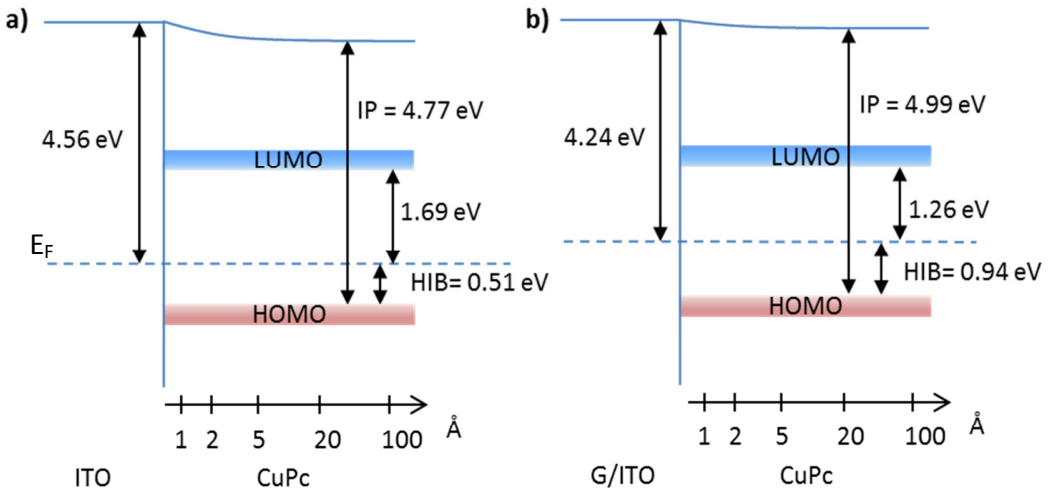

Figure 3-5 Schematic drawings showing the energy level diagrams of CuPc deposited on (a) ITO and (b) G/ITO. The work function, HIB and IP values are derived from PES measurements while the transport gap (2.20 eV) which defines the position of the LUMO is obtained from literature.[24] The position of E_F is denoted by the blue dashed line, while the HOMO and LUMO positions are represented by the pink and blue bands respectively.

The valence band features of CuPc on ITO and G/ITO in Figure 3-1 (b) & Figure 3-3 (b) respectively, together with the calculated IP of CuPc on the two substrates, can provide insights about the molecular orientation of CuPc.[23,27] The larger ionization energy of CuPc on G/ITO may be indicative of a change in orientation from standing on ITO to a more tilted configuration on G/ITO. Toader *et al.* has also reported that features in the valence band of CuPc can provide information about the average orientation of CuPc molecules.[27] First, the band encompassing HOMO-2 to HOMO-5 of CuPc [marked ' * ' in Figure 3-1 (b) & Figure 3-3 (b)] is found to vary the most with CuPc molecular orientation. The centroid of this band, together with the dominant orbital within the band, have been observed to shift to higher binding energy when the angle that CuPc molecules makes with the substrate increases (i.e. CuPc adopts a standing configuration on the substrate).[22,27] This band also has a smooth curvature near the apex when the molecules are in the lying configuration but appears as split features when the molecules are standing. Second, the HOMO-1 orbital, identified by an arrow in Figure 3-1 (b), is present for standing CuPc but almost absent for the tilted orientation due to the overlap with the HOMO-2 molecular orbital from the band marked ' * '. From our PES results, we observe a shift in the centre of gravity of the ' * ' band from 3.58 eV on ITO [Figure 3-1 (b)] to 3.38 eV in G/ITO [Figure 3-3 (b)]. Near the peak position of this band, the spectra for CuPc/ITO show split features while a singular feature is observed for CuPc/G/ITO. Finally, the HOMO-1 feature is absent in the former sample. These evidences from PES suggest that CuPc molecules have changed from a standing configuration on ITO to a tilted or lying orientation on G/ITO. However, these observations only provide qualitative inferences regarding the molecular orientation. Specific characterization techniques such as XRD and NEXAFS are additionally employed to provide direct evidence of the molecular orientation of CuPc.

3.3 Molecular Orientation of CuPc on ITO and G/ITO

Xiao *et al.*[16] and Mativetsky *et al.*[18] have previously used graphene transferred onto SiO_2 and glass substrates to control the orientation of CuPc molecules deposited on its surface. Their XRD results showed a mixture of standing and lying orientations of CuPc are present on the graphene modified substrates. Zhong *et al.* performed NEXAFS investigation on similar planar phthalocyanine molecules, F_{16}CuPc, deposited on G/ITO. The resultant average molecular angle ($38^o \pm 5^o$) suggest that the molecules are tilted, but not lying, on the substrate.[2] Based on these data, there is ambiguity concerning the structural templating effectiveness of graphene since the CuPc molecules do not appear completely templated. We propose that these observations are due to the partial coverage of the substrate by graphene due to the wet transfer process.[51] Furthermore, the graphene sheet may be damaged during the transfer.[52] This problem may be further exacerbated if the incident photon beams are larger than the substrate especially at low angle of incidence. Therefore, the resultant data for both XRD and NEXAFS measurements is a sum of the signals from the different orientations of CuPc on graphene and the exposed substrate.[a] In order to confirm the templating ability of graphene, we deposit CuPc directly onto as-received graphene on copper foil (G/Cu) to ensure nearly full coverage of the substrate by graphene, and to eliminate defects which arise during graphene transfer. In Chapter 5, we will perform detailed XRD analysis of CuPc deposited on pristine and transferred graphene.

The XRD spectra for CuPc powder, CuPc deposited on G/Cu, Cu foil, and a well-known structural template PTCDA,[6,53] are shown in Figure 3-6 (a). PTCDA is able to control the molecular orientation of CuPc from standing on bare ITO, to lying on PTCDA modified ITO.[6,53] By comparing the diffraction peaks between CuPc on PTCDA and on G/Cu, we can ascertain if graphene has similar structural templating ability as PTCDA.

[a] These scenarios apply to all the G/ITO samples used in this thesis unless otherwise stated.

The CuPc powder diffraction pattern showing all possible diffraction peaks from the α-polymorph of CuPc (i.e. randomly oriented crystals) is shown in Figure 3-6 (a) (bottom plot). The first peak at $2\theta = 6.8^{o}$ is due to the diffraction form the (1 0 0) plane. This peak is observed for CuPc deposited on weakly interacting substrates such as SiO_2 and ITO,[6,16–18,25,53] and corresponds to an orientation in which the CuPc molecules are standing almost perpendicular to the substrate.[54] The XRD spectrum for CuPc deposited on PTCDA/ITO is also shown in Figure 3-6

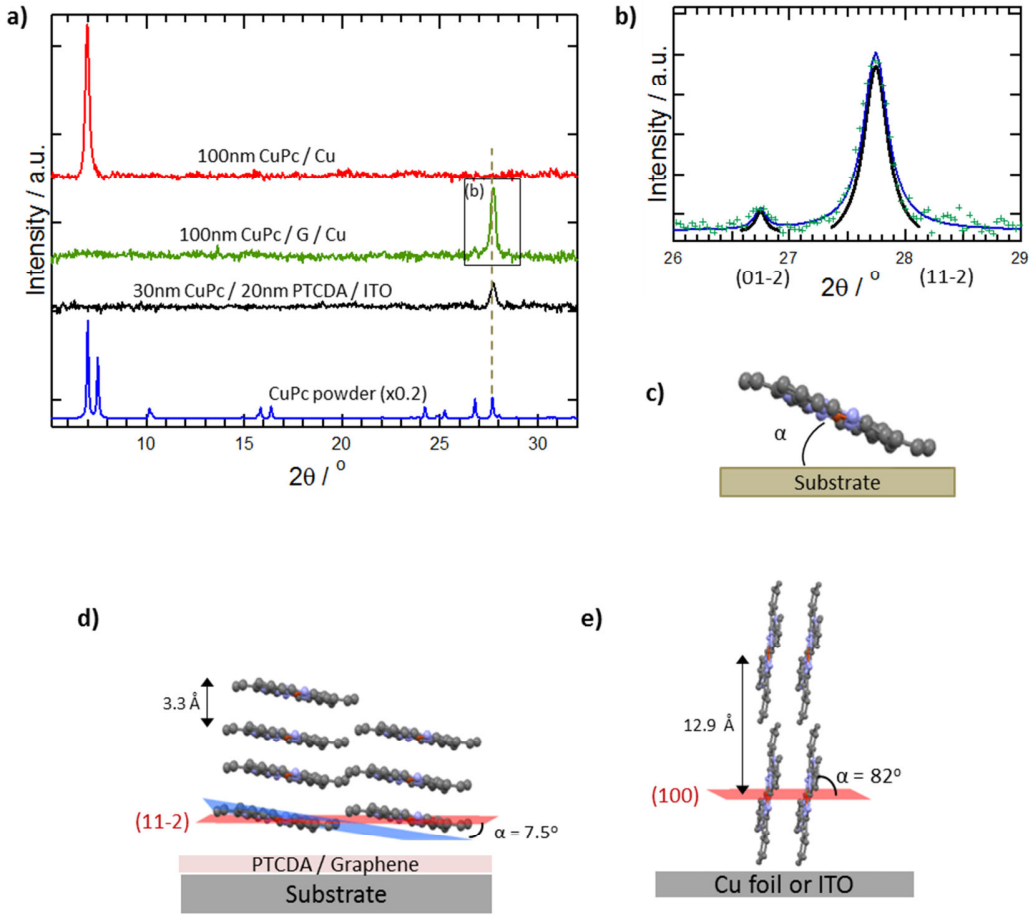

Figure 3-6 (a) XRD spectra of (blue spectrum) CuPc powder showing all possible diffractions from α-CuPc crystals (scaled for clarity), (black) 30 nm CuPc deposited on 20 nm PTCDA pre-covered ITO, (green) 100 nm CuPc on G/Cu and (red) 100 nm CuPc/Cu. The dashed grey line indicates the diffraction peak at 27.6°. (b) Close-up spectrum of the diffraction peaks of the 100 nm CuPc/G/Cu sample showing details of the fitted peaks (in black). These peaks correspond to the (01-2) and (11-2) planes at 26.6° and 27.6° respectively for α-CuPc. Schematic drawings showing (c) the angle α between the molecule and the substrate, (d) the 'lying orientation' on PTCDA or graphene covered substrates, and (e) the 'standing' molecular orientation of CuPc on weakly interacting substrates such as ITO.

(a) (black spectrum). A single diffraction peak at 27.6^{o}, shown by a grey dashed line in Figure 3-6 (a), implies that CuPc crystallites in the film are textured with respect to the substrate. This peak is due to diffractions from the (1 1 -2) plane of CuPc, and a small contribution from the (0 1 -2) plane of PTCDA. The molecular tilt plane of CuPc is 7.5^{o} with respect to the substrate (lying orientation) when the (1 1 -2) plane is preferentially parallel to the substrate. The absence of the CuPc (1 0 0) peak, and the emergence of a single diffraction peak at 2θ = 27.6^{o} in the CuPc/PTCDA/ITO spectrum indicates that CuPc molecules are lying parallel to the substrate.

Finally, XRD is performed on CuPc/G/Cu and Cu foil [Figure 3-6 (a), green and red plots respectively]. Cu foils were prepared by exposing a piece of G/Cu substrate to oxygen plasma to remove the graphene layer. The systematic absence of peaks compared to a fully randomly oriented powder [bottom spectrum, Figure 3-6 (a)] implies that the crystallites in CuPc films are textured with respect to the substrate. The CuPc/Cu spectrum shows a single diffraction peak at 6.8^{o}, indicating that (1 0 0) plane of CuPc is parallel to the substrate, and consequently the CuPc molecules are standing on the substrate. In marked contrast, the spectrum for CuPc/G/Cu resembles the spectrum of CuPc/PTCDA/ITO more closely. This suggests that graphene, like PTCDA, is able to control the molecular orientation of CuPc. A zoomed scan around the prominent peak of the CuPc/G/Cu spectrum [Figure 3-6 (b)] reveals two peaks centred at 2θ = 26.6^{o} and 27.6^{o}. These peaks are due to diffraction from the (0 1 -2) and (1 1 -2) planes of CuPc respectively.[54] Defining α to be the angle subtended by the molecular plane and the substrate plane [Figure 3-6 (c)], α = 9.0^{o} and 7.5^{o} when the (0 1 -2) and (1 1 -2) planes of CuPc respectively are preferentially parallel to the substrate. These results verify the effectiveness of graphene as a structural template for CuPc since all the molecules are nearly lying parallel to the substrate. Schematic diagrams illustrating the packing and orientation of CuPc molecules on PTCDA or graphene structure templates, and on substrates such as Cu foil or ITO, are shown in Figure 3-6 (d) and Figure 3-6 (e) respectively.

The preferred orientation of CuPc molecules on various substrates is due to the subtle interplay between intermolecular and interfacial interaction energies. On ITO substrates, the intermolecular interaction between CuPc molecules dominates over the molecule-substrate interaction, hence a standing geometry of CuPc molecules is observed.[25] Conversely on graphene, the π-π molecule-substrate interaction of CuPc on graphene dominates, resulting in a lying adsorption geometry of CuPc.[17,18,55] This lying geometry has also been observed on a similar substrate of graphite (HOPG).[20,56,57] Yin *et al.* previously calculated that the adsorption energy of CuPc on HOPG is significantly stronger than the intermolecular interaction between CuPc molecules. Although the absorption energies for CuPc on G/Cu are likely to be different from CuPc/HOPG due to the influence from the underlying substrate,[44] we propose that surface energies are similar to HOPG[17] since the orientation and crystallinity of CuPc on graphene and HOPG are similar.[23]

Next, the orientation of CuPc molecules in ultra-thin films in the range of Å is probed by NEXAFS. The capability of standard XRD is limited in this regime as diffraction from nano-sized crystallites might be too weak to be detected above the background substrate signal. NEXAFS on the other hand does not require crystallization of molecules as it records the transitions of all the molecules present within the beam size of the film. NEXAFS monitors the resonant transitions of electrons from the core level of an atomic species to the unoccupied molecular orbitals, such as the π* or σ* orbitals in aromatic molecules. As described in Section 2.2.2, angle dependent NEXAFS can be performed to determine the orientation of planar aromatic molecules such as CuPc on the various substrates. Two angles are used in all our NEXAFS measurement *viz.* $\theta = 20^{o}$ (grazing incidence) and $\theta = 90^{o}$ (normal incidence) where θ is defined according to the schematic in Figure 3-7 (a). Figure 3-7 (b) depicts a scenario during NEXAFS measurement where the incident photon beam probes a mixture of orientations of CuPc molecules. A similar situation has been previously described for XRD measurements.

Figure 3-7 (c) and (d) show the results obtained from NEXAFS N K-edge measurements on CuPc/ITO and CuPc/G/ITO respectively at θ = 20° and θ = 90° for two different film thicknesses. The sharp absorption peaks in the range of 397 – 404 eV are assigned to the resonant transitions from the N 1s core level into different π* states of CuPc whereas the broad absorption peaks at higher photon energies are attributed to the transition from N 1s to the σ* orbitals.[58] For the

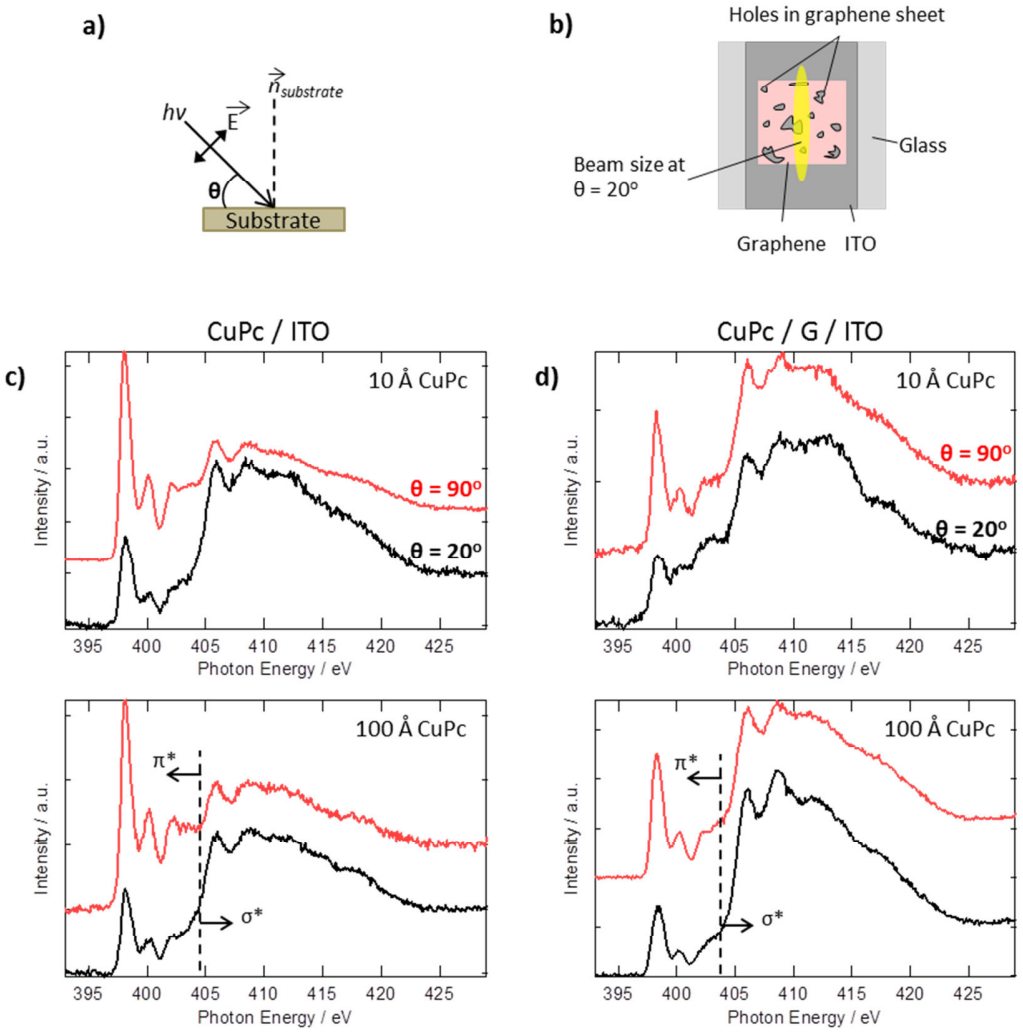

Figure 3-7 (a) Schematic diagram defining the incident beam angle θ in a NEXAFS setup. (b) Illustration showing graphene transferred onto ITO and the relative the size of the incident photon beam (8 mm x 1 mm) at θ = 20° (grazing incidence). At this angle the beam is larger than the graphene sheet, therefore the calculated CuPc molecular angle is an average of graphene covered areas and the bare substrate. Graphene sheet also tears during the transfer process and forms holes which reveal the underlying substrate. The sizes of the holes are exaggerated for clarity. Angle-dependent NEXAFS N *K*-edge spectra for 10Å and 100Å CuPc deposited on (c) ITO and (d) G/ITO at θ = 90° (red) and θ = 20° (black).

CuPc/ITO sample [Figure 3-7 (c)], the spectra for the 10 Å (top) and 100 Å (bottom) thick CuPc films reveal that the maximum intensity for the N 1s → π* transition is observed at normal incidence, while the transitions to the σ* orbitals are greatly enhanced at grazing incidence. The angular dependence of the NEXAFS confirms that the CuPc film is well-ordered on ITO and the molecules adopt a standing configuration. The average molecular tilt angle (α) can be estimated from the intensity ratio of the lowest energy π* transition at θ = 90° and θ = 20° [$R(\pi*) = \frac{I(\theta = 90^o)}{I(\theta = 20^o)}$]. The expression for I(θ) is found in Equation (2-8). For CuPc/ITO, α = 70° ± 5° for both low and high coverages of CuPc.

The same analysis is repeated for the NEXAFS spectra of CuPc/G/ITO shown in Figure 3-7 (d). The intensity of the π* resonant transitions varies with the incident angle, implying that the film is likely to be ordered. The angle α is estimated to be 63° ± 5° which is slightly lower than that of CuPc/ITO. This value is close to a random orientation (~54.7°) for CuPc molecules.[59] Related experiments of the deposition of planar molecules on pristine graphene,[60] transferred graphene[2,3,16,18] and HOPG[35,61,62] reveal a well ordered film with molecules lying almost flat on the substrate. We propose that the larger than expected tilt angle (63° *versus* nearly flat lying molecules) is mediated by 1) the roughness of the G/ITO substrate surface (cf. Figure 2-13) causing the molecules to attain a spread of orientations, and 2) the averaging effect of the beam over different orientations of CuPc as depicted in Figure 3-7 (b). These scenarios result in an apparent average random orientation of CuPc molecules on G/ITO. Using cross-section transmission electron microscopy (TEM), Gilchrist *et al.*[63] observed that CuPc molecules form nano-sized grains with a range of orientations on rough substrates such as ITO and even PTCDA/ITO. We propose that a similar situation occurs for CuPc deposited on the rough G/ITO substrate.

We have demonstrated in this chapter that control of the molecular orientation can be achieved by using a graphene template layer. However, the energy level diagrams shown in Figure 3-5 indicate that there is a trade-off of a significantly larger HIB when a layer of graphene is inserted between CuPc and ITO. Hence the anode structure of G/ITO requires further modification before the beneficial effects of a graphene template can be fully realised. To assess the impact of graphene-templated growth of CuPc on OPV device characteristics, a planar heterojunction OPV using a well-studied CuPc/C_{60}[6,64–66] active layer is fabricated. The results are referenced to devices using unmodified ITO substrates. The results are discussed in detail in the following section.

3.4 OPV Device Characterization using ITO and G/ITO as Anode Layer

A schematic drawing of the OPV structure that is used for device characterization is presented in Figure 3-8 (a) and (b). In our devices, the optional intermediate layer in the schematic ranges from PTCDA and graphene in this section, to a work function modifying layer (F_4-TCNQ) in the Chapter 5. The purpose of device fabrication and characterization is to compare the effects of modifying the molecular orientation of the donor layer against a reference unmodified OPV device. We commence the investigation by characterizing well-studied CuPc/C_{60} devices[6,64–66] with the donor CuPc layer in different stacking orientations: a standing CuPc layer in a reference device of 100 nm Al/12 nm BCP/40 nm C_{60}/30 nm CuPc/ITO (simplified as A/ITO where 'A' refers to '100 nm Al/12 nm BCP/40 nm C_{60}/30 nm CuPc') and a lying CuPc generated by inserting a 5 nm PTCDA interlayer (A/5 nm PTCDA/ITO) as structural template for CuPc.[6] It must be stressed that our results differ from the best published data due to an unoptimized deposition system and a large Al contact mask (0.12 cm^2 versus 0.08 cm^2 commonly used) which increases the series resistance and highlights non-uniformity and defects in our device architecture due to a large sampling area.[67,68] Furthermore, we record that the solar cell parameters vary between growth batches but show the same general trend. For comparison

purposes, we report the representative averaged data of several devices grown within the same batch, and include the rest of the data in Appendix B.

The effects of structural templating on the short-circuit current (J_{sc}) and open-circuit voltage (V_{oc}) parameters in our OPV device configuration - assuming an idealized defect-free case for both types of OPV - are predicted as follows 1) an enhancement in J_{sc} due to an improved charge transport as a consequence of a modified stacking direction and increased absorption efficiency of the CuPc,[6,17,64,69] and 2) V_{oc} that is dependent on the trade-off between the HIB and the offset between the HOMO of the donor molecule ($HOMO_D$) and LUMO of the acceptor molecule ($LUMO_A$). V_{oc} has been found to scale almost linearly with the difference between $HOMO_D$ - $LUMO_A$,[70,71] but at the same time is also affected by charge carrier losses at the interface due to large HIB.[72] For tilted or lying CuPc molecules, the enhancement in IP results in charges being trapped at the CuPc-G/ITO interface due to a larger HIB, yet simultaneously enhances the energetic offset between the acceptor and donor molecules (i.e. larger $HOMO_D$ - $LUMO_A$).[73]

Figure 3-8 (c) shows J-V curves under AM 1.5 solar illumination at 100 mW cm^{-2} for OPV cells with device structures A/ITO and A/5 nm PTCDA/ITO in red and black respectively. Their corresponding dark J-V curves are shown in the inset, and show good diode rectifying characteristics. As compared to the reference cell, the device with the PTCDA interlayer shows noticeable improvement in J_{sc} from 0.28 mA cm^{-2} to 0.40 mA cm^{-2} whilst their fill factors (FF) of 0.27 and V_{oc} of ~0.15 V remains essentially the same.

Both PTCDA and graphene interlayers on ITO share some similarities : they are able to modify the orientation of CuPc, but at the same time cause charges to build up at the anode interface due to an appreciable HIB (~0.9 eV for CuPc/G/ITO and 1.5 eV for CuPc/PTCDA/ITO[6]). In view of these similarities, we expect that our subsequent device of A/G/ITO should have the same trend as A/PTCDA/ITO, showing an improvement in J_{sc} while a possible loss in V_{oc}.

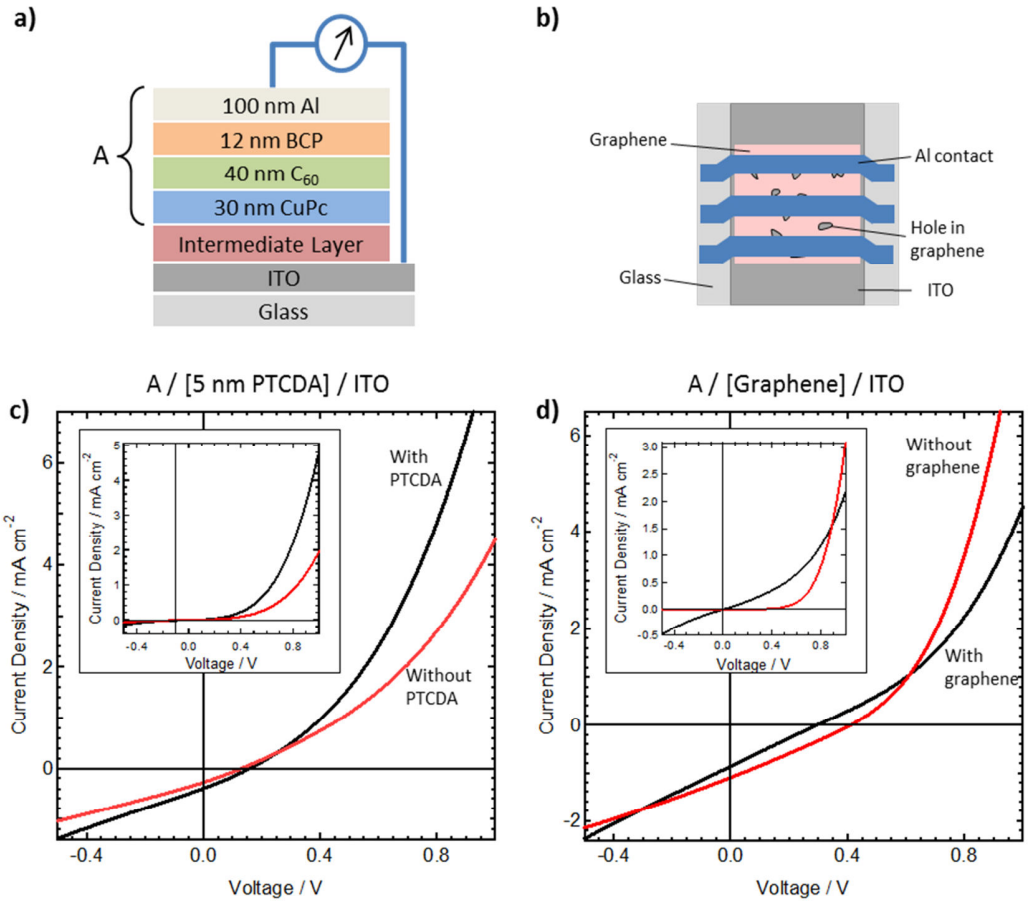

Figure 3-8 (a) Schematic diagram of the solar cell structure used in all solar cell characterization experiment. ' A ' refers to the structure 100 nm Al/12 nm BCP/40 nm C_{60}/30 nm CuPc while the intermediate layer is either 5 nm PTCDA or graphene in this chapter; 5 Å F_4-TCNQ or 5 Å F_4-TCNQ/graphene in Chapter 6; or entirely absent. (b) Top view drawing of G/ITO solar cell with Al top contacts (8.0 mm x 0.15 mm) in blue. The contacts overlap areas where graphene has torn and the underlying ITO substrate is revealed. Current density as a function of cell voltage (J-V) curves under 100 mW/cm^2 illumination for (c) red: A/ITO & black: A/5nm PTCDA/ITO, and (d) red: A/ITO & black: A/G/ITO. Inset: J-V curve of the devices under dark. Current leakage is very pronounced for the substrate modified by graphene interlayer in (c).

J-V curves of the reference device on ITO (red) and G/ITO (black) are shown in Figure 3-8 (d) together with their dark current in the inset. Diagnostics of the dark current J-V curves reveal that the A/ITO shows good diode rectifying characteristics in the dark, while significant leakage current in reverse bias, or low shunt resistance R_{sh}, is associated with the A/G/ITO device. R_{sh} is estimated from the gradient of the curve at 0 V external bias and is determined to be 1.4 kΩ cm^2 for in the A/G/ITO device and 600 kΩ cm^2 for A/ITO. The low value of R_{sh} for A/G/ITO is most

likely attributed to the very rough surface morphology of graphene transferred onto the ITO substrate at areas where graphene is torn and scrolled up, providing an alternative route for the current to flow. In addition to the large leakage current, the A/G/ITO device also suffers from large series resistance R_s. While the value of R_s should ideally be calculated at high forward bias at 2 V, the slopes of the J-V curve close to 1 V[74] can be used to compare R_s for the A/ITO and A/G/ITO. R_s for A/ITO is approximately 63 Ω cm^2 while that for A/G/ITO is 160 Ω cm^2. For both devices, the large surface contact area has a deleterious effect on R_s.[67] The large energy level mismatch at the CuPc-graphene interface and the high sheet resistance of graphene (~kΩ)[9,75,76] further contribute to increasing R_s for A/G/ITO devices.

The J-V curves under illumination [Figure 3-8 (d)] record a decrease in V_{oc} from 0.41 V to 0.31 V when a graphene interface layer is added to the anode. The loss in V_{oc} might stem from charge accumulation and recombination at the CuPc-G/ITO interface, or might be caused by large leakage current.[77,78] Structural templating by the graphene layer should result in an increase in J_{sc} due to improved hole mobility through CuPc. Instead we register a 30% reduction in J_{sc} from 1.06 mA cm^{-2} for the A/ITO device to 0.71 mA cm^{-2} for the A/G/ITO device. We attribute this to the larger R_s present in the A/G/ITO device, thereby reducing the photogenerated current flowing through the device. In fact, both A/G/ITO and A/ITO devices suffer from high R_s which is evident from the nearly linear J-V curve under illumination up to $V_{oc,}$[67] but R_s for A/G/ITO is more pronounced as the graphene interlayer adds to the series resistance present in the OPV device. In their simulation, Servaites *et al.* determined that the maximum FF attainable for samples with high R_s beyond a critical threshold is constant since it is limited by the straight line curve at values below V_{oc}.[67] We observe similar values of FF for A/G/ITO (FF = 0.25) and A/ITO (FF = 0.27) in our experiment despite obtaining smaller values for J_{sc} and V_{oc} and a larger R_s for the former sample. This implies that the value of R_s for intrinsic A/ITO is already larger than the

threshold value as suggested by Servaites *et al.*, therefore increasing R_s in A/G/ITO results does not cause a significant variation in FF despite lower J_{sc} and V_{oc} values.

The effect of reducing J_{sc} and V_{oc} in the G/ITO device halved the power conversion efficiency when compared against the reference cell on ITO. It is noteworthy that large leakage current and high R_s are usually associated with transferred graphene (without further modification) used either as an anode or transferred onto substrates,[2,76] suggesting that this is an inherent difficulty associated with graphene. This may arise from the large sheet resistance compared to ITO (for a graphene only anode), and also the roughness and imperfection of the graphene surface. The latter is evident as coating the surface of graphene with a layer of MoO_x or PEDOT:PSS to planarize and uniformly cover the surface can significantly reduce current leakage.[9,76]

3.5 Conclusion and Future Work

We have confirmed the remarkable ability of single to bi- layer graphene to control the orientation of CuPc deposited on its surface using NEXAFS and XRD techniques, further complemented by inferences from photoemission data. While CuPc molecules 'stand' on the non-interacting ITO, subtending an angle of around 82^o between the molecular plane and the substrate, the tilt angle is reduced to around 10^o when deposited on G/Cu, adopting a 'lying' configuration. The latter orientation of CuPc has the potential to improve J_{sc} in OPV devices due to enhanced orbital overlap leading to higher charge mobility between adjacent molecules. PES studies show negligible chemical interactions between CuPc and ITO or G/ITO surfaces. However, the change in orientation of CuPc molecules comes at a cost of a larger HIB which has a detrimental effect on charge extraction at the electrode. The test OPV devices with G/ITO at the anode side performed poorly due to the large HIB leading to high R_s, and also due to large leakage currents in the G/ITO devices. In view of these drawbacks with using graphene alone as a template layer, it is desirable to select a work function modifier layer to lower the HIB,

simultaneously reduce the R_s by increasing sheet conductivity through doping, while maintaining the templating ability of graphene. This study will be the focus for the subsequent two chapters.

Looking forward, the strategy of using graphene to control molecular orientation can be extended to a variety of poly-aromatic planar molecules in other organic semiconductor devices such as OLED. The ability to synthesize large scale roll-to-roll graphene[75] coupled with improvement in CVD graphene transfer techniques to a variety of substrates with different properties[7] makes it possible to scale up this templating strategy on technologically important substrates for commercial applications.

3.6 References

1. Nair, R. R. *et al.* Fine structure constant defines visual transparency of graphene. *Science* **320,** 1308 (2008).

2. Zhong, S. *et al.* CVD graphene as interfacial layer to engineer the organic donor-acceptor heterojunction interface properties. *ACS Appl. Mater. Interfaces* **4,** 3134–40 (2012).

3. Ying Mao, H. *et al.* Chemical vapor deposition graphene as structural template to control interfacial molecular orientation of chloroaluminium phthalocyanine. *Appl. Phys. Lett.* **99,** 093301 (2011).

4. Schlaf, R., Murata, H. & Kafafi, Z. Work function measurements on indium tin oxide films. *J. Electron Spectros. Relat. Phenomena* **120,** 149–154 (2001).

5. Park, Y., Choong, V., Gao, Y., Hsieh, B. R. & Tang, C. W. Work function of indium tin oxide transparent conductor measured by photoelectron spectroscopy. *Appl. Phys. Lett.* **68,** 2699 (1996).

6. Sullivan, P., Jones, T. S., Ferguson, a. J. & Heutz, S. Structural templating as a route to improved photovoltaic performance in copper phthalocyanine/fullerene (C60) heterojunctions. *Appl. Phys. Lett.* **91,** 233114 (2007).

7. Song, J. *et al.* A general method for transferring graphene onto soft surfaces. *Nat. Nanotechnol.* **8,** 356–62 (2013).

8. Kim, K. S. *et al.* Large-scale pattern growth of graphene films for stretchable transparent electrodes. *Nature* **457,** 706–10 (2009).

9. Wang, Y., Tong, S. W., Xu, X. F., Ozyilmaz, B. & Loh, K. P. Interface engineering of layer-by-layer stacked graphene anodes for high-performance organic solar cells. *Adv. Mater.* **23,** 1514–8 (2011).

10. Gomez De Arco, L. *et al.* Continuous, highly flexible, and transparent graphene films by chemical vapor deposition for organic photovoltaics. *ACS Nano* **4,** 2865–73 (2010).

11. Lee, S. T., Wang, Y. M., Hou, X. Y. & Tang, C. W. Interfacial electronic structures in an organic light-emitting diode. *Appl. Phys. Lett.* **74,** 670 (1999).

12. Gross, M. *et al.* Improving the performance of doped pi-conjugated polymers for use in organic light-emitting diodes. *Nature* **405,** 661–5 (2000).

13. Friend, R. H. *et al.* Electroluminescence in conjugated polymers. *Nature* **397,** 121–128 (1999).

14. Mason, M. G. *et al.* Characterization of treated indium–tin–oxide surfaces used in electroluminescent devices. *J. Appl. Phys.* **86,** 1688 (1999).

15. Wu, C. C., Wu, C. I., Sturm, J. C. & Kahn, A. Surface modification of indium tin oxide by plasma treatment: An effective method to improve the efficiency, brightness, and reliability of organic light emitting devices. *Appl. Phys. Lett.* **70,** 1348 (1997).

16. Xiao, K. *et al.* Surface-induced orientation control of CuPc molecules for the epitaxial growth of highly ordered organic crystals on graphene. *J. Am. Chem. Soc.* **135,** 3680–7 (2013).

17. Singha Roy, S., Bindl, D. J. & Arnold, M. S. Templating Highly Crystalline Organic Semiconductors Using Atomic Membranes of Graphene at the Anode/Organic Interface. *J. Phys. Chem. Lett.* **3,** 873–878 (2012).

18. Mativetsky, J. M., Wang, H., Lee, S. S., Whittaker-Brooks, L. & Loo, Y.-L. Face-on stacking and enhanced out-of-plane hole mobility in graphene-templated copper phthalocyanine. *Chem. Commun.* **50,** 5319–5321 (2014).

19. Verlaak, S. *et al.* Electronic Structure and Geminate Pair Energetics at Organic-Organic Interfaces: The Case of Pentacene/C60 Heterojunctions. *Adv. Funct. Mater.* **19,** 3809–3814 (2009).

20. Chen, W., Qi, D.-C., Huang, H., Gao, X. & Wee, A. T. S. Organic-Organic Heterojunction Interfaces: Effect of Molecular Orientation. *Adv. Funct. Mater.* **21,** 410–424 (2011).

21. Koch, N. *et al.* Influence of molecular conformation on organic/metal interface energetics. *Chem. Phys. Lett.* **413,** 390–395 (2005).

22. Chen, W. *et al.* Molecular Orientation-Dependent Ionization Potential of Organic Thin Films. *Chem. Mater.* **20,** 7017–7021 (2008).

23. Chen, W., Qi, D. & Huang, Y. Molecular Orientation Dependent Energy Level Alignment at Organic - Organic Heterojunction Interfaces. *J. Phys. Chem. C* 12832–12839 (2009).

24. Zahn, D. R. T., Gavrila, G. N. & Gorgoi, M. The transport gap of organic semiconductors studied using the combination of direct and inverse photoemission. *Chem. Phys.* **325,** 99–112 (2006).

25. Peisert, H. *et al.* Order on disorder: Copper phthalocyanine thin films on technical substrates. *J. Appl. Phys.* **90,** 466 (2001).

26. Witte, G. & Wöll, C. Growth of aromatic molecules on solid substrates for applications in organic electronics. *J. Mater. Res.* **19,** 1889–1916 (2011).

27. Toader, T., Gavrila, G., Braun, W., Ivanco, J. & Zahn, D. R. T. Valence band fine structure of copper phthalocyanine thin films: Effect of molecular orientation. *Phys. Status Solidi* **246,** 1510–1518 (2009).

28. Gavrila, G., Seifert, S., Braun, W. & Zahn, D. R. T. *Electronic Properties of Highly Ordered CuPc Thin Films*. 516–518

29. Fukagawa, H. *et al.* Origin of the highest occupied band position in pentacene films from ultraviolet photoelectron spectroscopy: Hole stabilization versus band dispersion. *Phys. Rev. B* **73,** 245310 (2006).

30. Chen, W. *et al.* Tuning the hole injection barrier at the organic/metal interface with self-assembled functionalized aromatic thiols. *J. Phys. Chem. B* **110,** 26075–80 (2006).

31. Amy, F., Chan, C. & Kahn, A. Polarization at the gold/pentacene interface. *Org. Electron.* **6,** 85–91 (2005).

32. Wan, A., Hwang, J., Amy, F. & Kahn, A. Impact of electrode contamination on the α-NPD/Au hole injection barrier. *Org. Electron.* **6,** 47–54 (2005).

33. Hill, I. & Kahn, A. Combined photoemission/in vacuo transport study of the indium tin oxide/copper phthalocyanine/N,N′-diphenyl-N,N′-bis(l-naphthyl)-1,1′biphenyl-4,4″diamine molecular organic semiconductor system. *J. Appl. Phys.* **86,** 2116–2122 (1999).

34. Cho, S. & Piper, L. Soft X-ray spectroscopy of C60/copper phthalocyanine/MoO3 interfaces: role of Reduced MoO3 on energetic band alignment and improved performance. *J. Phys. Chem. B* **114,** 18252–18257 (2010).

35. Chen, W. *et al.* Molecular orientation dependent interfacial dipole at the F16CuPc/CuPc organic heterojunction interface. *Appl. Phys. Lett.* **92,** 063308 (2008).

36. Dufour, G. *et al.* Copper phthalocyanine on Si(111)-7 × 7 and Si(001)-2 × 1 surfaces: an X-ray photoemission spectroscopy and synchrotron X-ray absorption spectroscopy study. *Surf. Sci.* **319,** 251–266 (1994).

37. Schwieger, T., Peisert, H., Golden, M., Knupfer, M. & Fink, J. Electronic structure of the organic semiconductor copper phthalocyanine and K-CuPc studied using photoemission spectroscopy. *Phys. Rev. B* **66,** 155207 (2002).

38. Peisert, H., Knupfer, M. & Fink, J. Electronic structure of partially fluorinated copper phthalocyanine (CuPCF4) and its interface to Au (100). *Surf. Sci.* **515,** 491–498 (2002).

39. Ottaviano, L. *et al.* Thin and ultra-thin films of nickel phthalocyanine grown on highly oriented pyrolitic graphite: an XPS, UHV-AFM and air tapping-mode AFM study. *Surf. Sci.* **373,** 318–332 (1997).

40. Kim, J.-H. *et al.* Work function engineering of single layer graphene by irradiation-induced defects. *Appl. Phys. Lett.* **103,** 171604 (2013).

41. Yu, Y.-J. *et al.* Tuning the graphene work function by electric field effect. *Nano Lett.* **9,** 3430–4 (2009).

42. Sque, S. J., Jones, R. & Briddon, P. R. The transfer doping of graphite and graphene. *Phys. status solidi* **204,** 3078–3084 (2007).

43. Duhm, S. *et al.* Orientation-dependent ionization energies and interface dipoles in ordered molecular assemblies. *Nat. Mater.* **7,** 326–32 (2008).

44. Wu, Q.-H., Hong, G., Ng, T. W. & Lee, S. T. Substrate effect on the electronic structures of CuPc/graphene interfaces. *Appl. Phys. Lett.* **100,** 161603 (2012).

45. Shi, Y., Dong, X., Chen, P., Wang, J. & Li, L.-J. Effective doping of single-layer graphene from underlying SiO2 substrates. *Phys. Rev. B* **79,** 115402 (2009).

46. Zhong, J.-Q. *et al.* Energy level realignment in weakly interacting donor-acceptor binary molecular networks. *ACS Nano* **8,** 1699–707 (2014).

47. Luo, Z. *et al.* Modulating the electronic structures of graphene by controllable hydrogenation. *Appl. Phys. Lett.* **97,** 233111 (2010).

48. Novoselov, K. S. *et al.* Two-dimensional gas of massless Dirac fermions in graphene. *Nature* **438,** 197–200 (2005).

49. Lin, Y.-C. *et al.* Graphene annealing: how clean can it be? *Nano Lett.* **12,** 414–9 (2012).

50. Akaike, K., Kanai, K., Ouchi, Y. & Seki, K. Impact of Ground-State Charge Transfer and Polarization Energy Change on Energy Band Offsets at Donor/Acceptor Interface in Organic Photovoltaics. *Adv. Funct. Mater.* **20,** 715–721 (2010).

51. Li, X. *et al.* Transfer of large-area graphene films for high-performance transparent conductive electrodes. *Nano Lett.* **9,** 4359–63 (2009).

52. Liang, X. *et al.* Toward clean and crackless transfer of graphene. *ACS Nano* **5,** 9144–53 (2011).

53. Warner, M. *et al.* Spin-based diagnostic of nanostructure in copper phthalocyanine-C60 solar cell blends. *ACS Nano* **6,** 10808–15 (2012).

54. Hoshino, A., Takenaka, Y. & Miyaji, H. Redetermination of the crystal structure of alpha-copper phthalocyanine grown on KCl. *Acta Crystallogr. B.* **59,** 393–403 (2003).

55. Xiao, K., Liu, Y. Q., Yu, G. & Zhu, D. B. Organic field-effect transistors using copper phthalocyanine thin film. *Synth. Met.* **137,** 991–992 (2003).

56. Huang, Y. L. *et al.* Scanning tunneling microscopy investigation of self-assembled CuPc/F16CuPc binary superstructures on graphite. *Langmuir* **26,** 3329–34 (2010).

57. Yin, S., Wang, C., Xu, B. & Bai, C. Studies of CuPc Adsorption on Graphite Surface and Alkane Adlayer. *J. Phys. Chem. B* **106,** 9044–9047 (2002).

58. Willey, T. M. *et al.* Electronic structure differences between H(2)-, Fe-, Co-, and Cu-phthalocyanine highly oriented thin films observed using NEXAFS spectroscopy. *J. Chem. Phys.* **139,** 034701 (2013).

59. Stöhr, J. *NEXAFS Spectroscopy*. (Springer, 1992).

60. Ren, J. *et al.* Properties of copper (fluoro-)phthalocyanine layers deposited on epitaxial graphene. *J. Chem. Phys.* **134,** 194706 (2011).

61. Chen, W. *et al.* Orientation-controlled charge transfer at CuPc/F16CuPc interfaces. *J. Appl. Phys.* **106,** 064910 (2009).

62. Wong, S., Huang, H. & Huang, Y. Effect of fluorination on the molecular packing of perfluoropentacene and pentacene ultrathin films on Ag (111). *J. Phys. Chem. C* **114,** 9356–9361 (2010).

63. Gilchrist, J. B. *et al.* Uncovering the Buried Interface in Molecular Photovoltaics. *Accept. by Adv. Funct. Mater.*

64. Cheng, C. H. *et al.* Organic solar cells with remarkable enhanced efficiency by using a CuI buffer to control the molecular orientation and modify the anode. *Appl. Phys. Lett.* **97,** 083305 (2010).

65. Peumans, P. & Forrest, S. R. Very-high-efficiency double-heterostructure copper phthalocyanine/C60 photovoltaic cells. *Appl. Phys. Lett.* **79,** 126 (2001).

66. Heutz, S., Sullivan, P., Sanderson, B. M., Schultes, S. M. & Jones, T. S. Influence of molecular architecture and intermixing on the photovoltaic, morphological and spectroscopic properties of CuPc–C60 heterojunctions. *Sol. Energy Mater. Sol. Cells* **83,** 229–245 (2004).

67. Servaites, J. D., Yeganeh, S., Marks, T. J. & Ratner, M. A. Efficiency Enhancement in Organic Photovoltaic Cells: Consequences of Optimizing Series Resistance. *Adv. Funct. Mater.* **20,** 97–104 (2010).

68. Xue, J., Uchida, S., Rand, B. P. & Forrest, S. R. 4.2% efficient organic photovoltaic cells with low series resistances. *Appl. Phys. Lett.* **84,** 3013 (2004).

69. Rand, B. P. *et al.* The Impact of Molecular Orientation on the Photovoltaic Properties of a Phthalocyanine/Fullerene Heterojunction. *Adv. Funct. Mater.* **22,** 2987–2995 (2012).

70. Scharber, M. C. *et al.* Design Rules for Donors in Bulk-Heterojunction Solar Cells—Towards 10 % Energy-Conversion Efficiency. *Adv. Mater.* **18,** 789–794 (2006).

71. Brabec, C. J., Sariciftci, N. S. & Hummelen, J. C. Plastic Solar Cells. *Adv. Funct. Mater.* **11,** 15–26 (2001).

72. Blakesley, J. C. & Neher, D. Relationship between energetic disorder and open-circuit voltage in bulk heterojunction organic solar cells. *Phys. Rev. B* **84,** 075210 (2011).

73. Wang, C., Turinske, A. J. & Gao, Y. Orientation-dependent ionization potential of CuPc and energy level alignment at C60/CuPc interface. *Appl. Phys. B* **113,** 361–365 (2013).

74. Servaites, J. D., Ratner, M. a. & Marks, T. J. Organic solar cells: A new look at traditional models. *Energy Environ. Sci.* **4,** 4410 (2011).

75. Bae, S. *et al.* Roll-to-roll production of 30-inch graphene films for transparent electrodes. *Nat. Nanotechnol.* **5,** 574–8 (2010).

76. Park, H., Rowehl, J. a, Kim, K. K., Bulovic, V. & Kong, J. Doped graphene electrodes for organic solar cells. *Nanotechnology* **21,** 505204 (2010).

77. Perez, M. D., Borek, C., Forrest, S. R. & Thompson, M. E. Molecular and morphological influences on the open circuit voltages of organic photovoltaic devices. *J. Am. Chem. Soc.* **131,** 9281–6 (2009).

78. Li, N., Lassiter, B. E., Lunt, R. R., Wei, G. & Forrest, S. R. Open circuit voltage enhancement due to reduced dark current in small molecule photovoltaic cells. *Appl. Phys. Lett.* **94,** 023307 (2009).

Chapter 4 : F_4-TCNQ Thin Film Properties

4.1 Introduction

The work in the previous chapter assessed the potential of using graphene as an interlayer on ITO. Whilst graphene has been shown to be an effective structural template to control the orientation of the donor layer CuPc in an OPV device, the low work function of G/ITO substrate as compared to the IP of the CuPc results in an unfavourable hole extraction and consequently large series resistance at the anode interface. Potential strategies to reduce the hole injection barrier include coating the substrate with high work function materials such as polymer poly(ethylenedioxythiophene) doped with poly(styrenesulfonate) (PEDOT:PSS),[1–3] transition metal oxides[4–7] such as MoO_3 and V_2O_5, or small molecules such as tetrafluoro-tetracyanoquinodimethane (F_4-TCNQ)[8–11] to increase the substrate work function. While these strategies can also be applied to the G/ITO anode to ensure energetically favourable contact with CuPc, the work function modifying interface layer should be carefully chosen such that the structural templating property of graphene is not affected, as for instance by covering graphene surface with several nanometers of PEDOT:PSS or transition metals. Instead its templating effect should propagate beyond the interface layer to the subsequent CuPc donor layer.

F_4-TCNQ is a planar π-conjugated molecule [molecular structure shown in Figure 4-1 (a)] with strong electron accepting properties and is widely used to dope the hole transport or donor layers in organic semiconductor devices such as OLED with much success.[12–15] This is achieved through reduction of the HIB between the electrode and active layer, narrowing of the space charge region, and also through increasing hole conductivity.[12,13,16,17] More recently, a thin layer of F_4-TCNQ independently evaporated onto ITO demonstrated improved hole injection from the organic layer to the anode by lowering the energetic barrier at that interface through the formation

of dipoles.[9–11,18] P-doping of epitaxial graphene on silicon carbide (G/SiC) with F_4-TCNQ results in significant increase in work function due to the formation of surface dipoles as established experimentally by PES.[19,20] These experimental results on G/SiC were also reproduced by theoretical simulations by Pinto *et al.*[21] The relaxed structure of monolayer F_4-TCNQ on graphene grown on / transferred onto relatively flat substrates such as G/SiC and G/Si respectively is reported to be flat-lying.[19,21,22] Our motivation for selecting F_4-TCNQ as a work function modifier for G/ITO stems from the results of the experiments in Refs [19-22]. These experiments suggest that F_4-TCNQ may simultaneously increase the substrate work function while propagating the templating property of graphene beyond the F_4-TCNQ interlayer. The latter may be achieved through π-π interactions between the flat lying F_4-TCNQ molecules and the subsequent CuPc donor layer.

It is important to highlight that the results obtained in Refs [19-22] may not be directly translatable to our G/ITO anode. While F_4-TCNQ is able to significantly increase the work function of an atomically flat and clean model system of G/SiC as investigated in Refs [19-21], its effect on our rough (cf. Figure 2-13) and inherently impure (cf. Figure 3-4) G/ITO solar cell anode is unknown and may differ from G/SiC. G/SiC has limited commercial applications in organic semiconductor devices as compared to G/ITO due to its high cost. Structurally, although the orientation of *monolayer* F_4-TCNQ molecules on *relatively flatter* G/SiC and G/Si substrates has been determined through NEXAFS, XRD and simulation,[19,21,22] information concerning structural analysis of F_4-TCNQ *thin film* on *rough* G/ITO (and ITO) anode is not available in literature. Most importantly, Refs [19-22] did not study the effect of interface doping of graphene with F_4-TCNQ on the electronic and structural properties of the subsequently deposited organic layers (CuPc in our case) in a solar cell device configuration. The absence of this information means that the effectiveness of interface doping of graphene using F_4-TCNQ remains unproven.

In this chapter, we perform a systematic in-depth investigation of the electronic properties of F_4-TCNQ deposited on ITO and G/ITO[b] to determine if F_4-TCNQ is potentially a suitable work function modifier for our substrates from the energetics point of view. We also investigate the molecular orientation and morphology of the F_4-TCNQ molecules on both substrates. We begin the study by calibrating the film thickness of F_4-TCNQ deposited in an OMBD system, followed by PES studies of the interface electronic structures. A combination of NEXAFS and XRD measurements will provide information about the molecular orientation, while the imaging techniques such as SEM and AFM will be used to uncover the morphology and topography of the F_4-TCNQ crystals. The effect of pre-covering ITO and G/ITO with F_4-TCNQ on the electronic and structural properties of CuPc will follow in Chapter 5.

4.2 Calibration of F_4-TCNQ Film Thickness

Prior to thin film studies of F_4-TCNQ, it is crucial to calibrate the film thickness by tuning the tooling factor of the QCM in the OMBD chamber to compensate for the distance between the QCM and substrate. Since F_4-TCNQ molecules do not follow a layer-by-layer growth mode but instead form islands when deposited on ITO[8,23] (and also on G/ITO as will be seen from the SEM analysis in Figure 4-5 and backed up by PES data which will be discussed in Section 4.3), techniques to measure the average film height using AFM or step profilometer prove to be inadequate for determining the thickness of the film deposited. Hence a solution-based method was used to determine the actual amount of F_4-TCNQ deposited by dissolving the film and comparing to a calibration curve established with solutions of known concentration. This was then used to calibrate the QCM.

Figure 4-1 (b) plots the absorbance spectra of a series of known concentrations of F_4-TCNQ dissolved in dichloromethane (DCM) as a function of wavelength. The absorbance spectra can be

[b] The data (electronic and structural) obtained for all G/ITO samples will be an average of the graphene covered ITO area and also bare ITO unless otherwise stated. This is due to the incomplete coverage of ITO by graphene, and defects in the transferred graphene sheet (cf. Chapter 3 for details).

fitted with three peaks: the most prominent and intense peak (i) at 391 nm, a less intense peak (ii) at 368 nm and a shoulder peak (iii) at 346 nm. The separation between adjacent peaks is ~0.2 eV which corresponds to the most prominent vibration in F_4-TCNQ molecules.[24] Therefore, peak (i) is assigned to an intramolecular π-π* transition of a neutral molecule;[25] while peaks (ii) and (iii) are vibronic progressions. The optical band gap derived from this data is 3.1 eV which within the range of reported values between 2.9 – 3.2 eV.[26–28]

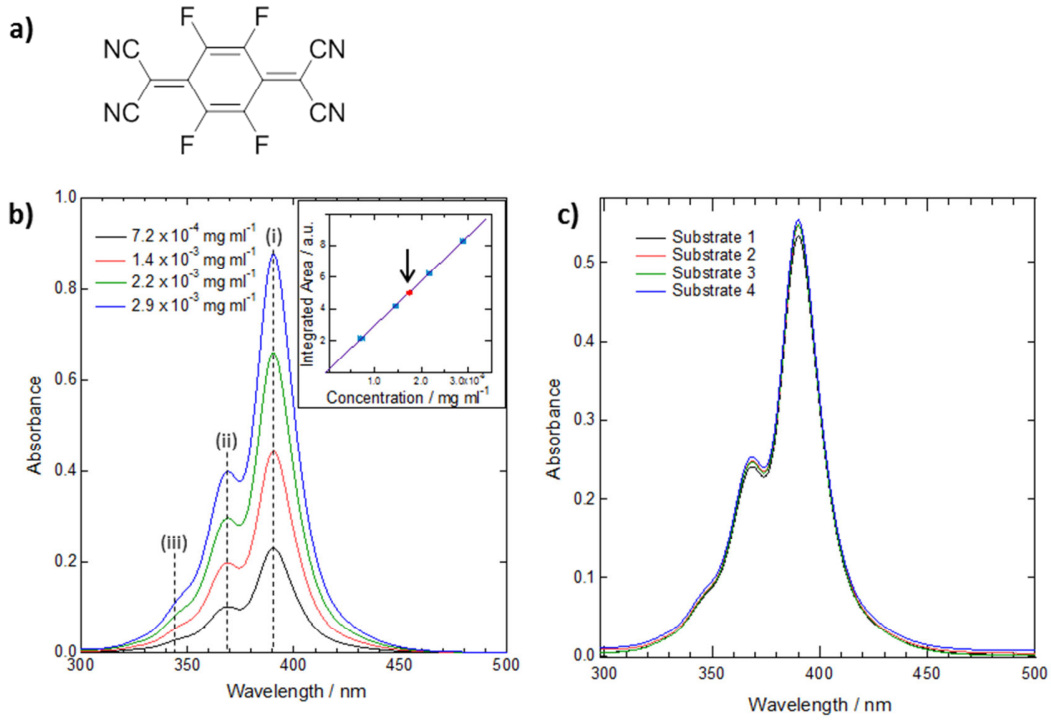

Figure 4-1 (a) Chemical structure of F_4-TCNQ. UV-Vis absorbance spectra as a function of versus wavelength for (b) varying concentrations of powdered F_4-TCNQ dissolved in DCM and (c) 80 nm nominal thickness F_4-TCNQ deposited on glass and dissolved in DCM. Inset in (b): Plot of best fit line for the integrated area of the main peak (i) of F_4-TCNQ absorbance spectra (centred at 391 nm) as a function F_4-TCNQ concentration. Position of the red marker on the line (highlighted by an arrow) indicates the integrated area of the major peak of the dissolve film in (c).

The integrated area of peak (i) has a linear relationship with the mass concentration of F_4-TCNQ according to Beer-Lambert law [Equation (2-13)] and is exemplified by the plot shown in the inset in Figure 4-1 (b). The overall error associated with the calculations is approximately ±5.9 x 10^{-5} mg/ml which originates mainly from estimation of the mass of the F_4-TCNQ powders and instrumental errors when measuring out the volumes of the solutions.

Figure 4-1 (c) shows the absorbance spectra for F_4-TCNQ films grown in an OMBD chamber and subsequently dissolved in DCM. F_4-TCNQ films with a nominal thickness of 80 nm were grown together on identical substrates ['Substrate 1 - 4' in Figure 4-1 (c)] which have an area of 3.1 ± 0.3 cm^2. These substrates were subsequently dissolved in 20 ± 2 ml DCM and the absorbance spectra are plotted in Figure 4-1 (c). The average integrated area of the peak centred at 391 nm in Figure 4-1 (c) is plotted as a red marker on the straight line in the inset Figure 4-1 (b). The corresponding concentration of the dissolved film can be determined from the graph. From the density of F_4-TCNQ, back calculations indicate that the actual thickness is 14% less than the nominal thickness. The tooling factor was varied by the same amount for all subsequent depositions to account for the difference.

4.3 Electronic Structure of F_4-TCNQ on ITO and G/ITO

Figure 4-2 (a) shows the evolution of the UPS spectra in the low kinetic energy region for increasing thickness of F_4-TCNQ film deposited on ITO. All the spectra in Figure 4-2 were measured using He I (21.2 eV) excitation and the corresponding error with measurement is ±0.05 eV. The work function of the substrate is determined from the linear cutoff position of the low kinetic energy spectrum, and the value of the sample work function as a function of film thickness is shown in Figure 4-2 (b). The magnitude of the change in work function depends on the thickness of the absorbed film. Following the deposition of 0.5 Å F_4-TCNQ, the vacuum level shifts to higher kinetic energy, corresponding to an increase in work function of 0.65 eV. The overall increase in sample work function is 1.28 eV when the F_4-TCNQ coverage is 2 Å. For F_4-TCNQ coverage greater than 5 Å, the work function saturates at 5.12 eV and remains constant up to the film thickness investigated in this experiment. The large change in work function at the interface is due to electron transfer from ITO to the electronegative F_4-TCNQ molecules, thereby creating a dipole at the interface.[9,29] The magnitude of the dipole is 1.37 eV. Charge transfer at the substrate-F_4-TCNQ interface has been reported on a variety of substrates.[20,30] The transferred

charge(s) are thought to be distributed around the cyano groups of the molecules,[19,31,32] and reside in new states that appear within the bandgap.[29,30] These new states are investigated by studying the valence band spectra of F_4-TCNQ/ITO.

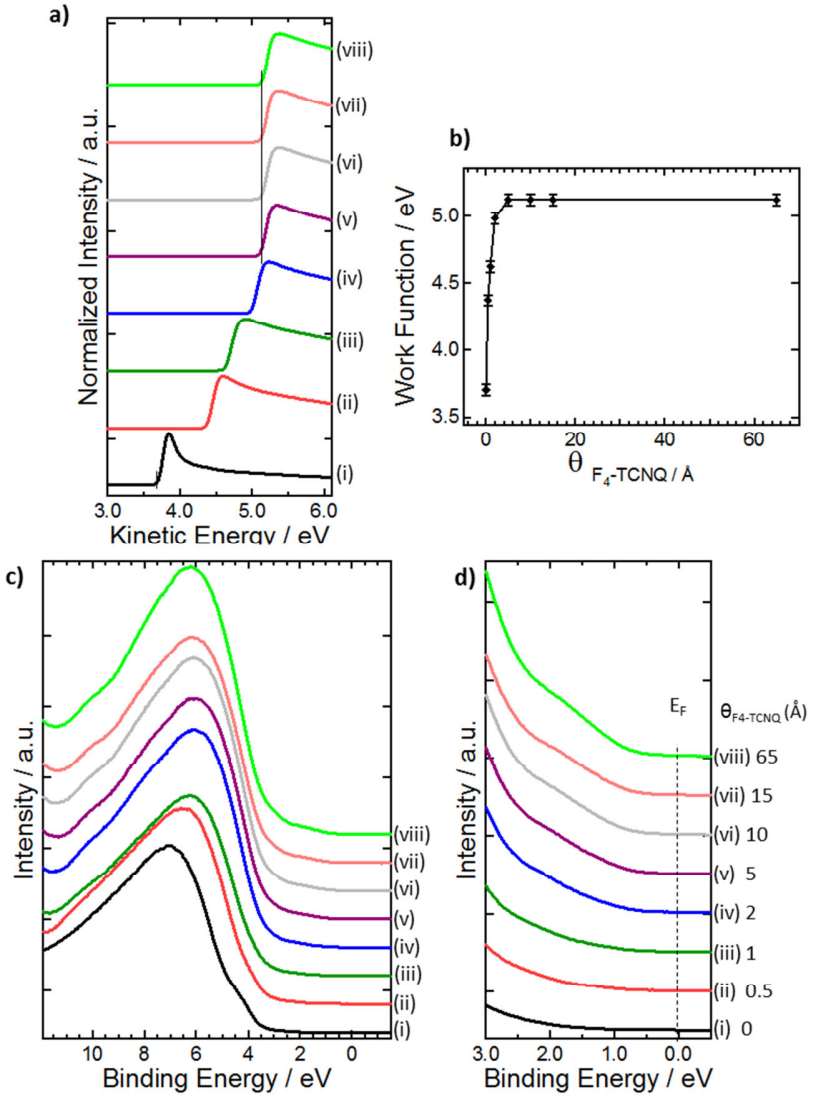

Figure 4-2 UPS spectra evolution of F_4-TCNQ deposited onto ITO. (a) UPS spectra at low kinetic energy region, and (b) plot of sample work function with increasing F_4-TCNQ thickness. (c) Valence band spectra at low binding energy and (d) near the Fermi level region of spectra from (c). $\theta_{F4\text{-}TCNQ}$ refers to the thickness of the F_4-TCNQ film.

The UPS spectra of F_4-TCNQ deposited on ITO at the valence band region are shown in Figure 4-2 (c), and its corresponding close-up spectra near the Fermi level in Figure 4-2 (d). The spectrum of 2 Å F_4-TCNQ/ITO shows the emergence of a broad feature located within the

binding energy range of 1 eV to 2.5 eV below E_F. While this feature is not clearly defined, it is not derived from the neutral F_4-TCNQ molecule as there is no density of states at this energy range for the neutral form.[29] The location of this feature is consistent with the charge transfer features (between 0.3 – 2.5 eV) reported experimentally by Koch *et al.*[30] and Chen *et al.*[20] for F_4-TCNQ on Au and epitaxial graphene respectively, and also agrees with DFT calculations of the density of states of anionic F_4-TCNQ.[29] These observations suggest that this feature corresponds to the new states that are formed within the band gap of neutral F_4-TCNQ and originates from the strong electron transfer from ITO to F_4-TCNQ molecules.

In order to better resolve this charge transfer feature, the experiment was repeated using synchrotron based PES utilizing 60 eV polarised light to improve surface sensitivity (cf. Figure 2-3). The valence band spectra shown in Figure 4-3 (a) clearly reveal the emergence of features between 0.1 – 2.2 eV binding energy upon deposition of 1 Å of F_4-TCNQ on ITO. With increasing F_4-TCNQ film thickness, the intensity of the features decrease but their position remain unchanged. Following subtraction of the substrate signal, the features can be fitted with 2 Gaussian curves centred at 1.61 eV and 0.80 eV as shown in Figure 4-3 (b). These peaks have been assigned to the relaxed state of the HOMO and the partially filled LUMO state of the molecules respectively.[30] The weakening intensity of these features with increasing film thickness [Figure 4-3 (a)] indicates that charge transfer takes place exclusively at the substrate-molecule interface, and that additional molecules adsorb on interfacial layer in their neutral form.

Despite significant change in the sample work function with F_4-TCNQ coverage, few changes take place at the valence band region [Figure 4-2 (c)]. The lack of clear (bulk, neutral) F_4-TCNQ features in the valence band spectra and minimal attenuation of the substrate signal has also been reported by Fehse *et al.*.[9] We propose that this can be ascribed to two reasons: first, the valence band spectrum of bare ITO which extends to low binding energy may overlap with and mask the valence band features of the neutral molecule. Second, dipole-dipole repulsion between ionized

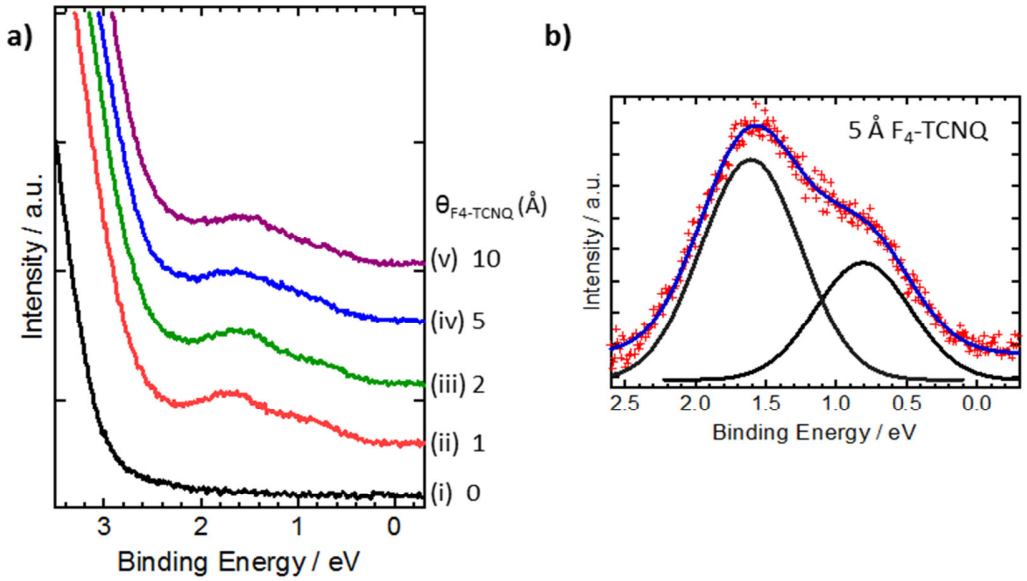

Figure 4-3 (a) PES spectra of F_4-TCNQ on ITO at low binding energy near the Fermi level measured with 60 eV synchrotron radiation. Distinct charge transfer features centred around 0.6 eV and 1.6 eV below the Fermi level are visible at this photon energy. (b) Fitted charge transfer peaks from the 5Å F_4-TCNQ spectrum in (a) following subtraction of the substrate signal.

F_4-TCNQ molecules may hinder complete wetting of the substrate at low coverage.[33] Incomplete coverage of the surface by F_4-TCNQ may also be caused surface contaminants and absorbed carbon (cf. Figure 3-2) which ultimately limits the number of 'clean' sites which F_4-TCNQ can favourably bind to and carry out charge transfer with. For the submonolayer coverage of F_4-TCNQ used in their experiment, Fehse *et al.* proposed that F_4-TCNQ molecules preferentially adsorb on these limited clean sites. Once these 'clean' sites are saturated with F_4-TCNQ molecules, additional F_4-TCNQ molecules may bind to the interfacial F_4-TCNQ molecules resulting in an increase of the island height; or to the 'contaminated' sites resulting in higher surface coverage.[8,23] In these scenarios, further charge transfer with the substrate is reduced,[34] and thus both the surface dipole contribution to the substrate work function and interface states near the Fermi level would be diminished. This model is able to explain the initial large change in work function due to interfacial charge transfer, followed by the saturation of the work function at higher film coverage since charge transfer is greatly reduced. The lack of distinct F_4-TCNQ valence band features when deposited on ITO implies that much of the substrate remains

exposed, suggesting that severe islanding of F_4-TCNQ molecules has taken place. This type of growth mode is termed Volmer–Weber in which molecular islands start appearing without completely wetting the substrate.[35] It occurs when the intermolecular interaction is stronger than the interfacial interactions. This growth mode has been reported for F_4-TCNQ deposited on ITO[8,23] and on epitaxial graphene.[19]

The UPS spectra of F_4-TCNQ deposited on G/ITO are shown in Figure 4-4. Figure 4-4 (a) shows the secondary electron cutoff position with increasing F_4-TCNQ film thickness and (b) plots the change in work function as a function of film thickness. The work function of the bare G/ITO substrate (spectrum (i)) before F_4-TCNQ deposition is 4.26 eV. As seen from the sample of F_4-TCNQ deposited on ITO, the vacuum level across the interface is very sensitive to the formation of interface dipoles. An upward shift in vacuum level or an increase in work function by 0.48 eV was observed within the first 2 Å of F_4-TCNQ deposited. Further increasing the film thickness results in a gradual increase in work function and a maximum value of 4.88 eV is obtained for the 65 Å film. The increase in sample work function indicates p-doping of the underlying graphene layer through electron transfer from graphene to F_4-TCNQ molecules. Consequently, an interface dipole of 0.62 eV is formed between F_4-TCNQ and G/ITO.

The magnitude of the vacuum level shift obtained in this experiment is significantly lower than the experimental values reported by Chen *et al.*[20] for F_4-TCNQ deposited on epitaxial graphene on silicon carbide (SiC) and calculations by Pinto *et al.*[21]. Both groups recorded a larger relative change in substrate work function, and also a larger maximum work function attained. The difference between our results and theirs may be caused by the organic impurities, including residual PMMA, present on our G/ITO substrate [cf. C 1s spectra in Figure 3-4], and also the roughness of G/ITO substrates (Figure 2-13). As mentioned in the preceding paragraphs, surface contaminants diminish charge transfer at the interface, resulting in lower values of work function.

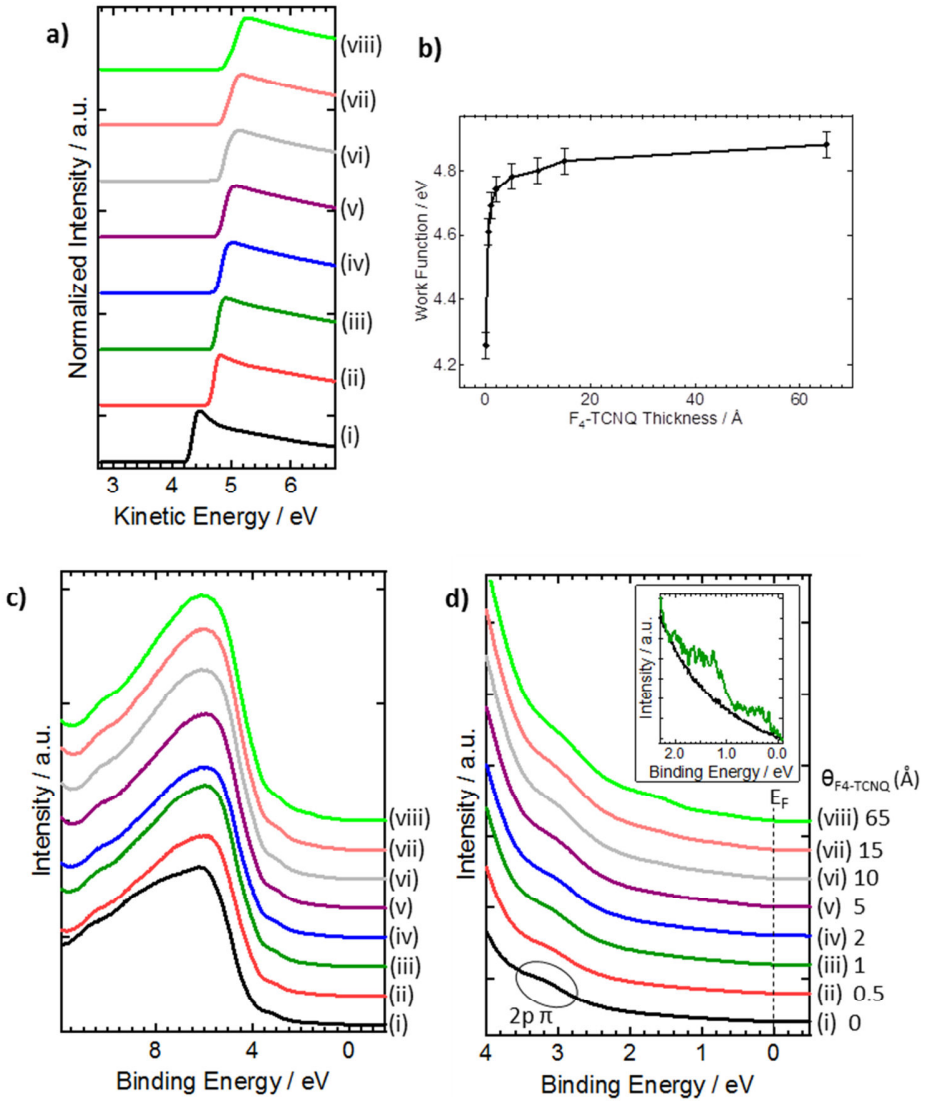

Figure 4-4 UPS spectra evolution of F_4-TCNQ deposited on graphene transferred onto ITO (G/ITO). (a) Spectra at low kinetic energy region, (b) plot of sample work function against F_4-TCNQ thickness. (c) Valence band spectra at low binding energy and (d) near the Fermi level. The characteristic 2p π feature of graphene at about 3.2 eV below Fermi level is circled in (d). Inset in (d) shows the high resolution spectra of 1 Å F_4-TCNQ/G/ITO (green) and G/ITO (black) obtained using 60 eV synchrotron radiation. All other spectra were measured with photon energy of 21.2 eV.

The roughness of the substrate influences the direction of the dipole moment which in turn affects the degree of charge transfer and the sample work function.[38–40] On rough substrates such as G/ITO and ITO the direction of the dipoles is non-uniform thus giving an average effect on the work function.[23] In comparison, Chen *et al.* and Pinto *et al.* results were based on relatively cleaner and smoother substrates. Finally, the electronic properties at the F_4-TCNQ-graphene

interface may also be affected by the underlying substrate.[41] Therefore, differences between F_4-TCNQ deposited on epitaxial graphene on SiC and graphene transferred onto ITO are expected since the electronic properties of the underlying substrate might not be fully screened by a layer of graphene.

The valence band spectrum of bare G/ITO in the vicinity of the Fermi level shows the characteristic 2p π state of graphene located around 3 eV below E_F [Figure 4-4 (d)]. This signal from graphene does not appear to attenuate with increasing F_4-TCNQ thickness possibly because large areas of the substrate are uncovered at low molecular coverage as explained in the preceding paragraphs. Furthermore, the neutral F_4-TCNQ molecules have a photoemission signal that overlaps with the 2p π state at around 3 eV.[20,30,42] Similar to F_4-TCNQ deposited on ITO, the charge transfer features for F_4-TCNQ deposited on G/ITO (between 0.3 – 2.0 eV) can be resolved using synchrotron radiation as shown in the inset in Figure 4-4 (d). Those features provide evidence for strong charge transfer between F_4-TCNQ and G/ITO.

The difference in wettability and adhesion of F_4-TCNQ molecules on ITO as opposed to G/ITO can be deduced by comparing the absolute values of work function and their relative change for the same film thickness [Figure 4-2 (b) and Figure 4-4 (b)]. Smaller values obtained for both parameters on G/ITO substrate suggest poorer surface coverage by F_4-TCNQ. This is because the interface area has direct implications on the electron transfer between the molecule and substrate.[20,29,30] The difference in coverage is visualised through SEM images of 50 nm F_4-TCNQ films grown on ITO and G/ITO shown in Figure 4-5. Figure 4-5 (a) and (b) which are the lower magnification SEM images for F_4-TCNQ on ITO and G/ITO respectively reveal that F_4-TCNQ crystallites pack more densely on ITO as compared to G/ITO. The projected area, or total surface coverage, of F_4-TCNQ crystallites on G/ITO is approximately 50% of the substrate, which is 10% lower than the 60% coverage on ITO as determined from the higher magnification images [Figure

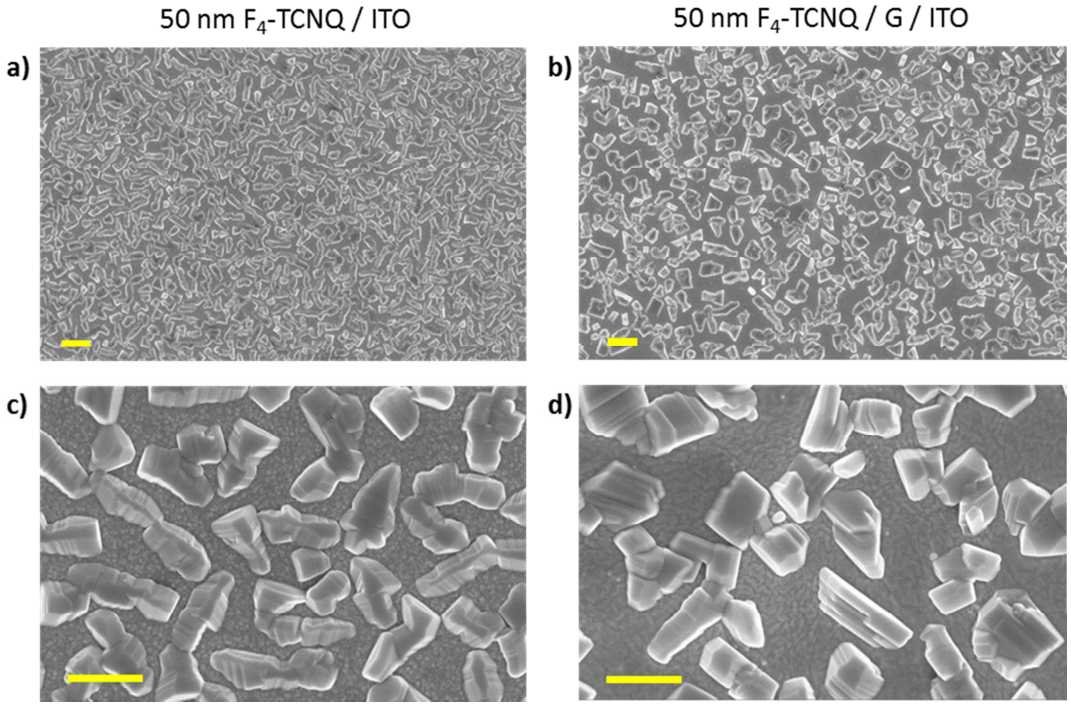

Figure 4-5 SEM images of 50 nm F_4-TCNQ on (a) & (c) ITO and (b) & (d) G/ITO imaged at (top row) x10000 and (bottom row) x50000 magnification. Higher surface coverage of ITO by F_4-TCNQ as compared to G/ITO indicates better wettability of F_4-TCNQ on ITO. Scale bars are (a) & (b) 2 μm and (c) & (d) 1 μm respectively.

4-5 (c) and (d)]. This reveals that F_4-TCNQ molecules preferentially wet ITO as compared to G/ITO, and suggests that the interfacial interaction is stronger in the previous sample.

Figure 4-5 (c) and (d) also reveal differences in the morphology of the crystallites deposited on different substrates in more detail. Firstly, the crystallites on G/ITO have a spread of morphologies, with a significant fraction of crystallites that have approximately square lateral sizes, together with some elongated crystallites. On the other hand, the crystallites on ITO appear predominantly more elongated. Secondly, the F_4-TCNQ crystallites on G/ITO have sharper edges, while on ITO the edges are sloping. These observations could suggest that F_4-TCNQ has different preferred growth directions on the two substrates. This is further investigated in the next section which focuses on structural analysis.

4.4 Structural Analysis of F_4-TCNQ on ITO and G/ITO

The molecular orientations of F_4-TCNQ on ITO and G/ITO are determined by NEXAFS for thin films at the substrate interface, and XRD for thicker films to probe the bulk orientation. The

collated results for both NEXAFS and XRD investigations are shown in Figure 4-6. The NEXAFS N K-edge spectra for 10 Å F_4-TCNQ films on ITO and G/ITO as a function of synchrotron light incidence angle θ are shown in Figure 4-6 (a) and (b) respectively. The first three absorption peaks between 395 – 405 eV are assigned to the resonance transitions from the N 1s core level to π* states, while the higher energy broad absorption features between 405 – 425 eV are due to the transitions to the σ* states. The first (i) and third (iii) absorption peaks which are located at 397.3 eV and 400.6 eV respectively are attributed to transitions to distinct out-of-plane π* molecular orbitals.[19,43–45] The second (ii) peak centred at 399.5 eV is reported to be an overlap of two orthogonal π* orbitals of the cyano group – one orbital lies perpendicular to and the other parallel to the molecular.[19,43,44] The latter is termed 'σ-like π* resonance' due to the orientation of the molecular orbital rather than the electronic transition involved.[19] On both G/ITO and ITO substrates, peaks (i) and (iii) both show similar angular dependency indicating that the molecular orientation is similar on both substrates. In order to evaluate the angle α subtended by the molecular plane and the substrate, we determine the ratio of absorption intensities at grazing and normal incidence for peak (i) [$R(\pi *) = \frac{I(\theta = 90^o)}{I(\theta = 20^o)}$]. F_4-TCNQ molecules adopt a tilted orientation on G/ITO with $\alpha = 36^o \pm 5^o$ while on ITO $\alpha = 44^o \pm 5^o$. We use XRD to relate the crystal packing of F_4-TCNQ with the observed tilt angle.

The results of the XRD spectra for 50 nm F_4-TCNQ films are collated in Figure 4-6 (c) – (e). The symbol '#' denotes the peak derived from the (2 1 1) plane of the ITO substrate.[46] At the first glance, the spectra of F_4-TCNQ deposited on ITO (red scan) and G/ITO (green scan) in Figure 4-6 (c) look almost identical with a diffraction feature around 19°. However zoomed scans about the diffraction feature which are shown in Figure 4-6 (d) and (e) reveal that it comprises two peaks at 18.8° and 19.0°; the ratio of the peaks vary on the different substrates. (This separation is larger than the instrumental broadening of 0.08°.)[47] The lower angle Bragg peak is due to the diffraction from the (2 1 1) plane and the higher angle peak is from the (0 2 0) plane parallel to

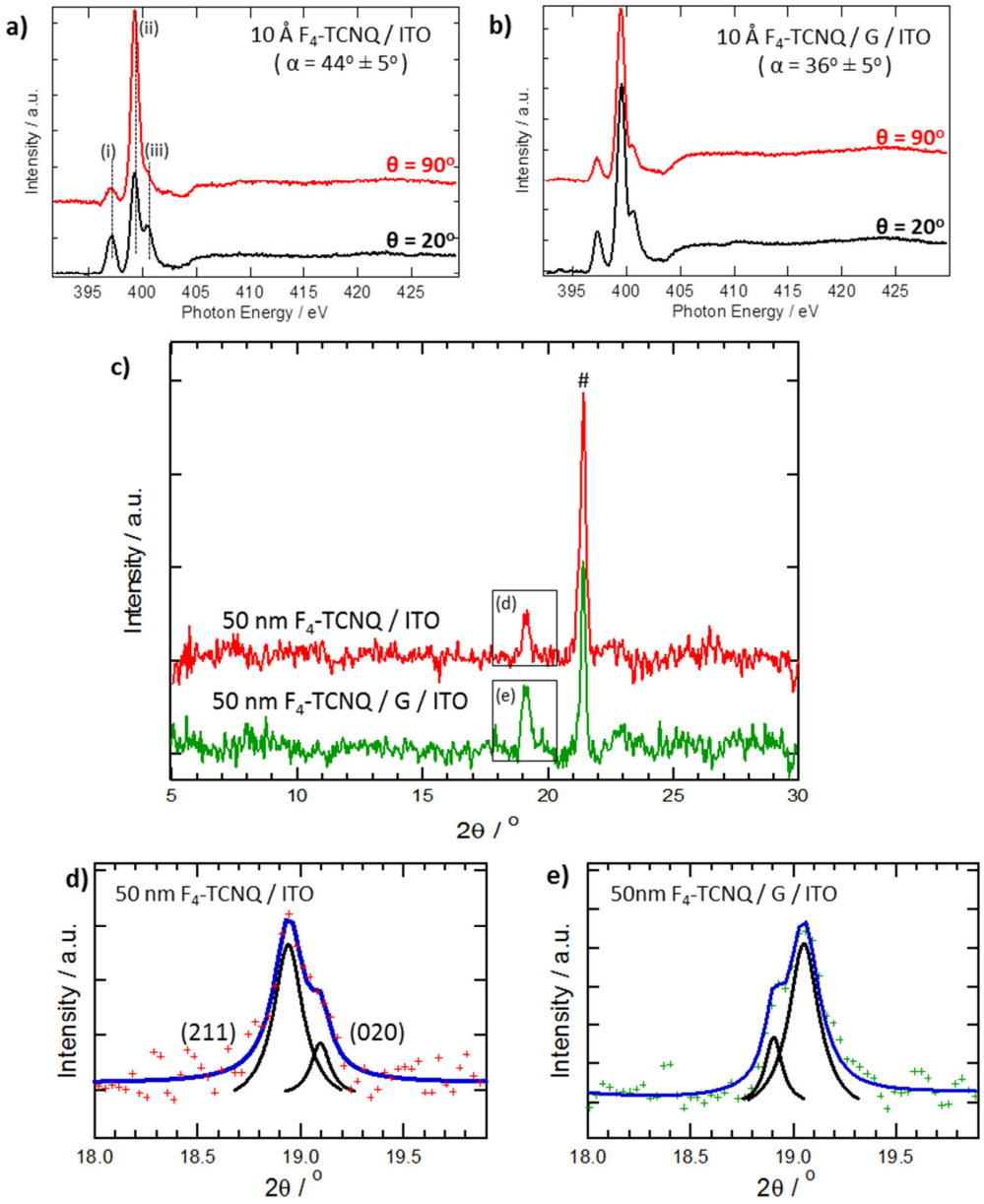

Figure 4-6 Angle dependent NEXAFS N K-edge spectra for 10Å F_4-TCNQ on (a) ITO and (b) G/ITO, with α = 44° ± 5° and α = 36° ± 5° respectively. Peaks (i) – (iii) corresponds to resonant transitions to the π* orbitals. (c) XRD pattern of F_4-TCNQ thin film on (top, red) ITO and (bottom, green) G/ITO. '#' denotes the peak derived from ITO substrate. The diffraction peak ~19° in (c) corresponds to the overlap of the (2 1 1) plane at 18.8° and (0 2 0) plane at 19.0°. The fitted peaks (black) are shown in (d) for ITO and (e) for G/ITO.

the substrate.[48] On ITO, it appears that the diffraction peak from the (2 1 1) plane is more prominent, while the (0 2 0) diffraction peak is more prominent for G / ITO. For the (2 1 1) plane aligned preferentially parallel to the substrate, four molecular orientations are present, forming angles of 61.1°, 71.1°, 83.5° and 22.9° (an average of 59.7°) with respect to the substrate; for the

(0 2 0) plane, the molecular tilt angle is 36.9° with respect to the substrate plane for all the molecules. Schematic drawings of the orientation of molecules along the (2 1 1) plane on ITO and (0 2 0) plane on G/ITO are shown in Figure 4-7 (a) and (b) respectively.

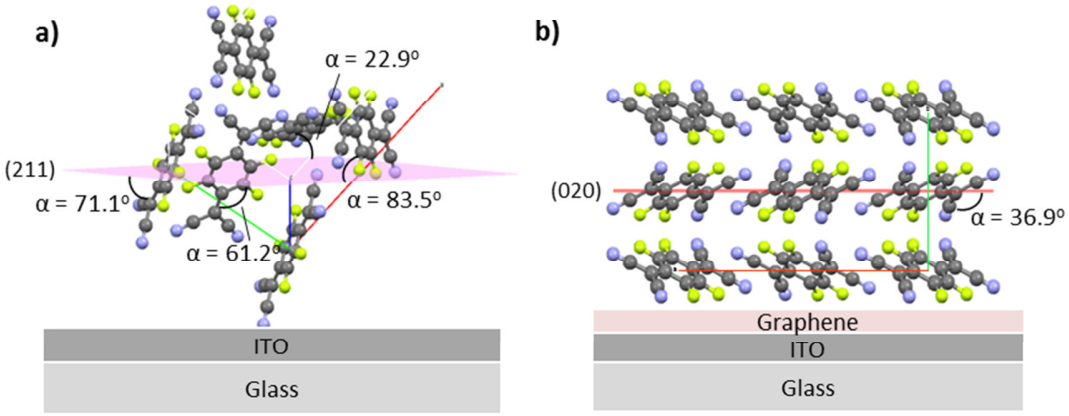

Figure 4-7 Schematic drawings showing the molecular orientations of F_4-TCNQ with (a) the (2 1 1) plane parallel to to ITO and (b) the (0 2 0) plane parallel to the ITO. The angles that the molecules make with the plane are detailed in the images. The unit cell axes are shown as red for the a-axis, green for b-axis and blue for c-axis. The c-axis in (b) projects into the plane of the paper.

The fitting results for XRD agree with NEXAFS data which reveal a larger α for ITO as compared to G/ITO. On G/ITO, the molecules are oriented to maximize the total projection of their π-plane on the substrate, thereby enhancing π-π interfacial interaction with graphene. The tilted orientation on graphene has also been observed by Chen *et al.*[19] and Pinto *et al.* [21]. In addition, the geometry of molecules in the (0 2 0) plane appears to maximize interaction between the aromatic ring, cyano group and/or fluorine atoms, and the substrate. On the other hand, F_4-TCNQ molecules on ITO substrate form large angles, suggest repulsion between the electronegative cyano groups and/or fluorine atoms and the exposed oxide surface. The 'standing' geometry of F_4-TCNQ may reduce the overall interaction between the molecular side groups by limiting its projected area on ITO. Next we attempt to quantify the percentage contribution of each of the plane to the final diffraction pattern and to relate it to the NEXAFS N K-edge results.

The preferred orientation of the film can be estimated by calculating the texture coefficient (TC_{hkl}) using the equation[49]

$$TC_{hkl} = \frac{\frac{I(hkl)}{I_O(hkl)}}{\frac{1}{n}\sum_i^n \frac{I(hkl)_i}{I_O(hkl)_i}} \quad (4\text{-}1)$$

where I(hkl) is the diffraction intensity of the (h k l) plane from the sample in an XRD spectrum, I_o(hkl) is the diffraction intensity of the (h k l) plane in a fully randomly oriented F_4-TCNQ powder and n is the total number of diffractions considered. For TC_{hkl} greater than unity, the corresponding (h k l) plane of F_4-TCNQ films has preferential orientation with respect to the substrate. The values of I(hkl), I_o(hkl) and TC_{hkl} for F_4-TCNQ films on ITO and G/ITO are summarized in Table 4-1. The proportion of grains textured along a particular plane parallel to the substrate can also be determined by comparing the relative normalized intensities of the peaks [I(hkl)/I_0(hkl)] using the following equation:

$$\%(h\ k\ l) = \frac{\frac{I(hkl)}{I_O(hkl)}}{\sum\frac{I(hkl)_i}{I_O(hkl)_i}} \quad (4\text{-}2)$$

For the F_4-TCNQ/ITO sample, 86% of the grains are textured with their (2 1 1) plane parallel to the substrate, and the remaining 14% with their (0 2 0) plane parallel to the substrate. For the F_4-TCNQ on G/ITO, the values are 34% for the (2 1 1) plane, and 66% for the (0 2 0) plane preferentially parallel to the substrate.

The relative abundance of each of these diffraction planes in the F_4-TCNQ films on ITO and G/ITO, together with the angle subtended by the molecular and substrate planes (Figure 4-7) allow us to estimate the average molecular angle that should be detected in NEXAFS measurements. The calculated angles from the XRD specta are $\alpha_{XRD} = 56^o \pm 5^o$ and $\alpha_{XRD} = 44^o \pm 5^o$ for F_4-TCNQ/ITO and F_4-TCNQ/G/ITO. These angles are systematically larger than the actual angles obtained by NEXAFS measurements, namely $\alpha_{NEXAFS} = 44^o \pm 5^o$ and $\alpha_{NEXAFS} = 36^o \pm 5^o$ for

	F_4-TCNQ / ITO		F_4-TCNQ / G / ITO	
Plane	(2 1 1)	(0 2 0)	(2 1 1)	(0 2 0)
Peak position (2θ) / °	18.8	19.0	18.8	19.0
Peak intensity of F_4-TCNQ film, I(hkl) / counts	530	134	273	816
Peak intensity of F_4-TCNQ power I_o(hkl) / counts	1419	2169	1419	2169
Texture coefficient, TC_{hkl}	1.72	0.28	0.68	1.32
Proportion of the (h k l) plane contributing to the diffraction intensity / %	86	14	34	66
Expected average molecular tilt angle /°	56		44	

Table 4-1 Summary of the peak intensities of the (2 1 1) and (0 2 0) in the F_4-TCNQ/ITO and F_4-TCNQ /G/ITO films, as well as F_4-TCNQ powder diffraction.

F_4-TCNQ/ITO and F_4-TCNQ/G/ITO respectively. This may be due to the presence of nano-size crystallites with other planes preferentially parallel to the substrate other than the (2 1 1) and (0 2 0) planes, but the signals are too weak to be determined in our XRD spectrum. Furthermore, there may be other planes that are tilted away from the parallel to the substrate, and their diffraction peaks are therefore not visible in the θ-2θ geometry of XRD.

Finally, we relate the observed morphology of F_4-TCNQ crystallites to the preferred orientation of the crystal planes on ITO and G/ITO. Previously in the SEM images in Figure 4-5 (b) and (c), the shape of F_4-TCNQ crystallites on ITO and G/ITO appear different, especially at the edges where the F_4-TCNQ crystallites on G/ITO appear sharper and steeper as compared to of F_4-TCNQ/ITO. In order to quantify the angle that the edge of the crystallite makes with the substrate plane (edge angle), we used AFM to probe the topography of the sample. The AFM images of 50 nm F_4-TCNQ/ITO and 50 nm F_4-TCNQ/G/ITO, prepared in the same deposition as the samples used previously for SEM imaging, are shown in Figure 4-8 (a) and (b). Figure 4-8 (c) shows an example of a line profile drawn across a crystallite [yellow dashed line in Figure 4-8 (a)] and the

determination of an edge angle. The average angle is 45° ± 3° for F_4-TCNQ/ITO and 62° ± 3° for F_4-TCNQ/G/ITO. The steeper angle for F_4-TCNQ/G/ITO agrees well with the SEM results in Figure 4-5 that showed sharper and less sloping angles for F_4-TCNQ/G/ITO as compared to F_4-TCNQ/ITO.

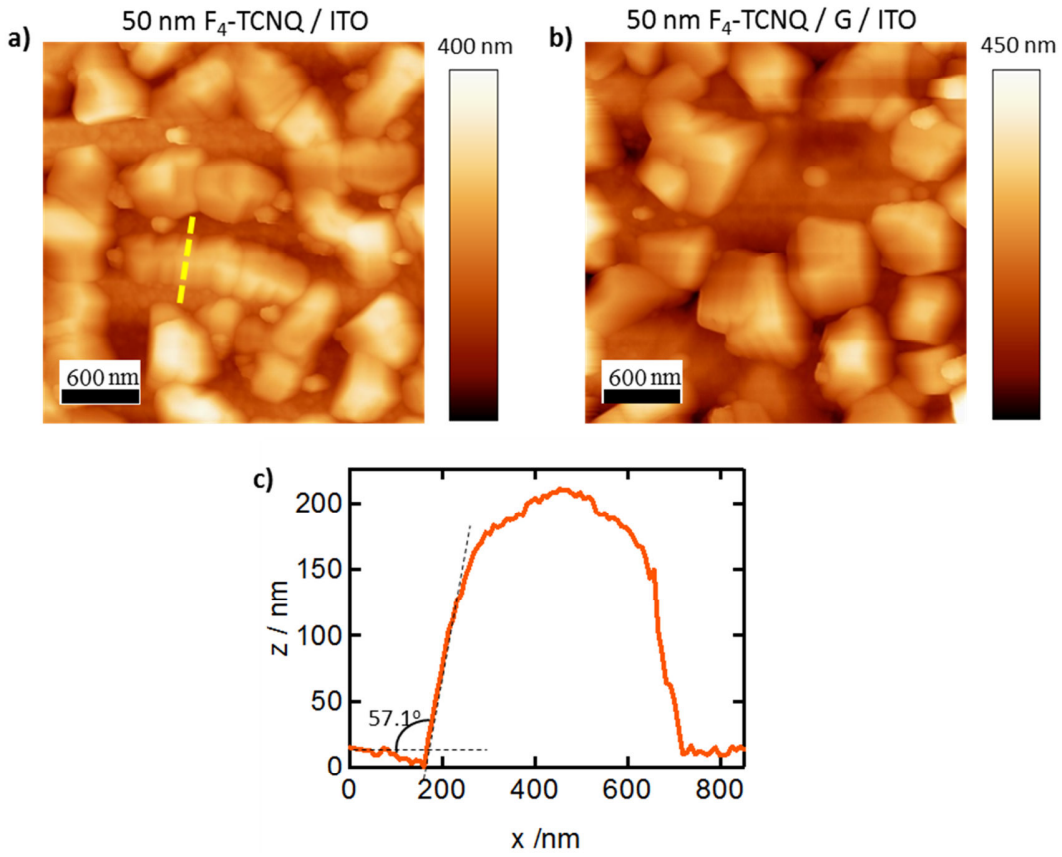

Figure 4-8 4 µm x 4 µm AFM images of (a) 50 nm F_4-TCNQ/ITO and (b) F_4-TCNQ/G/ITO. The angles that the crystal edge makes with the substrate were extracted from the line profiles (an example given in (c)) drawn across and perpendicular to the edge of the crystal as shown by the yellow dashed lines in the images. The average angles are (a) 45°and (b) 63° averaged over 70 measurements each.

We attempt to rationalize the edge angles based on our knowledge of crystal orientations from XRD (Figure 4-6). For the (0 2 0) crystal plane parallel to the substrate, both the {1 0 0} and {0 0 1} planes form right angles with respect to the substrate [Figure 4-7 (a)]. Therefore the edge of the crystallite is expected to be a sharp 90°. On the other hand, for the (2 1 1) plane, the {1 0 0}, {0 1 0} and {0 0 1} planes form angles of around 50°, 60° and 55° respectively. Therefore the average edge angle of the crystallite should be 55° when the (2 1 1) plane is parallel to the

substrate. The edge angles obtained by AFM, $45^{o} \pm 3^{o}$ and $62^{o} \pm 3^{o}$ for F_4-TCNQ/ITO and F_4-TCNQ/G/ITO respectively, are smaller than the predicted values most probably due to three-dimensional growth of smaller crystallites on the existing crystallites.[50,51] The F_4-TCNQ crystallites on ITO and G/ITO substrates also have two planes preferentially parallel to the substrate and therefore their crystallites show a spread of angles. This spread of angles can be observed visually in Figure 4-5, and from the collection of angles measured from the AFM images (Appendix C). The standard deviation for edge angles is about 12^{o} for F_4-TCNQ films on ITO and G/ITO. Finally, the AFM tip may not be able to measure steep angles accurately due to several factors such as the tip geometry, scan rate, and the creep of the piezoelectric motor.[52]

4.5 Conclusion

In this chapter, we study the electronic and structural properties of F_4-TCNQ deposited onto ITO and G/ITO. By pre-covering ITO and G/ITO with ultrathin layers of F_4-TCNQ (several Å), the substrate work function increases significantly due to electron transfer from the substrate to the molecules. Since charge transfer takes place only at the substrate-molecule interface, the substrate work function depends on the wetting of F_4-TCNQ on the substrate. SEM images show that F_4-TCNQ molecules wet ITO 10% more than on G/ITO, corroborating the larger work function in the former sample.

XRD measurements reveal that F_4-TCNQ films are textured on ITO and G/ITO with the (2 1 1) and (0 2 0) planes preferentially parallel to the substrate. The predominant plane of the grains parallel to the substrate is the (2 1 1) plane for ITO, and the (0 2 0) plane for G/ITO. In the (0 2 0) plane, all the molecules form an angle of around 37^{o} with the substrate and appear to maximize the projection of the π-plane onto the substrate. On the other hand, the molecules along the (2 1 1) plane adopt a variety of high angles, probably suggesting repulsion between the electronegative groups on F_4-TCNQ and the substrate. These results are in good agreement with NEXAFS

measurement that reveal a larger tilt angle for F_4-TCNQ molecules on ITO as compared to G/ITO. Finally, the edges of the F_4-TCNQ crystallites are steeper on G/ITO, forming an angle of around 63°, while on ITO it is 45° as determined by AFM. We relate this observation to the relative angles that the unit cell of F_4-TCNQ crystals forms with the substrate in its preferred orientation on ITO or G/ITO.

Increase in the substrate work function to about 4.9 eV (close to the ionization potential of phthalocyanine molecules of ~5 eV) can be achieved with only 5 Å F_4-TCNQ deposited on G/ITO. The ultrathin layer of F_4-TCNQ interlayer required to modify the work function, together with the predominantly tilted orientation of F_4-TCNQ molecules on G/ITO, may enable the propagation of the structural templating property of graphene beyond F_4-TCNQ. Therefore, F_4-TCNQ is a potential interface layer to increase the low work function of the G/ITO (cf. Chapter 3) substrate without compromising the structural templating property of graphene. Details of this will be investigated in Chapter 5.

4.6 References

1. Zhang, F. L., Gadisa, a., Inganäs, O., Svensson, M. & Andersson, M. R. Influence of buffer layers on the performance of polymer solar cells. *Appl. Phys. Lett.* **84,** 3906 (2004).

2. Roman, B. L. S., Mammo, W., Pettersson, L. A. A., Andersson, M. R. & Inganäs, O. High Quantum Efficiency Polythiophene / C 60 Photodiodes. **41296,** 774–777 (1998).

3. Wang, Y., Tong, S. W., Xu, X. F., Ozyilmaz, B. & Loh, K. P. Interface engineering of layer-by-layer stacked graphene anodes for high-performance organic solar cells. *Adv. Mater.* **23,** 1514–8 (2011).

4. Cho, S. & Piper, L. Soft X-ray spectroscopy of C60/copper phthalocyanine/MoO3 interfaces: role of Reduced MoO3 on energetic band alignment and improved performance. *J. Phys. Chem. B* **114,** 18252–18257 (2010).

5. Shrotriya, V., Li, G., Yao, Y., Chu, C.-W. & Yang, Y. Transition metal oxides as the buffer layer for polymer photovoltaic cells. *Appl. Phys. Lett.* **88,** 073508 (2006).

6. Steim, R., Choulis, S. A., Schilinsky, P. & Brabec, C. J. Interface modification for highly efficient organic photovoltaics. *Appl. Phys. Lett.* **92,** 093303 (2008).

7. Irwin, M. D., Buchholz, D. B., Hains, A. W., Chang, R. P. H. & Marks, T. J. p-Type semiconducting nickel oxide as an efficiency-enhancing anode interfacial layer in polymer bulk-heterojunction solar cells. *Proc. Natl. Acad. Sci.* **105,** 2783–2787 (2008).

8. Tyagi, P., Kumar, A., Giri, L. I., Dalai, M. K. & Tuli, S. Exciton quenching by diffusion of 2,3,5,6-tetrafluoro-7,7',8,8' -tetra cyano quino dimethane and its consequences on joule heating and lifetime of organic light-emitting diodes Priyanka. *Opt. Lett.* **38,** 3854–3857 (2013).

9. Fehse, K. *et al.* Energy level alignment of electrically doped hole transport layers with transparent and conductive indium tin oxide and polymer anodes. *J. Appl. Phys.* **102,** 073719 (2007).

10. Baek, S. H. *et al.* Enhancement of the Hole Injection and Hole Transport in Organic Light Emitting Devices Utilizing a 2,3,5,6-Tetrafluoro-7,7,8,8-tetracyano-quinodimethane Doped Hole Transport Layer. *Mol. Cryst. Liq. Cryst.* **498,** 258–264 (2009).

11. Dong, M.-S., Wu, X.-M., Hua, Y.-L., Qi, Q.-J. & Yin, S.-G. Highly Efficient Simplified Organic Light-Emitting Diodes Utilizing F4-TCNQ as an Anode Buffer Layer. *Chinese Phys. Lett.* **27,** 127802 (2010).

12. Gao, W. & Kahn, A. Controlled p doping of the hole-transport molecular material N, N′-diphenyl-N, N′-bis (1-naphthyl)-1, 1′-biphenyl-4, 4′-diamine with tetrafluorotetracyanoquinodimethane. *J. Appl. Phys.* **94,** 359–366 (2003).

13. Gao, W. & Kahn, A. Controlled p-doping of zinc phthalocyanine by coevaporation with tetrafluorotetracyanoquinodimethane: A direct and inverse photoemission study. *Appl. Phys. Lett.* **79,** 4040 (2001).

14. Zhou, X. *et al.* Very-low-operating-voltage organic light-emitting diodes using a p-doped amorphous hole injection layer. *Appl. Phys. Lett.* **78,** 410 (2001).

15. Blochwitz, J., Pfeiffer, M., Fritz, T. & Leo, K. Low voltage organic light emitting diodes featuring doped phthalocyanine as hole transport material. *Appl. Phys. Lett.* **73,** 729 (1998).

16. Gao, W. & Kahn, A. Electronic structure and current injection in zinc phthalocyanine doped with tetrafluorotetracyanoquinodimethane: Interface versus bulk effects. *Org. Electron.* **3,** 53–63 (2002).

17. Walzer, K., Maennig, B., Pfeiffer, M. & Leo, K. Highly efficient organic devices based on electrically doped transport layers. *Chem. Rev.* **107,** 1233–71 (2007).

18. Wang, J., Liu, J., Huang, S. & He, G. Enhancing the Hole Injection and Transporting of Organic Light-Emitting Diodes by Utilizing Gradient Doping. *Mol. Cryst. Liq. Cryst.* **574,** 129–134 (2013).

19. Chen, W., Qi, D., Gao, X. & Wee, A. T. S. Surface transfer doping of semiconductors. *Prog. Surf. Sci.* **84,** 279–321 (2009).

20. Chen, W., Chen, S., Qi, D. C., Gao, X. Y. & Wee, A. T. S. Surface transfer p-type doping of epitaxial graphene. *J. Am. Chem. Soc.* **129,** 10418–22 (2007).

21. Pinto, H., Jones, R., Goss, J. P. & Briddon, P. R. p-type doping of graphene with F4-TCNQ. *J. Phys. Condens. Matter* **21,** 402001 (2009).

22. Song, J. *et al.* A general method for transferring graphene onto soft surfaces. *Nat. Nanotechnol.* **8,** 356–62 (2013).

23. Rana, O. *et al.* Modification of metal-organic interface using F4 -TCNQ for enhanced hole injection properties in optoelectronic devices. *Phys. status solidi* **209,** 2539–2545 (2012).

24. Raman FTIR of F4-TCNQ. Accessed 11 June 2014. at <http://www.sigmaaldrich.com/spectra/rair/RAIR010368.PDF>

25. Eckhardt, C. J. & Pennelly, R. R. Metallic reflection of the TCNQ molecular crystal. *Chem. Phys. Lett.* **9,** 572–574 (1971).

26. Djurovich, P. I., Mayo, E. I., Forrest, S. R. & Thompson, M. E. Measurement of the lowest unoccupied molecular orbital energies of molecular organic semiconductors. *Org. Electron.* **10,** 515–520 (2009).

27. Chen, D.-Y. *et al.* Application of F4TCNQ doped spiro-MeOTAD in high performance solid state dye sensitized solar cells. *Phys. Chem. Chem. Phys.* **14,** 11689–94 (2012).

28. Gao, Z. Q. *et al.* An organic p-type dopant with high thermal stability for an organic semiconductor. *Chem. Commun.* **1,** 117 (2008).

29. Braun, S. & Salaneck, W. R. Fermi level pinning at interfaces with tetrafluorotetracyanoquinodimethane (F4-TCNQ): The role of integer charge transfer states. *Chem. Phys. Lett.* **438,** 259–262 (2007).

30. Koch, N., Duhm, S., Rabe, J., Vollmer, A. & Johnson, R. Optimized Hole Injection with Strong Electron Acceptors at Organic-Metal Interfaces. *Phys. Rev. Lett.* **95,** 237601 (2005).

31. Tseng, T.-C. *et al.* Charge-transfer-induced structural rearrangements at both sides of organic/metal interfaces. *Nat. Chem.* **2,** 374–9 (2010).

32. Romaner, L. *et al.* Impact of Bidirectional Charge Transfer and Molecular Distortions on the Electronic Structure of a Metal-Organic Interface. *Phys. Rev. Lett.* **99,** 256801 (2007).

33. Soos, Z. G. & Topham, B. J. Surface dipole of F4TCNQ films: Collective charge transfer and dipole–dipole repulsion in submonolayers. *Org. Electron.* **12,** 39–44 (2011).

34. Wan, A., Hwang, J., Amy, F. & Kahn, A. Impact of electrode contamination on the α-NPD/Au hole injection barrier. *Org. Electron.* **6,** 47–54 (2005).

35. Oura, K., Katayama, M., Zotov, A. V., Lifshits, V. G. & Saranin, A. A. *Surface Science: An Introduction*. (Springer Berlin Heidelberg, 2003).

36. Schlaf, R., Murata, H. & Kafafi, Z. Work function measurements on indium tin oxide films. *J. Electron Spectros. Relat. Phenomena* **120,** 149–154 (2001).

37. Park, Y., Choong, V., Gao, Y., Hsieh, B. R. & Tang, C. W. Work function of indium tin oxide transparent conductor measured by photoelectron spectroscopy. *Appl. Phys. Lett.* **68,** 2699 (1996).

38. Fukagawa, H. *et al.* The Role of the Ionization Potential in Vacuum-Level Alignment at Organic Semiconductor Interfaces. *Adv. Mater.* **19,** 665–668 (2007).

39. Chen, W., Qi, D.-C., Huang, H., Gao, X. & Wee, A. T. S. Organic-Organic Heterojunction Interfaces: Effect of Molecular Orientation. *Adv. Funct. Mater.* **21,** 410–424 (2011).

40. Rusu, P. C. & Brocks, G. Surface dipoles and work functions of alkylthiolates and fluorinated alkylthiolates on Au(111). *J. Phys. Chem. B* **110,** 22628–34 (2006).

41. Wu, Q.-H., Hong, G., Ng, T. W. & Lee, S. T. Substrate effect on the electronic structures of CuPc/graphene interfaces. *Appl. Phys. Lett.* **100,** 161603 (2012).

42. Duhm, S., Glowatzki, H., Rabe, J. P., Koch, N. & Johnson, R. L. Spontaneous charge transfer at organic-organic homointerfaces to establish thermodynamic equilibrium. *Appl. Phys. Lett.* **90,** 122113 (2007).

43. Fraxedas, J. *et al.* Characterization of the unoccupied and partially occupied states of TTF-TCNQ by XANES and first-principles calculations. *Phys. Rev. B* **68,** 195115 (2003).

44. Sing, M. *et al.* Structural vs electronic origin of renormalized band widths in TTF-TCNQ: An angular dependent NEXAFS study. *Phys. Rev. B* **76,** 245119 (2007).

45. Bässler, M., Fink, R., Buchberger, C. & Väterlein, P. Near edge X-ray absorption fine structure resonances of quinoide molecules. *Langmuir* **16,** 6674–6681 (2000).

46. Kurdesau, F., Khripunov, G., da Cunha, A. F., Kaelin, M. & Tiwari, A. N. Comparative study of ITO layers deposited by DC and RF magnetron sputtering at room temperature. *J. Non. Cryst. Solids* **352,** 1466–1470 (2006).

47. Mauthoor, S. Structural Analysis of Molecular Nanostructures and Thin Films. (2011).

48. Emge, T., Maxfield, M., Cowan, D. & Kistenmacher, T. Solution and Solid State Studies of Tetrafluoro-7,7,8,8-Tetracyano-p-Quinodimethane, TCNQF4. Evidence for Long-Range Amphoteric Intermolecular Interactions and Low-Dimensionality in the Solid State Structure. *Mol. Cryst. Liq. Cryst.* **65,** 161–178 (1981).

49. Barrett, C. S. & Massalski, T. B. *Structure of metals : crystallographic methods, principles and data.* (Oxford ; New York : Pergamon, 1980).

50. Ehrlich, G. Atomic View of Surface Self-Diffusion: Tungsten on Tungsten. *J. Chem. Phys.* **44,** 1039 (1966).

51. Schwoebel, R. L. Step Motion on Crystal Surfaces. *J. Appl. Phys.* **37,** 3682 (1966).

52. Canale, C., Torre, B., Ricci, D. & Braga, P. C. Recognizing and avoiding artifacts in atomic force microscopy imaging. *Methods Mol. Biol.* **736,** 31–43 (2011).

Chapter 5 : Modification of ITO and G/ITO Anodes with F_4-TCNQ

5.1 Introduction

In the preceding chapters, it has been shown that graphene can be used as a structural template in small molecule organic photovoltaic devices to control the stacking orientation of molecules on its surface. Such ordered packing with the stacking axis perpendicular to the substrate has the potential to enhance anisotropic properties in the active layer such as charge mobility and optical absorption which are beneficial for OPV devices.[1] However photoemission studies reveal that the modification of ITO with a thin layer of graphene has a deleterious effect on the interfacial energetics by creating an unfavourably large barrier that is nearly twice that of the unmodified ITO (cf. Section 3-2). In the previous sections we have highlighted that this problem may be addressed by including a thin layer of F_4-TCNQ to modify the surface. On the G/ITO substrate, a mere 5 Å of F_4-TCNQ is able to cause a significant change in work function, thus potentially reducing the charge injection barrier between the anode and CuPc. The predominant orientation of F_4-TCNQ on G/ITO at low coverage is facilitated by interfacial π-π interactions such that all the molecules are orientated at the same tilt angle with respect to the substrate. This strongly suggests that the templating property of graphene may be propagated beyond the F_4-TCNQ layer to the subsequent CuPc deposited on top.

In this chapter, we combine the work of the previous two chapters to show that molecular modification of G/ITO substrate is able to reduce the hole injection barrier at the anode-CuPc interface as predicted, yet without affecting the desirable orientation of CuPc. This will be studied in parallel with a reference structure utilizing unmodified ITO. Finally OPV devices based on the ITO and G/ITO anodes are fabricated to determine if these fundamental improvements at the

microscopic level can translate into improved device performance. To our knowledge, investigations concerning the simultaneous control of the structural and electronic properties of the active layer on device performance have not reported before.

5.2 Structural Properties of CuPc

The structural properties of CuPc films are studied using XRD and NEXAFS in this section. For XRD investigations, we begin by using a 'model' substrate of G/Cu due to the almost full coverage of the substrate by graphene, and the absence of defects introduced during the transfer process as mentioned in Chapter 3. Next, we continue the investigations of CuPc films on G/Si and G/ITO to show that surface roughness can affect the interpretation of XRD results. The corresponding bare substrates of Cu, Si and ITO will be studied in parallel to compare the effect of a graphene interlayer. The section concludes with NEXAFS investigations of CuPc on our target substrates of G/ITO and ITO.

5.2.1 CuPc Deposited on F_4-TCNQ Pre-covered G/Cu and Cu

From the outset of the project, we determined that the purpose of graphene in organic solar cell devices is as a structural template layer to modify the orientation of CuPc. Therefore it is imperative to ensure that this property is preserved even with the inclusion of a thin layer (5 Å) of F_4-TCNQ on its surface. For reliable comparison of the orientation, we performed XRD characterization of a 100 nm CuPc film deposited on F_4-TCNQ pre-covered G/Cu so that the results are directly comparable with Figure 3-6 (a). The rationale for using as-received G/Cu instead of transferred graphene is to ensure almost full coverage of the surface by graphene so that molecules interact with only one type of surface (as opposed to G/ITO in which part of the ITO is exposed while the other part is modified by graphene), and to limit variations between substrates caused by the graphene transfer process.

For our XRD data, we use the structure of α-CuPc reported by Hoshino *et al.*[2] to interpret the diffraction pattern. The α-phase of CuPc is formed when the molecules are deposited on weakly interacting substrates at room temperature.[3] Figure 5-1 (a) shows the results of the XRD measurements operated in θ-2θ configuration. G/Cu foil does not contribute any peaks within this range as the foremost Bragg diffractions occur above $2\theta = 35^{o}$. Therefore, the diffraction peaks obtained from the measurements are unambiguously attributed to diffractions from the CuPc molecular film. Regardless of the inclusion of F_4-TCNQ, both films appear to satisfy identical diffraction conditions. A close-up slow scan around the vicinity of the diffraction peaks for 100 nm CuPc/5 Å F_4-TCNQ/G/Cu is shown in Figure 5-1 (b). It confirms that the peak positions are at 26.6^{o} and 27.6^{o} which correspond to diffraction from the (0 1 -2) and (1 1 -2) planes respectively, and indicates that the molecules lie nearly parallel to the substrate. These peaks are the same as the diffraction peaks for 100 nm CuPc/G/Cu [cf. Figure 3-6 (b)]. To confirm that the templating effect originates from the graphene interlayer, samples of 100 nm CuPc and 5 Å F_4-TCNQ deposited directly on Cu foil were prepared. Cu foils were prepared by exposing a piece of G/Cu substrate to oxygen plasma to remove the graphene layer. The spectrum of 100 nm CuPc/5 Å F_4-TCNQ/Cu foil is plotted in Figure 5-1 (a). There are no contributions from the (0 1 -2) and (1 1 -2) planes but instead a new diffraction feature at approximately 7^{o} is observed for the film grown on Cu foil, thus providing clear indication that a single layer of graphene is able to alter and control the molecular orientation of CuPc even in the presence of 5 Å F_4-TCNQ. The diffraction feature marked (c) in Figure 5-1 (a) can be fitted by two peaks at 6.9^{o} and 7.3^{o} which arises from the (1 0 0) and (0 0 1) planes satisfying the diffraction conditions respectively [Figure 5-1 (c)]. Molecules that stack along the (1 0 0) and (0 0 1) planes are considered 'standing' on the substrate since the angles subtended by the substrate and molecular plane are 82^{o} and 67^{o} respectively and are a consequence of intermolecular interaction dominating over the less favourable interaction with the substrate [cf. Figure 3-6 (e)].

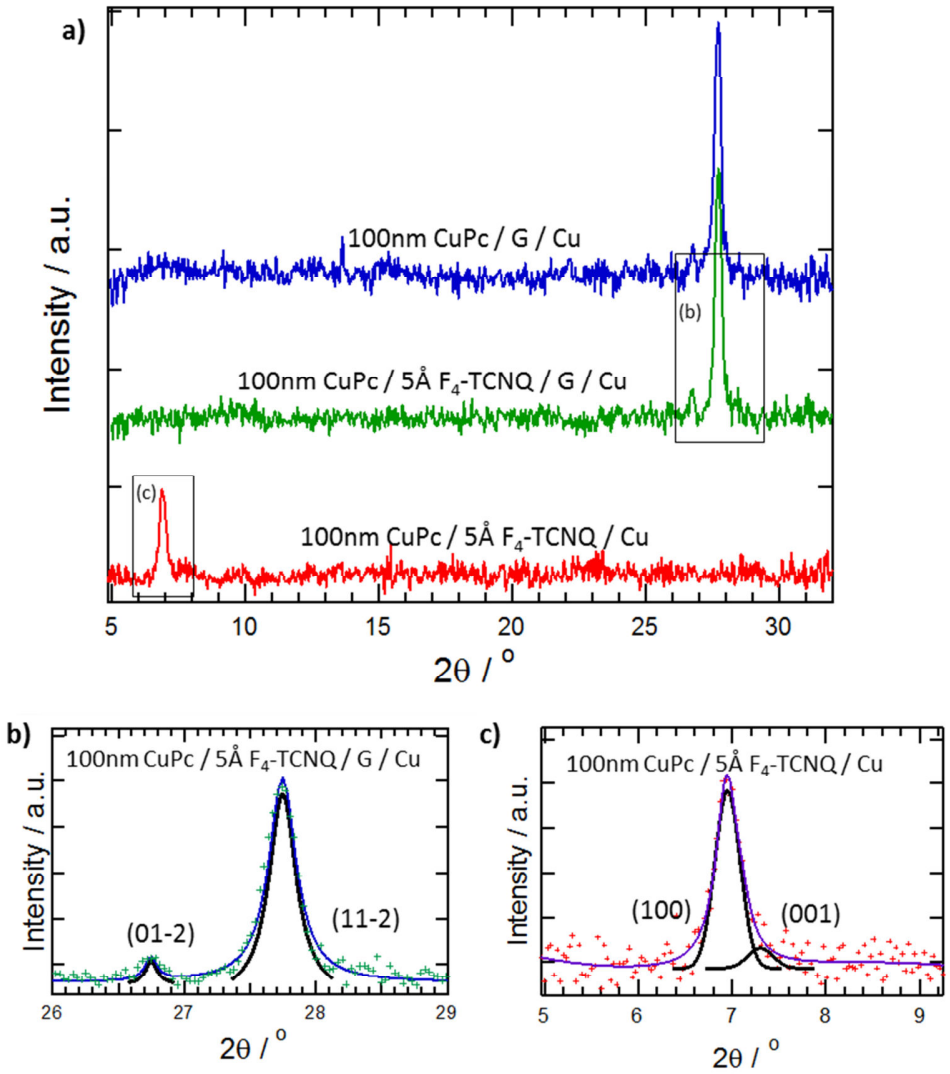

Figure 5-1 XRD spectra of CuPc deposited on various substrates to confirm that the templating effect of graphene is unaffected by the inclusion of 5 Å F_4-TCNQ. (a) Wide scan spectra of 100 nm CuPc/G/Cu (top) and 100 nm CuPc/5 Å F_4-TCNQ/G/Cu (middle) show similar diffraction peaks; 100 nm CuPc/5 Å F_4-TCNQ/Cu (bottom) indicates that the change in orientation of CuPc arises from the graphene interlayer. (b) & (c) Details of the fitted diffraction peaks for 100 nm CuPc/5 Å F_4-TCNQ/G/Cu and 100 nm CuPc/5 Å F_4-TCNQ/Cu respectively.

Depositing CuPc on the idealized substrate of G/Cu allows us to draw conclusions regarding the effectiveness of graphene as structural template for CuPc regardless of whether a thin layer of F_4-TCNQ is present. On technological important substrates such as G/Si and G/ITO, we expect that the XRD results will not be identical due to an incomplete coverage of graphene over the whole substrate. Since the XRD beam is larger than the substrate and samples the whole substrate area, the resultant XRD spectra for CuPc film deposited on G/Si and G/ITO is expected to show

contributions from both the graphene modified and bare ITO areas. In addition, surface roughness of the ITO substrate increases complexity through disordering of the crystallites giving rise to less well textured films. In the following section, we explore the effects of surface roughness and partial coverage of the surface on XRD measurements.

5.2.2 CuPc Deposited on F_4-TCNQ Pre-covered Si & G/Si, and ITO & G/ITO

Figure 5-2 shows the results of XRD spectra for a series of film thicknesses on (a) Si and graphene transferred onto Si (G/Si) substrates, and (b) ITO and G/ITO. Diffraction peaks from the substrates are marked ' ^ ' for Si and ' # ' for ITO. A diffraction peak at 6.9^o - associated with the standing orientation of CuPc on the substrate - is present in all the spectra, including the graphene modified Si and ITO samples. However, this peak is absent from the CuPc/F_4-TCNQ/G/Cu sample as seen in Section 5.2.1, thus indicating that the additional defects introduced during the transfer of graphene (cf. Section 2.3.2) interfere with the templating property of graphene. In other words, the peak at 6.9^o for CuPc deposited on the graphene modified samples can be attributed as arising from the defective regions of the graphene sheet (including tears, holes, residues etc.). The detrimental effect that such defects have on graphene's templating property has been previously observed, but not interpreted.[4] Indeed, Figure 5-2 (a) shows that comparing between films of the same thickness on Si and G/Si, there is an additional diffraction peak on the graphene modified samples that is derived from the lying geometry of CuPc on graphene. Furthermore the intensity of the (1 0 0) peak is attenuated for both the 30nm and 100 nm thick CuPc films on 5 Å F_4-TCNQ/G/Si as compared to their unmodified silicon substrate counterparts.

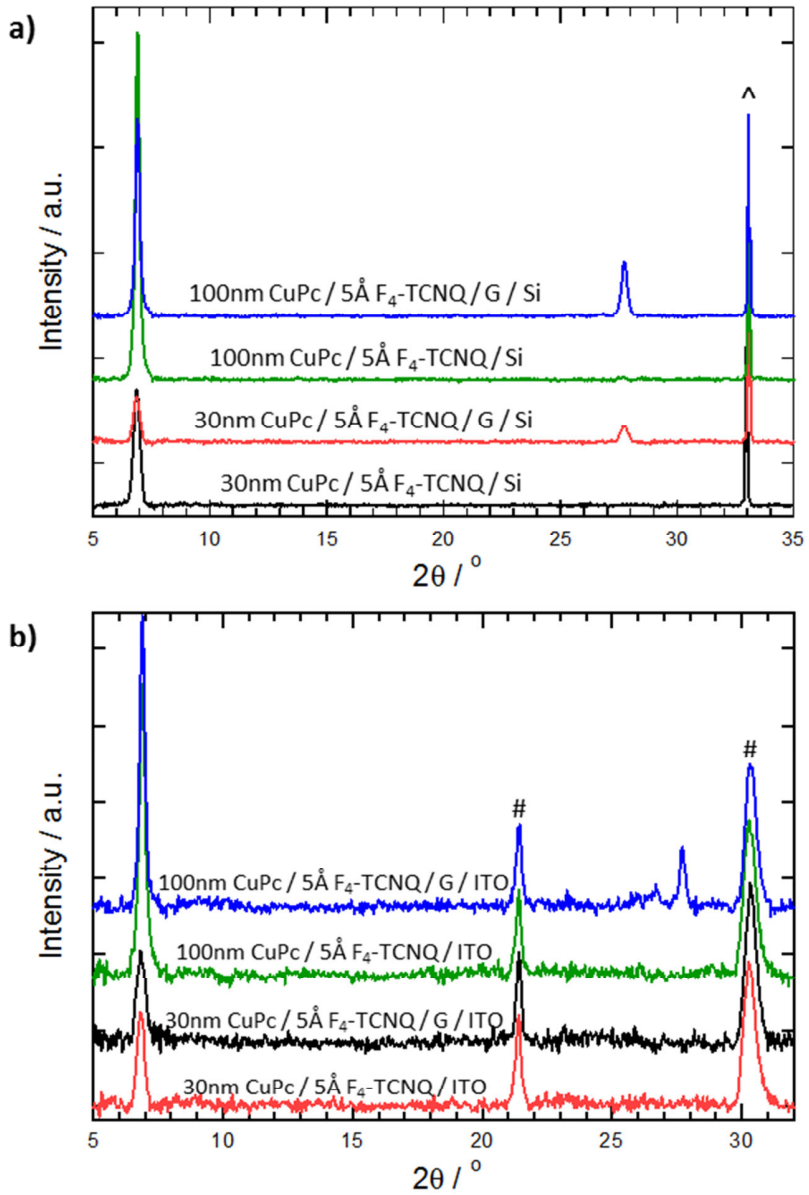

Figure 5-2 XRD spectra of 30 nm and 100 nm CuPc on 5 Å F_4-TCNQ pre-covered (a) Si and G/Si, (b) ITO and G/ITO, to show the effectiveness of transferred graphene as a structural template. Templated α-CuPc diffraction peak at ~27^o is present on all graphene modified surfaces except 30 nm CuPc/5 Å F_4-TCNQ/G/ITO. The presence of this feature on G/Si in (a) at the same molecular coverage indicates that the rough ITO surface results in a greater distribution of crystal orientation, resulting in weak diffraction intensity. All spectra show a diffraction peak centered ~6.8^o as the incident beam is significantly larger than the graphene modified area at all 2θ angles, hence diffraction from the unmodified areas are also detected. ' # ' denotes diffraction peaks originating from the ITO substrate and '^' from the Si substrate.

Increasing the film thickness from 30 nm to 100 nm CuPc results in an enhancement of the (1 0 0) and (1 1 -2) diffractions for the G/Si sample, accompanied by a decrease in full width half maximum (FWHM) of both diffraction peaks. Using Scherrer's equation[5] [Equation (2-11)] which relates the particle size to the inverse of the diffraction peak FWHM, the sizes of the

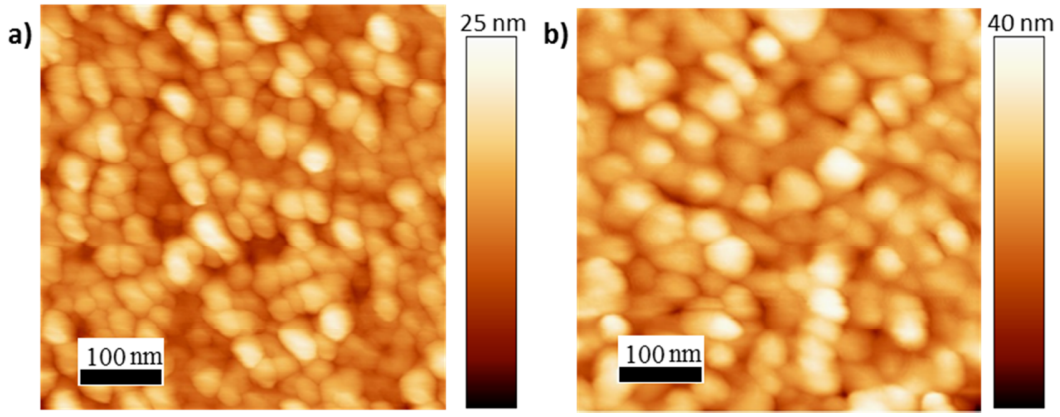

Figure 5-3 500 nm x 500 nm AFM images of (a) 30 nm and (b) 100 nm thick CuPc/5 Å F_4-TCNQ/G/Si showing the larger crystallite size with thicker films. The average grain size is approximately (a) 30 nm ± 5 nm and (b) 42 nm ± 7 nm. The RMS roughness is (a) 3.6 nm and (b) 6.2 nm respectively.

crystallites are found to be 25 ± 5 nm and 31 ± 6 nm for the 30 nm CuPc/5 Å F_4-TCNQ/G/Si and 100 nm CuPc/5 Å F_4-TCNQ/G/Si films respectively. Although Scherrer's equation probes sizes normal to the substrate as compared to lateral sizes measured by AFM, we assume that the crystallites are nearly spherical,[6] therefore the relative difference in the calculated sizes should be representative of the difference in the lateral sizes. This observation correlates with the AFM images (Figure 5-3) which reveal an average grain size of 30 nm ± 5 nm for the 30 nm thick CuPc film as compared to the 42 nm ± 7 nm grain size for the 100 nm CuPc film.

The effect of surface roughness on the molecular orientation can be deduced by contrasting the XRD spectra for the 30 nm thick CuPc films on G/Si with G/ITO. Without the spectra of the 100 nm CuPc/5 Å F_4-TCNQ/G/ITO sample shown in Figure 5-2 (b), and the 30 nm and 100 nm CuPc/5 Å F_4-TCNQ/G/Si samples for comparison [Figure 5-2 (a)], the diffraction spectrum for the 30nm CuPc/5 Å F_4-TCNQ/G/ITO sample by itself may be incorrectly interpreted. This is because the spectra of 30 nm CuPc/5 Å F_4-TCNQ/G/ITO and 30 nm CuPc/5 Å F_4-TCNQ/ITO appear identical i.e. the graphene interlayer appears ineffective at templating CuPc molecules. However from the data of the 30nm CuPc/5 Å F_4-TCNQ/G/Si film described earlier, we know that this is not the case. Furthermore, when the thickness of CuPc is increased to 100 nm on F_4-

TCNQ pre-covered G/ITO, the emergence of diffraction peaks at 26.6° and 27.6°, which are similar to those observed on the G/Cu substrate [Figure 5-1 (a)], provide direct evidence of the templating property of graphene. Dissimilarity between diffraction spectra for the 30nm CuPc/5 Å F_4-TCNQ film on G/Si and G/ITO is attributed to the roughness of the underlying substrate, which prevents effective crystallisation of the thinner films.

The difference in substrate roughness between Si and ITO is clearly visualized in the high resolution cross-section TEM images[7] shown in Figure 5-4 (a) and (b) respectively.[c] Whereas the Si substrate forms a sharp and flat interface with the molecular film, the ITO substrate shows local height variations of 10 – 15 nm. The rough ITO substrate has also previously been imaged by AFM and is shown in Figure 2-13. In the CuPc film on Si, fringes with spacing of 1.3 nm appear parallel to the substrate as shown in the zoom-in image in Figure 5-4 (c). These fringes are formed from diffraction of the (1 0 0) plane of the α-CuPc film and confirms the crystallinity and texture of the film. On the Si substrate, they show good continuity and are well ordered with respect to the substrate. On the other hand, while fringes with the same spacing are also resolved on the ITO substrate [Figure 5-4 (d)], it is apparent that they are less well defined and attain a greater range of orientation which appears to be mediated by the substrate grains. In other words, the CuPc film is not as well textured on the ITO film as on the Si film and is likely nanocrystalline on the former substrate. We propose that this loss of texture and the formation of nanocrystals also apply to CuPc deposited on G/ITO since the substrate is also very rough (cf. Figure 2-13), resulting in indiscernible diffraction from the (1 1 -2) plane parallel to the substrate at 30 nm film thickness.

Finally we perform NEXAFS measurement on thin CuPc films deposited on ITO and G/ITO pre-covered with 5 Å F_4-TCNQ to uncover the orientation of CuPc on the substrates. As ascertained in Section 3.3, the data obtained for the orientation of CuPc on G/ITO must be treated with

[c] All the TEM images were taken by James Gilchrist

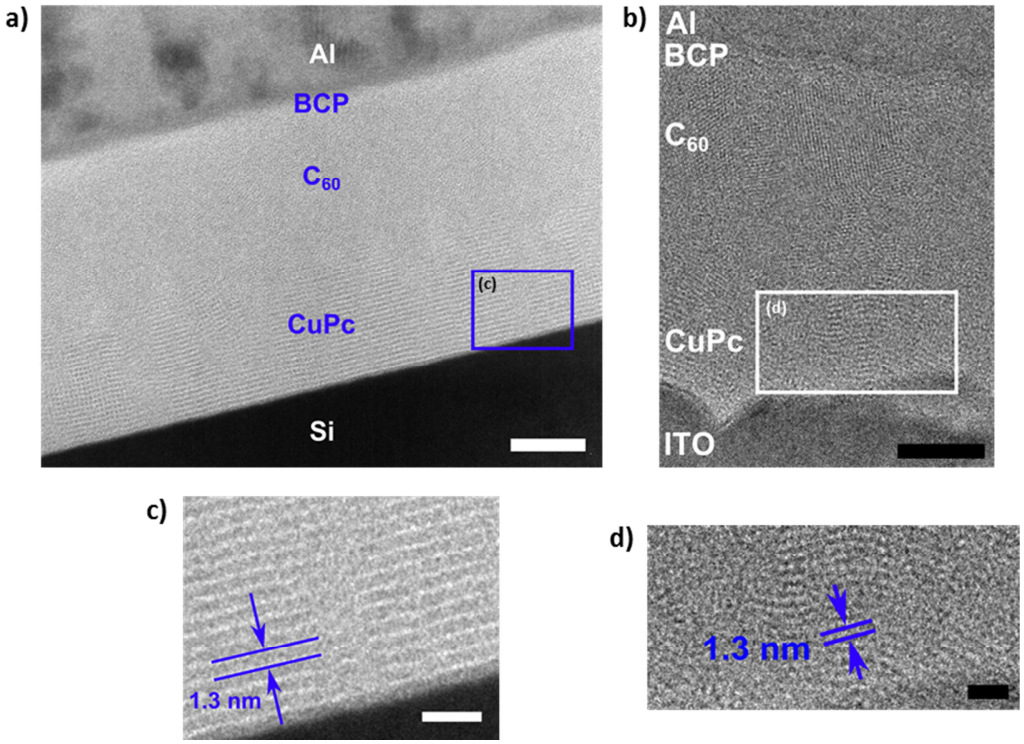

Figure 5-4 High resolution TEM images of 100 nm Al/12 nm BCP/40 nm C_{60}/30 nm CuPc on (a) Si and (b) ITO. Lattice fringes of CuPc are clearly visible on Si but not as distinct on ITO. (c) and (d): Details of the CuPc (1 0 0) fringes with lattice spacing of 1.3 nm on Si and ITO respectively. Greater spread of orientation of the fringes in (d) is due to substrate roughness. Scale bars are 20 nm for (a) and (b), 5 nm for(c) and (d). Images taken by James Gilchrist.

caution since there are defects or holes within the graphene sample, resulting in an average orientation of the molecules deposited directly on G/ITO and those on ITO. In addition, the beam size at grazing incidence ($\theta = 20^{o}$) is 1 mm x 8 mm which is larger than our graphene sheet.

The NEXAFS N K-edge data for 5 Å F_4-TCNQ pre-covered ITO and G/ITO are subtracted from the CuPc spectra prior to analysis since N 1s transitions can occur for both F_4-TCNQ and CuPc molecules. The spectra originating from the CuPc films only are shown in Figure 5-5 after subtracting the contributions from F_4-TCNQ [cf. Figure 4-6 (a) and (b)]. A simple direct subtraction of the F_4-TCNQ signal is performed under the assumption that the F_4-TCNQ molecules do not diffuse significantly into CuPc, and the orientation of F_4-TCNQ molecules are not affected by the subsequent deposition of CuPc molecules. Therefore, we treat the N 1s transitions to the unoccupied orbitals in CuPc and F_4-TCNQ as separate entities. However the

resultant spectra at grazing incidence ($\theta = 90^o$) for thin film (10 Å) CuPc on ITO and G/ITO shown in red in the top graphs of Figure 5-5 (a) and (b) deviate from the pure CuPc film (cf. Figure 3-7 (c) and (d) of bulk CuPc/ITO and G/ITO) implying that the assumptions are incorrect.

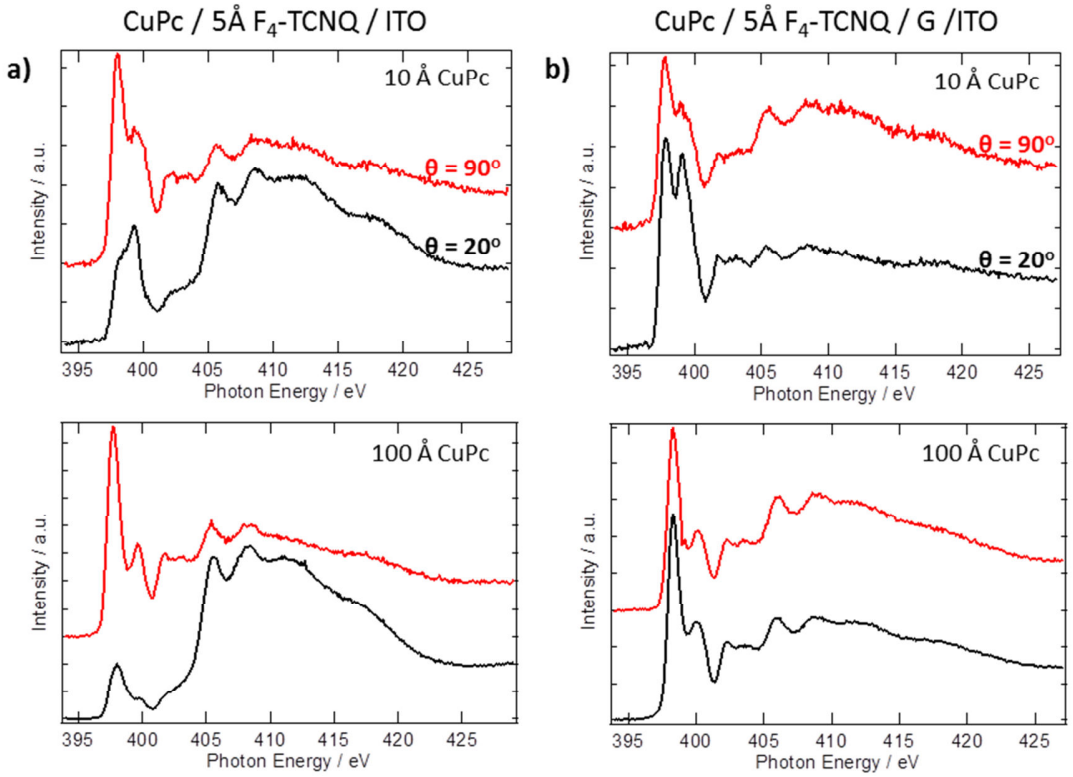

Figure 5-5 Angle dependent NEXAFS N *K*-edge spectra for 10 Å (top) and 100 Å (bottom) CuPc deposited on 5 Å F_4-TCNQ pre-covered (a) ITO and (b) G/ITO. The F_4-TCNQ N *K*-edge signals have been subtracted and only the spectra of CuPc films are shown. The angle that the molecular plane makes with the substrate is (a) $\alpha = 72^o \pm 5^o$ and (b) $\alpha = 51^o \pm 5^o$ at both low and high CuPc molecular coverages.

We propose that molecular mixing of F_4-TCNQ and CuPc has taken place near the substrate interface due to diffusion of the F_4-TCNQ molecules, resulting in an overlap of the resonant transition signals. When the thickness of CuPc is increased, the NEXAFS plots revert to the pure CuPc resonance transition characteristics,[8,9] indicating that molecular mixing of CuPc and F_4-TCNQ occurs strongly only near the substrate interface. The diffusion of F_4-TCNQ molecules into a CuPc film will be studied in more detail in the next chapter.

The intensities of N 1s transitions to individual π^* and σ^* orbitals for CuPc film deposited on F_4-TCNQ pre-covered ITO show angle dependence as revealed in Figure 5-5 (a). Intensity of

resonance transitions to π* orbitals is greatly enhanced at normal incidence and diminished at grazing incidence, while the converse is observed for the N 1s → σ* transitions. By comparing the ratio of I(90°)/I(20°) for the first peak, the average molecular tilt angle is determined to be α = 78° ± 5° for both thin film and bulk coverage of CuPc on 5 Å F_4-TCNQ/ITO. This in good agreement with NEXAFS data for CuPc of the same thickness deposited directly on ITO which has an approximate tilt angle of 70°. The intensities of the π* and σ* transitions for CuPc deposited on 5 Å F_4-TCNQ/G/ITO vary with the angle of incident radiation in a manner contrary to the film deposited on ITO – transitions to the π* orbitals are diminished at normal incidence and enhanced at grazing incidence. Accordingly, CuPc molecules have a smaller tilt angle on 5 Å F_4-TCNQ/G/ITO compared to the ITO substrate. The calculated average tilt angle is α = 51° ± 5°. This value is an average angle between the lying (templated) and standing (non-templated) orientations of CuPc molecules which co-exist on the G/ITO sample as revealed by the XRD diffraction spectra shown previously in Figure 5-2 (b). Similar results were obtained for the CuPc/G/ITO sample in Section 3.3. Collectively, NEXAFS and XRD measurements confirm that pre-covering G/ITO with 5 Å F_4-TCNQ before subsequent deposition of CuPc does not have a deleterious effect on the templating property of graphene.

5.3 Optical Absorption of CuPc on F_4-TCNQ Pre-Covered ITO and G/ITO

Optical absorption of CuPc is highly anisotropic as the probability of optical transitions (I_{opt}) scales with the square of the scalar product of the transition dipole moment $\vec{M}$ of the molecule and the electric field vector $\vec{E}$ of the incident light according to Equation (5-1).

$$I_{opt} \propto \left(\vec{M} \cdot \vec{E}\right)^2 \qquad (5\text{-}1)$$

For the planar CuPc molecule, the dipole moment lies along the plane of the molecule in the direction of the N-Cu-N axis.[10,11] Therefore an associated benefit of the graphene-templated lying orientation of CuPc is the larger absorption strength of light at normal incidence due to the larger overlap between $\vec{M}$ and $\vec{E}$ vectors depicted schematically in Figure 5-6 (b). The absorbance

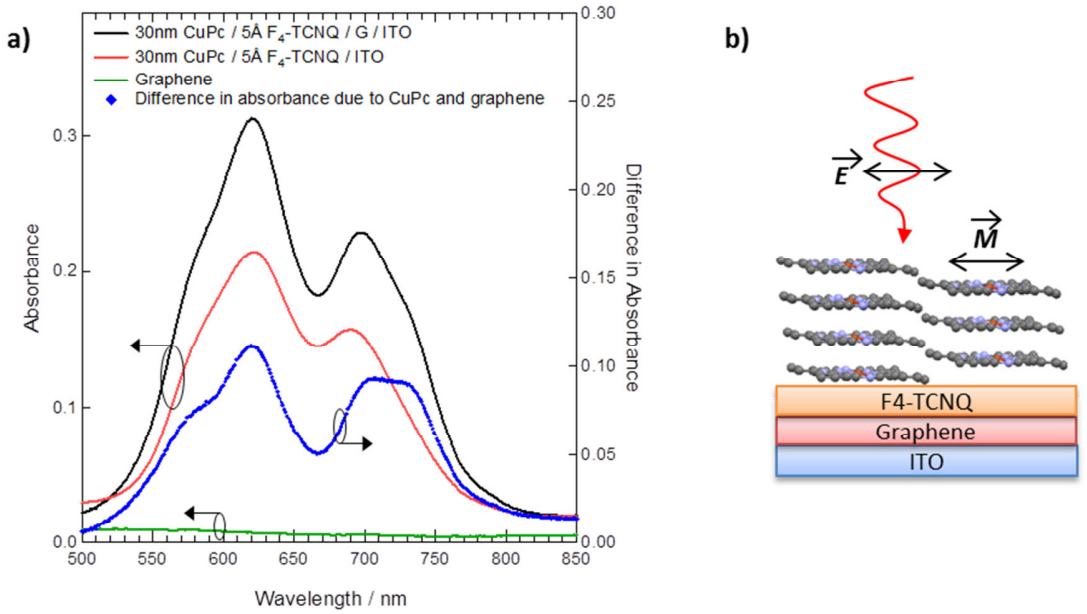

Figure 5-6 (a) (left axis) UV-Vis spectra of absorbance versus wavelength for 30 nm CuPc on 5 Å F_4-TCNQ pre-covered ITO and G/ITO substrates and graphene; (right axis) the difference in absorbance between the two samples. (b) Maximum light absorption occurs when the electric field vector of the incident light ($\vec{E}$) and transition moment of the molecule ($\vec{M}$) are parallel.

spectra for CuPc deposited on 5 Å F_4-TCNQ pre-covered ITO and G/ITO shown in Figure 5-6 (a) display two main peaks centred at around 620 nm and 690 nm (Q-band) which is typical of CuPc films.[3,6,12] The Q-band of CuPc has been assigned to the first and second π-π* transitions in the CuPc macrocycle.[13,14]

The optical absorption for 30 nm CuPc/5 Å F_4-TCNQ/G/ITO (black spectrum) is significantly higher than for the 30 nm CuPc/5 Å F_4-TCNQ/ITO sample (red spectrum). The difference in absorption cannot be attributed solely to the additional light absorbed by the graphene interlayer which theoretically absorbs ~2.3% of the visible light for a monolayer of graphene,[15] since our

graphene is predominantly mono- to bi- layer as determined in Section 2.3.2.1. The experimentally determined value of graphene absorbance in our experiment is ~2% as shown in Figure 5-6 (a) (green spectrum), which is similar to values obtained by other groups for graphene transferred onto transparent substrates.[16–18] While this observation is in direct conflict with the theoretical lower limit of 2.3% absorption per layer of graphene,[15] no attempts have been made to explain the observation. A simple reason for the lower than expected absorbance, or conversely higher transmission, through graphene may be attributed to holes introduced in the graphene sheet during the transfer process of graphene (Figure 2-12 and Figure 2-13), or that the beam size is slightly larger than the graphene sheet. Therefore, the resultant absorption has contributing components from graphene and bare ITO. Regardless of the exact absorption strength of graphene, it is clear that the difference in absorption between the two organic samples on ITO and G/ITO is primarily due to the different orientations of CuPc molecules on the different substrates. Using the predominant molecular tilt angles determined for CuPc on 5 Å F_4-TCNQ/ITO ($\alpha = 82^o$) and 5 Å F_4-TCNQ/G/ITO ($\alpha = 10^o$), we determine that ~50% increase in absorbance is expected for the latter sample if all the molecules are lying on the substrate [Equation (5-1)]. This value is larger than the 43% enhancement calculated from the integral areas of the absorbance spectra in Figure 5-6 (a). This is because CuPc molecules are not fully templated over the whole beam area as explained previously.

Ultimately, the choice of pre-covering G/ITO with a layer of F_4-TCNQ is to reduce the unfavourably large HIB of nearly 1 eV (cf. Section 3.2) in a solar cell device without detrimental modification to graphene's structural template property. Promising data from these orientation studies encourage pursuing F_4-TCNQ as a work function modifier for G/ITO. In the next section, the interfacial energetics between CuPc and G/ITO anode pre-covered with F_4-TCNQ are explored to assess the effectiveness of F_4-TCNQ in reducing the HIB. The results are compared

against our reference sample of CuPc/5 Å F_4-TCNQ/ITO to determine how graphene affects the energy levels at interfaces.

5.4 Interfacial Energetics of CuPc on F_4-TCNQ Pre-Covered ITO and G/ITO

The energy level alignment at the organic-organic and organic-substrate interfaces are determined by PES upon sequential deposition of F_4-TCNQ and CuPc onto ITO and G/ITO. Figure 5-7 (a) shows the evolution of the PES spectra in the low kinetic energy region for increasing thickness of CuPc deposited on 5 Å F_4-TCNQ pre-covered ITO. The substrate spectrum is denoted as (i), and the spectrum of 5 Å F_4-TCNQ/ITO is denoted (ii) 0^+. Labels (iii) to (vii) correspond to increasing thickness of the CuPc film deposited on 5 Å F_4-TCNQ/ITO. The valence band spectra of the CuPc/5 Å F_4-TCNQ/ITO film is shown in Figure 5-7 (b), and its corresponding close-up spectra near the Fermi level is shown in Figure 5-7 (c). Upon deposition of 5 Å F_4-TCNQ on ITO, a large increase in work function is observed as seen by the upward shift in vacuum level from Figure 5-7 (a). This is due to the transfer of electrons from ITO to the electronegative F_4-TCNQ molecules. An interface dipole with a magnitude of 1.08 eV pointing from F_4-TCNQ to the substrate is formed. Valence band features at low binding energy near the Fermi level [labelled (ii) in Figure 5-7 (b) and (c)] which appear following the deposition of F_4-TCNQ are attributed to the partial filling of the LUMO and the relaxed HOMO in F_4-TCNQ.[19,20] These results are consistent with F_4-TCNQ thin film studies by PES and UPS in Section 4.3.

Upon depositing 1 Å CuPc onto 5 Å F_4-TCNQ/ITO, the sample work function decreases by 0.30 eV from 5.33 eV to 5.03 eV at the CuPc/F_4-TCNQ interface; a further 0.32 eV decrease in work function is recorded when an additional 4 Å CuPc is deposited. Beyond this thickness, the work function begins to decrease more gradually and almost plateaus beyond 10 Å CuPc film. The sample work function finally saturates at 4.53 eV for the bulk film. These results are unlike the

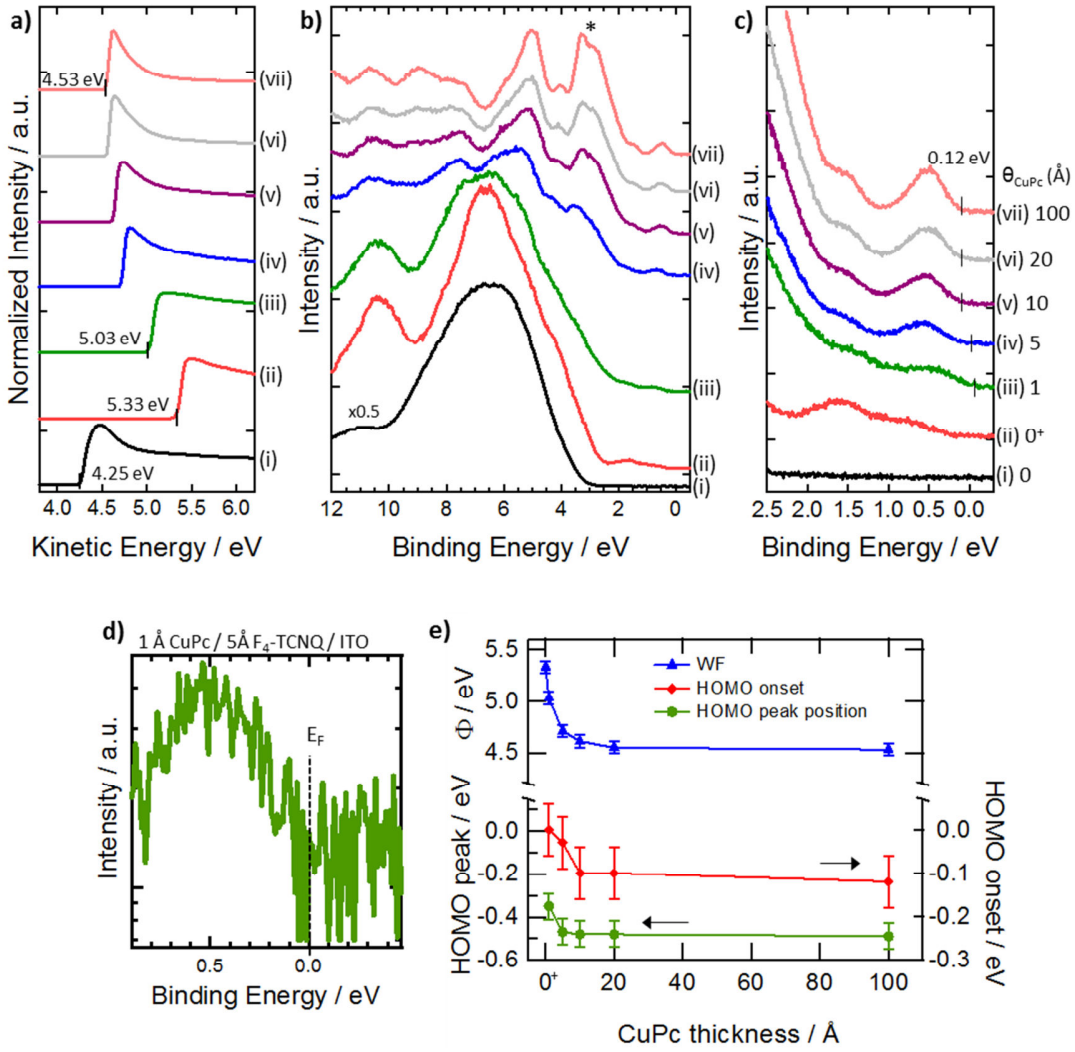

Figure 5-7 Synchrotron based PES spectra evolution of CuPc on 5 Å F_4-TCNQ pre-covered ITO. ' 0^+ ' denotes 5 Å F_4-TCNQ pre-covered ITO. (a) Low kinetic energy region, (b) valence band spectra at low binding energy and (c) near the Fermi level region. ' * ' in (b) shows orientation dependence as is the case for Figure 3-1 (b). (d) Plot of 1 Å CuPc/5 Å F_4-TCNQ/ITO, after subtracting the background signal, shows that CuPc HOMO extends to the Fermi edge at this molecular thickness. (e) Plot of work function (Φ), energy of the HOMO onset and HOMO peak positions with respect to the Fermi level at 0 eV as a function of CuPc thickness.

near vacuum level alignment observed for CuPc/ITO in Section 3.2, suggesting that the difference in observation may be due to interaction at the CuPc-F_4-TCNQ interface.

Upon evaporating CuPc molecules onto 5 Å F_4-TCNQ/ITO, the valence band spectra in Figure 5-7 (b) reveal the emergence of CuPc derived features. Similar to the spectra for CuPc/ITO in Figure 3-1 (b), the feature marked ' * ' in the valence band plot [Figure 5-7 (b)] can be interpreted

as the CuPc molecules adopting a predominantly standing orientation.[21] The HOMO onset for the spectrum of 1 Å CuPc/5 Å F_4-TCNQ/ITO appears to extend to E_F as shown in Figure 5-7 (c). To visualize this more clearly, the valence band spectrum of 5 Å F_4-TCNQ/ITO is subtracted from the spectrum of 1 Å CuPc/5 Å F_4-TCNQ/ITO and the resultant spectrum is plotted in Figure 5-7 (d). Clearly, the HOMO onset at this CuPc thickness extends to 0 eV (E_F), in other words, the Fermi level is pinned at the HOMO onset.[22] At higher CuPc coverage, the HOMO onset appears to gradually move away from the Fermi level towards higher binding energy before saturating at 0.12 eV. Concomitant variations in the HOMO peak positions with CuPc film thickness are also observed. Figure 5-7 (e) summarises the changes in work function, HOMO peak position and HOMO onset as a function of CuPc thickness. It reveals that there are two contributions to the net change in work function – first, a dipole of 0.68 eV at the CuPc/F_4-TCNQ interface; second, a mild band bending of 0.12 eV away from the interface.

To interpret the observations at the vacuum level and valence band regions for the system of CuPc/5 Å F_4-TCNQ/ITO, we invoke the gap state model that has been used to explain Fermi level pinning at the interface and the gradual band bending-like change in HOMO onset position away from the interface.[22,23] It has been proposed that the HOMO (and consequently LUMO) band tails into the HOMO-LUMO gap by several hundred meV due to intrinsic structural defects and imperfect crystal packing[24,25] with their density of states (DOS) decaying away from the HOMO (or LUMO) into the band gap.[26] These states are termed ‘gap states’ according to their location within the band gap. Although the density of these gap states are small, they are able to participate in charge transfer and are therefore involved in determining the final positions of the HOMO and LUMO with respect to the Fermi level.[22,26–30] The origin of band bending due to the gap states can be explained in terms of space-charge accumulation at the interface. To achieve thermal equilibrium between two interfaces (e.g. CuPc and 5 Å F_4-TCNQ/ITO for this case) at the Fermi level upon contact, charge transfer can take place at the interface resulting in excess

positive charges accumulating in the gap states of the CuPc organic film. A built-in potential is formed across the interface and displaces the frontier orbitals of the organic film further from the Fermi level, thus limiting the magnitude of charge transfer.[29,30] We expect that defect induced gap states are intrinsic to our samples prepared on ITO and G/ITO due to imperfect crystallinity and numerous grain boundaries, which are evident from the TEM images shown previously in Figure 5-4 (b) and (d).

Near the interface between CuPc and F_4-TCNQ/ITO, the work function of 5 Å F_4-TCNQ/ITO is 5.33 eV which is significantly larger than the IP of standing CuPc (~4.77 eV). Assuming simple vacuum level alignment, the position of CuPc HOMO and its gap states lie above the Fermi level of the F_4-TCNQ/ITO substrate. Upon contact, electron transfers spontaneously from the gap states and HOMO of CuPc to F_4-TCNQ, resulting in a dipole moment pointing from F_4-TCNQ to CuPc. With only 1 Å CuPc deposited, depletion of all the electrons from the occupied gap states of CuPc alone is insufficient for the system to attain thermodynamic equilibrium due to the large initial energy offset. Therefore electrons from the HOMO are also transferred to F_4-TCNQ, resulting in the Fermi level being pinned at the HOMO leading edge as shown in Figure 5-7 (d). At this point however, the substrate work function is still 0.26 eV larger than the IP of standing CuPc due to the low coverage of the latter. Consequently, increasing the CuPc film thickness to 5 Å results in further electron transfer to F_4-TCNQ via the depletion of the gap states electrons. Since the energy offset at this thickness is half the initial difference, depletion of the electrons from the gap state alone is sufficient to satisfy thermodynamic equilibrium and the Fermi level is located within the gap states instead of being pinned at the HOMO onset as seen in Figure 5-7 (d).

Beyond 5 Å CuPc deposited on 5 Å F_4-TCNQ/ITO, the energy misfit between CuPc and the underlying substrate is small; therefore, the magnitude of charge transfer is greatly reduced as assessed from the smaller change in work function shown in Figure 5-7 (e). Thermodynamic

equilibrium can therefore be achieved via electron transfer from a narrower energy range within the gap state, and the Fermi level is located at the top of the gap state. Beyond 10 Å CuPc, charge transfer almost ceases as the newly deposited CuPc molecules are not in direct contact with F_4-TCNQ. The minor change in work function of 0.07 eV may be attributed to disordering in the bulk film which has been also observed for CuPc deposited directly on ITO[31] (cf. Section 3-2). The positions of the HOMO onset and HOMO peak position also remain invariant beyond 10 Å CuPc, in good agreement with the lack of interaction with the underlying substrate.

The degree of charge transfer at the interface can be estimated from the Helmholtz equation[27] given as

$$\Delta V = \frac{\mu \cos\theta}{\varepsilon\, \varepsilon_0} \qquad (5\text{-}2)$$

where ΔV is the interface dipole measured from the vacuum level shift, μ is the dipole density, θ is the angle subtended by the dipole and the surface normal, ε is the dielectric constant of CuPc, and ε_0 is the dielectric constant of vacuum. The dielectric constant of CuPc is approximated to be 3.4,[32] θ is estimated from thin film NEXAFS results to be 12°, and the dipole density is 1 per 12.1 Å x 3.8 Å.^{2} Using the observed shift in vacuum level at the interface of 0.68 eV, the induced dipole density is 0.60 e Å. We estimate the length of the dipole to be approximately 5 Å, thus yielding a charge transfer of 0.12 electrons per molecule at the interface. Ultimately, the HIB of the system is 0.12 eV which is a significant reduction from the 0.51 eV originally obtained for CuPc deposited directly onto ITO (cf. Section 3.2). The dominant mechanism in lowering HIB is the increase in substrate work function through the formation of interface dipoles.[19] The lower HIB has implications on charge accumulation and recombination in the CuPc active layer when this structure is used in an OPV device.

Energy level alignment between CuPc and F_4-TCNQ pre-deposited on G/ITO is likewise investigated and the results are presented in Figure 5-8. The effect of depositing a thin layer of F_4-

TCNQ is to increase the sample work function to 4.95 eV as shown in Figure 5-8 (a). This places the Fermi level of the 5 Å F_4-TCNQ/G/ITO sample at approximately the same energy as the IP of lying CuPc molecules (4.99 eV); therefore, the HOMO onset position at low CuPc coverage [spectrum (iii) in Figure 5-8 (b)] appears to extend to the Fermi level which is a reasonable scenario. The smaller energy offset at the CuPc-F_4-TCNQ/G/ITO interface implies that charge transfer is not as strong as between CuPc-F_4-TCNQ/ITO since thermodynamic equilibrium is nearly attained. The PES spectra for CuPc/5 Å F_4-TCNQ/G/ITO show an apparent vacuum level alignment and invariant HOMO positions up to 10 Å CuPc film. Beyond this thickness, downwards band bending-like change in both vacuum level and HOMO positions are observed.

We propose that the observed behaviour of the vacuum level and HOMO features is mainly attributed to the diffusion of F_4-TCNQ into the CuPc film. This has been previously inferred from the NEXAFS data. Details concerning the diffusion of F_4-TCNQ through CuPc films will be presented in Chapter 6. Low molecular weight F_4-TCNQ diffusion through similar phthalocyanine molecules such as ZnPc has been reported.[33–36] Due to a concentration gradient, the diffused species is the highest at the CuPc-F_4-TCNQ interface.[37] The spectral features and energy levels of the CuPc film close to the F_4-TCNQ interface may therefore originate from the doped F_4-TCNQ:CuPc film. PES data obtained for ZnPc intentionally doped with F_4-TCNQ show similar behavior at low molecular coverage where the vacuum level and valence band features of the film are nearly invariant in energy.[38] The PES features farther from the interface are derived only from the CuPc film due to reduced intermolecular doping away from the interface. Alternatively, the observed behaviour of the PES spectra may be ascribed to CuPc molecules not following a layer-by-layer growth mode on the substrate,[39] resulting in the incident electron beam probing a mixture of F_4-TCNQ/G/ITO areas in addition to CuPc clusters on the surface.

In these scenarios, the positions of the vacuum level can be interpreted as an average of neutral and ionized molecules. This effect diminishes at higher CuPc coverage when 1) the doping of

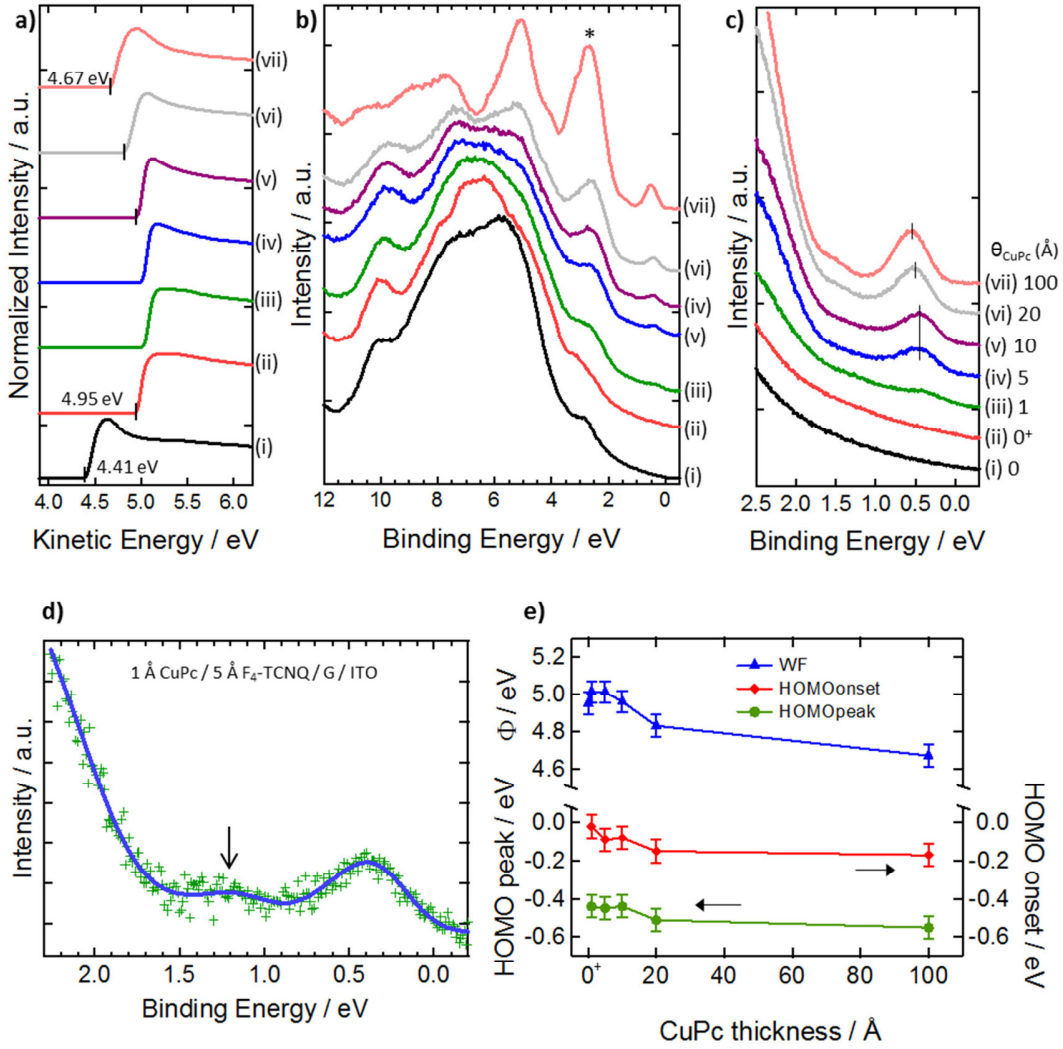

Figure 5-8 Synchrotron based PES spectra evolution of CuPc on 5 Å F_4-TCNQ pre-covered G/ITO. 5 Å F_4-TCNQ pre-covered substrate is denoted ' 0^+ ' (a) Low kinetic energy region, (b) valence band spectra at low binding energy and (c) near the Fermi level region. ' * ' in (b) has the same meaning as in Figure 3-3 (b). (d) 1 Å CuPc/5 Å F_4-TCNQ/G/ITO spectra near the Fermi level after background subtraction showing a broad asymmetrical HOMO feature, and a feature marked by an arrow that neither originates from neutral CuPc or F_4-TCNQ. (e) Plot of work function (Φ), energy of the HOMO onset and HOMO peak positions as a function of CuPc thickness.

CuPc by F_4-TCNQ is reduced away from the interface, and/or 2) the size of the CuPc clusters increases and thus masks the contributions from the underlying F_4-TCNQ/G/ITO. Close to the Fermi level, the HOMO feature up to 10 Å CuPc film appears broader and asymmetrical in comparison to the 100 Å film. We assume that the latter is representative of CuPc films since it is at a considerable distance from the substrate interface and looks similar to the PES spectrum for

CuPc/G/ITO in Figure 3-3(b). The spectrum of 1 Å CuPc/5 Å F_4-TCNQ/G/ITO, following background subtraction, is shown in Figure 5-8 (d) and clearly reveals the asymmetrical HOMO feature, and the appearance of an additional valence band feature (marked by an arrow). These features cannot be accounted for by neutral CuPc and F_4-TCNQ molecules alone, and therefore indicate that the spectrum may be a superposition of neutral and ionized molecules.[34] The feature at 1.3 eV may be attributed to the relaxed HOMO of ionized F_4-TCNQ molecules,[19] or derived from the formation of hybrid HOMO and LUMO levels upon the formation of a charge transfer complex[40] as suggested by Jäckel *et al.*.

Beyond 10 Å thickness, the HOMO onset and HOMO peak shift to higher binding energy, accompanied by a downward shift in vacuum level by ~0.2 eV. The cause of this band bending-like shift due to formation of a space-charge layer has been explained for the CuPc/F_4-TCNQ/ITO sample, and can possibly extend to several nanometers into the bulk film.[28] The HIB for the thicker CuPc film is determined to be 0.17 eV, over a five-fold decrease from the unmodified G/ITO anode (cf. Section 3.2). This result asserts the potential of using F_4-TCNQ as a work function modified for G/ITO since successful reduction in HIB is obtained without compromising the templating ability of graphene. Finally, the energy diagrams for CuPc deposited on 5 Å F_4-TCNQ/ITO and 5 Å F_4-TCNQ/G/ITO are illustrated schematically in Figure 5-9 (a) and (b) respectively. The LUMO position is obtained from literature.[41] In Figure 5-9 (b) for CuPc deposited on 5 Å F_4-TCNQ/G/ITO, the CuPc region close to the F_4-TCNQ interface is depicted as dashed lines due to the uncertainty of the HOMO, and hence LUMO, positions.

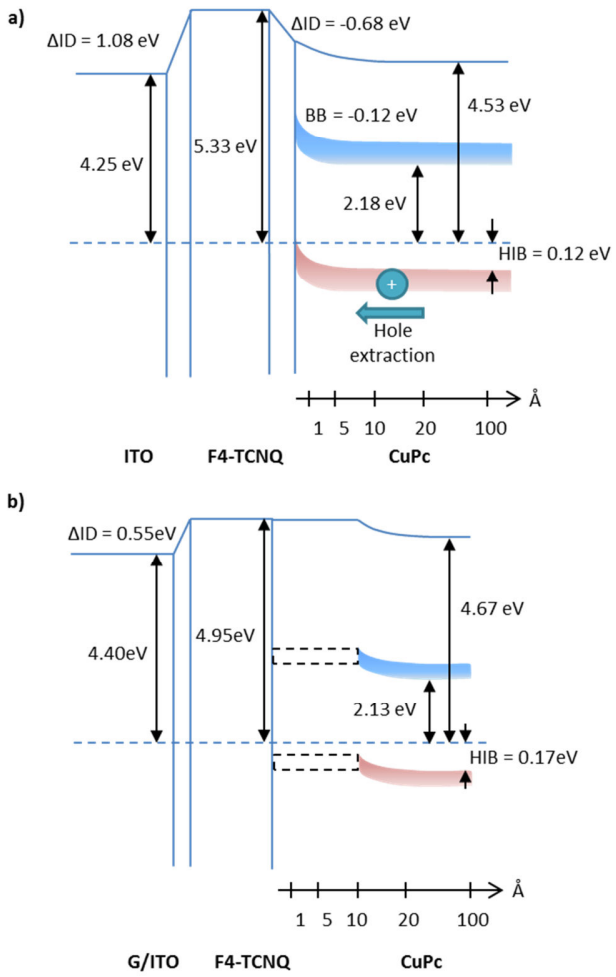

Figure 5-9 Energy level diagrams for CuPc on pre-covered F_4-TCNQ on (a) ITO and (b) G/ITO. The direction of hole extraction in an organic solar cell is indicated by the horizontal arrow in (a) on the HOMO onset band (pink). The magnitudes of the band bending (BB), work function and HIB are shown. The position of the LUMO (blue band) is obtained from literature.[41] (b) Uncertainty in the HOMO (and correspondingly LUMO) onset position at low CuPc coverage is marked by the dashed boxes.

5.5 Morphology of CuPc on F_4-TCNQ Pre-Covered ITO and G/ITO

The effect of modifying ITO with a layer of graphene on the resulting CuPc crystallites and overall topography is revealed by AFM in Figure 5-10. CuPc forms nano-size grains on the order of around 30 nm on both substrates which is typical of polycrystalline films.[6,42] The grains of CuPc appear spherical or elliptical on 5 Å F_4-TCNQ/G/ITO which is similar to CuPc grown on Si in Figure 5-3 (a); however when deposited onto ITO, the morphology of the grains looks

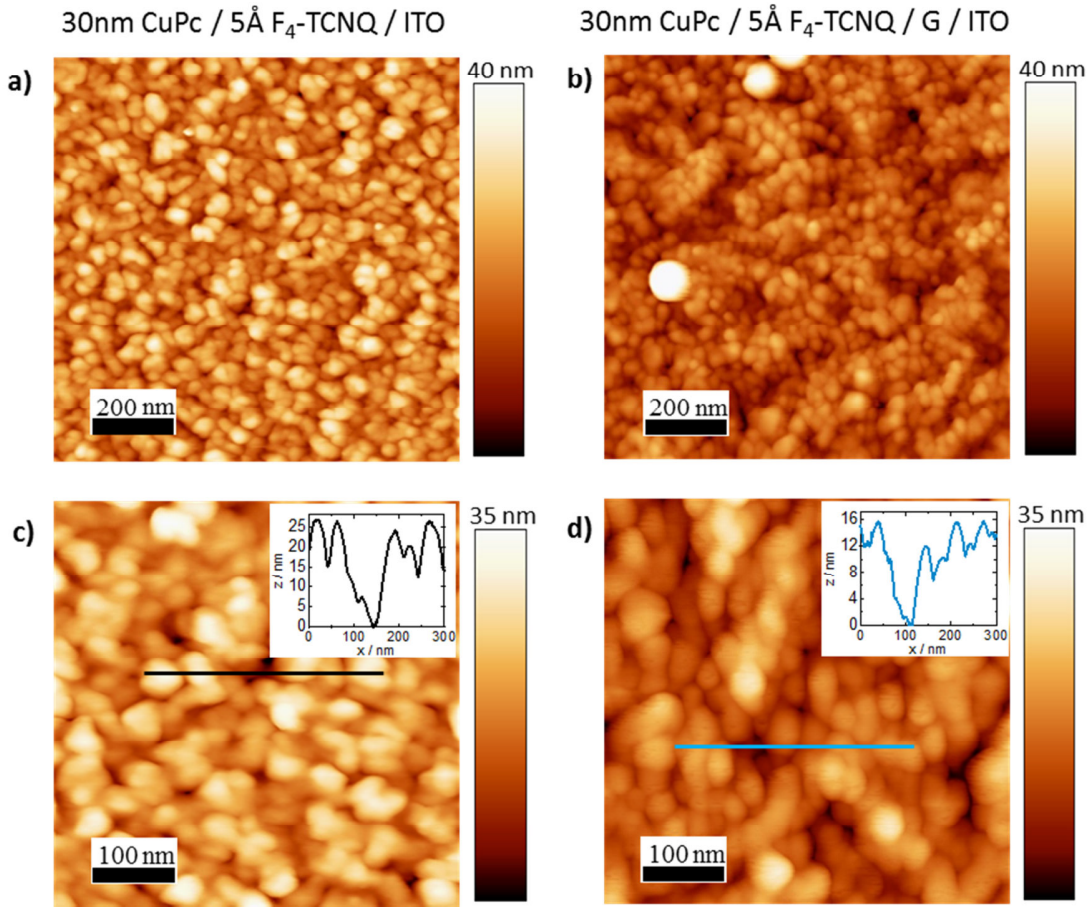

Figure 5-10 (a) 1 μm x 1 μm and (c) 500 nm x 500 nm topographic AFM images of 30 nm CuPc/5 Å F_4-TCNQ/ITO. (b) & (d) is similar to (a) & (c) respectively but for 30 nm CuPc/5 Å F_4-TCNQ/G/ITO. Insets in (c) and (d) show line profiles across the image. The RMS roughness (a) 5.5 nm, (b) 5.4 nm, (c) 5.1 nm and (d) 5.0 nm. [The high islands in (b) were excluded during RMS calculations]. Height (z-axis) scale bar is shown besides each image.

distinctly different and instead appears to be mediated by the substrate's morphology (cf. Figure 2-13). CuPc grains appear different on F_4-TCNQ pre-covered ITO and G/ITO substrates as the undulating grains of the ITO substrate are 'smoothed out' or masked by graphene as seen from Figure 2-13. Several pinholes that appear as dark patches are observed within the CuPc films. Detailed analysis indicates that the vertical height variation across these trenches is over 15 nm as shown in the line scan profiles in Figure 5-10 (c) and (d) (insets). These pinholes may give rise to leakage current when an OPV device is fabricated using this design. The root mean square (RMS) roughness of CuPc deposited on 5 Å F_4-TCNQ/ITO and 5 Å F_4-TCNQ/G/ITO are comparable at 5.5 nm and 5.4 nm respectively averaged over several 1 μm x 1 μm images. Finally, the total

surface area that the CuPc film presents to the subsequent C_{60} film in an OPV device, in other words the D/A interface area, is an important parameter in determining the photogenerated current – larger areas imply more accessible sites for exciton dissociation at the interface. The ratios of the total surface area of CuPc normalized to the flat scan area are comparable at 1.17 and 1.15 for CuPc/5 Å F_4-TCNQ/ITO and CuPc/5 Å F_4-TCNQ/G/ITO respectively. Overall, the topography, total surface area and morphology of CuPc films grown on both substrates are similar and therefore these parameters may be neglected when comparing the solar cell parameters for these devices.

An important caveat is that the AFM images and the parameters derived from the images shown in Figure 5-10 (b) and (d) for CuPc/5 Å F_4-TCNQ/G/ITO are for the ideal case when graphene is continuous and have few visible defects under an optical microscope. In OPV devices which utilize electrodes that are 7 orders of magnitude larger than the imaged area (0.12 cm^2 versus 1 μm^2), it is inevitable that some areas will contain graphene damaged during the transfer process resulting in scrolling and buckling of graphene film at the edges such as shown in the SEM images in Figure 5-11 (a) and (b) (after CuPc and 5 Å F_4-TCNQ deposition). Although the RMS roughness close to the 'damaged' area is comparable with the 'pristine' areas as determined from the AFM image in Figure 5-11 (c), the vertical height variation of the former is on average larger and extends up to 30 nm as indicated by the line profile [Figure 5-11 (d)] drawn across the Figure 5-11 (c). Such situation is not ideal for OPV devices using graphene as a template later: first, we are unable to measure the intrinsic solar cell parameters due solely to pristine graphene since there will be areas of ITO that are not modified by graphene prior to molecular deposition. Second, large variation in vertical height may cause shorting by providing a conducting path between both cathode and anode. Finally scrolled up graphene, which is unable to serve its original templating purpose, might have the same effect as surface contaminants by acting as charge traps, thereby hindering the efficient extraction of photogenerated charges. The following

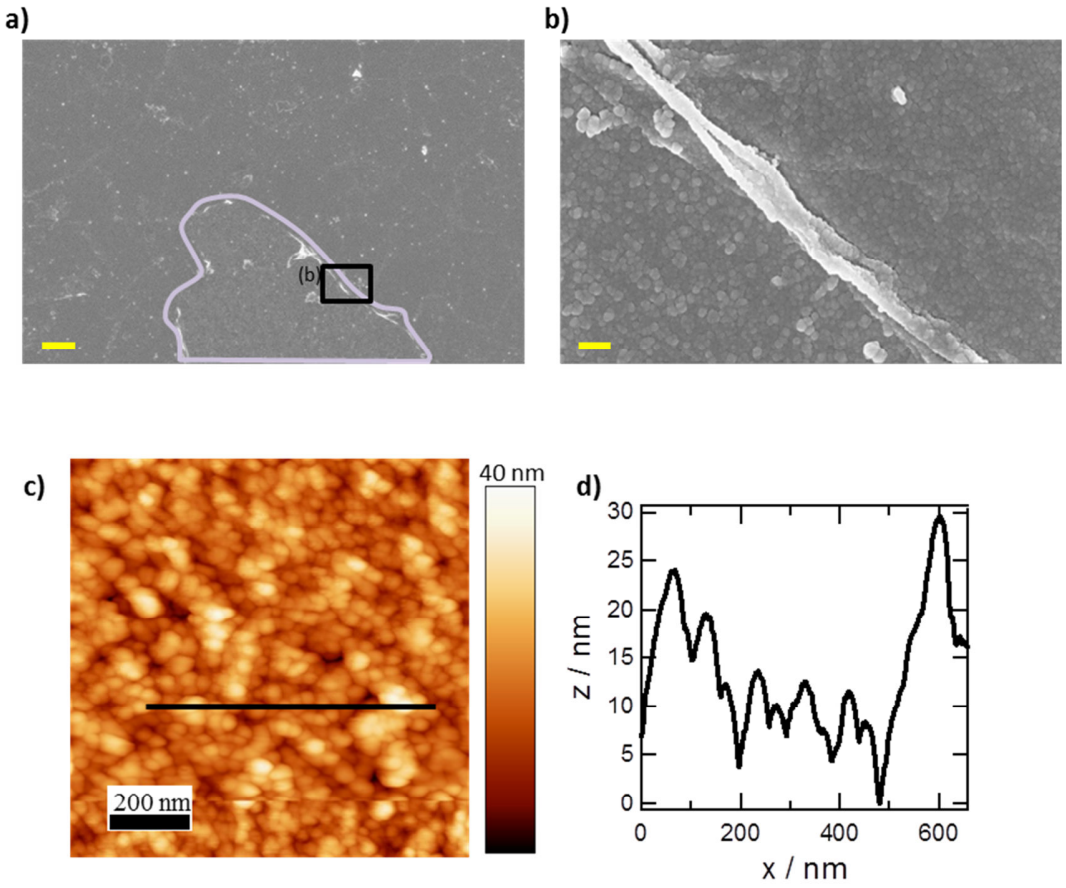

Figure 5-11 (a) and (b) SEM images of 30nm CuPc/5Å F_4-TCNQ/G/ITO at x1000 and x100000 respectively. Scale bars are (a) 2 µm and (b) 200 nm. The purple loop encloses an area where graphene is absent due to the tearing of graphene during transfer, i.e. CuPc and F_4-TCNQ are grown directly on ITO. (b) Corresponding magnified image of the area marked in (a) showing the scrolling of graphene and subsequent deposition of CuPc and F_4-TCNQ at the 'damaged' interface. (c) 1 µm x 1 µm AFM image of CuPc/5 Å F_4-TCNQ/G/ ITO near a 'damaged' interface as described in (a) & (b). Black surface line profile indicates height variations of up to 30 nm at certain areas (d).

section confirms that these effects indeed limit solar cell performance for devices fabricated on G/ITO anode.

5.6 Device Characterization of OPV

To probe the effect of molecular orientation of CuPc and lowering of the HIB on OPV device performance, we fabricated planar heterojunction OPV devices according to the schematic illustration in Figure 3-8 (a) : 100 nm Al/12 nm BCP/40 nm C_{60}/30 nm CuPc/5 Å F_4-TCNQ/G/ITO (or A/5 Å F_4-TCNQ/G/ITO following the notation in the schematic) and 100 nm

Al/12 nm BCP/40 nm C_{60}/30 nm CuPc/5 Å F_4-TCNQ/ITO (or A/5Å F_4-TCNQ/ITO). These devices are characterized by J-V measurements and their parameters are compared against each other, and also to their counterparts previously evaluated in Section 3.4 which lack the F_4-TCNQ layer i.e. devices with larger HIB. All growth parameters being equal, we propose that the device A/5 Å F_4-TCNQ/G/ITO should perform better than the reference cell A/ITO based on the modification of the CuPc molecular orientation and also the more favourable energy level alignment in the former. Templating of CuPc molecules is caused by the graphene interlayer, while interfacial doping with 5 Å F_4-TCNQ causes a reduction in HIB at the anode. However the drawback of including graphene is the high surface roughness and aggregation of graphene sheets at areas where graphene is damaged during the transfer process, an effect that we first proposed in Section 3.4 to account for the unexpectedly poor J_{sc} of A/G/ITO device, and confirmed via SEM and AFM images in Section 5.5.

The physical properties of CuPc films, including carrier mobility, charge transfer and optical absorption are highly anisotropic.[1,3,12,43,44] As mentioned in Section 1.1.2, for small molecule based OPV, it is desirable that the stacking axis is perpendicular to the substrate (i.e. CuPc molecules are lying on the substrate) to maximize charge transport and optical absorption. Therefore, graphene OPV devices (A/5 Å F_4-TCNQ/G/ITO) should have an enhanced J_{sc} as compared to the non-templated devices (A/5 Å F_4-TCNQ/ITO). For planar OPV devices, potential loss (V_{oc}) at the D/A interface is inevitable due to their energy offset. Further losses at the electrodes occur when a large barrier of extraction is present, resulting in charge accumulation and recombination at the active layer-electrode interfaces.[45] Five-fold reduction of the HIB at the anode is successfully achieved by pre-covering G/ITO with 5 Å F_4-TCNQ while four-fold decrease is obtained for the ITO substrate. While the near ohmic contact between the HOMO of CuPc and the modified anode should enhance charge extraction leading to lower recombination losses, we are cautious in predicting an improvement in V_{oc} since it is also directly related to the

offset between the HOMO of the donor and the LUMO of the acceptor. Doping the anode with F_4-TCNQ modifies the electronic properties and energy levels of the CuPc thin film; this may affect the subsequent energy level alignment between CuPc and C_{60} acceptor molecule at the D/A interface. Thus the overall V_{oc} recorded in a device will be a balance of these two related factors.

Figure 5-12 (a) shows the average J-V curves in the dark and (b) illuminated for OPV with device structures A/5 Å F_4-TCNQ/G/ITO in black and A/5 Å F_4-TCNQ/ITO in red. Dark current characteristics provide information about series (R_s) and shunt resistance (R_{sh}) of the devices. Whereas A/5 Å F_4-TCNQ/ITO device exhibits the typical diode rectifying characteristics, large leakage current (low R_{sh}) is observed for A/5 Å F_4-TCNQ/G/ITO device as seen from significant current density in reverse bias [Figure 5-12 (a)].[45] The R_{sh} recorded for A/5 Å F_4-TCNQ/G/ITO is 0.9 kΩ cm^2 which is ~35% smaller than the 1.4 kΩ cm^2 for A/G/ITO, an effect which we attribute to different quality of transferred graphene rather than of physical origin. Low R_{sh} provides an alternate path for current to flow from one electrode to the other, thereby reducing V_{oc} across the OPV device. We correlate this observation with AFM and SEM data from Figure 5-10 and Figure 5-11 which reveal pinholes within the CuPc film, and additional high features attributed to damaged graphene. Current leakage may also originate from the deposition of hot metal cathode that can penetrate the film to reach the anode thus forming a conducting path between the electrodes. However we rule this out as the dominant factor for the large leakage current observed for A/5 Å F_4-TCNQ/G/ITO and A/G/ITO since it should similarly affect the cells fabricated on ITO anode as they were prepared in the same growth. R_s for A/5 Å F_4-TCNQ/G/ITO and A/5 Å F_4-TCNQ/ITO, which is calculated from the gradient of the dark curves near 1 V external bias, are 58 Ω cm^2 and 59 Ω cm^2 respectively. Significant improvement in R_s is for A/5 Å F_4-TCNQ/G/ITO compared to A/G/ITO (R_s = 160 Ω cm^2) can be attributed to the lowering of sheet resistance of graphene by doping with F_4-TCNQ.[46]

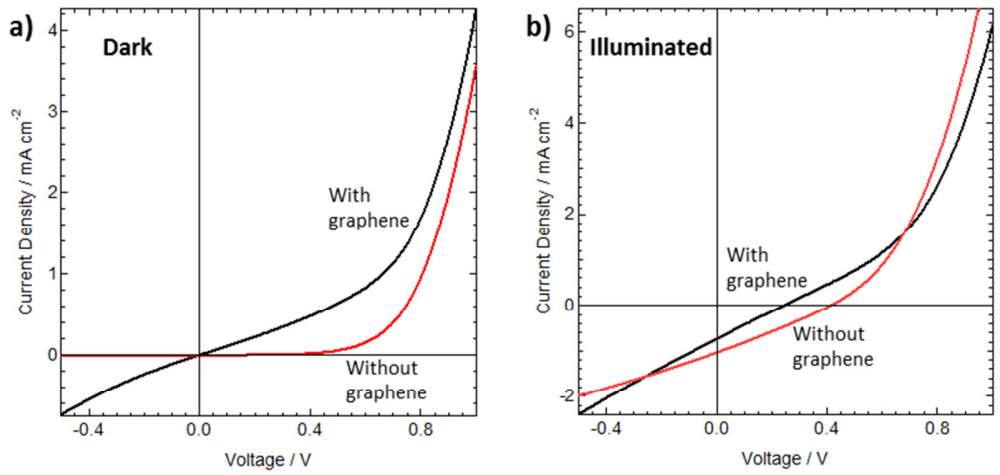

Figure 5-12 Current density as a function of cell voltage (J-V) curves under (a) dark and (b) 100 mW/cm^2 illumination for red: A/5 Å F_4-TCNQ/ITO and black: A/5 Å F_4-TCNQ/G/ITO. Graphene device shows large current leakage and poorer performance as compared to the device without graphene.

Despite improvements to R_s, HIB and the optical absorption, these results fail to translate into better device parameters for A/5 Å F_4-TCNQ/G/ITO. 40% decrease in J_{sc} and 30% decrease in V_{oc} are observed for A/5 Å F_4-TCNQ/G/ITO (J_{sc} = 0.7 mA cm^{-2} , V_{oc} = 0.26 V) in comparison to A/5 Å F_4-TCNQ/ITO device (J_{sc} = 1 mA cm^{-2} , V_{oc} = 0.41 V). The A/5 Å F_4-TCNQ/G/ITO device also underperformed when compared against A/G/ITO in terms of V_{oc}. Both A/ITO and A/5 Å F_4-TCNQ/ITO devices have similar figures of merit despite the lowering of the HIB in the latter through molecular modification. Taking our cue from A/ITO and A/5 Å F_4-TCNQ/ITO devices, we suggest that the hole injection at the anode may not be the limiting factor in our (unoptimized) devices. For instance, the FF is limited by the high R_s in all the devices.[47] The situation is worse for devices fabricated on G/ITO as they have further variability of the quality of graphene and areas of non-uniformity i.e. damaged graphene or areas without graphene. We correlate the effect of current leakage current on the recorded V_{oc} by comparing A/5 Å F_4-TCNQ/G/ITO device with A/G/ITO in which the former which experiences larger leakage current also has a simultaneous lowering of V_{oc}. These issues associated with our devices mask the full potential that could have

been achieved by our modified device structure, and do not provide a fair platform for comparison of key device parameters.

5.7 Conclusion and Outlook

We have analysed the effect of modifying G/ITO and ITO with a thin layer of F_4-TCNQ on the orientation and energy level alignment on CuPc, as well as OPV device performance using 5 Å F_4-TCNQ/G/ITO as the anode. Templating of CuPc molecules such that they are 'lying' almost parallel to the substrate is achieved by G/ITO even with the inclusion of F_4-TCNQ, while CuPc on F_4-TCNQ/ITO still retains its standing configuration as on ITO. UV-Vis investigation reveals that an additional benefit associated with templating of CuPc molecules is the enhancement of light absorption normal to the substrate by over 40% as compared to the CuPc molecules standing perpendicular to the substrate. This is especially beneficial for solar cell devices since more energy can be harvested for the same active layer thickness. Small HIB of 0.17 eV and 0.12 eV are obtained for CuPc deposited on F_4-TCNQ modified G/ITO and ITO respectively, a notable decrease from 0.94 eV and 0.51 eV for the unmodified CuPc/G/ITO and CuPc/ITO samples respectively. These results suggest that F_4-TCNQ is a suitable work function modifier for G/ITO without having any measurable deleterious effect on the templating property of graphene. All these improvements however fail to translate into improved solar cell device performance. Conversely the device fabricated on 5 Å F_4-TCNQ/G/ITO perform worse than our reference device deposited on ITO in all aspects of V_{oc}, J_{sc}, FF and ultimately power conversion efficiency. We attribute the poor performance to the difficulty of obtaining continuous pristine graphene over the active areas probed, resulting in large leakage currents and due to the high roughness caused by damaged graphene. The latter may potentially act as charge traps hindering charge collection at the anode. Similar OPV parameters obtained for devices fabricated on ITO and 5 Å F_4-TCNQ/ITO in which the latter has a smaller HIB suggest that the HIB may not be the limiting factor in our (unoptimized) setup.

In order to identify the actual effect that CuPc templating and lowering of the HIB has on solar cell device parameters, it is imperative that the device structure is first optimized and the active areas only measure the effect from pristine graphene. The latter may be achieved by reducing the size of the active area (top contact mask size) or by increasing the area of pristine graphene. The roughness of ITO indirectly plays a part in damaging graphene since it allows water to be trapped between graphene and ITO during the wet transfer process. Evaporation of the trapped liquid pushes against graphene that is delicately balanced on protruding ITO grains separated by troughs of water and causes it to break. Alternatively, a modified method of graphene transfer such as the soft-transfer method proposed by Song *et al.*[46] can be considered. Only when these issues have been addressed can a fair assessment of the devices be made.

To elucidate the interaction between F_4-TCNQ and CuPc on G/ITO, controlled sub-monolayer growth of F_4-TCNQ and CuPc on atomically flat HOPG substrate can be investigated via STM. STM allows imaging of individual molecules and information about the DOS of the molecules can be determined through dI/dV plots as a function of tip bias. This allows us to map the variation of the DOS of individual molecules upon interaction between F_4-TCNQ and CuPc, as opposed to PES measurements which averages over several clusters of molecules. Alternatively, ultrahigh precision and low background PES[22,24,25] can be used for more accurate determination of surface states near the substrate interface at low CuPc coverage. Coupled with theoretical calculation of the actual relaxation energy of CuPc to determine the position of the ionized valence states, the spectrum of CuPc deposited on F_4-TCNQ/G/ITO near the substrate interface can be decomposed into its respective components to understand the contributions from the various DOS near the Fermi level.

Looking forward, we propose that with slight variation of the experimental methodology, the use of ITO electrodes can be eliminated in organic solar cells. Patterned graphene can be transferred to flexible polymers such as PET before sequential deposition F_4-TCNQ and the subsequent solar

cell active layers and contacts. While the concept of graphene-based electrodes to replace ITO in organic solar cell devices has been widely explored,[46,48–50] to our knowledge no group has simultaneously utilized the templating property of graphene and work function modification using 5 Å F_4-TCNQ in small molecule organic solar cell devices. Furthermore, the high sheet resistance of graphene electrodes (kΩ/□) can be reduced by doping with F_4-TCNQ.[46] Therefore, our proposed simple modification of the anode design might have potential in enhancing the performance of flexible organic solar cells utilizing planar polyaromatic molecules with similar electronic properties as the active layer.

5.8 References

1. Rand, B. P. *et al.* The Impact of Molecular Orientation on the Photovoltaic Properties of a Phthalocyanine/Fullerene Heterojunction. *Adv. Funct. Mater.* **22,** 2987–2995 (2012).

2. Hoshino, A., Takenaka, Y. & Miyaji, H. Redetermination of the crystal structure of alpha-copper phthalocyanine grown on KCl. *Acta Crystallogr. B.* **59,** 393–403 (2003).

3. Sullivan, P., Jones, T. S., Ferguson, a. J. & Heutz, S. Structural templating as a route to improved photovoltaic performance in copper phthalocyanine/fullerene (C60) heterojunctions. *Appl. Phys. Lett.* **91,** 233114 (2007).

4. Lee, W. H. *et al.* Surface-directed molecular assembly of pentacene on monolayer graphene for high-performance organic transistors. *J. Am. Chem. Soc.* **133,** 4447–54 (2011).

5. Scherrer, P. No Title. *Göttinger Nachrichten Gesell.* **2,** 98 (1918).

6. Heutz, S., Sullivan, P., Sanderson, B. M., Schultes, S. M. & Jones, T. S. Influence of molecular architecture and intermixing on the photovoltaic, morphological and spectroscopic properties of CuPc–C60 heterojunctions. *Sol. Energy Mater. Sol. Cells* **83,** 229–245 (2004).

7. Gilchrist, J. B., Basey-Fisher, T. H., Chang, S. C' E.*, Scheltens, F., McComb, D. W. & Heutz, S. Uncovering the Buried Interface in Molecular Photovoltaics. *Adv. Funct. Mater.* **24**, 6473-6483 (2014).

8. De Oteyza, D. G. *et al.* Inversed linear dichroism in F K-edge NEXAFS spectra of fluorinated planar aromatic molecules. *Phys. Rev. B* **86,** 075469 (2012).

9. Nardi, M. V. *et al.* Electronic properties of CuPc and H2Pc: an experimental and theoretical study. *Phys. Chem. Chem. Phys.* **15,** 12864–81 (2013).

10. Foweraker, A. R. & Jennings, B. R. Orientation of the electronic transitions in crystalline copper phthalocyanine by means of electric dichroism. *Spectrochim. Acta Part A: Mol. Spectrosc.* **31,** 1075–1083 (1975).

11. Kadish, K., Guilard, R. & Smith, K. M. *The Porphyrin Handbook: Phthalocyanines : properties and materials*. (Elsevier Science, 2003).

12. Cheng, C. H. *et al.* Organic solar cells with remarkable enhanced efficiency by using a CuI buffer to control the molecular orientation and modify the anode. *Appl. Phys. Lett.* **97,** 083305 (2010).

13. Farag, A. A. M., Optical absorption studies of copper phthalocyanine thin films. *Opt. Laser Technol.* **39,** 728–732 (2007).

14. Davidson, a. T. The effect of the metal atom on the absorption spectra of phthalocyanine films. *J. Chem. Phys.* **77,** 168 (1982).

15. Nair, R. R. *et al.* Fine structure constant defines visual transparency of graphene. *Science* **320,** 1308 (2008).

16. Reina, A. *et al.* Large area, few-layer graphene films on arbitrary substrates by chemical vapor deposition. *Nano Lett.* **9,** 30–35 (2009).

17. Wang, Z. *et al.* Technology ready use of single layer graphene as a transparent electrode for hybrid photovoltaic devices. *Physica E: Low-dimensional Syst. Nanostructures* **44,** 521–524 (2011).

18. Pirruccio, G., Martín Moreno, L., Lozano, G. & Gómez Rivas, J. Coherent and broadband enhanced optical absorption in graphene. *ACS Nano* **7,** 4810–7 (2013).

19. Koch, N., Duhm, S., Rabe, J., Vollmer, A. & Johnson, R. Optimized Hole Injection with Strong Electron Acceptors at Organic-Metal Interfaces. *Phys. Rev. Lett.* **95,** 237601 (2005).

20. Romaner, L. *et al.* Impact of Bidirectional Charge Transfer and Molecular Distortions on the Electronic Structure of a Metal-Organic Interface. *Phys. Rev. Lett.* **99,** 256801 (2007).

21. Toader, T., Gavrila, G., Braun, W., Ivanco, J. & Zahn, D. R. T. Valence band fine structure of copper phthalocyanine thin films: Effect of molecular orientation. *Phys. Status Solidi B* **246,** 1510–1518 (2009).

22. Mao, H. Y. *et al.* Mechanism of the Fermi level pinning at organic donor–acceptor heterojunction interfaces. *Org. Electron.* **12,** 534–540 (2011).

23. Zhong, S. *et al.* The role of gap states in the energy level alignment at the organic–organic heterojunction interfaces. *Phys. Chem. Chem. Phys.* **14,** 14127 (2012).

24. Sueyoshi, T., Fukagawa, H., Ono, M., Kera, S. & Ueno, N. Low-density band-gap states in pentacene thin films probed with ultrahigh-sensitivity ultraviolet photoelectron spectroscopy. *Appl. Phys. Lett.* **95,** 183303 (2009).

25. Sueyoshi, T. *et al.* Band gap states of copper phthalocyanine thin films induced by nitrogen exposure. *Appl. Phys. Lett.* **96,** 093303 (2010).

26. Yogev, S. *et al.* Fermi Level Pinning by Gap States in Organic Semiconductors. *Phys. Rev. Lett.* **110,** 036803 (2013).

27. Fukagawa, H. *et al.* The Role of the Ionization Potential in Vacuum-Level Alignment at Organic Semiconductor Interfaces. *Adv. Mater.* **19,** 665–668 (2007).

28. Lange, I. *et al.* Band Bending in Conjugated Polymer Layers. *Phys. Rev. Lett.* **106,** 216402 (2011).

29. Hwang, J. *et al.* Photoelectron Spectroscopic Study of the Electronic Band Structure of Polyfluorene and Fluorene-Arylamine Copolymers at Interfaces. *J. Phys. Chem. C* **111,** 1378–1384 (2007).

30. Tang, J. X., Lau, K. M., Lee, C. S. & Lee, S. T. Substrate effects on the electronic properties of an organic/organic heterojunction. *Appl. Phys. Lett.* **88,** 232103 (2006).

31. Fukagawa, H. *et al.* Origin of the highest occupied band position in pentacene films from ultraviolet photoelectron spectroscopy: Hole stabilization versus band dispersion. *Phys. Rev. B* **73,** 245310 (2006).

32. Shi, N. & Ramprasad, R. Dielectric properties of Cu-phthalocyanine systems from first principles. *Appl. Phys. Lett.* **89,** 102904 (2006).

33. Gao, W. & Kahn, A. Controlled p-doping of zinc phthalocyanine by coevaporation with tetrafluorotetracyanoquinodimethane: A direct and inverse photoemission study. *Appl. Phys. Lett.* **79,** 4040 (2001).

34. Gao, W. & Kahn, A. Controlled p doping of the hole-transport molecular material N, N′-diphenyl-N, N′-bis (1-naphthyl)-1, 1′-biphenyl-4, 4′-diamine with tetrafluorotetracyanoquinodimethane. *J. Appl. Phys.* **94,** 359–366 (2003).

35. Dong, M.-S., Wu, X.-M., Hua, Y.-L., Qi, Q.-J. & Yin, S.-G. Highly Efficient Simplified Organic Light-Emitting Diodes Utilizing F4-TCNQ as an Anode Buffer Layer. *Chinese Phys. Lett.* **27,** 127802 (2010).

36. Duhm, S. *et al.* Interdiffusion of molecular acceptors through organic layers to metal substrates mimics doping-related energy level shifts. *Appl. Phys. Lett.* **95,** 093305 (2009).

37. Wang, J., Liu, J., Huang, S. & He, G. Enhancing the Hole Injection and Transporting of Organic Light-Emitting Diodes by Utilizing Gradient Doping. *Mol. Cryst. Liq. Cryst.* **574,** 129–134 (2013).

38. Gao, W. & Kahn, A. Electronic structure and current injection in zinc phthalocyanine doped with tetrafluorotetracyanoquinodimethane: Interface versus bulk effects. *Org. Electron.* **3,** 53–63 (2002).

39. Witte, G. & Wöll, C. Growth of aromatic molecules on solid substrates for applications in organic electronics. *J. Mater. Res.* **19,** 1889–1916 (2004).

40. Jäckel, F. *et al.* Investigating Molecular Charge Transfer Complexes with a Low Temperature Scanning Tunneling Microscope. *Phys. Rev. Lett.* **100,** 126102 (2008).

41. Zahn, D. R. T., Gavrila, G. N. & Gorgoi, M. The transport gap of organic semiconductors studied using the combination of direct and inverse photoemission. *Chem. Phys.* **325,** 99–112 (2006).

42. Mativetsky, J. M., Wang, H., Lee, S. S., Whittaker-Brooks, L. & Loo, Y.-L. Face-on stacking and enhanced out-of-plane hole mobility in graphene-templated copper phthalocyanine. *Chem. Commun.* **50,** 5319–5321 (2014).

43. Singha Roy, S., Bindl, D. J. & Arnold, M. S. Templating Highly Crystalline Organic Semiconductors Using Atomic Membranes of Graphene at the Anode/Organic Interface. *J. Phys. Chem. Lett.* **3,** 873–878 (2012).

44. Lunt, R. R., Benziger, J. B. & Forrest, S. R. Relationship between crystalline order and exciton diffusion length in molecular organic semiconductors. *Adv. Mater.* **22,** 1233–6 (2010).

45. Park, H., Brown, P. R., Bulović, V. & Kong, J. Graphene as transparent conducting electrodes in organic photovoltaics: studies in graphene morphology, hole transporting layers, and counter electrodes. *Nano Lett.* **12,** 133–40 (2012).

46. Song, J. *et al.* A general method for transferring graphene onto soft surfaces. *Nat. Nanotechnol.* **8,** 356–62 (2013).

47. Servaites, J. D., Yeganeh, S., Marks, T. J. & Ratner, M. A. Efficiency Enhancement in Organic Photovoltaic Cells: Consequences of Optimizing Series Resistance. *Adv. Funct. Mater.* **20,** 97–104 (2010).

48. Kim, K. S. *et al.* Large-scale pattern growth of graphene films for stretchable transparent electrodes. *Nature* **457,** 706–10 (2009).

49. Wang, Y., Tong, S. W., Xu, X. F., Ozyilmaz, B. & Loh, K. P. Interface engineering of layer-by-layer stacked graphene anodes for high-performance organic solar cells. *Adv. Mater.* **23,** 1514–8 (2011).

50. Gomez De Arco, L. *et al.* Continuous, highly flexible, and transparent graphene films by chemical vapor deposition for organic photovoltaics. *ACS Nano* **4,** 2865–73 (2010).

Chapter 6 : Diffusion of F_4-TCNQ Molecules

6.1 Introduction

F_4-TCNQ molecules have been used successfully as a p-dopant of hole transport and active layers in OLED and OPV devices.[1–6] However, low molecular weight F_4-TCNQ is volatile and has low sticking coefficient thus increasing its propensity to diffuse through organic layers due to a concentration gradient.[3,7–9] This can lead to unintentional and uncontrolled doping of the subsequent layers which might have detrimental effects on the device. For instance, F_4-TCNQ diffusion to the emissive layer in OLED devices may lead to exciton dissociation due to the strong electron accepting property of F_4-TCNQ thereby quenching light emission.[4,10] Gao *et al.* probed the diffusion of F_4-TCNQ through polycrystalline ZnPc and amorphous α-NPD film using XPS by following the evolution of F 1s signal at the surface of the film to show the effect of crystallinity on diffusion.[3] They found that diffusion in polycrystalline ZnPc film occurs very rapidly and the intensity of the F 1s signal appears to saturate within tens of minutes from the onset of diffusion, while no diffusion was detected through the amorphous α-NPD film even after heating the film close to the sublimation temperature of F_4-TCNQ. More recently, Tyagi *et al.* used TOF-SIMS to determine the diffusion length of F_4-TCNQ in the presence of an external electric field through α-NPD as a function of F_4-TCNQ interlayer thickness.[11] They found that F_4-TCNQ diffuses through α-NPD at room temperature and the diffusion length is even larger than the film thickness used by Gao *et al.* regardless of the application of an external electric field. The conflicting observations may be due to the sensitivity of the two techniques used, where TOF-SIMS is able to detect in the parts per million (ppm) range while XPS is usually limited to parts per thousands (ppth) range.[12] It is further noted that both groups deposited F_4-TCNQ on different substrates, suggesting that the strength of the molecule-substrate interaction might have an effect on the diffusion of molecules. While F_4-TCNQ diffusion through organic materials has been extensively mentioned,[3,6–10,13] in-depth investigations concerning the various factors

which may exacerbate the quantity of the diffused species or the rate of diffusion have not been carried out.

In the organic systems fabricated on ITO and G/ITO in Chapter 5, we utilized F_4-TCNQ to modify the work function of the underlying substrate. A concentration gradient of F_4-TCNQ is set up between the ITO interface and the exposed CuPc surface. Therefore, the diffusion of the volatile F_4-TCNQ molecule through the CuPc bulk film, which might result in gradient doping of the films rather than only interface doping,[14] is a concern. PES data from Section 5.4 suggests that diffusion of F_4-TCNQ into CuPc has taken place close to the substrate interface. If the diffusion of F_4-TCNQ in CuPc films extends to the D/A interface in an organic solar cell device, it may modify the energy levels at that interface, resulting in inefficient exciton separation. We propose that the enhanced π-π interaction between the planar F_4-TCNQ molecules and underlying graphene film (cf. Section 4.4) may result in stronger interfacial adhesion, thus impeding the diffusion of F_4-TCNQ through the film as compared to structures deposited onto ITO. On the other hand, the vertical columnar packing of CuPc molecules on F_4-TCNQ/G/ITO (cf. Section 5.2) may enhance molecular diffusion of F_4-TCNQ as proposed by Gao *et al*..[3] Therefore, there are two main competing factors in our samples, namely substrate-F_4-TCNQ interaction and the packing of CuPc molecules, which can govern the rate and quantity of the diffused species.

In this chapter, we use TOF-SIMS to investigate the diffusion profiles of F_4-TCNQ into CuPc films when the films are deposited onto ITO, G/ITO and G/Cu. By comparing their profiles, we present a qualitative analysis of 1) the rate of F_4-TCNQ diffusion through CuPc films which have different packing orientations, and 2) an investigation of the effect of substrate-molecule interaction on the quantity of the diffused species. In addition, we also attempt to quantify the concentration of F_4-TCNQ molecules that diffuse into the bulk CuPc in the absence of calibration standards. This is performed by co-depositing a known amount of F_4-TCNQ in a CuPc matrix and comparing the intensity of the F^- signal of the fully diffused sample.

To ascertain if the concentration of F^- is sufficiently high to be detected by TOF-SIMS, we estimate the number of F^- fragments per unit volume in a uniformly and fully diffused sample. Based on the density of F_4-TCNQ molecules (1.65 g/cm^3) and the thicknesses of the F_4-TCNQ (5 Å) and CuPc (100 nm) films, the concentration of F_4-TCNQ in a CuPc film is approximately 2 x 10^{19} atoms/cm^3. This value is above the detection limit of F^- ions[15] in TOF-SIMS (~10^{16} atoms/cm^3) and therefore we regard this as a suitable technique for our investigation. The advantage of using TOF-SIMS for depth profiling is its high sensitivity; yet it is still challenging to use this technique on soft organic samples due to the ease of sample damage upon bombardment by the primary ion beam[16] and the need to probe molecular rather than elemental composition. However, optimization and control of the operating conditions of current and accelerating voltage,[17] and the development of cluster ion sources[18] have made it possible to extend this technique to organic and even biological samples in recent years.[19–21]

6.2 Diffusion of Interface F_4-TCNQ into Bulk CuPc Film Deposited on ITO, G/ITO and G/Cu

Figure 6-1 (a) shows a representative SIMS raw data plot of selected negative secondary ion fragment counts as a function of sputter time. Sputtering of the films was performed from the exposed side of CuPc films as shown by the direction of the arrow in the schematic in Figure 6-1 (b). The area shaded in grey in Figure 6-1 (a) marks the region where the TOF-SIMS detector is saturated by ion counts; C^- and C_4^- fragments which have their counts in this saturation regime are deemed too high to be accurately included in subsequent analysis due to detector saturation effects. To convert the x-axis from sputter time into depth in the absence of secondary physical measurements (eg. contact profilometer), we consider the point at which the CH^- signal drops by half its average value over the maximum plateau region, as the point at which the ion beam has just reached the substrate surface.[17] From the calibration of the thickness of the molecular film using QCM, this should correspond to a depth of 100 nm ± 5 nm. The total crater depth in Figure 6-1 (a) is therefore approximately 100 nm. The

horizontal axis on the top of Figure 6-1 (a) shows the diffusion profiles as a function of crater depth. According to the schematic in Figure 6-1 (b), x = 0 nm is designated as the exposed CuPc surface while 100 nm corresponds to the organic film-substrate interface. The CH^- fragment is chosen due to its stability in counts over a long sputter time, significantly high counts yet well below the detector saturation regime, and also the narrow deviation in CH^- counts between all the samples measured. The profile of the substrate 'marker layer' (In^- counts for ITO and Cu^- counts for Cu foil) is used as a secondary check to determine the accuracy of depth estimation.[22] The sputter time at which the CH^- counts are halved should coincide with the end of the prominent rising slope of the In^- or Cu^- counts before it plateaus out, which signals that the sputter beam has reached the bulk interface of the ITO substrate.

We note that this method of determining the sample thickness may suffer from poor accuracy due to 1) the knock-on effect by the primary ion beam which degrades depth resolution,[23] and 2) microscopic roughness of the surfaces especially for ITO (cf. Figure 2-13). Using a silicon substrate which has a sharp interface, the SIMS instrumental depth resolution is estimated to be approximately 3 nm (Appendix D). This is significantly smaller than the observed width of the slopes in the In^- and CH^- profiles near the substrate interface which is approximately 25 nm [Figure 6-1 (a)]; this slope is therefore attributed primarily to substrate roughness. The In^- signals are detected when the top of the ITO clusters are exposed to the sputter ion beam. The signal becomes more intense with increasing crater depth until it saturates beyond the ITO interface at x = 100 nm at which point a uniform film of ITO is present.[24]

Since slight changes in experimental conditions such as the beam energy might affect the absolute counts detected, the F^- counts of each sample are scaled relative to the CH^- counts (which is in turn adjusted to an average of 10^4 counts at the plateau region for all the samples). The adjusted F^- counts allow for more reliable comparison of the fluorine content present between samples. This procedure is verified against the $C_3H_2NCu^-$ counts, which are scaled in the same manner as F^-. The $C_3H_2NCu^-$ is a fragment that originates from CuPc. Due to the similar packing density of CuPc films (i.e. same matrix) and the same mass of the film

deposited regardless of the substrate, the $C_3H_2NCu^-$ counts should be the same across all the samples.

At the start of each depth profile, there is a transient, or 'pre-equilibrium', region due to the non-steady state sputter yield.[23,25,26] In this region, it appears that the F^- signal is enhanced, while the CH^- signal is depleted as compared to their bulk signal [Figure 6-1 (a)]. From the

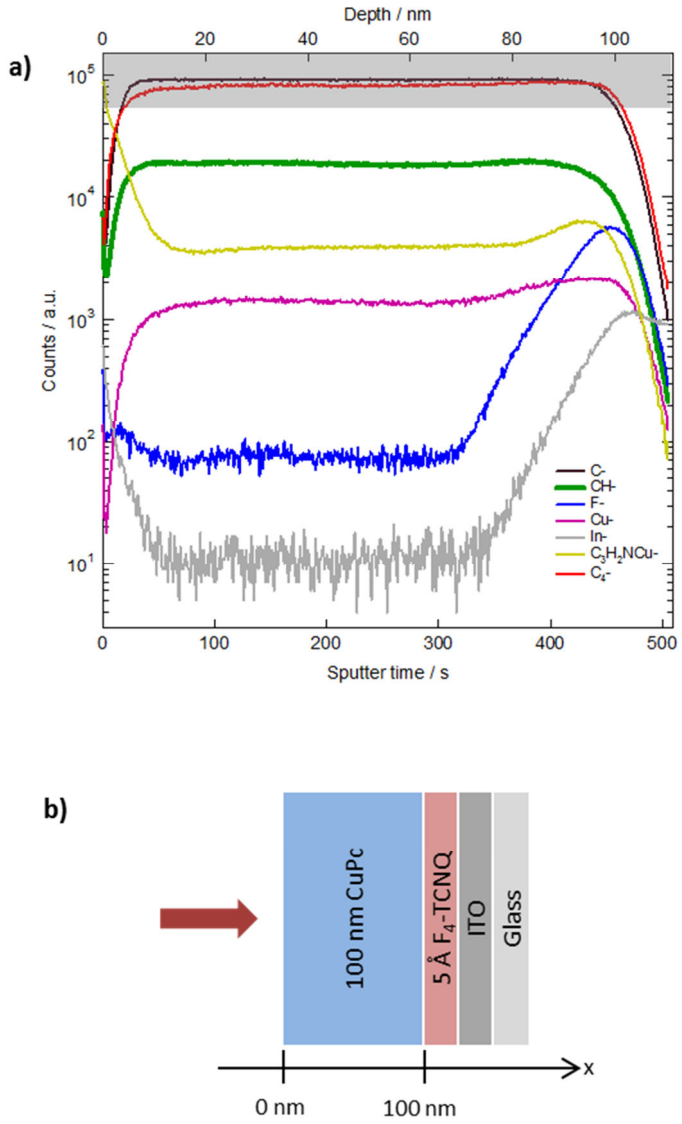

Figure 6-1 (a) Representative raw data plot of negative secondary ion counts as a function of sputter time (bottom axis) and crater depth (top axis) for 100 nm CuPc/5 Å F_4-TCNQ/ITO fully diffused sample. The grey shaded areas mark the region where the detector is saturated by ion counts. CH^- fragment shows significantly high and very stable counts for all the measured samples, hence the F^- counts will be normalized to the respective CH^- counts in each measurement. (b) Schematic diagram showing the direction of sputter as indicated with a bold arrow.

CH^- signal in Figure 6-1 (a), this region is estimated to be approximately 10 nm. During the pre-equilibrium region, it is impossible to extract quantitative information about the target's

composition. Due to this difficulty, the region between x = 0 to 10 nm will not be discussed in all subsequent profiles.

To investigate the diffusion of F_4-TCNQ through CuPc, it is important to establish the baseline fluorine contaminant present in our samples within the CuPc films and also at the substrate interface. This will help to eliminate confusion in subsequent measurements and distinguish between counts arising from intrinsic fluorine impurities and those due to actual F_4-TCNQ diffusion. Samples of 100 nm CuPc deposited onto clean ITO, freshly prepared G/ITO and as-received G/Cu substrates were prepared for this investigation. Figure 6-2 (a) shows the F^- depth profile for 100 nm CuPc prepared on ITO, G/ITO and G/Cu. The 100 nm CuPc/G/Cu sample shows a very low level of F^- counts of ~10 throughout the bulk CuPc and at the interface, indicating an insignificant amount of fluorine containing compounds both within the sublimation-purified CuPc powder and at the organic-substrate interface. Close to the substrate interface, there is a very slight enhancement of F^- counts which may be caused by surface fluorine contamination[15] or interface enhancement effect.[27] Both the 100nm CuPc/G/ITO and 100nm CuPc/ITO samples also show very low F^- counts in the bulk CuPc, but a steep increase in intensity near the substrate interface from around x = 70 nm. The shape and position of this slope coincides with the In^- profile, shown as a red curve at the bottom of the graph in Figure 6-2 (a). Since this trend is specific to ITO and G/ITO samples, we propose that the F^- ions originate from the intrinsic fluorine impurity in the commercial ITO substrate (Appendix E). The F^- profiles of 100 nm CuPc/ITO and 100 nm CuPc/G/ITO appear similar despite the inclusion of graphene, indicating that neither graphene nor the graphene transfer process introduced significant amounts of fluorine contaminants.

6.2.1 Influence of CuPc Molecular Packing on F_4-TCNQ Diffusion Dynamics

Having determined the baseline fluorine contamination in our samples, we probe the F^- profiles for the samples containing 5 Å F_4-TCNQ. Figure 6-2 (b) – (d) compare the F^-

diffusion profiles for 100 nm CuPc/5 Å F_4-TCNQ deposited on (b) G/Cu, (c) G /ITO and (d) ITO. All the samples were prepared together but analysed by TOF-SIMS at two different sessions. The 'fresh' samples were measured immediately after deposition (with a lapse of about 90 minutes to load the samples and to attain the required pressure), while the 'diffused' samples were kept in a glove box for one month before measurement. The lapse in time of about a month at room temperature is to ensure that the F_4-TCNQ molecules are fully diffused into the CuPc matrix and the systems have ideally reach diffusion equilibrium. We commence our analysis by comparing the F^- profiles for the 'fresh' and 'diffused' samples to determine the effect of time on the depth distribution of F^- fragments.

By comparing the TOF-SIMS profiles between the F_4-TCNQ containing samples and their controls, we observe that the diffusion of F_4-TCNQ has clearly taken place through the CuPc film. This is evident from the F^- fragments which are detected throughout the bulk film at a significantly higher level than the baseline count. The F^- counts are almost constant in the bulk CuPc film up to x = 70 nm, and the F^- counts increases steeply close to the substrate. This suggests that there are at least two distinct regions of F_4-TCNQ diffusion, 1) F_4-TCNQ molecules that are influenced by the substrate-molecule interaction near the surface and 2) the highly diffusive F_4-TCNQ species in the bulk CuPc film. The effect of the substrate will be analysed in more detail in the next section.

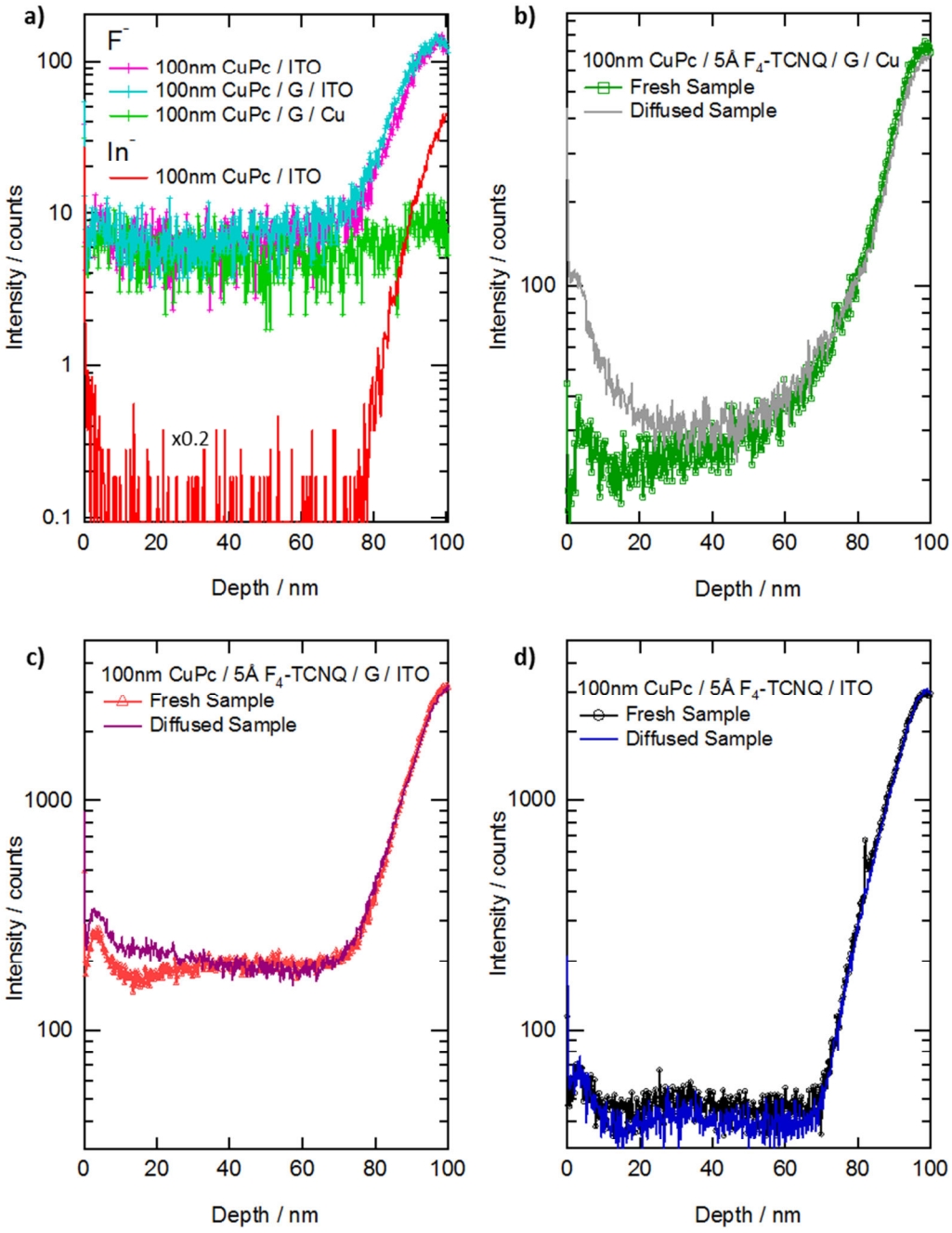

Figure 6-2 Intensity of F^- counts as a function of depth, with x = 0 nm referring to the exposed CuPc surface. (a) 'Control' samples without F_4-TCNQ to determine the concentration of F^- present at the substrate interface and in CuPc. (b) – (d) 100 nm CuPc/5 Å F_4-TCNQ on (b) G/Cu, (c) G/ITO and (d) ITO. 'Fresh' samples which were measured immediately after deposition are compared against similar samples that were measured one month after deposition ('diffused' samples), thus allowing the fluorine containing molecules to be fully diffused in the CuPc matrix. (c) and (d) are plotted on the same y-scale for ease of comparison.

'Fresh' F^- profiles of 100 nm CuPc/5 Å F_4-TCNQ/G/Cu, 100 nm CuPc/5 Å F_4-TCNQ/G/ITO and 100 nm CuPc/5 Å F_4-TCNQ/ITO shown in Figure 6-2 (b) - (d) respectively reveal that diffusion has taken place at room temperature in the CuPc film within 90 minutes of growth. These results corroborate previous findings that F_4-TCNQ fully diffuses through a similar

host matrix of ZnPc within 80 minutes of growth.[7,9] From previous XRD studies in Section 5.2 and cross-section TEM,[24] we infer that CuPc films form nano-sized crystals. Therefore F_4-TCNQ molecules are able to diffuse rapidly through the grain boundaries of CuPc.

For the 'diffused' F^- spectra, there is an obvious enhancement of F^- counts at the exposed CuPc surface for the 100 nm CuPc/5 Å F_4-TCNQ/G/Cu and 100 nm CuPc/5 Å F_4-TCNQ/G/ITO samples as compared to the 'fresh' samples. This data suggests that migration of F_4-TCNQ within the CuPc films on graphene modified surfaces is a dynamic process. The exposed surface of the film is a region of higher energy; therefore the fluorine molecules are preferentially drawn towards the surface with increasing time. On the other hand, both 'fresh' and 'diffused' F^- plots for the 100 nm CuPc/5 Å F_4-TCNQ/ITO sample appear almost identical indicating that diffusion equilibrium is rapidly achieved. We have excluded additional surface fluorine contamination as the cause of the increase in F^- counts since all three samples prepared on G/Cu, G/ITO and ITO were stored in the same manner in a glove box, but only the samples grown on graphene show an enhancement of surface fluorine [Figure 6-2 (b) and (c)]. Furthermore the F^- profiles for the films on G/Cu and G/ITO are affected up to approximately x = 40 nm and not solely at the exposed CuPc surface.

Nabok *et al.* has calculated that the exposed surface energy of π-conjugated molecules differs for various crystal planes and has related it to the preferential packing direction of the molecules.[28] In Section 5.2, we have determined that CuPc molecules are oriented differently on F_4-TCNQ pre-covered ITO and graphene modified surfaces – whereas they pack with their (1 0 0) plane parallel to the substrate in the former, it is the (1 1 -2) plane that is parallel to the substrate for the latter. The exposed (1 0 0) plane of CuPc has minimum surface energy as inferred from the preferred packing orientation of CuPc molecules on weakly interacting substrates.[29–31] We propose that the higher surface energy of the (1 1 -2) plane may be the driving force for continual dopant diffusion to the surface to minimize surface free energy of CuPc deposited on G/ITO and G/Cu substrates.[32] Hu *et al.* recently determine that the diffusion pathways and corresponding energy barriers vary between crystal planes,

particularly so at the exposed interface where the film may become distorted by the diffused dopants.[33] Therefore the diffusion profile of F_4-TCNQ in CuPc film depends on the strength of the diffusion barriers presented to F_4-TCNQ when going from the bulk phase to the substrate and vice versa. Complementary theoretical calculations would be required to verify the actual energy of the individual surfaces of CuPc and its effect on F_4-TCNQ diffusion.

6.2.2 Effect of Interfacial Interaction on F_4-TCNQ Diffusion

Next we compare the effect of interfacial interaction on F_4-TCNQ diffusion by examining the profiles for 100 nm CuPc/5 Å F_4-TCNQ/G/Cu and 100 nm CuPc/5 Å F_4-TCNQ/G/ITO in Figure 6-2 (b) and (c) respectively. The orientation of CuPc molecules on F_4-TCNQ pre-covered G/Cu and G/ITO is similar; hence the difference in their diffusion profiles can be attributed to the interaction between F_4-TCNQ and G/Cu or G/ITO. Despite both substrates being modified by a layer of graphene, the potential of the underlying substrate may not be fully screened by a layer of graphene.[34] For instance, the interaction between metals and π-conjugated molecules such as F_4-TCNQ can be enhanced by the overlap between the d-orbitals of the metal and π-orbitals from the molecules.[35,36]

Since the normalized background of F^- counts for the 100 nm CuPc/G/Cu film is about 10 counts throughout the CuPc film, any enhancement in F^- counts in the F_4-TCNQ containing sample is due to molecular diffusion of F_4-TCNQ. The Gaussian shaped F^- profile is typical of diffusion where the concentration gradient is low.[11,37] The diffusion length, L_D, of F_4-TCNQ is related to the FWHM of the Gaussian fitted profile of F^- counts by the following equations:

$$\sigma = \sqrt{2}\, L_D \qquad (6\text{-}1)$$

$$FWHM = 2.355\, \sigma \qquad (6\text{-}2)$$

where σ and FWHM are the standard deviation and the full width half maximum of the fitted (half) Gaussian distribution respectively as shown in Figure 6-3.[37] L_D is calculated to be 5.6 nm ± 0.2 nm for 100 nm CuPc/5 Å F_4-TCNQ/G/Cu. It must be noted that a single Gaussian curve is unable to fit the F^- profile adequately between x = 60 nm to 80 nm as shown by the shaded yellow portion in Figure 6-3 (a). While we did not investigate the origin of this observation in this report,[d] the F^- profile suggests that diffusion of F_4-TCNQ may be influenced by, or involves, at least three different mechanisms for the sample of 100 nm CuPc/5 Å F_4-TCNQ/G/Cu – 1) tightly bound F_4-TCNQ near the substrate interface from x = 80 to 100nm; 2) weakly bound F_4-TCNQ from x = 60 to 80 nm, and 3) highly diffusive F_4-TCNQ in the bulk CuPc (Figure 6-4).

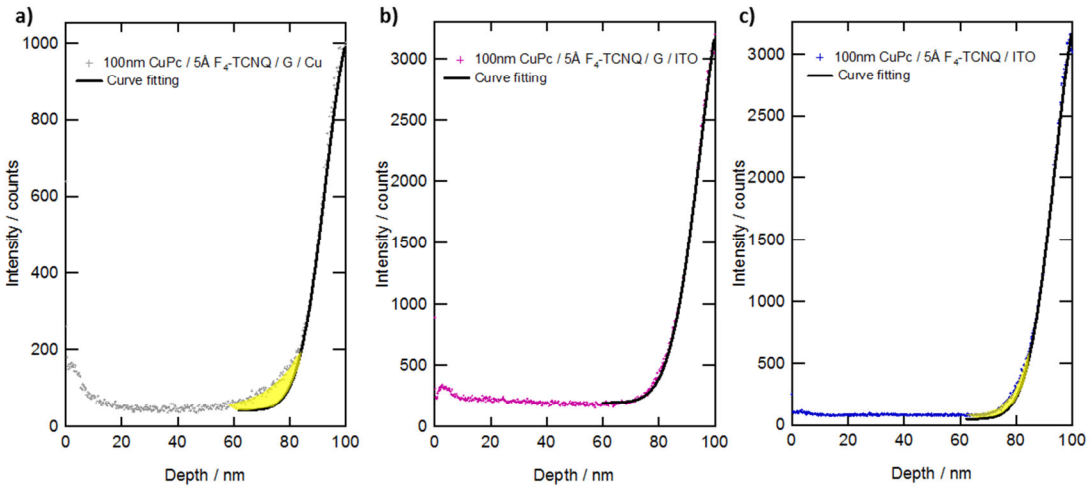

Figure 6-3 Curve fitting (black curve) for the various F^- profiles for 100nm CuPc/5 Å F_4-TCNQ on (a) G/Cu, (b) G/ITO and (c) ITO. The (half) Gaussian curve fitting does not fit the profiles of (a) and (c) well between x = 60 – 80nm as shown by the yellow shaded area.

Interpretation of the results for 100 nm CuPc/5 Å F_4-TCNQ/G/ITO shown in Figure 6-2 (c) on the other hand is not as straightforward as that for 100 nm CuPc/5 Å F_4-TCNQ/G/Cu since the substrate contains appreciable amounts of fluorine and it is therefore difficult to decouple the origin of fluorine from the substrate or the molecular film. The F^- counts for 100 nm CuPc/5 Å F_4-TCNQ/G/ITO however are significantly higher than the background counts by at least one order of magnitude in the bulk CuPc film and nearly 2 orders of magnitude near the

[d] The F^- profiles may be a convolution of a Gaussian curve and non-steady state Fickian diffusion.

substrate surface. Therefore we can approximate the F^- counts in 100 nm CuPc/5 Å F_4-TCNQ/G/ITO sample to originate almost exclusively from the F_4-TCNQ molecules. This approximation may also be extended to the sample prepared on ITO.

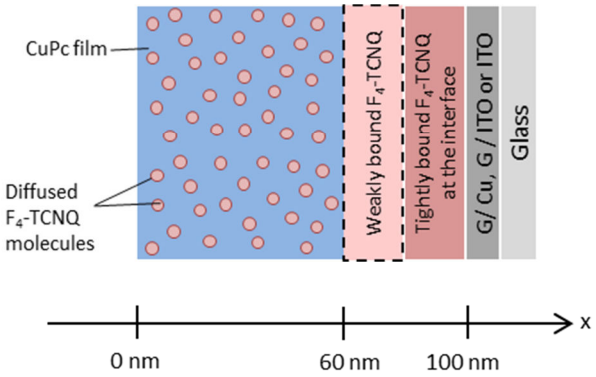

Figure 6-4 Schematic drawing showing F_4-TCNQ molecules at different distances from the substrate. F_4-TCNQ molecules are tightly bound at the substrate interface, and fully diffused in the bulk CuPc film. On G/ Cu and ITO substrates, there may be an intermediate region, shown by the dashed outline, where F_4-TCNQ molecules are weakly bound.

F_4-TCNQ diffusion in the 100 nm CuPc/5 Å F_4-TCNQ/G/ITO sample is more severe as compared to the sample on G/Cu since the normalized fluorine counts in the bulk CuPc film is about five times higher for the former as compared to the latter sample. The F^- counts near the substrate interface for the 100 nm CuPc/5 Å F_4-TCNQ/G/ITO sample can be fitted with a single (half) Gaussian curve [Figure 6-3 (b)] and the calculated diffusion length is approximately 7.6 nm ± 0.2 nm. For F_4-TCNQ in the 100 nm CuPc/5 Å F_4-TCNQ/G/ITO sample, there appears to be only two distinct regions, namely the bound F_4-TCNQ molecules at the substrate interface, and the fully diffused species, as indicated in Figure 6-4.

The longer L_D and higher concentration of diffused species for the sample on G/ITO indicate that the interfacial interaction between F_4-TCNQ and G/Cu is stronger than with G/ITO. This enables F_4-TCNQ to diffuse from the substrate into the bulk film more readily and in higher quantities on G/ITO. Still, the majority of the F_4-TCNQ molecules appear to be 'held' in the vicinity of the substrate interface for both substrates. The high concentration of F_4-TCNQ molecules close to the G/ITO substrate enables it to participate in charge transfer with CuPc molecules, resulting in the formation of new electronic states near the Fermi level at low

CuPc coverage as detected by PES (cf. Figure 5-8). Further from the interface, the concentration of F_4-TCNQ decreases and therefore charge transfer with CuPc is diminished.

6.2.3 Diffusion of F_4-TCNQ through CuPc Deposited on ITO *versus* G/ITO

Finally, we compare the diffusion profiles of F_4-TCNQ through a CuPc matrix when deposited on ITO as compared to G/ITO. Their spectra from Figure 6-2 (c) and (d) are plotted together and presented in Figure 6-5. There are two major parameters which differ between the samples, namely the orientation of the CuPc molecules and the substrate-F_4-TCNQ interaction, both of which can affect the diffusion profiles of F_4-TCNQ. The shape of the F^- profiles of 100 nm CuPc/5 Å F_4-TCNQ/ITO and 100 nm CuPc/5 Å F_4-TCNQ/G/ITO appear similar with relatively constant F^- counts in the bulk CuPc film, and a steady increase in counts beyond x = 70 nm up to the substrate interface.

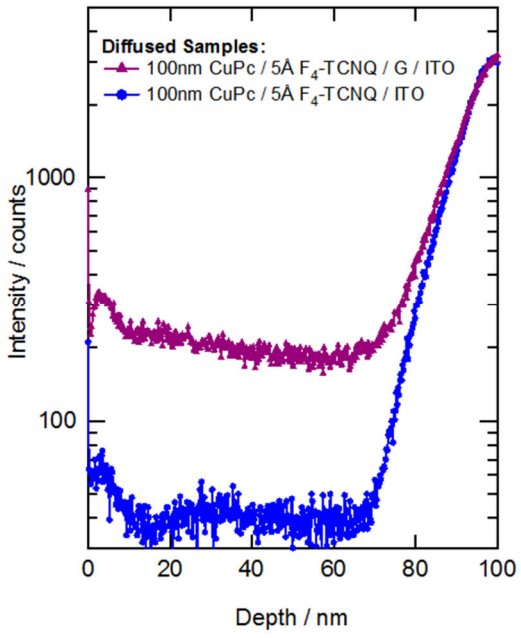

Figure 6-5 F^- depth profiles for fully diffused samples on ITO (blue circles) and G/ITO (purple triangle) respectively.

The slope of the F^- counts appears to increase more rapidly near the substrate (from x = 70 to 100 nm) for the sample on ITO as compared to the sample on G/ITO. L_D is calculated to be 6.8 nm ± 0.2 nm for 100 nm CuPc/5 Å F_4-TCNQ/ITO which is smaller than the 7.6 nm ± 0.2

nm previously obtained for 100 nm CuPc/5 Å F_4-TCNQ/G/ITO sample. Similar to the sample deposited on G/Cu sample, the F^- profile for 100 nm CuPc/5 Å F_4-TCNQ/ITO is not fitted well by a single curve as shown in Figure 6-3 (c), indicating that different diffusion mechanisms are present for the ITO and G/ITO samples. Collectively, the smaller L_D and the more rapidly rising F^- profile near the substrate interface for 100 nm CuPc/5 Å F_4-TCNQ/ITO imply that the interaction between F_4-TCNQ and ITO is stronger than F_4-TCNQ with G/ITO. This is in good agreement with the previously inferred substrate-F_4-TCNQ interaction strength from PES spectra of F_4-TCNQ thin films deposited on ITO and G/ITO in Section 4.3, and the SEM image in Figure 4-5. Both PES data and SEM images reveal that F_4-TCNQ molecules preferentially wet ITO as compared to G/ITO, implying that there is a preferable interaction between F_4-TCNQ and ITO.

Clearly the quantity of the diffused F_4-TCNQ in CuPc is higher for the organic films prepared on G/ITO as compared to ITO. In addition to the weaker interfacial adhesion between G/ITO and F_4-TCNQ, several other factors such as 1) numerous grain boundaries originating from nanocrystallites (cf. Section 5.2.2); 2) the less textured templated CuPc film (Figure 5-2); and 3) the columnar stacking of CuPc molecules almost perpendicular to the substrate[3] may facilitate diffusion of F_4-TCNQ through CuPc film deposited on G/ITO. Therefore the simplistic view of π-π interaction between graphene and F_4-TCNQ itself is inadequate to predict the relative quantity of F_4-TCNQ that diffuse from the G/ITO interface into the bulk film as compared to ITO, as the diffusion depends on a myriad of factors. It appears that the majority of the F_4-TCNQ molecules are restricted near the substrate interface for the 100 nm CuPc/5 Å F_4-TCNQ/ITO sample, resulting in a low concentration of diffused species detected in the bulk CuPc film. Although interfacial adhesion with F_4-TCNQ is deemed to be weaker for the 100 nm CuPc/5 Å F_4-TCNQ/ITO, the F^- profile indicates that a significant quantity of F_4-TCNQ molecules are still found close to the substrate interface.

There are currently no calibration standards for F_4-TCNQ which may allow us to directly quantify the amount of F_4-TCNQ molecules that have diffused into CuPc. In the next section,

we present a method to provide an estimate of the quantity of the diffused species. The values obtained should be treated with caution as there are several assumptions involved in the methodology and calculations. Our objective is to provide an estimate of the concentration which may allow us to comment on the effect of bulk doping on solar cell performance, and to relate it to the observed PES data for G/ITO and ITO samples.

6.3 Co-deposition of F_4-TCNQ and CuPc as a Method to Estimate Dopant Diffusion

A 'calibration standard' to estimate the dopant concentration in CuPc was prepared by co-depositing a known quantity of F_4-TCNQ into a CuPc host matrix. This sample was kept aside for between one and four months before measurement to allow the F_4-TCNQ molecules to be fully, and possibly uniformly, diffused in the CuPc matrix. The average F^- counts in the CuPc matrix should correspond to the mol% of the deposited F_4-TCNQ. We make the following assumptions in this section: first, F_4-TCNQ molecules have a sticking coefficient of unity during deposition in CuPc, and second, the matrix effects are similar in both sets of samples.

6.3.1 Preparation of Co-deposited Films

The concentration of F_4-TCNQ used for all the previous experiments detailed in Section 6.2, in mol%, can be calculated using the following considerations: there are 4 F_4-TCNQ molecules per unit cell volume of 1120 Å,[38] while there is 1 CuPc molecule per unit cell volume 582 Å.[39] The mol% for 5 Å F_4-TCNQ in 100 nm CuPc is

$$\frac{5*(\frac{4}{1120})}{1000*(\frac{1}{582})} * 100\% \approx 1.0\ mol\% \qquad (6\text{-}3)$$

In order to emulate these samples as a co-deposited mixed film, a growth rate of ~0.005 Å/s is required which is not detectable by the QCM. Therefore, a higher concentration of F_4-TCNQ was used for the preparation of the sample. For this experiment, 5 nm of F_4-TCNQ was co-

deposited in a matrix of 95 nm CuPc to achieve a total thickness of 100 nm on ITO. The concentration of F_4-TCNQ in this sample is ~11 mol%.

ITO substrates were chemically cleaned *ex situ* before loading them into the high vacuum OMBD chamber as described in the experimental section (Section 2.3.1). The base pressure of the system was 7 x 10^{-7} mbar and increased only marginally during film deposition. CuPc and F_4-TCNQ molecules were evaporated onto the substrates from separate Knudsen cells with growth rates of 0.95 Å/s and 0.05 Å/s respectively as monitored by separate QCMs. The variation in growth rates as a function of time was also recorded and plotted in Figure 6-6 (a). The samples were kept in a glove box and measured after one month and four months to allow the F_4-TCNQ molecules to be uniformly diffused in CuPc and to reach a state of diffusion equilibrium. The data obtained from the TOF-SIMS analysis were scaled in a similar manner as described in Section 6.2.

6.3.2 F^- Profiles for Co-Deposited Samples

Figure 6-6 (b) plots the F^- counts as a function of crater depth for the co-deposited sample measured one month and four months after deposition of the thin film.

Even after a lapse of four months, the measured F^- profiles appear similar to the sample measured after one month within 10% fluctuation which may be due to slight variation in instrumental parameters. This implies that a state of F_4-TCNQ diffusion equilibrium along the x-axis (depth) is already attained within one month. This is in good agreement with the observation that F_4-TCNQ molecules diffusion through CuPc occurs on a timescale of below ~90 minutes. Contrary to our initial expectation of homogeneous molecular diffusion that should result in a relatively flat F^- depth profile [dashed pink line in Figure 6-6 (b)], we obtain a non-uniform profile which implies that F_4-TCNQ molecules are not evenly distributed in the three dimensional film. However, the variation in F^- counts is not random but instead follows the fluctuations of the F_4-TCNQ deposition rate as indicated by the arrows between Figure 6-6 (a) and (b). In other words, the fully diffused F^- profile in CuPc appears to have a strong

correlation with the initial concentration of F_4-TCNQ. It should be pointed out that the fluctuations in F^- profile with depth [Figure 6-6 (b)] is much less (~ ±30% around the average value of F^- counts) as compared to the fluctuations in the growth rate (~ ±60% around 0.05 Å/s) [Figure 6-6 (a)]. This suggests that only around 50% of the F_4-TCNQ molecules remain 'pinned' at their initial deposited positions while the rest of the molecules have diffused away from their initial positions.

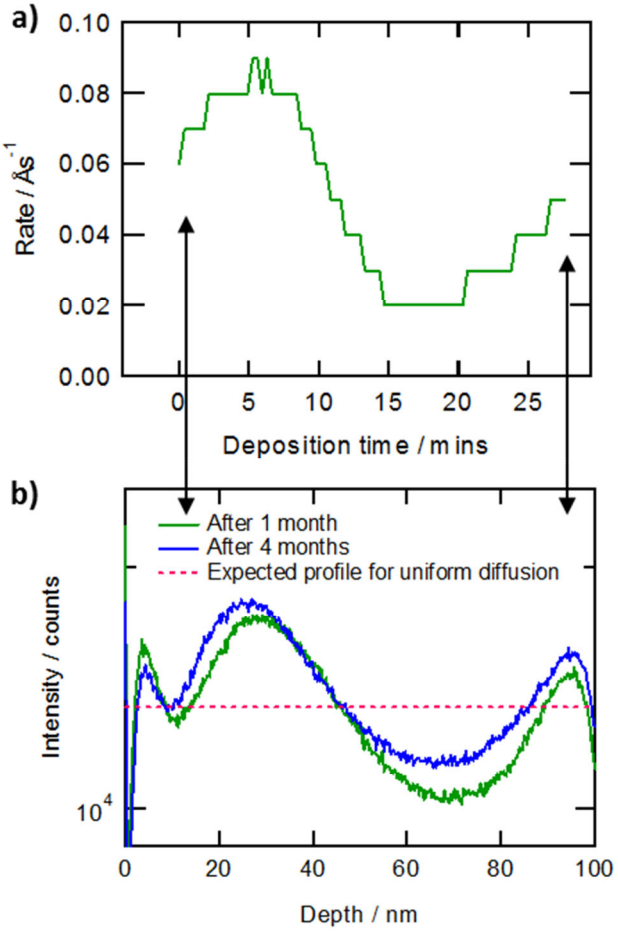

Figure 6-6 (a) Plot of deposition rate as a function of deposition time for F_4-TCNQ molecules in a CuPc matrix. (b) F^- profile of co-deposited sample consisting of 11 mol% F_4-TCNQ : 89 mol% CuPc measured after (green) 1 month, (blue) 4 months. The dashed pink line is the expected F^- profile for uniform diffusion. The region of the graph between the arrows marked in (a) and (b) identify that the variation in F- intensity with depth in (b) is related to the deposition rate of the F_4-TCNQ in the CuPc matrix.

To estimate the relationship between F^- counts and the concentration of F_4-TCNQ in the film, we average the total number of F^- counts from x = 10 nm to 90 nm (to exclude the pre-equilibrium region and substrate effects) for the 11 mol% F_4-TCNQ sample measured after one month of growth, and obtain a value of 1.3 x 10^4 counts. We repeated this for another co-

deposited sample with 6.5 mol% F_4-TCNQ concentration and the average F^- counts is 7.3 x 10^3 (Appendix F). From the control samples shown in Figure 6-2 (a), we ascertain that the average background F^- counts in the absence of F_4-TCNQ molecules (0 mol% F_4-TCNQ) is about 10 counts. By performing a linear fit of the average F^- counts (y) as a function of F_4-TCNQ concentration (x), and constraining the y-intercept (average counts) to the background counts of ~10 counts,[e] we obtain a calibration equation of

$$y = 1165x + 10 \qquad (6\text{-}4)$$

For the 100 nm CuPc/5 Å F_4-TCNQ/G/ITO sample, the average F^- counts in the bulk CuPc film is 1.9 x 10^2 which corresponds to a F_4-TCNQ concentration of 0.2 mol% that has doped the film. The average F^- counts for 100 nm CuPc/5 Å F_4-TCNQ/ITO sample on the other hand is only 41, hence the total diffused F_4-TCNQ concentration is 0.03 mol%. We estimate that the errors are in excess of 20% of the calculated value due to the fluctuations in F^- counts [(Figure 6-6 (b)], and due to the limited number of points used to plot the calibration curve.

These values indicate that diffusion of F_4-TCNQ molecules is almost one order of magnitude higher for 100 nm CuPc/5 Å F_4-TCNQ/G/ITO as compared to 100 nm CuPc/5 Å F_4-TCNQ/ITO. About 20% of the deposited F_4-TCNQ molecules diffused from the interface of G/ITO to bulk CuPc while only 3% of the molecules diffused from ITO when compared to the expected total F_4-TCNQ concentration (1 mol%). The vast difference in diffused quantity is the result of poorer interfacial adhesion of F_4-TCNQ with G/ITO, and is further aided by the structure and morphology of CuPc films on G/ITO, as explained in Sections 6.2.2 and 6.2.3.

The higher concentration of the diffused species in the G/ITO sample corresponds well with PES data previously obtained in Section 5.4 which reveals that CuPc and F_4-TCNQ form a new mixed state close to the G/ITO substrate. On the other hand, only interface charge

[e] We constrained the y-intercept to be approximately 10 counts during curve fitting as the best fit line of the points in the absence of limits will intercept the y-axis at a negative value which is physically not possible

transfer is observed for the films deposited on ITO substrate due to lower quantities of the diffused F_4-TCNQ species. In terms of solar cell device performance, the doping levels for CuPc in both 100 nm CuPc/5 Å F_4-TCNQ/G/ITO and 100 nm CuPc/5 Å F_4-TCNQ/ITO samples are lower compared to samples which are intentionally doped in organic semiconductor devices.[7] This suggests that the diffused species should not have a detrimental effect on the performance of the solar cell. On the contrary, F_4-TCNQ molecular doping on the order of three tenth of a percent has been shown to increase conductivity,[7,41] hence the unintentional doping within the whole organic film may be favourable in organic solar cells.

6.4 Conclusion and Outlook

We have investigated the diffusion of F_4-TCNQ through CuPc when deposited at the interfaces of G/Cu, G/ITO and ITO. Molecular diffusion of F_4-TCNQ through CuPc occurs within 90 minutes of deposition at room temperature on all samples. The diffusion profiles of F_4-TCNQ in CuPc deposited on graphene modified substrates change within one month, but the profiles of the film deposited on ITO remains nearly invariant over the same period of time. This suggests that the surface energy of the exposed CuPc film affects the diffusion profile over time as there is an additional driving force to lower surface energy. The surface energy is likely to be higher for the exposed (1 1 -2) CuPc plane (on G/Cu and G/ITO substrates) as compared to the (1 0 0) plane (on ITO). We also investigate the interfacial interaction between the substrate and F_4-TCNQ on the diffusion of F_4-TCNQ. Comparing the F^- profiles between the 100 nm CuPc/5 Å F_4-TCNQ/G/ITO and 100 nm CuPc/5 Å F_4-TCNQ/G/Cu sample, F_4-TCNQ diffusion is lower in the latter sample due to the stronger metal-F_4-TCNQ interaction, even through a layer of graphene.

The more pronounced F_4-TCNQ molecular diffusion in 100 nm CuPc/5 Å F_4-TCNQ/G/ITO as compared to 100 nm CuPc/5 Å F_4-TCNQ/ITO is consistent with our findings of weaker interfacial interaction in the former sample (cf. Section 4.3). Nano-sized crystals which form numerous grain boundaries for CuPc deposited on G/ITO, further aid the molecular diffusion.

By co-depositing a known amount of F_4-TCNQ in CuPc, and correlating the molecular concentration with average F^- counts, we are able to estimate the quantity of F_4-TCNQ diffused. Almost 20% of the deposited F_4-TCNQ in the sample 100 nm CuPc/5 Å F_4-TCNQ/G/ITO diffuses into the bulk CuPc resulting in an average F_4-TCNQ concentration of 0.2 mol% in CuPc. The concentration of F_4-TCNQ in CuPc is 0.03 mol% for the 100 nm CuPc/5 Å F_4-TCNQ/ITO which is 3% of the F_4-TCNQ deposited. The dopant concentrations for both films are low, and therefore should not have a detrimental effect on solar cell device performance. On the contrary, the mild doping of CuPc may enhance charge carrier mobility which may constitute an improved short circuit current in organic solar cell devices.

In this work we have presented a qualitative macro-scale description of F_4-TCNQ diffusion based on the inferences from the SIMS diffusion profiles. To confirm our interpretation of the systems, computational studies are required to calculate the energy of the various CuPc planes in the bulk film and at the exposed surface. In addition, the diffusion barrier energy for each of the CuPc orientations can be theoretically calculated to determine the preferred pathway for diffusion. Furthermore, complementary molecular dynamic simulations would be able to detail the evolution of F_4-TCNQ diffusion as a function of time and interaction forces in the system. This would enable us to understand the diffusion process from a molecular level.

In order to gain a better understanding regarding the evolution of F_4-TCNQ diffusion as a function of time, the deposition of the organic films should ideally be interfaced with the TOF-SIMS measurement chamber. This will reduce the time lapse between sample growth and measurement, thus the diffusion profiles can be investigated almost immediately following the onset of diffusion. Finally, we have probed the diffusion of F_4-TCNQ under static as-deposited conditions. However, for the proposed use of our structure in organic solar cells, the increase in sample temperature due to prolonged exposure to the sun has to be accounted for. This is because the diffusion constant varies as a function of temperature[42] and hence is more pronounced at elevated temperatures. This can be simulated *in situ* during TOF-SIMS measurement through radiative or resistive heating of the sample. Furthermore,

the built-in field in organic solar cells can also be simulated by application of an external field since ionized F_4-TCNQ molecules will be affected by the strength of the field leading to a change in depth profile.

6.5 References

1. Zhou, X. *et al.* Very-low-operating-voltage organic light-emitting diodes using a p-doped amorphous hole injection layer. *Appl. Phys. Lett.* **78,** 410 (2001).

2. Blochwitz, J., Pfeiffer, M., Fritz, T. & Leo, K. Low voltage organic light emitting diodes featuring doped phthalocyanine as hole transport material. *Appl. Phys. Lett.* **73,** 729 (1998).

3. Gao, W. & Kahn, A. Controlled p doping of the hole-transport molecular material N, N′-diphenyl-N, N′-bis (1-naphthyl)-1, 1′-biphenyl-4, 4′-diamine with tetrafluorotetracyanoquinodimethane. *J. Appl. Phys.* **94,** 359–366 (2003).

4. Huang, J. *et al.* Low-voltage organic electroluminescent devices using pin structures. *Appl. Phys. Lett.* **80,** 139 (2002).

5. Hanson, E. L., Guo, J., Koch, N., Schwartz, J. & Bernasek, S. L. Advanced surface modification of indium tin oxide for improved charge injection in organic devices. *J. Am. Chem. Soc.* **127,** 10058–62 (2005).

6. Dong, M.-S., Wu, X.-M., Hua, Y.-L., Qi, Q.-J. & Yin, S.-G. Highly Efficient Simplified Organic Light-Emitting Diodes Utilizing F4-TCNQ as an Anode Buffer Layer. *Chinese Phys. Lett.* **27,** 127802 (2010).

7. Gao, W. & Kahn, A. Controlled p-doping of zinc phthalocyanine by coevaporation with tetrafluorotetracyanoquinodimethane: A direct and inverse photoemission study. *Appl. Phys. Lett.* **79,** 4040 (2001).

8. Gao, W. & Kahn, A. Electronic structure and current injection in zinc phthalocyanine doped with tetrafluorotetracyanoquinodimethane: Interface versus bulk effects. *Org. Electron.* **3,** 53–63 (2002).

9. Duhm, S. *et al.* Interdiffusion of molecular acceptors through organic layers to metal substrates mimics doping-related energy level shifts. *Appl. Phys. Lett.* **95,** 093305 (2009).

10. Tyagi, P., Kumar, A., Giri, L. I., Dalai, M. K. & Tuli, S. Exciton quenching by diffusion of 2,3,5,6-tetrafluoro-7,7',8,8' -tetra cyano quino dimethane and its consequences on joule heating and lifetime of organic light-emitting diodes Priyanka. *Opt. Lett.* **38,** 3854–3857 (2013).

11. Tyagi, P., Dalai, M. K., Suman, C. K., Tuli, S. & Srivastava, R. Study of 2,3,5,6-tetrafluoro-7,7′,8,8′- tetracyano quinodimethane diffusion in organic light emitting diodes using secondary ion mass spectroscopy. *RSC Adv.* **3,** 24553 (2013).

12. Heard, P. J., Feeney, K. A., Allen, G. C. & Shewry, P. R. Determination of the elemental composition of mature wheat grain using a modified secondary ion mass spectrometer (SIMS). *Plant J.* **30,** 237–245 (2002).

13. Patankar, M., Joshi, K. & Narasimhan, K. Study of F4TCNQ dopant diffusion using transport measurements in organic semiconductors. *arXiv Prepr. arXiv1312.0223* 1–22 (2013).

14. Wang, J., Liu, J., Huang, S. & He, G. Enhancing the Hole Injection and Transporting of Organic Light-Emitting Diodes by Utilizing Gradient Doping. *Mol. Cryst. Liq. Cryst.* **574,** 129–134 (2013).

15. Martin, J. W. *et al.* Collection of airborne fluorinated organics and analysis by gas chromatography/chemical ionization mass spectrometry. *Anal. Chem.* **74,** 584–90 (2002).

16. Nguyen, T. C. *et al.* A Theoretical Investigation of the Yield-to-Damage Enhancement with Polyatomic Projectiles in Organic SIMS. *J. Phys. Chem. B* **104,** 8221–8228 (2000).

17. Brison, J., Muramoto, S. & Castner, D. G. ToF-SIMS Depth Profiling of Organic Films: A Comparison between Single-Beam and Dual-Beam Analysis. *J. Phys. Chem. C* **114,** 5565–5573 (2010).

18. Winograd, N. The Magic of Cluster SIMS. *Anal. Chem.* **77,** 142A–149A (2005).

19. Mouhib, T. *et al.* Molecular depth profiling of organic photovoltaic heterojunction layers by ToF-SIMS: comparative evaluation of three sputtering beams. *Analyst* **138,** 6801–6810 (2013).

20. Norrman, K. & Krebs, F. C. Lifetimes of organic photovoltaics: Using TOF-SIMS and 18O2 isotopic labelling to characterise chemical degradation mechanisms. *Sol. Energy Mater. Sol. Cells* **90,** 213–227 (2006).

21. Benninghoven, A. Chemical Analysis of Inorganic and Organic Surfaces and Thin Films by Static Time-of-Flight Secondary Ion Mass Spectrometry (TOF-SIMS). *Angew. Chemie Int. Ed. English* **33,** 1023–1043 (1994).

22. Py, M. A study of interfaces and nanostructures by time of flight mass spectrometry: towards a spatially resolved quantitative analysis. (2006).

23. Shimizu, N. & Hart, S. Applications of the ion microprobe to geochemistry and cosmochemistry. *Annu. Rev. Earth Planet. Sci.* **10,** 483–526 (1982).

24. Gilchrist, J. B., Basey-Fisher, T. H., Chang, S. C' E.*, Scheltens, F., McComb, D. W. & Heutz, S. Uncovering the Buried Interface in Molecular Photovoltaics. *Adv. Funct. Mater.* **24**, 6473-6483 (2014).

25. Dowsett, M. G., Ormsby, T. J., Cooke, G. A. & Chu, D. P. Ultralow energy secondary ion mass spectrometry and transient yields at the silicon surface. *J. Vac. Sci. Technol. B* **16,** 302 (1998).

26. Wittmaack, K. & Drummond, I. W. Transient Phenomena and Impurity Relocation in SIMS Depth Profiling using Oxygen Bombardment: Pursuing the Physics to Interpret the Data [and Discussion]. *Phil. Trans. R. Soc. Lond. A.* **354,** 2731–2764 (1996).

27. Storms, H. A., Brown, K. F. & Stein, J. D. Evaluation of a cesium positive ion source for secondary ion mass spectrometry. *Anal. Chem.* **49,** 2023–2030 (1977).

28. Nabok, D., Puschnig, P. & Ambrosch-Draxl, C. Cohesive and surface energies of π-conjugated organic molecular crystals: A first-principles study. *Phys. Rev. B* **77,** 245316 (2008).

29. Kambayashi, T. *et al.* Epitaxial Growth of a Copper-phthalocyanine on a Transparent Conductive Substrate with an Atomically Flat Surface. *Cryst. Growth Des.* **5,** 143–146 (2005).

30. Peisert, H. *et al.* Order on disorder: Copper phthalocyanine thin films on technical substrates. *J. Appl. Phys.* **90,** 466 (2001).

31. Sullivan, P., Jones, T. S., Ferguson, a. J. & Heutz, S. Structural templating as a route to improved photovoltaic performance in copper phthalocyanine/fullerene (C60) heterojunctions. *Appl. Phys. Lett.* **91,** 233114 (2007).

32. Ju Wook, L., Jeongyong, L., Sang-Gi, K., Kee-Soo, K. & Jin-Gun, K. Structural Modification of a Trench by Hydrogen Annealing. *J. Korean Phys. Soc.* **37,** 1034 (2000).

33. Hu, X. *et al.* Nitrogen atom diffusion into TiO2 anatase bulk via surfaces. *Comput. Mater. Sci.* **82,** 107–113 (2014).

34. Wu, Q.-H., Hong, G., Ng, T. W. & Lee, S. T. Substrate effect on the electronic structures of CuPc/graphene interfaces. *Appl. Phys. Lett.* **100,** 161603 (2012).

35. Braun, S., Osikowicz, W., Wang, Y. & Salaneck, W. Energy level alignment regimes at hybrid organic–organic and inorganic–organic interfaces. *Org. Electron.* **8,** 14–20 (2007).

36. Lichtenberger, D. L., Renshaw, S. K. & Bullock, R. M. Metal-acetylide bonding in (.eta.5-C5H5)Fe(CO)2C.tplbond.CR compounds. Measures of metal-d.pi.-acetylide-.pi. interactions from photoelectron spectroscopy. *J. Am. Chem. Soc.* **115,** 3276–3285 (1993).

37. Schubert, E. F. *Delta-doping of Semiconductors*. (Cambridge University Press, 1996).

38. Emge, T., Maxfield, M., Cowan, D. & Kistenmacher, T. Solution and Solid State Studies of Tetrafluoro-7,7,8,8-Tetracyano-p-Quinodimethane, TCNQF4. Evidence for Long-Range Amphoteric Intermolecular Interactions and Low-Dimensionality in the Solid State Structure. *Mol. Cryst. Liq. Cryst.* **65,** 161–178 (1981).

39. Hoshino, A., Takenaka, Y. & Miyaji, H. Redetermination of the crystal structure of alpha-copper phthalocyanine grown on KCl. *Acta Crystallogr. B.* **59,** 393–403 (2003).

40. Zhang, Y. *et al.* Molecular doping enhances photoconductivity in polymer bulk heterojunction solar cells. *Adv. Mater.* **25,** 7038–7044 (2013).

41. De Sio, A., Tunc, A. V., Parisi, J., Da Como, E. & von Hauff, E. Improving the photocurrent in low bandgap polymer: fullerene solar cells with molecular doping. in *SPIE Photonics Eur.* 84350E (2012).

42. Einstein, A. Über die von der molekularkinetischen Theorie der Wärme geforderte Bewegung von in ruhenden Flüssigkeiten suspendierten Teilchen. *Ann. Phys.* **322,** 549–560 (1905).

Chapter 7 : Thesis Summary

7.1 Thesis Summary

In this thesis, we aim to control the orientation of CuPc molecules in the donor layer of an OPV device, and to minimize the hole injection barrier between CuPc and the anode. We have presented a systematic modification of the anode ITO, by first overlaying graphene onto ITO as a structural template layer, and subsequently using an ultra-thin layer of F_4-TCNQ molecules to raise the substrate work function. Using a combination of PES, NEXAFS, XRD and J-V measurements, we attempted to relate the physical and electronic structure-function relationship of a CuPc small molecule based OPV device utilizing F_4-TCNQ/G/ITO as the anode. We show that using a combination of graphene template layer pre-covered with F_4-TCNQ is able to simultaneously able to cause CuPc molecules to nearly parallel to the substrate and reduce the hole injection barrier between CuPc and the anode.

In Chapter 3, successful templating of CuPc molecules deposited on as-received G/Cu is confirmed through XRD. Diffraction peaks originating from the (0 1 -2) and (1 1 -2) planes lying preferentially parallel to the substrate, in which the molecular plane of CuPc forms an angle of 9.0^o and 7.5^o with respect to the substrate respectively are observed. On the bare Cu foil, CuPc molecules are textured along the (1 0 0) plane, where the molecules are 'standing' on the substrate. These results provide definitive proof of the templating ability of graphene. It also suggests that ambiguity surrounding the templating property of transferred graphene for CuPc at room temperature deposition is attributed to the damage sustained by the graphene sheet during the transfer process, and the incomplete coverage of the substrate by graphene. This is been confirmed by our NEXAFS spectra that suggest that CuPc deposited on G/ITO adopts on average a tilted orientation, rather than the expected 'lying' orientation, due to the averaging effect of the beam. PES measurements reveal that inserting a graphene template layer on ITO lowers the substrate work function and leads to an increase in HIB

from 0.51 eV for CuPc/ITO to 0.94 eV for CuPc/G/ITO. Therefore, the G/ITO anode alone is not an ideal structure for OPV devices; further modification of the substrate is required to reduce the HIB.

In Chapter 4, we investigate F_4-TCNQ as a work function modifier for the G/ITO anode system, and compare the results against ITO. The work function of G/ITO increases to ~4.9 eV with 5 Å F_4-TCNQ deposited, while that of ITO is raised to ~5.1 eV. This is due to the transfer of electrons from the substrate to F_4-TCNQ molecules, resulting in the formation of dipoles at the substrate-molecule interface. PES data and SEM images reveal that F_4-TCNQ molecules have better wettability, or interfacial interaction, with ITO as compared to G/ITO. Structurally, on G/ITO, the F_4-TCNQ thin film appears textured along the (0 2 0) plane. Along this plane, the projection of the molecular plane, the fluorine and the cyano groups of F_4-TCNQ molecules onto graphene are maximized. In contrast, F_4-TCNQ molecules deposited onto ITO form large angles with the substrate, indicating that repulsion between the electronegative cyano and fluorine side groups of F_4-TCNQ with ITO surface may be the driving factor for this orientation. The orientation of the F_4-TCNQ molecules on G/ITO suggests that the templating property of graphene may be propagated through the F_4-TCNQ layer.

The strategies of using graphene as a template layer, and an ultra-thin F_4-TCNQ film to raise the work function of G/ITO are combined in Chapter 5. First, we confirm that inserting the F_4-TCNQ film does not interfere with the orientation of CuPc deposited on our model system G/Cu. Next we show that CuPc films are similarly textured on G/ITO, although the (1 0 0) diffraction observed in non-templated CuPc films is present. This observation is due to the issues addressed previously in Chapter 3. In addition, we discuss the effect of substrate roughness on the resulting crystallite size, and how this can lead to erroneous interpretation of graphene structural template. The optical absorptivity of CuPc is ~43% higher following templating due to the larger overlap between the transitional dipole moment of CuPc and the electric field vector of light. Through PES, we determine that raising the effective substrate

work function using F_4-TCNQ is able to reduce the HIB to 0.17 eV and 0.12 eV for CuPc/F_4-TCNQ/G/ITO and CuPc/F_4-TCNQ/ITO respectively. Collectively, the templated CuPc molecules, which have been shown to enhance charge and exciton transport perpendicular to the substrate, the enhanced optical absorptivity and the low HIB for CuPc/F_4-TCNQ/G/ITO should translate into superior OPV device performance. However, this is not observed in our OPV devices due primarily to the poor quality of the transferred graphene, and the high series resistance of the unoptimized cells. However, we rationalize that if these issues can be overcome, there should be a significant improvement in OPV device performance based on this design strategy.

The diffusion of F_4-TCNQ molecules through the CuPc matrix is studied in Chapter 6. This is motivated by reports of the propensity of F_4-TCNQ molecules to diffuse through organic materials. Using TOF-SIMS to perform depth profiling, we investigate the effect of the packing order of CuPc on the rate of diffusion of F_4-TCNQ, and the interfacial interaction between F_4-TCNQ and the substrate (G/ITO, G/Cu and ITO) on the quantity of the diffused species. Molecular diffusion of F_4-TCNQ through CuPc occurs within 90 minutes of deposition at room temperature on all the samples. The diffusion profiles of F_4-TCNQ in CuPc deposited G/ITO and G/Cu show an enhancement in surface counts after one month. The surface energy of the exposed CuPc film deposited on these substrates may be the additional driving force for F_4-TCNQ diffusion. Diffusion of F_4-TCNQ molecules on G/ITO is more pronounced than that on G/Cu, revealing the role of interfacial interaction on the quantity of diffused F_4-TCNQ. Similarly, F_4-TCNQ diffusion is more pronounced for the film on G/ITO as compared to ITO, corroborating the findings of poorer interfacial adhesion between F_4-TCNQ and G/ITO in Chapter 4. The columnar one dimensional structure of CuPc in the latter is suggested to enhance diffusion through the bulk film. Finally, we fabricated a 'characterization standard' to determine the concentration of the diffused species. We find that the majority of F_4-TCNQ molecules are still tightly bound close to the substrate interface, while the dopant concentration of F_4-TCNQ in CuPc is only 0.03 mol% and 0.2 mol% for the

ITO and G/ITO samples respectively. At these concentrations, F_4-TCNQ does not appear to have any deleterious effect on the OPV device.

7.2 Future Work

Presently one of the biggest issues that we face in this dissertation is the poor quality of transferred graphene. This problem may be addressed by using a new method of graphene transfer proposed by Song *et al.*[1] that allows for controllable and precise placement of graphene on a variety of substrates, with minimum residue from the transfer process. This is required to fully elucidate the impact of our anode modification on OPV device performance. We propose that by transferring pre-patterned graphene to a flexible substrate, our design strategy may be extended to a flexible OPV small molecule device to simultaneously template planar polyaromatic molecules with similar electronic properties as the active layer, reduce the HIB barrier, and dope graphene sheet to reduce sheet resistance.

Concerning the valence band spectra of CuPc/F_4-TCNQ/G/ITO in Chapter 5, the mixed CuPc – diffused F_4-TCNQ phase close to the G/ITO substrate interface is still not well explained. Techniques such as dI/dV characterization using *in-situ* STM at sub-monolayer coverage can be employed to provide information regarding local density of states of individual CuPc and F_4-TCNQ molecules before and after interaction. This technique can help to clarify if the mixed state observed in PES is a result of the formation of charge-transfer complexes, or otherwise due to averaging effect of the PES beam over ionized and neutral molecules, or both. In addition, TOF-SIMS reveals that F_4-TCNQ diffuses into the bulk CuPc film, and there are two distinct regions, namely, a tightly bound region of F_4-TCNQ close to the substrate interface which extends ~20 nm into CuPc, and diffused F_4-TCNQ in the bulk CuPc. The interactions between CuPc and F_4-TCNQ molecules over these distinct regions may vary, giving rise to evolving electronic properties of CuPc across the 100 nm thick CuPc film. The evolution of CuPc electronic properties over this thickness cannot be probed by PES alone due to limitation of sample charging at thicker films.[2] Instead, Kelvin probe force microscopy

(KPFM) which can measure the electronic properties of thick films over 100 nm, may be utilized to examine the degree of charge transfer between CuPc and F_4-TCNQ at increasing distances from the substrate interface. The evolution of the HIB and work function with increasing CuPc film thickness can also be studied. This technique may also be employed to study the band bending in the system of CuPc/F_4-TCNQ/ITO as the space charge region can extend several tens of nanometers.[2] Investigating the electronic properties of the CuPc film at the thickness used in solar cell devices (ie, 30 nm CuPc) will allow for more accurate assessment of pre-covering the substrate with a thin layer of F_4-TCNQ on device performance.

Finally, while preliminary TOF-SIMS work has provided much qualitative insights into the macroscopic diffusion of F_4-TCNQ into CuPc, quantitative data is still lacking. As explained in Chapter 6, theoretical calculations of the surface energy and diffusion barrier for each plane of CuPc molecules, together with molecular dynamic simulation showing the evolution of F_4-TCNQ diffusion through CuPc, is required for a more comprehensive understanding of the system. More sets of 'calibration standards' will help to reduce the uncertainty in the calculation of the concentration of diffused species. Finally, to relate the diffusion data directly to OPV devices, the effect of the temperature and internal electric field on the F_4-TCNQ diffusion profile has to be considered.

7.3 References

1. Song, J. *et al.* A general method for transferring graphene onto soft surfaces. *Nat. Nanotechnol.* **8,** 356–62 (2013).

2. Lange, I. *et al.* Band Bending in Conjugated Polymer Layers. *Phys. Rev. Lett.* **106,** 216402 (2011).

Appendix A – Characterization of G/Si

Graphene was first transferred onto SiO_2 (G/Si) before it was transferred onto ITO. As SiO_2 is flatter and G/SiO_2 has been well characterized, it was used as a model substrate to practice the transfer process. G/Si was characterized with (a) and (b) optical microscopy, (c) and (d) AFM, (e) SEM and (f) Raman spectroscopy as shown in Appendix A. The scale bars are 50 µm for the optical images, 500 nm for the AFM images, and 1 µm for the SEM image. Arrows in (a) – (d) reveal holes, tears or incomplete coverage in the graphene sheet, dashed circles highlight defects or residues and brighter streaks correspond to wrinkles. Similar observations have been made for G/ITO. The increasing dark contrast patches in (e) correspond to multilayer graphene. Raman spectroscopy in (f) reveals that the defect density of G/Si is significantly lower than G/ITO, indicating that the inherently rough ITO substrate is probably the main cause of the poor quality of graphene transfer.

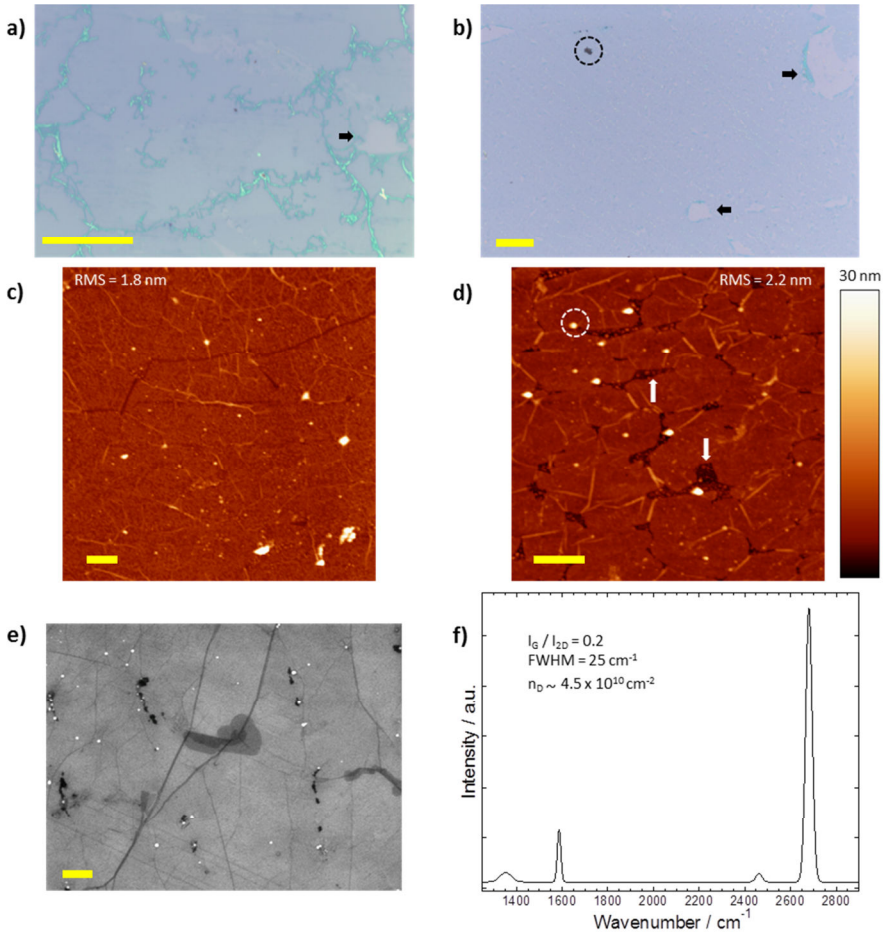

Appendix B – Solar Cell Data

The table shown in Appendix B summarises the solar cell device parameters for the different batches of solar cells fabricated. The cell structure is shown in Figure 3-8 (a).

Batch No.	Interlayer(s)					Ave Isc / A	Ave Jsc /mAcm-2	Ave Voc /V	Ave FF	PCE / %
	With F4-TCNQ		Without F4-TCNQ							
	Non-templated	With Graphene	Non-templated	With Graphene	With PTCDA					
1			✓			2.92E-04	2.36	0.39	0.35	0.33
				✓		1.52E-04	1.22	0.30	0.10	0.10
2			✓			3.44E-05	0.28	0.13	0.27	0.01
					✓	4.92E-05	0.40	0.15	0.27	0.02
3			✓			1.05E-04	0.84	0.25	0.26	0.05
				✓		6.63E-05	0.54	0.22	0.23	0.03
4	✓					6.91E-05	0.86	0.32	0.27	0.07
		✓				4.41E-05	0.64	0.29	0.24	0.05
5	✓					2.40E-04	1.00	0.41	0.27	0.11
		✓				8.25E-05	0.66	0.20	0.24	0.04
			✓			1.32E-04	1.06	0.41	0.27	0.12
				✓		9.50E-05	0.77	0.31	0.24	0.05

Appendix C – Edge Angles of F_4-TCNQ Crystallites

The tables in Appendix C show the values of the measured edge angles (in degrees) of F_4-TCNQ crystallites on G/ITO and ITO from AFM images.

Edge Angles of F4-TCNQ/G/ITO in degrees								
76	53	61	53	67	76	42	53	61
74	61	84	62	31	66	61	66	62
53	67	45	59	80	73	74	52	60
78	81	55	84	81	72	75	54	51
67	58	50	84	54	71	71	52	66
50	71	58	66	86	55	79	58	57
68	50	48	44	44	54	76	76	64
73	44	72	76	80	54	53	50	65
44	71	52	86	50	77	49	61	62
56	59	58	57	61	60	74	54	64
Average angle/ deg		62						
Standard deviation		12						

Edge Angles of F4-TCNQ/ITO in degrees								
53	54	55	34	54	47	34	25	43
37	41	66	49	53	47	39	33	43
32	38	40	21	34	47	62	63	45
51	46	44	44	46	42	44	50	43
35	47	50	36	36	45	45	48	72
50	55	79	40	42	38	32	76	69
38	50	50	54	45	45	42	26	55
35	53	26	38	45	60	49	45	52
34	55	31	54	50	42	31	45	34
42	67	40	30	38	49	39	44	80
Average angle/ deg		45						
Standard deviation		12						

Appendix D – Depth Resolution for TOF-SIMS

The knock-on effect by the primary ions degrades the depth resolution in TOF-SIMS. According to the International Union of Pure and Applied Chemistry (IUPAC), the depth resolution Δz is given as the distance over which the change between 16% and 84% of the intensity of the profile at a sharp interface is measured. Using a co-deposited sample of CuPc and F_4-TCNQ molecules on Si as shown in Appendix D, Δz is estimated to be approximately 3 nm.

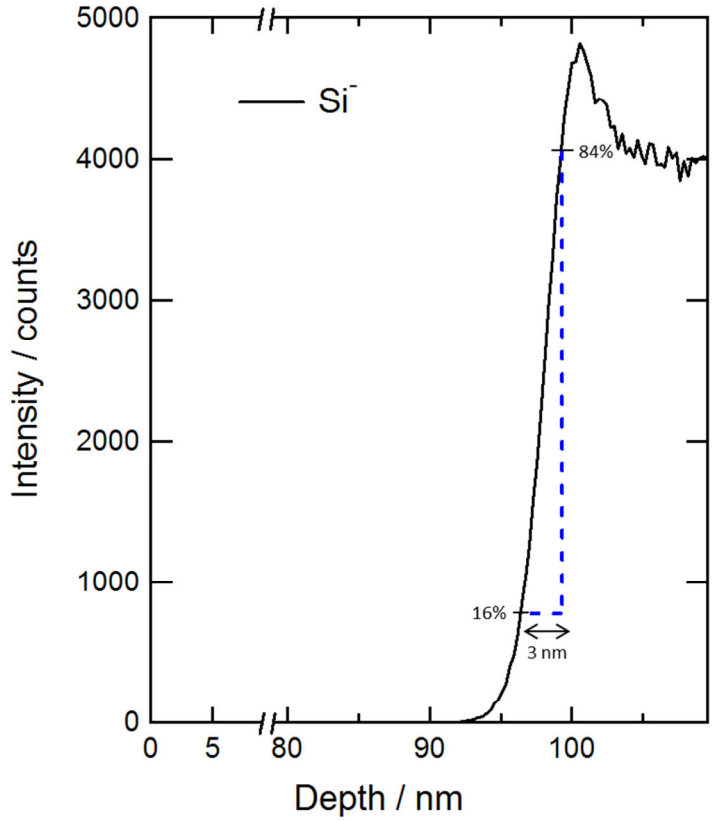

Appendix E – TOF-SIMS Depth Profile of ITO

The graph in Appendix E shows a TOF-SIMS profile as a function of sputter time through a clean ITO substrate. Significant F^- counts is detected at ITO surface and extends into the bulk ITO sample.

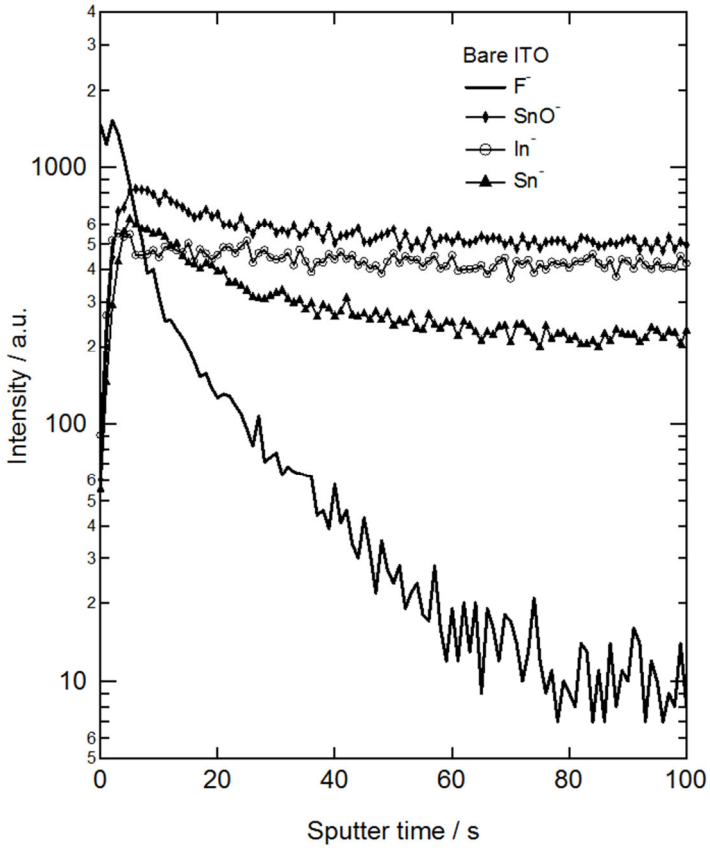

Appendix F – TOF-SIMS Depth Profile of 6.5mol% F_4-TCNQ Co-deposited with CuPc

The F^- depth profile of a co-deposited sample with 6.5 mol% F_4-TCNQ in CuPc deposited on ITO is shown in the graph Appendix F.